

Numerical Modelling of Suspension High Velocity

Oxy Fuel (S-HVOF) Thermal Spray

Thesis submitted in fulfilment of the requirements for the degree of

Doctor in Philosophy

Engineering.

August 2020,

By Sunil K. Chadha

Abstract

Suspension high velocity oxy fuel (SHVOF) thermal spray is an emerging technology used to deposit nano and submicron particles onto the surface of a component to form dense coatings with a fine microstructure. Coatings are deposited onto components to improve their performance by modifying the components surface properties. Numerical models have been employed within the open literature to improve the understanding of the process. This thesis focuses on development of a new thermal spray technology, a hybrid nozzle, that allows for the deposition of a composite coating formed from two materials with drastically different properties. Oxygen sensitive materials such as graphene nanoplatelets degrade when exposed to oxygen at high temperatures. A radial injection allows for a reduction of the time the particles are exposed to oxygen at high temperatures. A physical shroud has been designed based upon the modelling work within this thesis to prevent mixing of ambient oxygen within the jet. The physical shroud is combined with a shrouding gas to delay the mixing of oxygen. A combination of a radial injection, a physical shroud and a shrouding gas allows for a lower oxygen content within the jet and a reduction of the residence time of the particles within the jet. The axial injection within the combustion chamber can be simultaneously used for injecting a feedstock containing ceramic particles. The combined radial and axial injection are expected to allow for a significant improvement in the deposition of composite coatings. The hybrid nozzle is a completely new concept which offers fundamental changes over the traditional SHVOF thermal spray design.

Numerical models employed within the literature to predict the flow behaviour within SHVOF thermal spray have suffered from a number of flaws. The prior combustion models employed over predict the gas temperature within the combustion chamber when compared to the adiabatic flame temperature. Additionally, prior combustion

models demonstrate unphysical species compositions away from the flame front. This thesis employs a robust treatment to model the combustion reaction within SHVOF thermal spray to better predict the combustion chamber temperature and species composition. This approach avoids the overprediction in the adiabatic flame temperature as seen with the global single step mechanism currently employed within the literature to model SHVOF thermal spray. Additionally, the numerical models to determine the heat transfer coefficient previously employed within the literature underpredict the particle temperatures by as much as 40 % when compared to experimental measurements. This thesis evaluates the effects of the Mach number and the Knudsen number on the Nusselt number to better predict the heat transfer coefficient for the suspension particles. The models are validated against ensemble averaged inflight particle temperature measurements obtained from the commercially available Accuraspray G4 diagnostic system. It is shown that accounting for Mach number effects better predicts the particle temperature however accounting for Knudsen number effects provides the most accurate prediction of the heat transfer to particles within suspension high velocity oxy fuel thermal spray.

Finally, this thesis presents the first ever high-fidelity investigation into the combustion chamber for SHVOF thermal spray using a coupled volume of fluid and discrete particle model with the large eddy simulation scale resolving method. This multiscale approach provides a significant reduction in the computational cost over the standalone volume of fluid framework and a significantly higher fidelity over the standalone discrete particle model framework. The framework has been developed to expand the understanding within an SHVOF thermal spray combustion chamber; to characterise and inform the injection for use in lower fidelity models. From this approach more representative suspension injection conditions can be used for lower fidelity DPM - RANS methods. From the numerical modelling undertaken a modified injector design is proposed to reduce clogging within the combustion chamber.

Journal Publications

Effect of nozzle geometry on the gas dynamics and evaporation rates of Suspension High Velocity Oxy Fuel (SHVOF) thermal spray: A numerical investigation By S. Chadha, R. Jefferson-Loveday and T. Hussain. *Surf. Coatings Technol.* **2019**, 371 (15), 78–89.

A Computational and Experimental Investigation into Radial Injection of Suspension in Suspension High Velocity Oxy Fuel (SHVOF) Thermal Spray. By S. Chadha, R. Jefferson-Loveday, F. Venturi, T. Hussain. *Thermal Spray. J. Therm. Spray Technol.* **2019**, 28 (6), 1126–1145.

Modelling Knudsen Number Effects in Suspension High Velocity Oxy Fuel Thermal Spray. By S. Chadha, R. Jefferson-Loveday and T. Hussain. *International Journal of Heat and Mass Transfer*, **2020**, 152

A High-Fidelity Simulation of the Primary Breakup Within Suspension High Velocity Oxy Fuel (SHVOF) Thermal Spray Using A Coupled VOF and DPM Model. By S. Chadha, R. Jefferson-Loveday and T. Hussain. *International Journal of Multiphase Flows*, **2020**,

Conference Proceedings

A Novel Numerical and Experimental Investigation into Radial Injection for Suspension High Velocity Oxy Fuel (SHVOF) Thermal Spray, By S. Chadha, R. Jefferson-Loveday, T. Hussain. *ITSC Conference Proceedings*, Pages 612-619, 2019.

Cold spraying of metallic powders onto polymeric substrates: Influence of gas preheating temperature on the coating deposition, By A. Sabard, A. Albassam, S. Chadha, T. Hussain *ITSC Conference Proceedings*, Pages 159-165, 2018.

Contents

Abstract	i
List of Figures:	x
List of Tables.....	xxii
Acronyms	xxiv
Chapter 1: Introduction	1
1.1 Surface Engineering and Thermal Spray.....	1
1.2 Applications for Thermal Spray Coatings.....	3
1.3 Suspension High Velocity Oxy Fuel (SHVOF) Thermal Spray Process	6
1.4 High Velocity Oxy Fuel Thermal Spray Attachments	7
1.5 Motivations.....	8
1.6 Aims and Objectives	11
Chapter 2: Literature Review	13
2.1 Compressible Effects.....	15
2.2 Combustion	19
2.3 Primary Breakup.....	22
2.4 Droplet Distribution	24
2.5 Secondary Droplet Breakup	26
2.6 Slurry Droplet Evaporation	30
2.7 Modelling High Velocity Oxy Fuel (HVOF) Thermal Spray	32
2.7.1 Effect of Combustion Model.....	33

2.7.2	Effect of Numerical Scheme	36
2.7.3	Effect of Equivalence Ratio	37
2.8	Modelling Suspension High Velocity Oxy Fuel Thermal Spray.....	40
2.8.1	Effect of Injection Droplet Diameter	41
2.8.2	Effect of Type of Injection.....	44
2.8.3	Comparison of Numerical Model to Accuraspray G3	50
2.8.4	Effect of Substrate Geometry.....	53
2.9	Modelling Suspension Plasma Spray Thermal Spray	60
2.9.1	Effect of Injection Conditions.....	61
2.9.2	Effect of Suspension Viscosity Model.....	69
2.9.3	Modelling Primary Breakup Within SPS.....	71
2.10	Developments Within Multiscale Multiphase Models	74
2.11	Diagnostic Techniques for SHVOF and SPS Thermal Spray.....	77
2.11.1	Accuraspray Diagnostic System	78
2.12	Summary of Literature Review.....	80
2.13	Thesis Organisation	81
Chapter 3:	Numerical Modelling	83
3.1	Basic Fluid Flows	83
3.2	Turbulence Modelling	85
3.2.1	LES Models:	87
3.2.2	RANS Models:	90

3.2.3	Turbulent Boundary Layer	92
3.3	Combustion Modelling.....	94
3.4	Multiphase Modelling	97
3.4.1	Discrete Particle Model.....	97
3.4.2	Volume of Fluid Model:	105
3.4.3	Coupled Volume of Fluid and Discrete Particle Model.....	107
3.5	Numerical Algorithm	109
Chapter 4: Investigation into the Effect of the Nozzle Geometry onto the Gas, Suspension and Particle Dynamics		112
4.1	Introduction:	112
4.2	SHVOF Nozzle Geometries	113
4.3	Modelling Methodology	115
4.4	Mesh Independence and Convergence	116
4.5	The Effect of the Nozzle Geometry on the Gas Velocity.....	120
4.6	The Effect of the Nozzle Geometry on the Gas Pressure	123
4.7	The Effect of the Nozzle Geometry on the Gas Temperature	125
4.8	Effect of the Nozzle Geometry on the Evaporation of Suspension.....	126
4.9	Effect of the Nozzle Geometry on the Inflight Particle Velocities	128
4.10	Effect of the Nozzle Geometry on the Inflight Particle Temperatures ..	129
4.11	Summary.....	131
Chapter 5: Development of a Hybrid Nozzle for Oxygen Sensitive Materials ...		132
5.1	Introduction	132

5.2	Modelling Methodology	135
5.3	Mesh Independence and Convergence	137
5.4	Comparison of Combustion Model	140
5.5	High Speed Imaging of Suspension Injection	145
5.6	Comparison of Numerical Model to High Speed Imaging.....	148
5.7	Investigation into the Effect of Suspension Flow Rate	153
5.8	Investigation into the Effect of Angle of Injection.....	165
5.9	Investigation into the Effect of the Injector Diameter.....	167
5.10	Effect of Shrouding Expansion Ratio on Gas Dynamics.....	172
5.11	Effect of Shrouding Gas on the Entrainment Within the Shroud	179
5.12	Effect of Shrouding on Inflight Particle Dynamics	186
5.13	Summary	192
Chapter 6: Investigation into the Effect of the Nusselt Number Correlation		196
6.1	Introduction	196
6.2	Modelling Methodology	201
6.3	Experimental Methodology	203
6.3.1	Inflight Measurements of Ensembled Averaged Particle Velocity and Temperature	203
6.3.2	Dynamic Light Scattering	205
6.3.3	Scanning Electron Microscope	205
6.4	Effect of the Nusselt Number Correlation on Gas Temperature and Evaporation Rates	206

6.5	Effect of the Nusselt Number Correlation on the Average Inflight Particle Velocities and Temperatures.....	209
6.6	Effect of the Nusselt Number Correlations on the Distribution of Inflight Particle Conditions Prior to Impact.....	211
6.7	Experimental Measurements of Inflight particle velocities and temperatures. 218	
6.8	Validation - Comparison of Nusselt Number Correlations to Accuraspray Measurements	222
6.9	Summary	229
Chapter 7: A High-Fidelity and Multi-Scale Investigation into the Primary Breakup		
	231	
7.1	Introduction	231
7.2	Modelling Methodology.....	235
7.3	Mesh Requirements for the Coupled VOF and DPM Framework.....	239
7.4	Effect of Co-Flow on the Gas Velocity and Gas Temperature Within the Combustion Chamber	242
7.5	Effect of the Co-Flow on the Primary Breakup.....	246
7.6	Effect of Co-Flow on Clogging within the Combustion Chamber	256
7.7	Summary	262
Chapter 8: Conclusion		
	264	
8.1	Key Findings	264
8.2	Contribution to Knowledge.....	271

8.3 Outline for Future Work.....	274
Chapter 9: Bibliography.....	276
Appendix I – Design of Shroud to Deposit Oxygen Sensitive Materials	303
Appendix II – UDF and UDM Developed for Suspension High Velocity Oxy Fuel Thermal Spray	308
Appendix III – Time Varying Accuraspray Measurements.....	316

List of Figures:

Figure 1-1: Categorization of different thermal spray processes [3].	2
Figure 1-2: Industrial application of thermal spray technology globally in 2019 [5].	3
Figure 1-3: Traditional gas turbine applications for spray coatings [9].	4
Figure 1-4: Coating on a hip implant [13].	5
Figure 1-5: SHVOF thermal spray gun in operation [14].	6
Figure 1-6: A shroud attachment onto a HVOF nozzle [16].	7
Figure 2-1: Cross section view of the Top-Gun SHVOF thermal spray gun [14].	14
Figure 2-2: Shock wave structures within an over-expanded flow [27] & [29].	17
Figure 2-3: Shock wave structures within an under-expanded flow [27] & [29].	18
Figure 2-4: Primary breakup regimes (a) Rayleigh, (b) first wind induced, (c) second wind induced and (d) atomization [40].	23
Figure 2-5: Fluid breakup regimes for jets exiting a nozzle [39]· [41].	24
Figure 2-6: Coaxial liquid nozzle and the features of the liquid jet injection [44].	25
Figure 2-7: Experimental measurements of the droplet SMD VS $We^{1/2}$ [44].	26
Figure 2-8: Regimes of secondary breakup [45].	26
Figure 2-9: Physical mechanism behind the bag breakup [45].	28
Figure 2-10: Physical mechanism behind the multimode breakup [45].	29
Figure 2-11: Physical mechanism behind the sheet thinning breakup [45].	29
Figure 2-12: Change in particle structure during phase change of suspension [52].	30
Figure 2-13: Static temperature predicted by the three combustion models [60].	34
Figure 2-14: Temperature profile predicted for high velocity oxy liquid fuel thermal spray by the eddy dissipation model [60].	35
Figure 2-15: Temperature profile predicted for high velocity oxy liquid fuel thermal spray by the laminar finite rate model [60].	35

Figure 2-16: Location of shocks obtained from (a) QUCIK scheme, (b) Experimental observations and (c) upwind scheme [60].	36
Figure 2-17: The adiabatic flame temperature vs. equivalence ratio for various fuel-air mixtures at STP [65].	38
Figure 2-18: The effect of the fuel-to-oxygen ratio at different standoff distances from the nozzle exit on the particle velocity [66].	39
Figure 2-19: The effect of the fuel-to-oxygen ratio on the inflight particle temperature [66].	39
Figure 2-20: Time required for different sized initial parent droplets to shed all their mass, with a varying breakup constant (B_1) of 1 and 10 [36].	41
Figure 2-21: Child droplet sizes for different initial parent droplets (a) and filtered results containing only initial primary child droplets (b) [36].	42
Figure 2-22: Time taken for droplet of varying sizes to shed 10% of their original mass by vaporization and breakup [36].	43
Figure 2-23: Different Injection types for liquid feedstocks (a) surface-type injection (STI) (b) group-type injection (GTI) (c) effervescent-type injection (ETI), and (d) design of effervescent-type injection-nozzle [67].	44
Figure 2-24: Comparison of the predicted results at varied GLR with Liu et al. and Qian et al. (a) 0.067, (b) 0.090, (c) 0.132, and (d) 0.176 [68].	45
Figure 2-25: (a) evaporation rate, (b) mass fraction of ethanol and (c) SMD of the ethanol droplets at different injection angles for a group type injector [67].	47
Figure 2-26: (a) evaporation rate, (b) mass fraction of ethanol and (c) SMD of the ethanol droplets at different GLR for an effervescent type injector [67].	49
Figure 2-27: Comparison of numerical modelling data to Accuraspray G3 measurements for the inflight particle velocities [19].	51

Figure 2-28: Comparison of numerical modelling data to Accuraspray G3 measurements for the inflight particle temperatures [19].	51
Figure 2-29: Particle temperature and spatial distributions at different standoff distances (SOD) [19].	52
Figure 2-30: Substrate geometries investigated (left) flat substrate and (right) cylindrical substrate [59].	53
Figure 2-31: Effects of substrate shape and location on gas velocity magnitude: velocity contours (left) and along centreline (right) [59].	54
Figure 2-32: The effect of substrate shape and standoff distance (L) on suspension/particle trajectory, velocity magnitude, and temperature [59].	56
Figure 2-33: Particle landing location distributions for various substrates and standoff distances [59].	57
Figure 2-34: Suspension plasma torch in operation coating a turbine blade [81]	60
Figure 2-35: Comparison between centreline temperature profiles obtained by RSM and standard $k-\epsilon$ models with experimental and numerical data [74].	62
Figure 2-36: Comparison of Jet Penetration between the numerical model and experimental measurements [74].	63
Figure 2-37: Effect of suspension injection velocity on the axial gas velocity, left hand side is side view pictures (symmetry plane) and right hand side is top view pictures [74].	64
Figure 2-38: Effect of suspension injection velocity on gas temperature, left hand side is side view pictures (symmetry plane) and right hand side is top view pictures [74].	65
Figure 2-39: Particle-size distributions at different distances from the nozzle exit. For injection velocity of 25.7 m/s [74].	66

Figure 2-40: Particle-temperature distributions at different distances from the nozzle exit. For injection velocity of 25.7 m/s [74].....	67
Figure 2-41: Particle-velocity distributions at different distances from the nozzle exit. For injection velocity of 25.7 m/s [74].....	67
Figure 2-42: The effect of suspension injector location and angle on the gas temperature (14°, 0°, and 14°, from left to right, respectively).(7, 1, and 17 mm, from <i>left to right</i> , respectively) [74].	68
Figure 2-43: Comparison of different suspension viscosity model to experimental data [73].	70
Figure 2-44: Interaction of a liquid column with an Ar-H ₂ plasma crossflow using the VOF model [21].	71
Figure 2-45: Interaction of a droplet with an Ar-H ₂ plasma crossflow using the VOF model [21].	72
Figure 2-46: Interaction of a liquid column with a Ar-H ₂ plasma crossflow using the VOF model [90].	73
Figure 2-47: Shadow photographs of a continuous water jet interacting with a dc plasma flow [90].	73
Figure 2-48: Pyrometer for characterization of the particles configured with a double-point measurement of Accuraspray G3 [107].	78
Figure 2-49: Pyrometer for characterization of the particles configured with a single-point measurement of Accuraspray 4.0 [107].	79
Figure 3-1: Fundamental concepts behind the RANS, LES and DNS turbulence models [112].	86
Figure 3-2: Energy Spectrum in turbulent flows [113].	87
Figure 3-3: Development of the boundary Layer [118].	92

Figure 3-4: Subdivisions of the near wall region [61].	93
Figure 3-5: Heat, Mass, and Momentum Transfer Between the Discrete and Continuous Phases [61].	97
Figure 3-6: Dynamic mesh refinement using a cut cell method	105
Figure 3-7: (a) Actual interface, (b) geo-reconstruct scheme and (c) donor acceptor scheme.	106
Figure 3-8: A Coupled VOF and DPM Model for Jet Breakup [134].	107
Figure 3-9: Droplet normalized radius standard deviation [left] and average radius surface orthogonality [right] [125].	108
Figure 3-10: Segregated Pressure Based Solution Algorithm	109
Figure 3-11: Coupled Pressure Based Solution Algorithm.	111
Figure 4-1: TopGun SHVOF gun with different nozzle types (a) and (b) for low melting temperature materials; (c) and (d) for high melting temperature materials	112
Figure 4-2: Suspension high velocity oxy fuel thermal spray torch design for the TopGun system [138].	113
Figure 4-3: Nozzle geometries evaluated within this study (a) 30-135-8, (b) 22-135-8 (c) 12-78-8 and (d) 0-78-8 nozzle	114
Figure 4-4: Centreline velocity magnitude for the 30-135-8 nozzle at three base cell spacings.	118
Figure 4-5: Centreline velocity magnitude for the 22-135-8 nozzle at three base cell spacings.	118
Figure 4-6: Centreline velocity magnitude for the 12-78-8 nozzle at three base cell spacings.	119

Figure 4-7: Centreline velocity magnitude for the 0-78-8 nozzle at three base cell spacings.....	119
Figure 4-8: Mesh for the four nozzle geometries considered (a) 0-78-8, (b) 12-78-8, (c) 22-135-8 and (d) 30-135-8 nozzles.....	120
Figure 4-9: Centreline gas velocity for the 30-135-8, 22-135-8, 12-78-8 and 0-78-8 nozzles, (NS) No Suspension and (S) Suspension.	121
Figure 4-10: Centreline static gas pressure for the 30-135-8, 22-135-8, 12-78-8 and 0-78-8 nozzles.	123
Figure 4-11: Centreline static gas temperature for the 30-135-8, 22-135-8, 12-78-8 and 0-78-8 nozzles, (NS) No Suspension and (S) Suspension.	125
Figure 4-12: Centreline evaporation rate for the 30-135-8, 22-135-8, 12-78-8 and 0-78-8 nozzles.	127
Figure 4-13: Average particle velocities for the 30-135-8, 22-135-8, 12-78-8 and 0-78-8 nozzles.	128
Figure 4-14: Average particle velocities for the 30-135-8, 22-135-8, 12-78-8 and 0-78-8 nozzles.	129
Figure 5-1: Hybrid nozzle design for SHVOF thermal spray (not drawn to scale).	134
Figure 5-2: Schematic of computational domain (Not drawn to scale).	135
Figure 5-3: Centreline velocity magnitude (Top) and static gas temperature (Bottom) on three different mesh densities (M1, M2 and M3).	138
Figure 5-4: Mesh employed for study with no shroud attachment.	139
Figure 5-5: Comparison of the centreline static gas temperature using the EDC and EDM combustion model with the adiabatic flame temperature.....	141

Figure 5-6: Effect of the combustion model on the prediction of the centreline species mass fraction plots for (a) H ₂ , (b) O ₂ and (c) H ₂ O	144
Figure 5-7: Schematic of experimental set up of high-speed camera and lighting system to image the radial injection of suspension.....	146
Figure 5-8: Design of injector used for a radial injection of suspension into the HVOF jet [159].....	147
Figure 5-9: Image of a radial injection of suspension into the flame with the distance of penetration and breakup from the jet axis outlined.....	148
Figure 5-10: Image of radial injection of an Al ₂ O ₃ and water suspension into a 75 kW flame with varying liquid injection flow rates of (a) 50 ml/min, (b) 100 ml/min, (c) 150 ml/min, (d) 200 ml/min, (e) 250 ml/min and (f) 300 ml/min.....	149
Figure 5-11: (a) Experimental values of the windward trajectories for suspension flow rates of 50 – 300 ml/min, (b) Comparison of experimentally obtained values of the windward trajectories to CFD for flow rates of 150 ml/min and 250 ml/min.	150
Figure 5-12: Comparison of experimental values of the jet breakup distance from the centreline to the numerically obtained values from CFD.	151
Figure 5-13: Centre plane contour of the gas velocity magnitude with varying suspension flow rates of 50, 100, 150, 200, 250 and 300 ml/min.....	153
Figure 5-14: CFD prediction of the centre line plots of the gas velocity magnitude with varying suspension flow rate.....	154
Figure 5-15: Centre plane contour of the static gas temperature with varying suspension flow rate from 50, 100, 150, 200, 250 and 300 ml/min.....	155
Figure 5-16: CFD prediction of the centre line plots of the static gas temperature with varying suspension flow rate.....	155

Figure 5-17: Plots of the Mach number with varying suspension flow rate from 50 - 300 ml/min displaying a bow shock preceding the suspension injection.	156
Figure 5-18: Suspension injection within the gas jet for varying suspension flow rate of 50, 100, 150, 200, 250 and 300 ml/min.	157
Figure 5-19: Suspension particle velocities at standoff distance of 85 mm; varying suspension flow rate of 50, 100, 150, 200, 250 and 300 ml/min.	159
Figure 5-20: Average inflight particle velocities at the suspension flow rates of 50, 100, 150, 200, 250 and 300 ml/min.	160
Figure 5-21: Particle temperatures at standoff distance of 85 mm for a varying suspension flow rate of 50, 100, 150, 200, 250 and 300 ml/min.	162
Figure 5-22: Average inflight particle temperature at for the suspension flow rates of 50, 100, 150, 200, 250 and 300 ml/min.	163
Figure 5-23: Average inflight particle velocity for the injection angle of +15, 0 and -15 degrees at a flow rate of 100 ml/min.....	166
Figure 5-24: Average inflight particle temperature for the injection angle of +15, 0 and -15 degrees at a flow rate of 100 ml/min.....	166
Figure 5-25: Suspension particle velocities at standoff distance of 85 mm for a varying diameter of injection of 0.3 mm, 0.45 mm and 0.6 mm.....	168
Figure 5-26: Average inflight particle velocity for a varying diameter of injection of 0.3mm, 0.45mm and 0.6mm.	169
Figure 5-27: Suspension particle temperatures at standoff distance of 85 mm for a varying diameter of injection of 0.3mm, 0.45mm and 0.6mm.	170
Figure 5-28: Average inflight particle temperature for a varying diameter of injection of 0.3mm, 0.45mm and 0.6mm.	171

Figure 5-29 (a), (b) and (c): Effect of the shroud exit diameter on oxygen mass fraction within the shroud (a) 24 mm, (b) 28 mm and (c) 32 mm (no suspension).	175
Figure 5-30: Effect of shroud expansion ratio onto the gas velocity.	176
Figure 5-31: Effect of shroud expansion ratio onto the gas temperature.	178
Figure 5-32: Oxygen mass fraction within the shroud at varying shrouding gas flow rates of (a) 0 g/s, (b) 1 g/s, (c) 2 g/s and (d) 3 g/s	181
Figure 5-33: Effect of gas shrouding mass flow rate on the centreline gas velocity within the shroud.	182
Figure 5-34: Effect of gas shrouding mass flow rate on the centreline gas temperature within the shroud.	183
Figure 5-35: Effect of shrouding on average inflight particle velocities	187
Figure 5-36: Effect of shrouding on average inflight particle temperatures	188
Figure 5-37: Effect of distance from the nozzle exit (standoff distance) on inflight particle velocities with a shroud attachment (a) 85 mm, (b) 105 mm, (c) 125 mm, (d) 145 mm, (e) 165 mm and (e) 185 mm.	190
Figure 5-38: Effect of distance from the nozzle exit (standoff distance) on inflight particle temperatures with a shroud attachment (a) 85 mm, (b) 105 mm, (c) 125 mm, (d) 145 mm, (e) 165 mm and (e) 185 mm.	191
Figure 5-39: Hybrid nozzle attached to the GTV Topgun SHVOF thermal spray system.	194
Figure 6-1: Convective heat transfer coefficient for a sphere in a rarefied gas at varying Mach numbers adapted from [129].	197
Figure 6-2: Effect of Knudsen number on different flow regimes, adapted from [26].	199
Figure 6-3: Accuraspray system in operation with SHVOF thermal spray.	203

Figure 6-4: Accuraspray measurement device positioning to the SHVOF thermal spray gun.	203
Figure 6-5: Centreline Gas temperature for the three Nusselt correlations.	206
Figure 6-6: Centreline evaporation rates for the three Nusselt correlations.	207
Figure 6-7: Average inflight particle temperatures for the three Nusselt correlations.	209
Figure 6-8: Average inflight particle velocities for the three Nusselt correlations.	210
Figure 6-9: Particle temperature distribution Ranz – Marshall (a), Kavanau (b) and compressible (c) correlations at a standoff distance (SOD) of 85 mm.	212
Figure 6-10: Particle liquid mass fraction distribution Ranz – Marshall (a), Kavanau (b) and compressible (c) correlations at a SOD of 85 mm.	214
Figure 6-11: Particle velocity distribution Ranz – Marshall (a), Kavanau (b) and compressible (c) correlations at a SOD of 85 mm.	216
Figure 6-12: Particle diameter distribution Ranz – Marshall (a), Kavanau (b) and compressible (c) correlations at a SOD of 85 mm.	217
Figure 6-13: Particle size distribution of Cr ₂ O ₃ particles in the suspension.	218
Figure 6-14: SEM image of Cr ₂ O ₃ particles within the suspension.	219
Figure 6-15: Particle velocity measurements at various standoff distances.	220
Figure 6-16: Particle temperature measurements at various standoff distances.	220
Figure 6-17: Comparison of inflight particle temperatures for the three Nusselt correlations with the Accuraspray measurements.	224
Figure 6-18: Particle Knudsen number in the supersonic region of the flow.	224
Figure 6-19: Comparison of inflight particle velocity for the three Nusselt correlations against the Accuraspray measurements.	226
Figure 7-1: Co-flow Injector design [204]	234

Figure 7-2: Geometry of SHVOF thermal spray nozzle.	235
Figure 7-3: Fully structured mesh for the SHVOF thermal spray combustion chamber.	236
Figure 7-4: Mesh around the VOF iso-surface coloured by the flow velocity magnitude for a co-flow velocity of 300 m/s.	241
Figure 7-5: Instantaneous velocity contours given in throughflows (TF) with (black) VOF iso-surfaces (We = 100) (A1) 36 TF, (A2) 43 TF, (A3) 50 TF, (We =180) (B1) 36 TF, (B2) 43 TF, (B3) 50 TF, (We = 415) (C1) 36 TF, (C2) 43 TF and (C3) 50 TF.	243
Figure 7-6: Instantaneous temperature contours given in throughflows (TF), (We = 100) (A1) 36 TF, (A2) 43 TF, (A3) 50 TF, (We =180) (B1) 36 TF, (B2) 43 TF, (B3) 50 TF, (We = 415) (C1) 36 TF, (C2) 43 TF and (C3) 50 TF.	245
Figure 7-7: Breakup Modes Within the Combustion Chamber	247
Figure 7-8: Instantaneous iso-surfaces of the liquid jet injection into the combustion chamber given in throughflows (We= 100) at (a) 46 TF and (b) 50 TF, (We= 180) at (c) 46 TF and (d) 50 TF, (We= 415) at (e) 46 TF and (f) 50 TF.	249
Figure 7-9: Droplet diameter distributions from primary breakup at Weber numbers (a) 100, (b) 180 and (c) 415.	253
Figure 7-10: Effect of co-flow velocity (a) 0 m/s, (b) 100 m/s and (c) 200 m/s on the Weber number of droplets subsequent to primary breakup.	254
Figure 7-11: Comparison of Sauter mean diameter (SMD) of droplets from primary breakup to existing experimental breakup literature.	255
Figure 7-12: Time averaged velocity at Weber numbers (a) 100, (b) 180 and (c) 415.	257

Figure 7-13: Time averaged axial centre line velocity profiles at the Weber numbers considered.258

Figure 7-14: Droplet diameter vs. average droplet velocity of the droplets formed from primary breakup.260

Figure 7-15: Liquid column and droplets within the combustion chamber coloured by the velocity magnitude for (a) $We = 100$, (b) $We = 180$ and (c) $We = 400$261

List of Tables

Table 2-1: Detailed H ₂ /O ₂ mechanism [32].	20
Table 2-2: Modes of secondary breakup varying with the Weber Number [46] & [47].	27
Table 2-3: Summary of injection conditions for different cases studied by [67].	46
Table 2-4: Summary of numerical modelling approaches employed within SHVOF thermal spray (ordered by date of publication)	58
Table 2-5: Summary of Injection Conditions Investigated	61
Table 2-6: Comparison of DPV-2000 and Accuraspray-G4 particle diagnostic systems	77
Table 4-1: Table of the boundary conditions.	116
Table 4-2: Summary of mesh features for meshes considered within the mesh independence test for the 30-135-8, 22-135-8, 12-78-8 and 0-78-8 nozzles.	117
Table 5-1: Table of the boundary conditions employed.	136
Table 5-2: Summary of mesh features for meshes considered within the mesh independence.	137
Table 6-1: Boundary conditions employed within the model.	202
Table 7-1: Table of boundary conditions employed	238
Table 7-2: Mean and standard deviation of log normal distribution for droplet diameter.	251
Table 7-3: Coefficients for the statistical fit between the droplet velocity and droplet diameter formed from primary breakup and coefficient of determination values.	259

Non-Dimensional Parameters

Symbol	Definition
Bi	Biot Number – ratio of heat transfer resistance inside the body to the surface of the body.
Kn	Knudsen Number - ratio of the molecular mean free path length to a representative physical length scale.
Ma	Mach Number- ratio of the flow velocity to the speed of sound through the fluid.
Oh	Ohnesorge Number – ratio of viscous forces to inertial and surface tension forces.
Pr	Prandtl Number – ratio of momentum diffusivity to thermal diffusivity.
Re	Reynolds Number – ratio of inertial forces to viscous forces.
Sc	Schmidt Number - ratio of momentum diffusivity and mass diffusivity.
St	Stokes Number - ratio of the particle to eddy response times.
Sh	Sherwood Number - ratio of the convective mass transfer to the rate of diffusive mass transport.
Ta	Taylor Number – Ratio of inertial forces due to rotation about an axis to viscous forces
We	Weber Number - ratio between the inertial force and the surface tension force.

Acronyms

Symbol	Definition
AMR	Adaptive Mesh Refinement
CFD	Computational Fluid Dynamics
CLS-VOF	Coupled Level Set - Volume of Fluid
CVOFDPM	Coupled Volume of Fraction Discrete Particle Model
DLS	Dynamic Light Scattering
DNS	Direct Numerical Simulation
DPM	Discrete Particle Model
DRW	Discrete Random Walk
EDC	Eddy Dissipation Concept
EDM	Eddy Dissipation Model
ETI	Effervescent Type Injector
FVM	Finite Volume Methods
GLR	Gas – Liquid [Mass Flow] Rate
GTI	Group Type Injector

HVOF	High Velocity Oxy Fuel
ISAT	In-Situ Adaptive Tabulation
KHRT	Kelvin-Helmholtz Rayleigh-Taylor
LES	Large Eddy Simulation
LS	Level Set
PDA	Phase Doppler Anemometry
RANS	Reynolds Averaged Navier Stokes
SHVOF	Suspension High Velocity Oxy Fuel
SMD	Sauter Mean Diameter
SOD	Standoff Distance
SPS	Suspension Plasma Spray
SRS	Scale Resolving Simulations
STI	Surface Type Injector
UDF	User Defined Function
UDM	User Defined Model
VOF	Volume of Fluid

Chapter 1: Introduction

1.1 Surface Engineering and Thermal Spray

Many components are exposed to harsh and corrosive environments, the surface of the component can degrade resulting in the failure of the component. The field of surface engineering aims to modify the surface properties of a component to achieve superior performance and durability. The surface of a material can be modified by metallurgical, mechanical, physical, and chemical processes, or by producing a thick layer or a thin coating. Thermal spray is a term that groups a range of industrial processes that deposit heated / molten particles onto the surface of a component to form a protective coating. Typically within thermal spray, an energy source is utilised to heat a feedstock material; the feedstock material can take the form of a powder or a suspension. The heated feedstock particles are accelerated onto a substrate using a gas stream. The combined kinetic and thermal energy of the particles allow the particles to bond to the surface of the substrate which build up to form a coating [1].

The thermal spray process came about at the start of the twentieth century when Dr. Max Ulrich Schoops developed a device to deposit metal droplets onto a substrate now referred to as “flame spray” [2]. Dr. Schoops device melted a wire in a flame generated by combustion, the metal droplets were then atomised by a compressed gas and propelled onto a substrate. Flame spray became the foundation for more advanced techniques such as high velocity oxy fuel thermal spray and suspension high velocity oxy fuel thermal spray. Coatings were incorporated onto the surface of components to improve the performance and increase the lifespan of the components. Thermal spray coatings provide a range of benefits which include:

- Improving the performance of the components by allowing for the operations of component at higher temperatures and allow for processes to operate at higher efficiencies.
- Increasing the component lifespan by improving the resistance to wear, corrosion and erosion.
- Reducing the costs to manufacture the component by allowing for a cheaper base material to be used alongside a more expensive coating.

There are several different thermal spray processes that can be used to apply coatings. One grouping of thermal spray processes was suggested by Pierre L. Fauchais et al, and is shown in figure 1-1 [4]. Thermal spray processes are characterized into two main groupings characterised by the process energy source. These groups are then further divided into the individual thermal spray process.

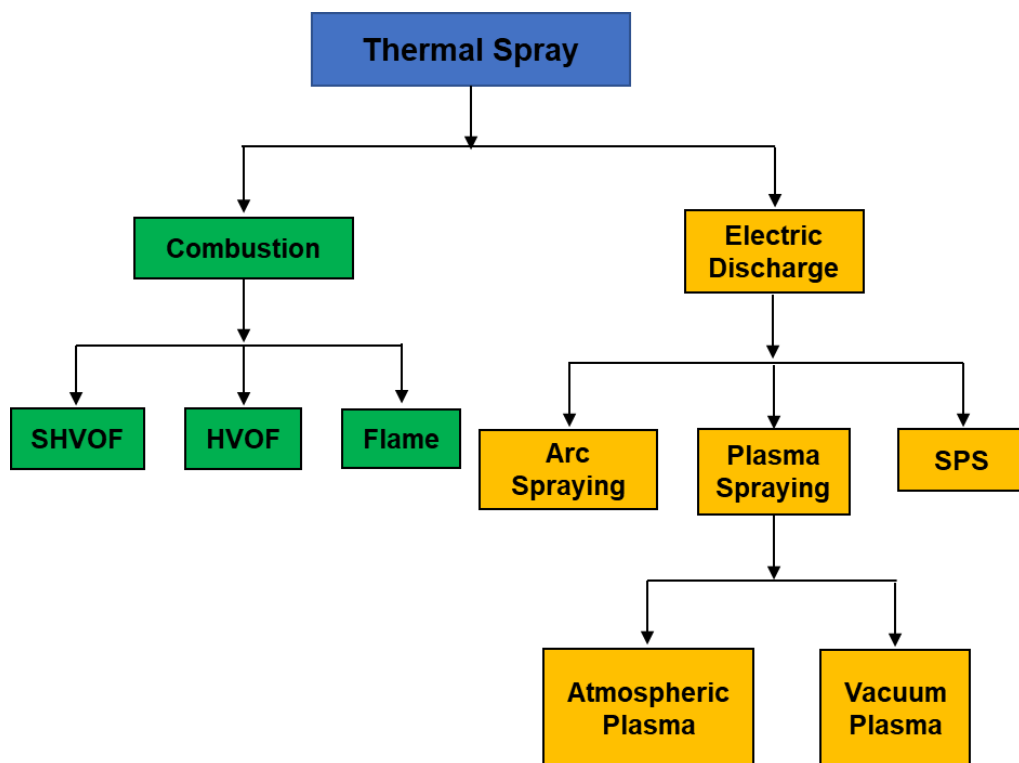


Figure 1-1: Categorization of different thermal spray processes [4].

1.2 Applications for Thermal Spray Coatings

Due to the overwhelming benefits that coatings can provide, the applications for thermal spray technologies have grown steadily. Early twentieth century thermal spray applications were primarily dominated by aerospace applications. Within recent years, more industries have utilised thermal spray technologies. Figure 1-2 shows an overview of the applications of thermal spray technology globally in 2019 [5].

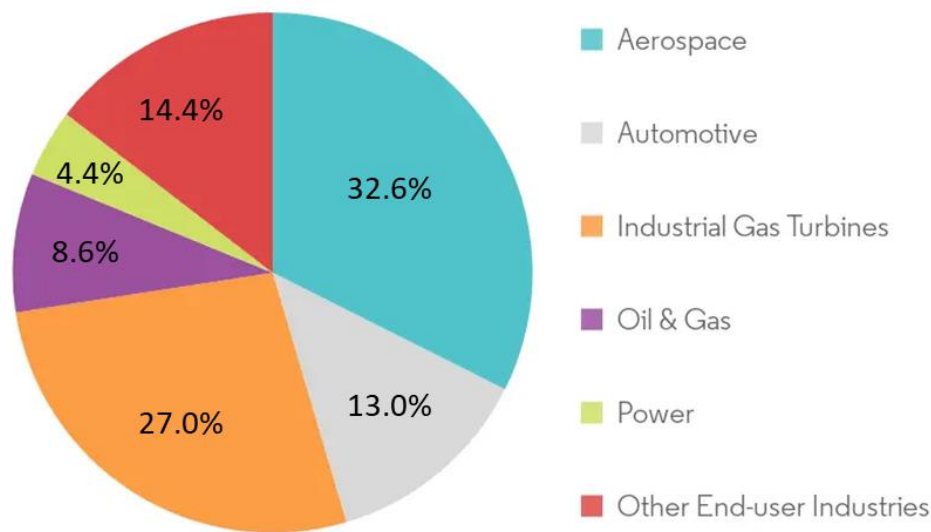


Figure 1-2: Industrial application of thermal spray technology globally in 2019 [6].

The goal to reduce CO₂ emissions to tackle climate change has demanded for higher engine and gas turbine efficiencies. Improvements in engine efficiencies requires gas turbines to operate at higher temperatures. An increase in the inlet gas turbine temperature of 200 °C can result in a 2 % increase in the turbine efficiency [3]. Thermal barrier coatings (TBC) are a multi-layered system used to reduce the substrate temperatures, protect against oxidation at high temperatures and resist corrosive environments. Thermal spray coatings are widely used throughout the gas turbine, they are employed on turbine blades to improve performance at higher temperatures [7]. Figure 1-3 shows a range of thermal spray applications within gas turbines.

Thermally sprayed coatings are found in every method of renewable energy generation. Corrosion resistant coatings alone are found in wind turbines, hydroelectric generators, biomass power plants and nuclear fission generators [8], [9].

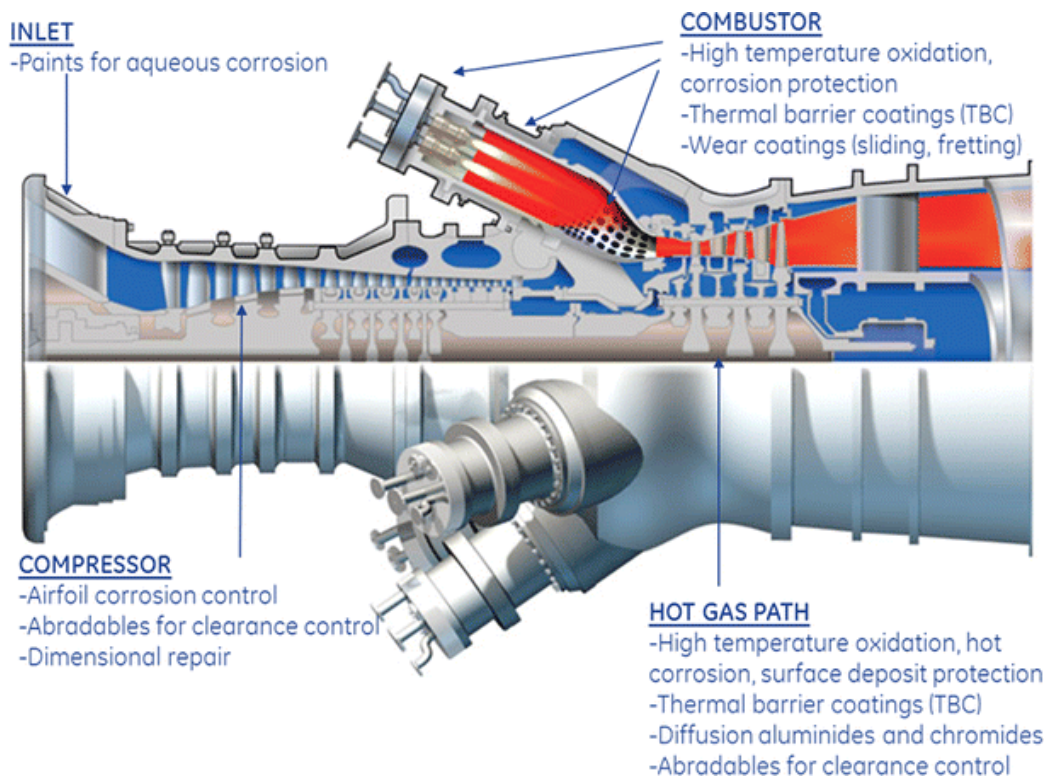


Figure 1-3: Traditional gas turbine applications for spray coatings [10].

Failures within powerplant boilers are often a result of corrosion and erosion of pipes at high temperatures. If the damaged components are not detected in time, they can lead to component failure and a subsequent system failure. Ceramic materials offer good protection against wear and corrosion due to their high hardness. Ceramic coatings from materials such as aluminium oxide or silicon carbide protect against corrosion and erosion of heated surfaces [11]. SHVOF thermally sprayed coatings allow for the production of high-quality coatings with a high hardness, high adhesion and a low porosity. Coatings employed within powerplant boilers have drastically improved the durability, performance and extended the lifetime of powerplant boilers.

SHVOF thermal spray coatings have also contributed significantly to advances within the field of medicine; thermally sprayed coatings are used within medical implants. Bioactive materials are materials that can prompt a biological response from biological tissues. Bioactive materials can trigger tissue regeneration and angiogenesis [12] which aids self-repair within the body. Bioactive glasses bond to the living tissue to create a stable interface for the trigger of biological responses within the body. Bioactive glasses are actively being researched to coat the surface of the implant with a bioactive material in the aim to stimulate tissue regeneration at the surface [13]. Hydroxyapatite (HA) coatings have been employed for hip and knee implants to enhance the implant stability. The Hydroxyapatite coatings create a surface interface for bone and tissue regeneration. Hydroxyapatite coatings have been found to be readily accepted by human tissues [14]. Figure 1-4 shows a Hydroxyapatite coating employed onto a hip implant.

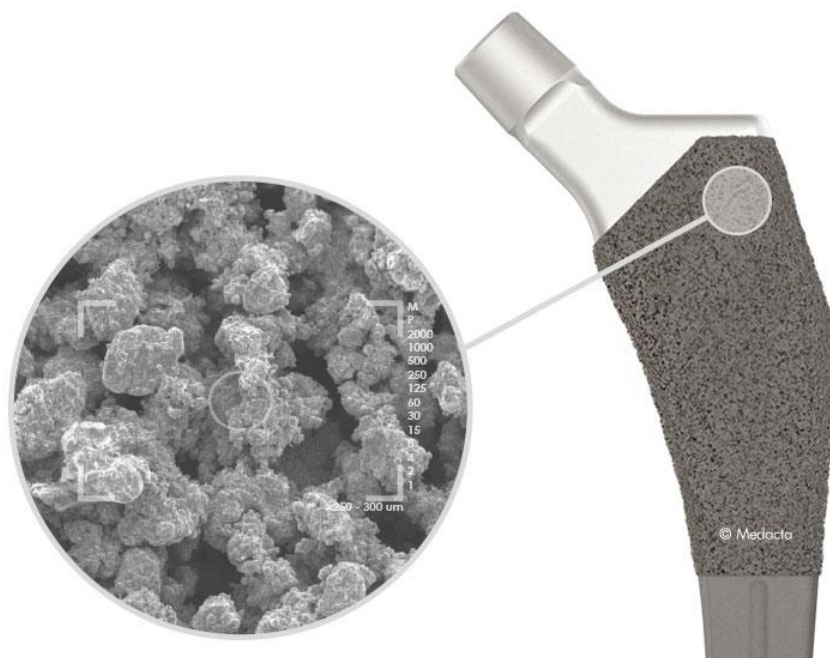


Figure 1-4: Coating on a hip implant [14].

1.3 Suspension High Velocity Oxy Fuel (SHVOF) Thermal Spray Process

Suspension high velocity oxy fuel (SHVOF) thermal spray is a process that utilises the energy from the combustion of premixed fuel and oxygen with optimised nozzle geometries to heat and accelerate particles within a suspension onto a substrate to form a coating. Within SHVOF thermal spray premixed fuel and oxygen are injected into a combustion chamber the fuel is oxidized. The gas temperatures can reach up to 3500 K [1]. The products from the combustion reaction are accelerated using an expansion nozzle where the combustion gasses can be accelerated up to 1250 m/s. If the conditions allow, shock waves are seen beyond the nozzle exit within the free jet. Once a stable gas jet is established suspension which comprises of a nano-particles dispersed within a liquid carrier are injected into the centre of the combustion chamber. The liquid is vaporised; the particles are then heated, melted and accelerated onto a substrate where the particles bond to the substrate to form a coating. Figure 1-5 shows a SHVOF thermal spray gun in operation.

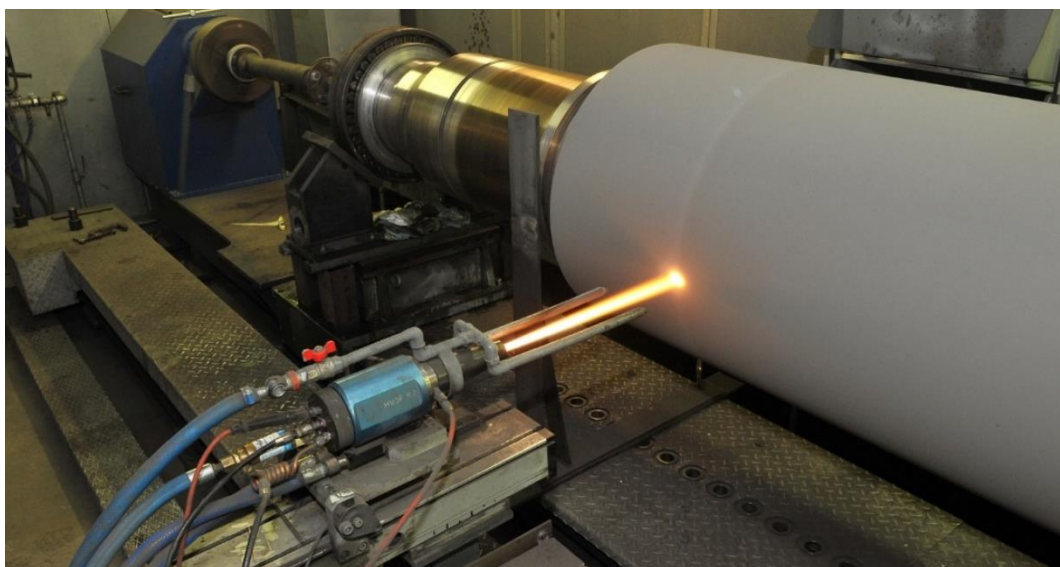


Figure 1-5: SHVOF thermal spray gun in operation [15].

1.4 High Velocity Oxy Fuel Thermal Spray Attachments

Graphene, copper and carbon nanotubes degrade and oxidise when exposed to oxygen at high temperatures. Graphene in particular has seen promising potential to reduce friction and wear in applications with moving mechanical parts [16]. Shrouding attachments can be added to the end of suspension high velocity oxy fuel thermal spray guns. Shrouds offer a number of advantages; they can increase the gas velocity, gas temperature. Typically, shrouds are employed to prevent the mixing of oxygen from the air into the jet. Figure 1-6 shows a shroud developed at the University of Toronto to increase the inflight particle velocities and temperatures [17]. In addition to improving the gas velocities and temperatures, shrouding attachments can reduce the mixing of ambient oxygen into the gas jet to improve the deposition of oxygen sensitive materials. A new thermal spray nozzle technology is designed to reduce degradation of oxygen sensitive materials. A hybrid nozzle is designed that allows for an axial injection, shrouding attachment, shrouding gas with a radial injection. The hybrid nozzle is a new concept that has been developed as a part of this thesis.

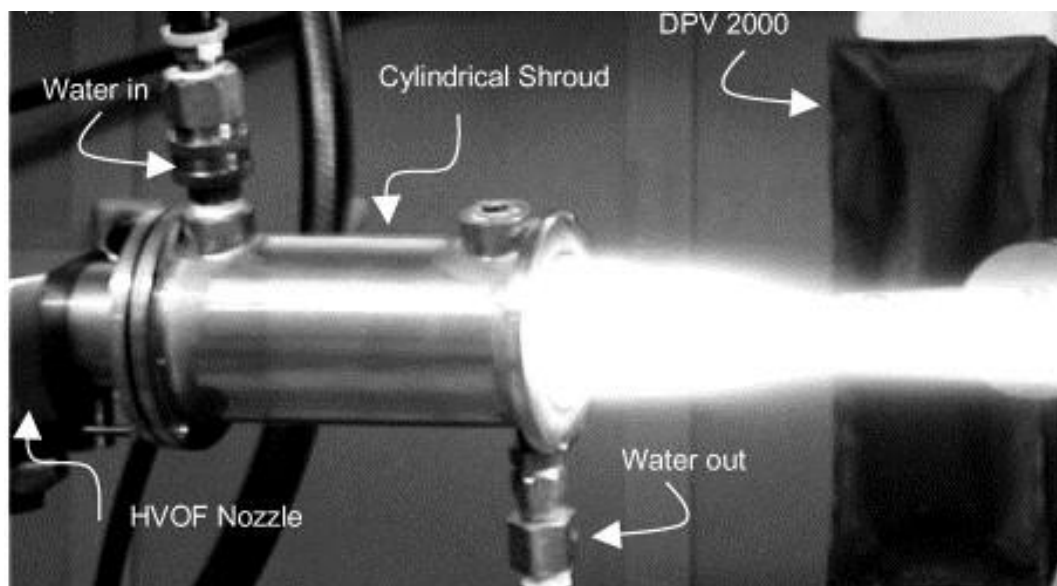


Figure 1-6: A shroud attachment onto a HVOF nozzle [17].

1.5 Motivations

Employing experimental investigations alone to understand more about SHVOF thermal spray are very limited within their scope. Experimental investigations are unable to provide us with any information about the process where there is not direct observational accessibility. Obtaining measurements from regions such as the combustion chamber is currently outside the capabilities of current experimental methodologies. There are a number of challenges that must be addressed these include; instrumentation must be sufficiently compact to obtain access to the very small combustion chamber and the experimental technique must be able to resolve the very short timescales and the very small length scales of the flow. Experimental investigations are also very expensive to conduct and computational investigations are more efficient at developing an understanding of a process. For example, to optimise the standoff distance, substrates must be polished, coatings must be deposited at a range of standoff distances and then are then analysed using a scanning electron microscope. This process is very time consuming and very expensive to conduct. When the operating conditions or materials used are varied this process must be repeated. Alternatively, using computational methods to optimise the standoff distance; one model can provide you with the optimum standoff distance at a given condition by determining the location where particle velocities and temperatures are at a maximum. This process is inexpensive and the flow characteristics can be obtained much more rapidly. More recently analysis tools have been developed to experimentally obtain inflight particle velocities and temperatures however these methods are limited as they only offer average inflight values [18].

There is still much to learn about SHVOF thermal spray and this thesis aims to address the following challenges outlined.

1. Our current understanding to design nozzles for SHVOF is built from optimising the nozzles for powder feedstock. Powder feedstock is typically of the order of 15 – 50 μm whilst suspension particles are of the order of 10 nm to sub-micron scales. Suspension particles are more susceptible to flow variations and very poor at maintaining their heat and momentum. Investigating the effect of the nozzle geometry will allow for a better understanding on designing the next generation of SHVOF thermal spray nozzles.
2. Additional oxygen is introduced into the gas flow through mixing of ambient oxygen into the jet. For oxygen sensitive materials, this can result in degradation of the feedstock material which has negative impact on the coating properties. Oxide content within the coating can produce microstructural defects which can degrade the mechanical, electrical, and thermal properties of the coating [19]. A novel hybrid nozzle thermal spray system has been modelled and designed to reduce the exposure time of oxygen sensitive materials to oxygen at high temperatures. This will improve the properties of the coating and reduce degradation of feedstock materials.
3. Improvements in the accuracy and fidelity of numerical models are required to build a thorough understanding of SHVOF thermal spray. Current approaches in numerical modelling of SHVOF thermal spray provides a poor prediction for the gas temperatures, particle temperatures and particle velocities [17], [20]. Previous numerical modelling approaches cannot capture the entire range of physics that occurs within SHVOF thermal spray. Previous modelling

approaches cannot capture the primary breakup within SHVOF thermal spray due to the computational cost associated with resolving breakup structures. The numerical models ignore the primary breakup and therefore, our understanding of which flow features cause clogging within the nozzle is very limited. With the vast improvements within computational resources that have been seen within the twenty-first century, there is a growing trend to move towards scale resolving simulations in a range of applications. Scale resolving simulations (SRS) have been applied to a range of applications including jets, gas turbine combustors and internal combustion engines to name a few [21], [22] & [23]. This thesis looks to improve the accuracy and fidelity of numerical models employed within SHVOF thermal spray to capture a greater range of physics within SHVOF thermal spray.

1.6 Aims and Objectives

The aim of this thesis is to **apply more physically representative numerical models for SHVOF thermal spray to improve the numerical accuracy and numerical fidelity**. This thesis aims to validate the numerical models employed by making direct comparisons with experimental measurements. This thesis aims to implement more appropriate numerical models and physically representative numerical models for SHVOF thermal spray. Parameter optimization is a long, expensive and time-consuming task to undertake experimentally. Computational investigations can provide an in-depth understanding of the process and enable the investigation of a range of parameters. The goal of this thesis is to supplement experimental parametric studies with a computational approach to develop a novel hybrid thermal spray nozzle that can deposit composite coatings formed from oxygen sensitive materials.

The objectives of this thesis include:

- Investigate the effect of the nozzle geometry using four commercially available nozzles to inform the design of the next generation of SHVOF thermal spray nozzle designs.
- Develop a novel hybrid thermal spray nozzle that allows for the deposition of composite coatings formed from oxygen sensitive materials. The nozzle should allow for two separate injections: axially into the combustion chamber and radially outside of the nozzle. Investigate the effect of the suspension injection conditions for a radial injection compare the numerical model to physical observations obtained using high speed imaging. Determine a suitable physical shrouding angle and a shrouding gas flow rate to propose a manufacturable design for the hybrid nozzle.

- Implement combustion models employed within SHVOF thermal spray that do not over predict the combustion chamber temperature when compared to the adiabatic flame temperature within the combustion chamber. Improve heat transfer models for particles within SHVOF thermal spray that better predict particle temperatures to avoid the under prediction of particle temperatures currently seen within the numerical models. Validate the numerical models through time of flight and two colour pyrometry methods at a range of standoff distances.
- Implement a model that is able to capture the primary breakup within SHVOF thermal spray to inform and characterise injections for lower fidelity numerical models. Modify the injector to optimise the flow behaviour within the nozzle to prevent clogging of suspension within the nozzle.

Chapter 2: Literature Review

Thermal spraying allows for the deposition of particles onto a substrate to provide a protective coating against wear and corrosion. High velocity oxy-fuel (HVOF) thermal spray process allows for the deposition of dense coatings with low degradation and oxidation [24]. With the success of HVOF thermal spray; industrial applications for coatings grew exponentially. However, there are certain limitations with the conventional HVOF thermal spray process. One of these limitations arises from the inability to reduce particle size further to that of nano-feedstock sizes. Coatings formed from nanoparticles provide enhanced properties in contrast to standard powder particles (5-45 μm) [25] & [26]. Conventional powder feeders are ineffective when dealing with feedstock sizes below 5 μm . Suspensions allows for an effective method to inject submicron particles into the combustion chamber without clogging of the feeder, as the suspension disperses the nanoparticles within a liquid medium. The development of Suspension High Velocity Oxy Fuel (SHVOF) thermal spray has allowed for effective handling of nanoparticle feedstock size which has enabled the deposition of coatings with a fine microstructure [25].

Within SHVOF thermal spray, premixed fuel and oxygen is injected into a high-pressure combustion chamber. The fuel undergoes oxidation and combusts, the combustion gasses are accelerated through a nozzle and barrel. Figure 2-1 shows a cross-section of the Top-Gun SHVOF thermal spray gun. When the flow at the outlet of the nozzle is under or over expanded the gas undergoes a series of expansive and compressive shocks, to equilibrate to atmospheric conditions. The series of expansions and compressions gives rise to shock waves within the flow. Once a steady flow field is established the suspension is injected into the combustion chamber. As the

suspension is injected into the combustion chamber, the suspension undergoes primary breakup, secondary breakup and evaporation [25]. The particles are then accelerated and heated as they travel through the gas; the particles impact the substrate where the particles deposit themselves forming a coating [15]. SHVOF thermal spray requires an understanding of wide range of physics. SHVOF thermal spray utilises the physics underlying combustion, compressible supersonic phenomenon, primary breakup, secondary breakup and phase change to name a few. Accurate numerical models should be able to capture the entire range of physics that spans the SHVOF thermal spray process.

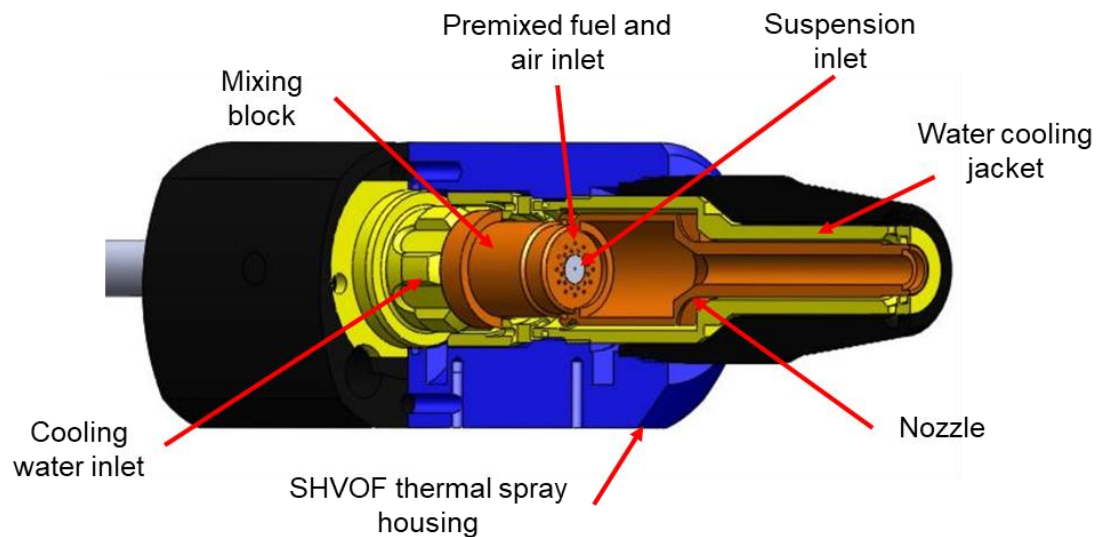


Figure 2-1: Cross section view of the Top-Gun SHVOF thermal spray gun [15]

This chapter provides a summary of the current understanding that governs the physical processes of SHVOF thermal spray. Relevant literature from HVOF and suspension plasma spray (SPS) thermal spray is also provided due to the wide overlap between the processes with SHVOF thermal spray. Additionally, a review of the literature that underlines the physical processes within SHVOF thermal spray is presented. Finally, a research gap is outlined which this thesis aims to address.

2.1 Compressible Effects

At low velocity changes within the fluid density are negligible and hence the incompressible theory of fluid flows provides an adequate understanding of the fluid flow. However, as the fluid's velocity increases the fluid experiences density variations and the compressible theory of fluid flows must be employed to obtain an adequate understanding of the flow. The Mach number (Equation 2.1) describes when the compressible effects become significant. The Mach number, Ma , is defined the ratio of the characteristic velocity of the fluid, U , to the speed of sound within the fluid, c . The flow is considered compressible if the Mach number is greater than 0.3 [27].

$$Ma = \frac{U}{c} \quad (Eq\ 2.1)$$

The local speed of sound through the fluid can be determined from equation 2.2. Where the ratio of specific heats of the fluid is given by γ , the specific gas constant is given by R and the temperature is given by T .

$$c = \sqrt{\gamma RT} \quad (Eq\ 2.2)$$

The flow can be characterised by the Mach number:

- $Ma < 0.3$: The flow is incompressible; the effects of density can be ignored.
- $0.3 > Ma > 0.7$: The flow is subsonic but compressible; there are density variations within the flow which must be modelled.
- $0.7 > Ma > 1$: The flow is transonic and density variations are significant.
- $Ma > 1$: The flow is supersonic; density effects are significant and shock waves exist within the flow.

When considering incompressible flows, the flow can be accurately described by the velocity components and the pressure within the fluid. When the flow becomes compressible, additional equations are required to model the density and temperature within the fluid.

The compressible Navier Stokes equations become significantly more complex when averaging due to the addition of the density as a variable. When decomposing the density, the velocity and the pressure variables into their fluctuating and mean components the complexity of the RANS equations can be reduced by employing Favre averaged variables. The Favre averaged variable, $\check{\phi}$, is given by equation 2.3 where the mean density is given by $\bar{\rho}$. This transformation allows for a significant reduction in the complexity of governing equations producing the Favre averaged Navier-Stokes equations.

$$\check{\phi} = \frac{\overline{\rho\phi}}{\bar{\rho}} \quad (Eq\ 2.3)$$

Shock waves can form within the free jet of the nozzle through processes of flow expansion and compression. Expansion is a process that converts the thermal energy from the combustion to kinetic energy within the gas. The expansion of the gas forms visible shock diamonds within the jet. The shape of the nozzle significantly affects the expansion of the jet as the flow expands against the walls of the nozzle.

Shock waves can be separated into three main categories [27]:

- Normal Shock – Occurs perpendicular to the medium’s flow direction.
- Oblique Shock – Occurs at an angle to the direction of flow.
- Bow Shock - Occurs upstream of the front of a blunt object when the upstream flow velocity exceeds Mach 1.

When the flow is over-expanded there is a lower gas pressure at the nozzle exit than that of the atmospheric pressure. The low pressure causes a compression of the flow which increases the flow pressure. However, the flow becomes over compressed such that the flow exceeds the atmospheric pressure. The overshoot results in an expansion of the flow to reduce the pressure to match that of the atmosphere. This process of compression, expansion, compression and so on is repeated until the flow pressure equilibrates with the atmospheric pressure [28]. A number of different shock wave structures can form within an over-expanded jet which depends heavily on the nozzle geometry. Several of the shock structures include an oblique and normal shock waves, Prandtl-Meyer expansion waves, and Prandtl-Meyer compression waves. Further discussion on the formation of different shock structures can be found in [29] and [30].

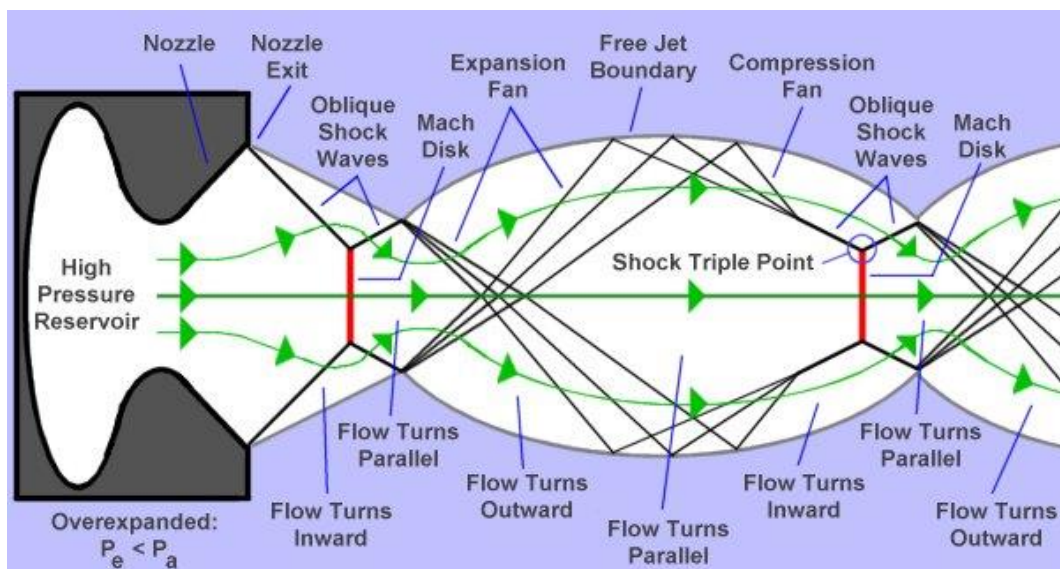


Figure 2-2: Shock wave structures within an over-expanded flow [28] & [30].

When the flow pressure at the exit exceeds that of the atmosphere the flow is referred to as under-expanded. A similar process occurs when the flow is under-expanded at the nozzle exit as shown in figure 2-3. The process of compression and expansion is identical to that of the over-expanded jet, however, the process is initiated with an expansion followed by a compression [28].

Viscous damping forces prevent this process of expansion and contraction from continuing on forever creating an infinite number of shock waves. The shear layer produces a viscous damping which dissipates energy within the shock structure. The viscous forces provide damping which equilibrates the pressure within the flow with that of the atmosphere this prevents the formation of further shock waves.

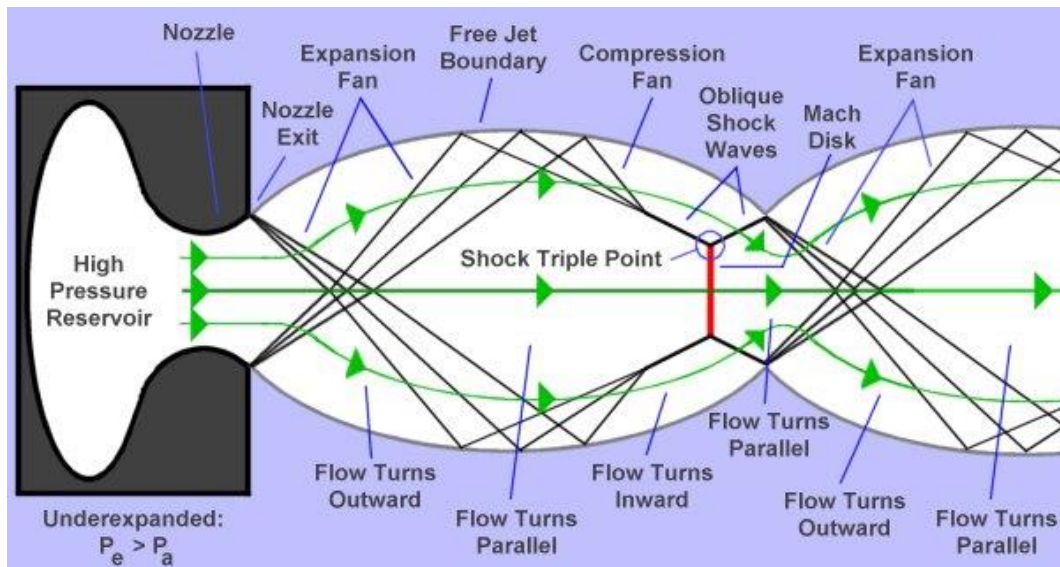


Figure 2-3: Shock wave structures within an under-expanded flow [28] & [30].

2.2 Combustion

Within SHVOF thermal spray the energy released from combustion is utilised to transfer heat and momentum from the gas to the particles to melt and adhere the particles to the surface of a substrate to form a coating. Combustion is an exothermic reaction that occurs when a fuel source is oxidized, it is a complicated process to understand due to the vast number of elementary reactions that govern the overall process. The simplest combustion reaction is the complete combustion of hydrogen at stoichiometric conditions (Equation 2.4).



When the reaction occurs at temperatures excess of 2000 K, the stable products dissociate due to strong thermal vibrations [31]. The dissociation of the products lowers the flame temperature due to the endothermic nature of the reaction. Additional reactions occur totalling 20 reactions that result in several additional species forming in the equilibrium mixture [32]. The detailed hydrogen combustion reaction mechanism for SHVOF thermal spray is given in table 2-1. The chemical rate of reaction, k , can be determined from the Arrhenius equation which is given by equation 2.5. Where A refers to the pre-exponential factor, n , refers to the temperature exponent, E_A , refers to the activation energy, T , refers to the temperature and R refers to the universal gas constant. Due to the vast number of reactions that occur and the number of different species that form; combustion is a very challenging and computationally expensive problem to solve.

$$k = AT^n e^{-\frac{E_A}{RT}} \quad (Eq\ 2.5)$$

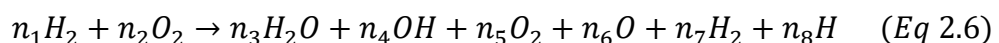
Table 2-1: Detailed H₂/O₂ mechanism [33].

	A	E_A (J/ kg.mol)	n
1. OH + H ₂ = H + H ₂ O	2.14E+05	1.443062E+07	1.520
2. O + OH = O ₂ + H	2.02E+11	0.000000E+00	-0.400
3. O + H ₂ = OH + H	5.06E+01	2.631736E+07	2.670
4. H + O ₂ = HO ₂	4.52E+10	0.000000E+00	0.000
5. OH + HO ₂ = H ₂ O + O ₂	2.13E+25	1.464400E+07	-4.827
6. H + HO ₂ = 2OH	15.00E+11	4.184000E+06	0.000
7. H + HO ₂ = H ₂ + O ₂	6.63E+10	8.895184E+06	0.000
8. H + HO ₂ = H ₂ O + O	3.01E+10	7.200664E+06	0.000
9. O + HO ₂ = O ₂ + OH	3.25E+10	0.000000E+00	0.000
10. 2OH = O + H ₂ O	3.57E+01	-8.836608E+06	2.400
11. 2H = H ₂	1.00E+12	0.000000E+00	0.000
12. H + OH = H ₂ O	2.21E+16	0.000000E+00	-2.000
13. H + O = OH	4.71E+12	0.000000E+00	-1.000
14. 2O = O ₂	1.89E+07	-7.480992E+06	0.000
15. 2HO ₂ = H ₂ O ₂ + O ₂	4.20E+11	5.013269E+07	0.000
16. 2OH = H ₂ O ₂	1.24E+11	0.000000E+00	-0.370
17. H ₂ O ₂ + H = HO ₂ + H ₂	19.80E+02	1.018804E+07	2.000
18. H ₂ O ₂ + H = OH + H ₂ O	3.07E+10	1.764393E+07	0.000
19. H ₂ O ₂ + O = OH + HO ₂	95.50E+02	1.661048E+07	2.000
20. H ₂ O ₂ + OH = H ₂ O + HO ₂	2.40E-02	-9.045808E+06	4.042

The equilibrium mixture can be determined using chemical equilibrium software NASA CEA [35] by determining the minimum Gibbs free energy of the system. A global reaction that accommodates the formation of secondary species can then be obtained. The global single step reaction for the combustion of hydrogen takes the form given within equation 2.6 where the constants n_i are to be determined by NASA CEA or another appropriate software package. The constants, n_i , depend upon many variables including combustion chamber pressure, combustion chamber temperature, oxygen-fuel ratio, mass flow rate and combustion chamber geometry [34]. An iterative approach can be employed with an initial guess with the combustion chamber pressure and temperature.

The coefficients n_i within equation 2.6 are determined by the iterative process outlined below:

1. The equilibrium mixture is obtained from an initial guess for the combustion chamber pressure and temperature using NASA CEA.
2. The balanced chemical reaction is determined from the equilibrium mixture which provides the global combustion reaction for Ansys Fluent.
3. A new combustion chamber temperature and pressure is obtained from Ansys Fluent.
4. The new combustion pressure and temperature provide an input for NASA CEA to determine the new equilibrium mixture.
5. Steps 2 - 4 are repeated until there is no notable change in the chemical composition.



2.3 Primary Breakup

As the suspension is injected into the combustion chamber the suspension forms a jet which undergoes primary and secondary breakup. The primary breakup plays an important role within SHVOF thermal spray as the process governs the size of droplets formed [36]. The size of the droplet plays an important role in the time required for the suspension droplet to completely vaporize its liquid component [37]. A rigorous understanding of the breakup within SHVOF thermal spray can allow for liquid vaporization to occur more rapidly. This allows greater time for particle heating and allows for greater particle temperatures upon impact of the substrate. Additionally, breakup within the combustion chamber plays a significant role in the droplet trajectories within the combustion chamber as shown in chapter 7. The particles that impact the nozzle walls result in clogging of the nozzles which is a serious problem within SHVOF thermal spray. This challenge can be addressed through a more thorough understanding of the breakup mechanism within SHVOF thermal spray.

$$Re = \frac{\rho u L}{\mu} \quad (Eq 2.7)$$

$$We = \frac{\rho u^2 L}{\sigma} \quad (Eq 2.8)$$

$$Oh = \frac{\sqrt{We}}{Re} = \frac{\mu}{\sqrt{\rho \sigma L}} \quad (Eq 2.9)$$

A significant amount of research has been undertaken to understand more about the primary breakup of jets exiting nozzles due to their wide range of applications. Injection nozzles are used in everywhere from suspension thermal spray, gas turbines, fuel injectors for nozzles and diesel engines to name a few. Ohnesorge et al. [38], Bjarne et al. [39] and Shao et al. [40] defined four droplet break-up regimes shown in figures 2-4 and 2-5. The break-up type is determined by the Reynolds number

(Equation 2.7) and Ohnesorge number (Equation 2.9) of the liquid exiting the nozzle. The Ohnesorge number is a function of the Weber number (Equation 2.8), the Weber number determines the ratio of fluid inertia to the fluids surface tension. The Reynolds number controls the length scales in the liquid jet turbulence, while the Weber number controls the tendency of the liquid jet to breakup [36].

Rayleigh break-up – Droplet breakup occurs far away from the nozzle and the droplets are bigger than the diameter of the nozzle (figure 2-4a).

First wind-induced break-up – Droplet breakup occurs several nozzle diameters downstream (figure 2-4b).

Second wind-induced break-up – Break-up begins a short distance downstream from the nozzle exit, the droplet diameter is smaller than nozzle diameter (figure 2-4c).

Atomisation – Droplet breakup occurs at the exit from the nozzle. The diameters are much smaller than the nozzle diameter (figure 2-4d).

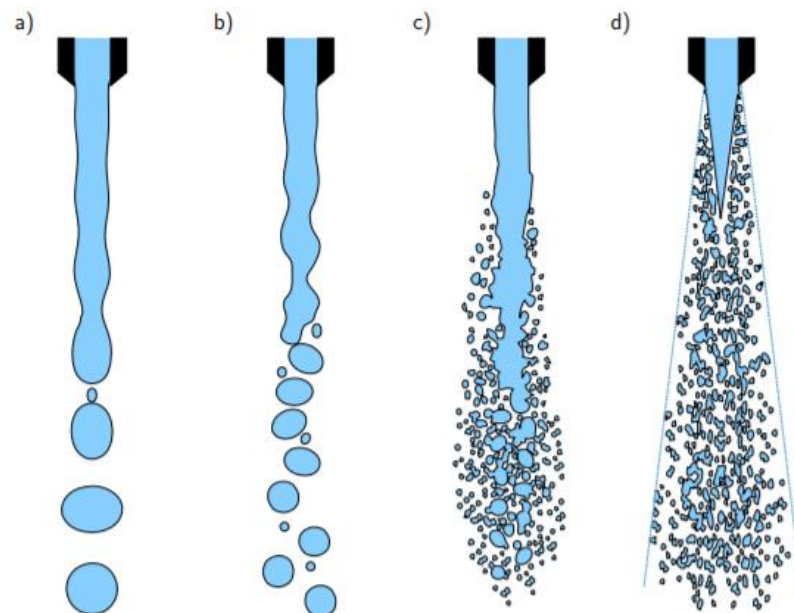


Figure 2-4: Primary breakup regimes (a) Rayleigh, (b) first wind induced, (c) second wind induced and (d) atomization [41].

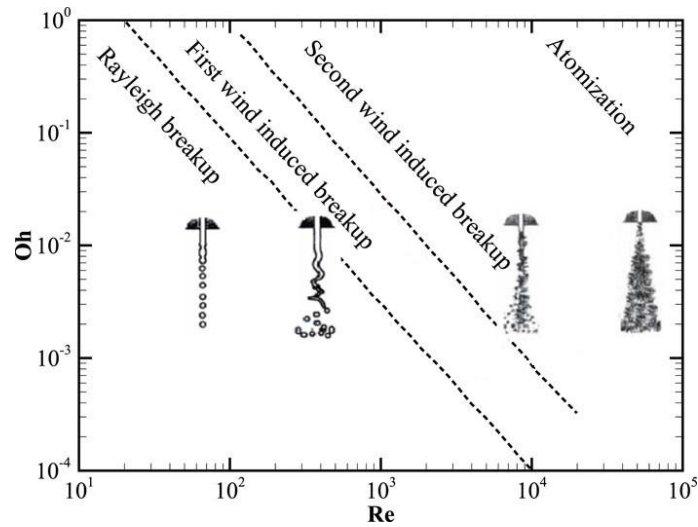


Figure 2-5: Fluid breakup regimes for jets exiting a nozzle [40]: [42].

2.4 Droplet Distribution

During the primary breakup of a liquid the droplets that form occupy a distribution of diameters. Typically to model the diameter distribution most commonly a Roslin – Rammler is employed, the Roslin – Rammler distribution is given by equation 2.10 [43]. The Roslin – Rammler distribution assumes there is an exponential relationship between the cumulative mass fraction, $Y(d)$, of droplets with a diameter less than, d . Where n refers to the spread parameter and \bar{d} refers to an “average” diameter. The average diameter is calculated from the value of diameter where the cumulative mass fraction is approximately equal to 0.368 and the spread parameter, n , is given by equation 2.11.

$$Y_d = 1 - e^{-\left(\frac{d}{\bar{d}}\right)^n} \quad (Eq\ 2.10)$$

$$n = \frac{\ln(1 - \ln(Y_d))}{\ln\left(\frac{d}{\bar{d}}\right)} \quad (Eq\ 2.11)$$

Alternative distributions such as the log normal distribution can be applied when the Roslin – Rammler distribution provides an inaccurate model of the distribution. The log normal distribution is useful in such cases where the log of the droplet diameter occupies a normal distribution [44]. The probability density function log normal distribution is given by equation 2.11. Within equation 2.12 μ and σ represent the mean and standard deviation of the log normal distributions respectively.

$$f(d|\mu, \sigma) = \frac{1}{d\sigma\sqrt{2\pi}} \exp\left(-\frac{(\log(x - \mu))^2}{2\sigma^2}\right) \quad (Eq 2.12)$$

Varga et al. [45] investigated the effect of the Weber number on the primary breakup of a jet in a coaxial flow; the nozzle configuration and the characteristic features of the breakup of the liquid jet are illustrated in figure 2-6. Within this investigation Varga et al. employed high speed imaging to visualise the flow exiting the nozzle in addition to this phase-doppler anemometry (PDA) was employed to measure the diameter of the droplets. Within the mentioned investigation Varga studied the effect of the Weber number on the Sauter mean diameter (SMD) as shown in figure 2-7. It can be seen from figure 2-7 that the SMD diameter decreases with an increase in the square root of the Weber number. It can also be seen that the rate of decrease in the droplet SMD with the Weber number is different for water than it is for ethanol.

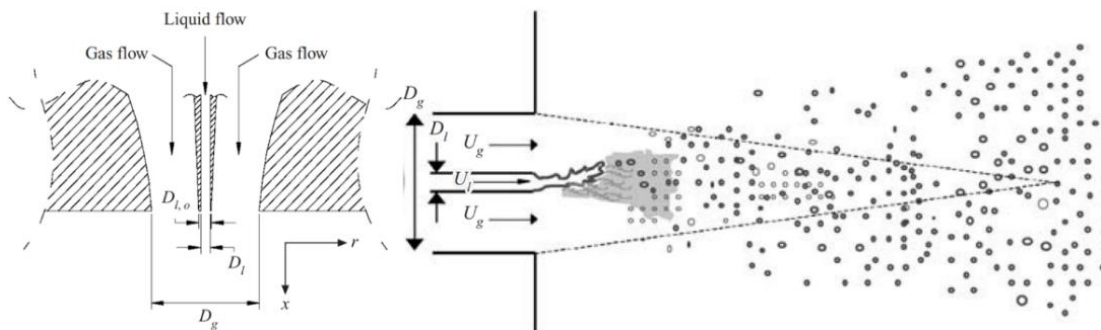


Figure 2-6: Coaxial liquid nozzle and the features of the liquid jet injection [45].

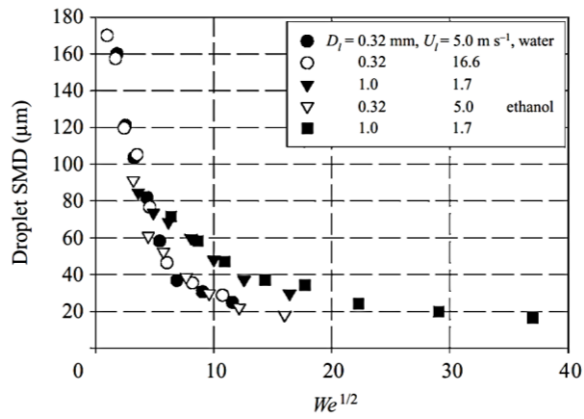


Figure 2-7: Experimental measurements of the droplet SMD VS $We^{1/2}$ [45].

2.5 Secondary Droplet Breakup

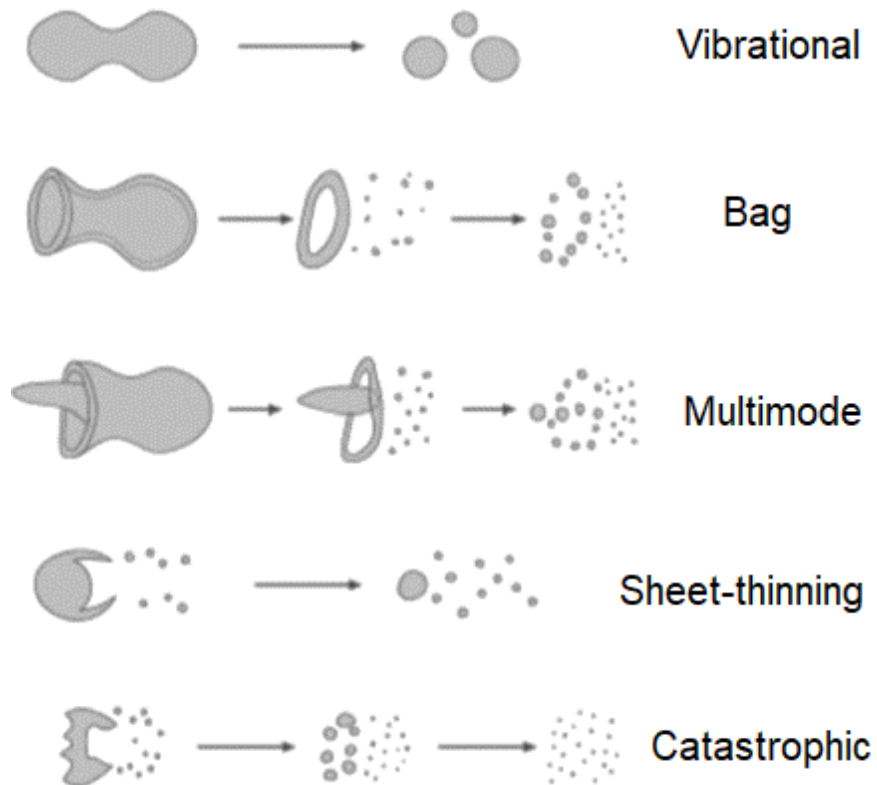


Figure 2-8: Regimes of secondary breakup [46].

Table 2-2: Modes of secondary breakup varying with the Weber Number [47] & [48].

Mode of breakup	Weber range
Vibrational	$0 < We < 11$
Bag	$11 < We < 35$
Multimode	$35 < We < 80$
Sheet-thinning	$80 < We < 350$
Catastrophic	$We > 350$

Droplets in a high-speed gas flow break up into smaller droplets, this process is known as secondary breakup. When a droplet is subjected to a disruptive flow field an unequal pressure distribution is created around the droplet. This results in the deformation of the spherical shape of the droplet. The interfacial tension and viscous forces work to prevent the deformation of the droplet. However, if the aerodynamic forces are sufficiently large the droplet will fragment into smaller droplets. The secondary breakup of the droplet can be characterised by the Weber number, Ohnesorge number and the Reynolds number. The mode of secondary breakup is dependent on the Weber number and the Ohnesorge number in particular. As the Weber number increases the tendency for droplet breakup increases and as the Ohnesorge number increases the tendency for the droplets to breakup decreases.

There are five modes for secondary breakup of droplets: vibrational, bag, multimode, sheet-thinning and catastrophic breakup which are outlined in figure 2-8 and table 2-3. A significant body of literature has been developed that aims to better understand the physical mechanisms that underpin the various modes of secondary breakup.

Liu et al. [49] proposed an initial breakup mechanism behind the bag breakup mode, the bag first breaks up into ligaments that align themselves to the flow field. Liu et al. [50] built upon the mechanism by proposing that the breakup is initiated by small holes that form within the bag either due to disturbances within the flow field or impurities within the droplet. The holes then act as an inception site for the breakup within the bag mechanism, figure 2-9 illustrates the mechanism behind the bag breakup.

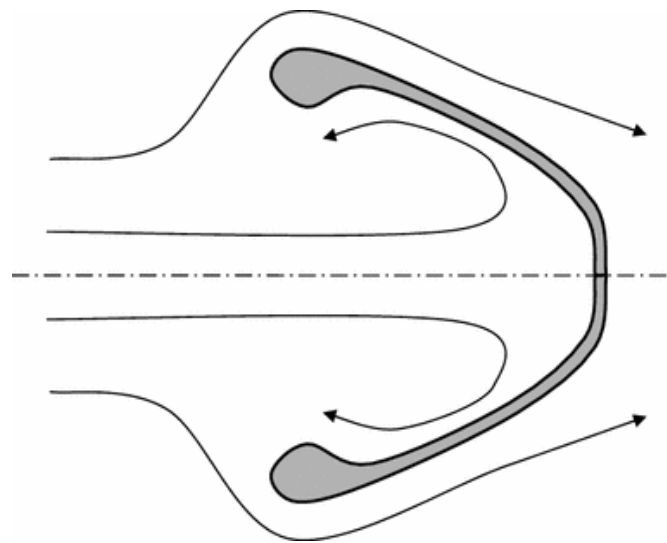


Figure 2-9: Physical mechanism behind the bag breakup [46].

At higher gas velocities a multimode breakup mechanism occurs which results in the atomization of the droplets. It is assumed that breakup of the droplets within this mode occurs when the aerodynamic forces and the shear forces are significant. Theofanous et al. [51] studied the Raleigh-Taylor instabilities that form on the leading edge of the droplet. Within this mechanism droplet deformation results in the formation of poles as with the bag mode. As the Weber number increases the surface tension forces are insufficient and the droplets continue to elongate. The edges of the droplet become so thin that droplets detach. Figure 2-10 shows the physical mechanism behind the multimode breakup.

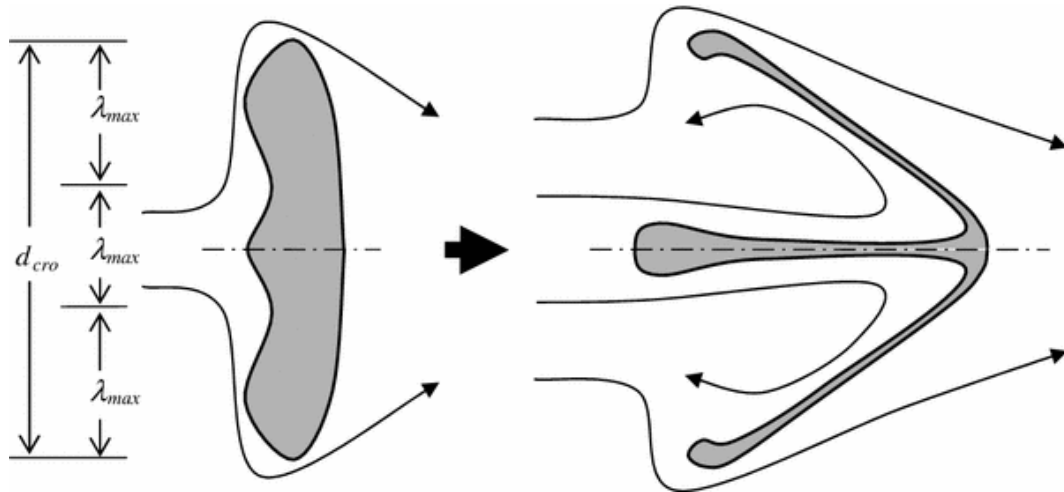


Figure 2-10: Physical mechanism behind the multimode breakup [46].

At higher gas velocities still, the breakup of the droplets takes the form of the sheet thinning mode of breakup. Nicholls et al. [52] proposed that as the droplet is accelerated within the flow field a boundary layer forms within the surface of the droplet. The boundary layer is unstable at the edges of the droplet which results in a stripping of daughter droplets from the parent droplet. Figure 2-11 shows the physical mechanism behind the sheet thinning mode of droplet breakup.

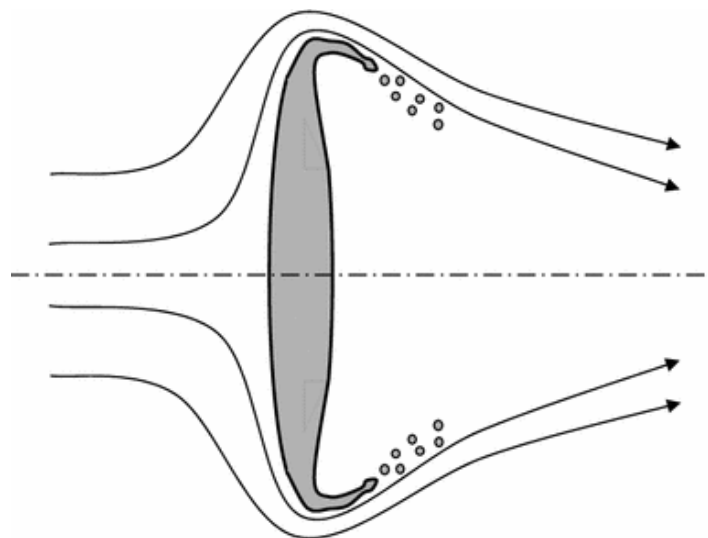


Figure 2-11: Physical mechanism behind the sheet thinning breakup [46].

2.6 Slurry Droplet Evaporation

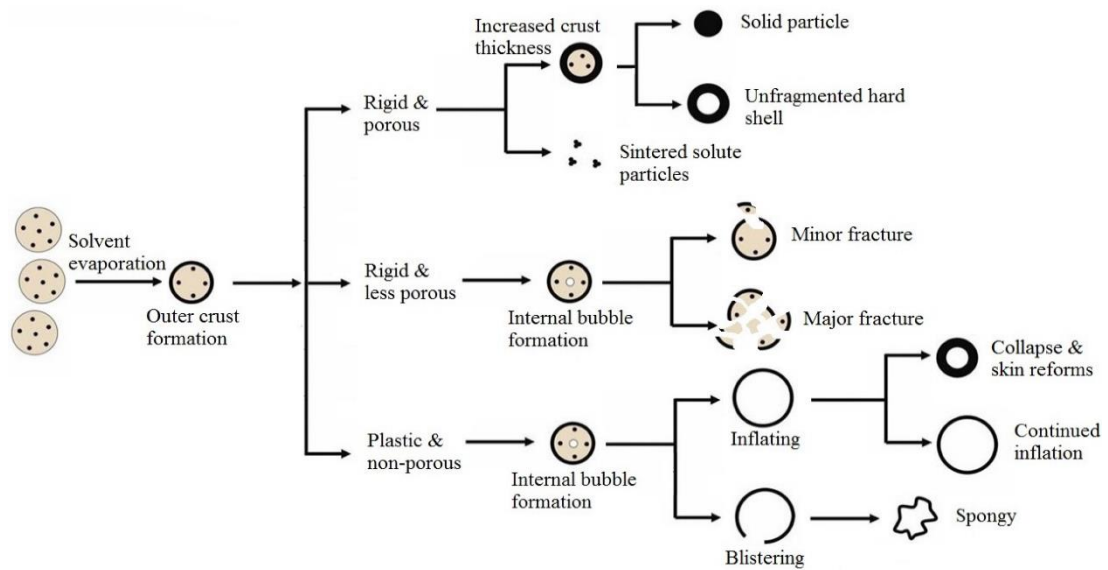


Figure 2-12: Change in particle structure during phase change of suspension [53].

There is a significant body of literature based around experimental and numerical investigations focusing on slurry droplet evaporation. Slurry droplets are comprised of liquid hydrocarbon and/or water with added nano or micro sized particles. Slurry droplets are very similar in composition to suspensions used in SHVOF thermal spray. Initially during evaporation of a slurry / suspension droplet the evaporation dynamics mimic that of a single component droplet. As the evaporation continues particles within the suspension migrate to the surface of the droplets forming a shell, as shown in figure 2-12. The shell structure is divided into three categories rigid and porous structure, rigid and less porous and finally plastic and non-porous structure.

When the shell is rigid and porous; liquid is able to easily diffuse out of the shell therefore the shell shape remains constant as evaporation progresses. The final shape for rigid and porous droplets is either an unfragmented shell or a solid particle. When the shell is rigid and less porous the rate of diffusion of the evaporating species through the shell decreases due to the reduction in porosity of the shell. Liquid becomes

trapped within the shell which results in an increase of pressure, the pressure increases which results in the formation of bubbles within the shell and eventually results in the fracturing of the shell. The level of fracturing of the shell is dependent upon the porosity of the shell and the evaporation rate of the evaporating species. For plastic and non-porous shells, a similar process to the rigid and less porous shell occurs. Where bubble formation takes places and the pressure within the shell increases. However, for plastic and non-porous shells the droplets can either swell and collapse or the shells can become very spongy [28].

For some slurry droplets there is a tendency for the droplets to explode during the vaporization process, this phenomenon is known by the term micro-explosions. For slurry droplets that are comprised of a mixture of particles water and a liquid fuel, water vapour condenses on the droplet surface producing a high concentration of water on the surface. Due to the higher concentration of ethanol within the droplet, the ethanol nucleates and forms bubbles within the droplet. This results in micro-explosions occurring within the droplet which results in a significant fragmentation of the droplets and the shell structures [54] & [55].

2.7 Modelling High Velocity Oxy Fuel (HVOF) Thermal Spray

Suspension high velocity oxy fuel (SHVOF) thermal spray developed out of a niche field within high velocity oxy fuel (HVOF) thermal spray. SHVOF thermal spray was developed to address the issue of clogging that occurred within conventional powder feeders when injecting particles with a diameter below around $5\ \mu\text{m}$. It was found that clogging of the feeders could be prevented by dispersing the particles within a liquid medium to form a suspension. The suspension could then be injected into the combustion chamber through a nozzle or an atomiser. The first successful experimental investigation which looked at injecting suspensions into a HVOF thermal spray device was patented in 2005 by Gadow et al. [56] and published in 2006 by Klilinger et al. [57]. HVOF thermal spray and SHVOF thermal spray are fundamentally identical with the only difference separating the two being the feedstock [58]. There is a more substantial body of literature focused on modelling HVOF thermal spray as this process has been around for a greater duration of time. Therefore, the studies focusing on modelling the gas phase within HVOF thermal spray provide a useful starting point to understand the SHVOF thermal spray process in more detail.

Initial investigations within the field of thermal spray looked at modelling the gas phase for HVOF thermal spray. Investigations have been undertaken to vary the combustion model and vary the numerical methods employed to solve the numerical models. This section outlines the relevant investigations conducted to model HVOF thermal spray that contribute to a greater understanding of modelling SHVOF thermal spray.

2.7.1 Effect of Combustion Model

Within HVOF thermal spray the single step global reaction is overwhelmingly employed to model the combustion, as this method significantly reduces the computational cost. However, in doing so there is a trade off in the fidelity of the combustion reaction. Local properties within the combustion chamber may differ greatly from the average value employed to determine the coefficients within equation 2.2. In addition, this the method of determining the coefficients does not account for the turbulence within the combustion chamber and the combustion chamber geometry. Finally, there is no way to determine the reaction rate for the global reaction that accounts for all of the sub reactions. The shortcomings of employing a global reaction to model the combustion make its use questionable. Nonetheless this has been the sole method employed within the vast number of SHVOF and HVOF thermal spray models due to the significant reduction in the computational cost over the detailed reaction mechanism [59], [37], [20] & [60].

There are a number of models available to determine the reaction rate within combustion. Kamnis et al. [61] investigated the effect of three combustion models with a single step reaction for propane combustion for HVOF thermal spray. The combustion reaction was modelled using the laminar finite rate, eddy dissipation model and the finite rate eddy dissipation model. Figure 2-13 shows static temperature predicted by the three combustion models investigated. It was seen that the finite rate eddy dissipation model and the eddy dissipation model obtained identical results. Within turbulent combustion the rate of reaction is limited by the turbulent mixing [62]. With the eddy dissipation model, it is assumed that the complex chemical kinetics can be ignored and that the rate of reaction can be determined by the rate of turbulent

mixing. The finite rate eddy dissipation model takes the limiting rate from the chemical kinetics and the turbulent mixing.

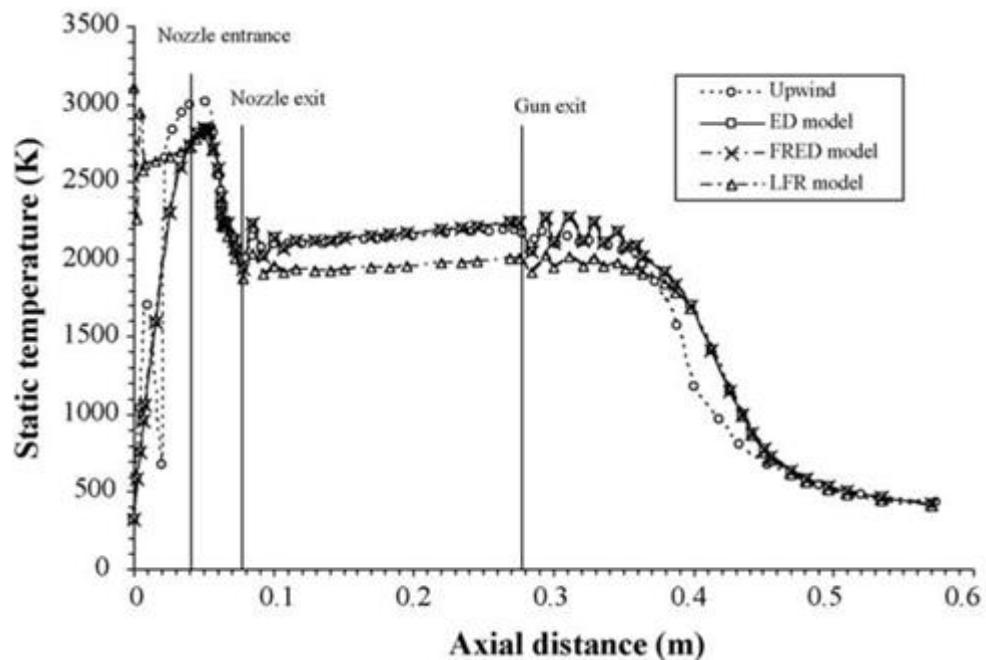


Figure 2-13: Static temperature predicted by the three combustion models [61].

Figure 2-14 shows the temperature profile predicted by the eddy dissipation model; the eddy dissipation model predicted a conical shape flame which occurs through the evolution of a cold inlet stream into a hot flame. Figure 2-15 shows the temperature profile predicted by the laminar finite rate model. The laminar finite rate model predicted that the flame is confined to a thin region around the centre of the combustion chamber. The laminar finite rate model predicts an instantaneous reaction with a maximum flame temperature of 3200 K occurring immediately after the inlet. A higher maximum flame temperature is seen with the laminar finite rate model and most the gas flow is concentrated in the centreline of the combustion chamber. This results in a higher gas velocity in the centre of the combustion chamber compared to the other regions of the combustion chamber. It was stated that practical experience on operating this HVOF systems identified that blockage do not occur inside the gun

in the region that is suggested with the flow field predicted by the laminar finite rate model. Examination on blocked guns show that powder particles accumulate on the internal surfaces of the combustion chamber. Small particles generally follow the flow field, their profiles of temperature and velocity align closely to that of the flow field. In such a case, the small powder particles are more likely to be projected towards the internal surfaces of the combustion chamber by the gas flow. Examination of the combustion chamber within blocked nozzles do not show blockages within the regions suggested by the laminar finite rate model [61].

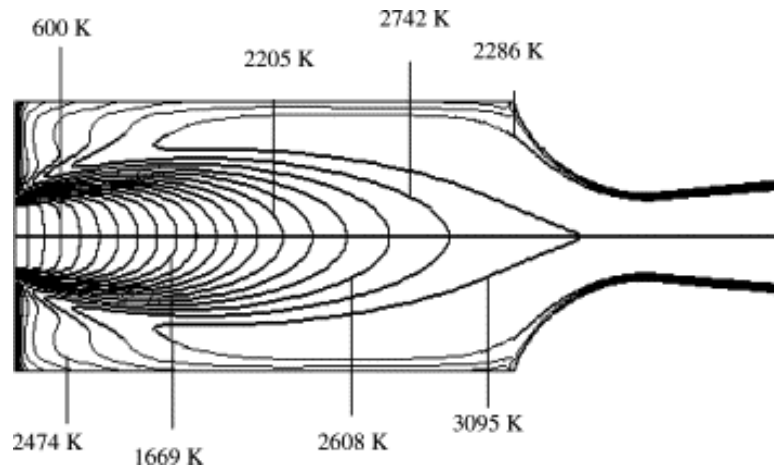


Figure 2-14: Temperature profile predicted for high velocity oxy liquid fuel thermal spray by the eddy dissipation model [61].

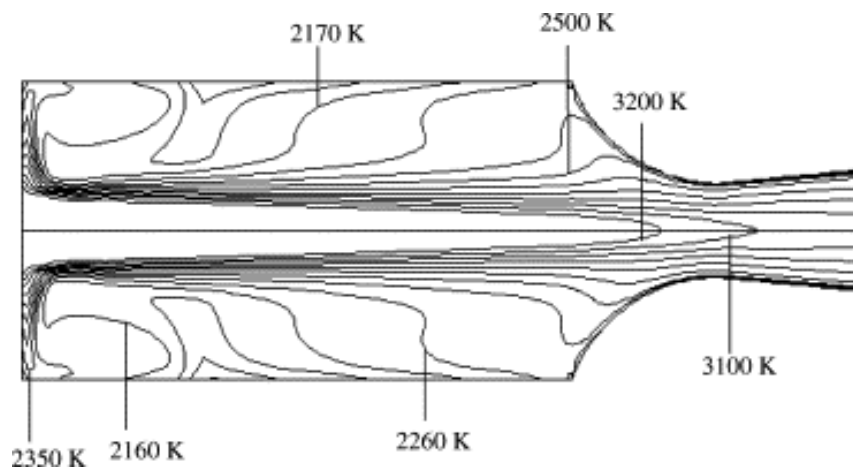


Figure 2-15: Temperature profile predicted for high velocity oxy liquid fuel thermal spray by the laminar finite rate model [61].

2.7.2 Effect of Numerical Scheme

The choice of numerical scheme can impact the accuracy and the stability of the solution. When modelling turbulent flows, a highly dissipative numerical scheme results in numerical dissipation into the solution. However, when modelling shock waves a dissipative numerical scheme is required to prevent spurious oscillations around shocks [63]. Low order upwind schemes such as first and second order upwind schemes are bounded and are very stable. Low order upwind schemes are, however, numerically dissipative and are not as accurate as high order or central based schemes. Certain numerical schemes have been designed to specifically resolve shocks such as the quadratic upwind interpolation (QUICK) scheme. The QUICK scheme is third order accurate and is more accurate on structured meshes aligned with the flow direction [64]. Kamnis et al. [61] investigated the effect of the numerical scheme on the location of the shocks. It was shown that the second order upwind scheme was only able to capture 2 shocks while the QUICK scheme was able to capture 6 shocks which matches closely to the experimental observations. Additionally, the location of the shocks lined up most accurately with the QUICK scheme as shown in figure 2-16.

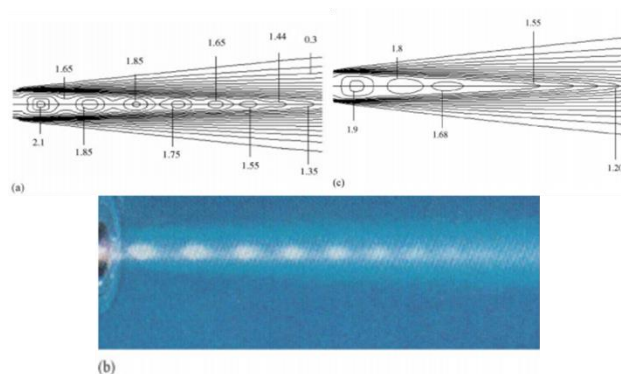


Figure 2-16: Location of shocks obtained from (a) QUICK scheme, (b) Experimental observations and (c) upwind scheme [61].

2.7.3 Effect of Equivalence Ratio

The ratio of fuel to oxidiser can significantly affect the flow field, the flame temperature, the inflight particle velocity and temperature to name a few. Therefore, it is important to understand what effect the ratio of fuel to oxidiser has on the HVOF thermal spray system. The ratio of oxygen to fuel can be quantified by the equivalence ratio, ϕ , which is defined by equation 2.13. Where m refers to the mass, n refers to the number of moles, the subscripts f and o refer to the fuel, oxidiser respectively. The subscript '*actual*' and '*stio*' refers to the actual quantity of fuel and oxidiser used; and the oxidiser ratio required for stoichiometric conditions respectively. Fuel rich environments are quantified at equivalence ratios greater than unity, $\phi > 1$ and fuel lean environments are quantified at equivalence ratios smaller than unity $\phi < 1$.

$$\phi = \frac{(m_f/m_o)_{actual}}{(m_f/m_o)_{stio}} = \frac{(n_f/n_o)_{actual}}{(n_f/n_o)_{stio}} \quad (Eq\ 2.13)$$

Figure 2-17 shows the effect of the equivalence ratio on the adiabatic flame temperature for several fuels at standard temperature and pressure (STP). It can be seen that the choice of fuel and the equivalence ratio both affect the adiabatic flame temperature. Additionally, the maximum flame temperature occurs at a weakly fuel rich environment. The combustion chamber pressure also affects the adiabatic flame temperature, as the adiabatic flame temperature increases with an increase in pressure [65]. The current understanding of the effect of equivalence ratio is built upon experiments taken at standard temperature and pressure and at adiabatic conditions. Additional investigations on how the equivalence ratio affects the flame temperature and gas velocity at SHVOF and HVOF operating conditions will allow optimum conditions to be employed. Additionally, SHVOF thermal spray can utilise ethanol-based suspensions to recover some of the heat lost through vaporization. There is no

literature available that looks specifically at the effect of the equivalence ratio with two fuel sources for SHVOF thermal spray. Further investigation will allow for optimization of injection conditions where ethanol-based suspensions are used.

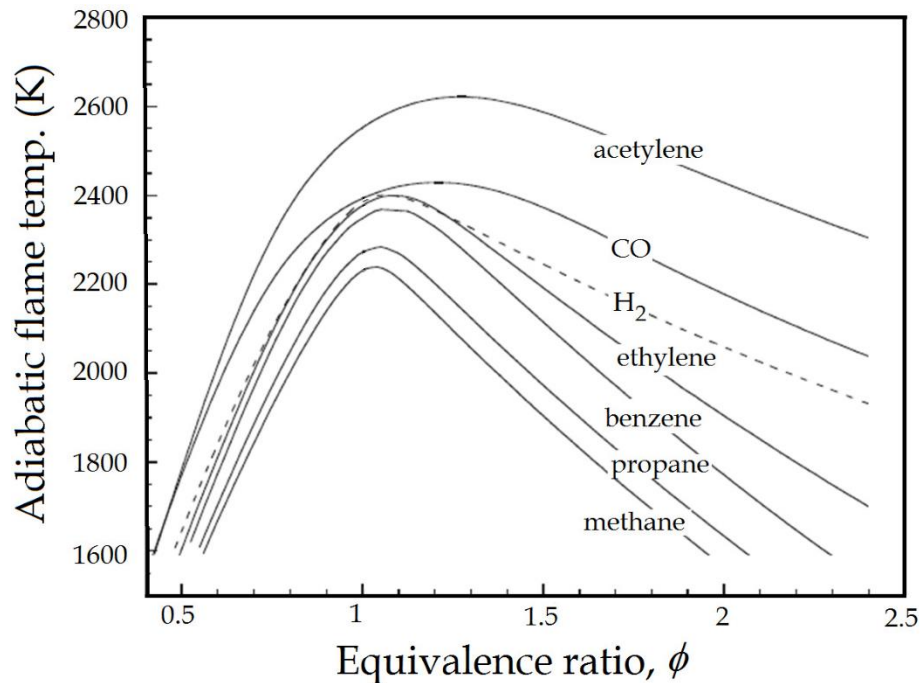


Figure 2-17: The adiabatic flame temperature vs. equivalence ratio for various fuel-air mixtures at STP [66].

Gu et al. [67] investigated the effect of stoichiometric ratio on inflight particle velocity and temperature. Four fuel to oxygen ratios were investigated from values ranging from 0.25 to 0.33. The effect of the fuel to oxygen ratio on the particle velocity and temperature is given by figure 2-18 and 2-19 respectively. It was seen that an increase in the fuel to oxygen ratio from 0.25 to 0.33 lead to an increase the particle velocity for the two particle diameters investigated. Additionally, it was seen that reducing the fuel to oxygen ratio from 0.322 to 0.248 lead to an increase in the particle temperature. Within this study a narrow window for the fuel and oxidizer ratio were investigated. To better the understanding of the effect of the equivalence ratio on the inflight particle characteristics both for SHVOF and HVOF thermal spray, it would be beneficial to

determine at which conditions are the maximum particle velocities and temperatures are witnessed.

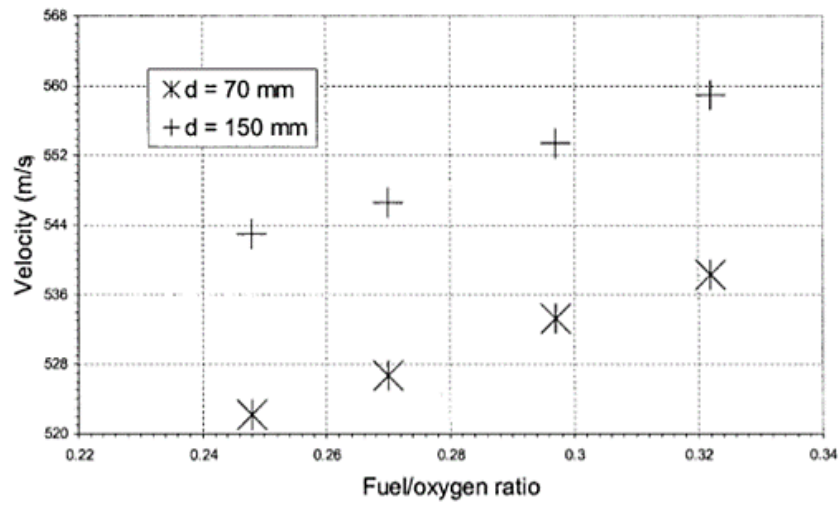


Figure 2-18: The effect of the fuel-to-oxygen ratio at different standoff distances from the nozzle exit on the particle velocity [67].

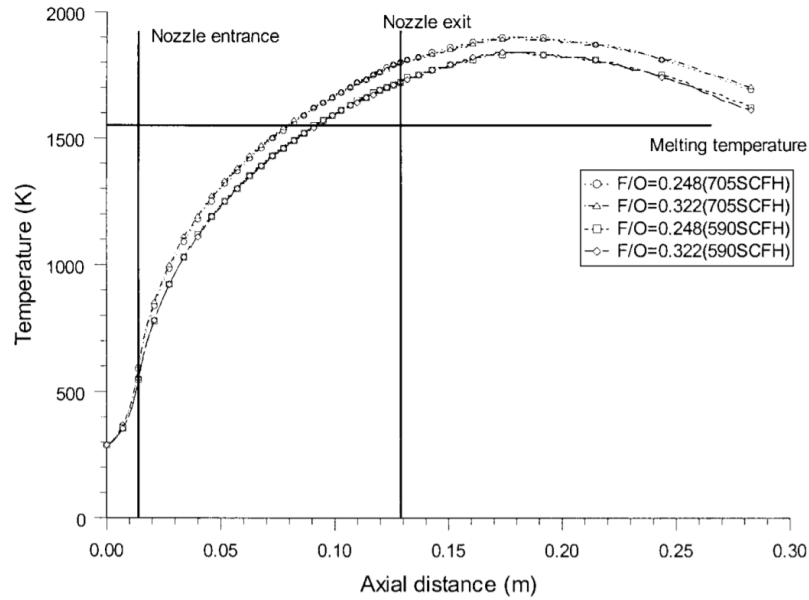


Figure 2-19: The effect of the fuel-to-oxygen ratio on the inflight particle temperature [67].

2.8 Modelling Suspension High Velocity Oxy Fuel Thermal Spray

Within suspension thermal spray a liquid feedstock is injected into the gas flow. The liquid feedstock is injected into the combustion chamber as injections into the combustion chamber allow for better heat and momentum transfer to particles. Injecting the suspension in the combustion chamber faces it's a unique set of challenges for instance this type of injection gives rise to the possibility of internal clogging of nozzles after long periods of spraying [58].

Typically, within SHVOF the liquid feedstock is injected into the combustion chamber which consists of the dispersing liquid, the solid submicron or nanosized particles and a chemical additive. As the suspension is injected into the combustion chamber the suspension undergoes primary breakup to form large liquid droplets. The large droplets undergo secondary breakup where they break up into fine droplets. The liquid component of the suspension then vaporizes where the particles are then accelerated and heated. If the gas temperature is sufficiently high the particles can melt, the molten particles can then lump together to form large agglomerates. These large agglomerates are impacted onto a substrate to form a coating on the surface [1].

There are a large number of parameters that affect the overall properties of the coating. These include the gas flow rate, suspension flow rate, suspension injector geometry, suspension composition, nozzle geometry and standoff distance to name a few. Understanding what effects different parameters have on the system can significantly enhance the properties of the coating.

2.8.1 Effect of Injection Droplet Diameter

Some of the first numerical investigations into modelling SHVOF thermal spray looked at injecting water droplets into the combustion chamber. Tabbara et al. [37] employed the discrete phase model (DPM) to inject water droplets into a JP5000 thermal spray gun. The discrete phase model is a droplet/particle tracking algorithm that models the interaction of droplets/particles with a continuous phase. This model is highly effective at modelling dispersed dilute regions of flow. Within the discrete phase model, droplets are injected into the computational domain where sub models to describe the underlying physics are employed.

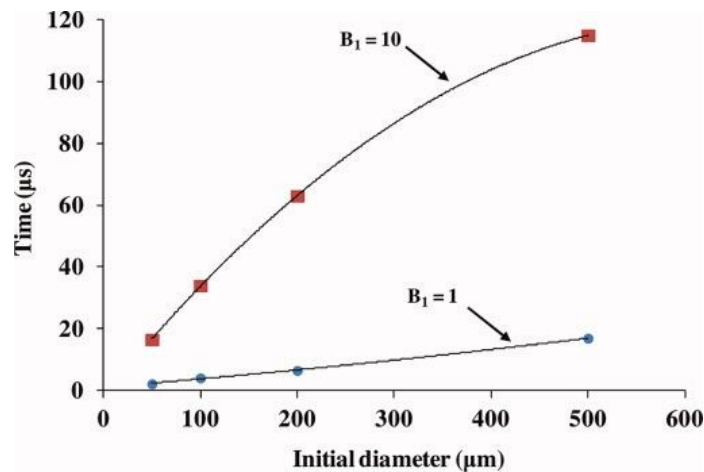


Figure 2-20: Time required for different sized initial parent droplets to shed all their mass, with a varying breakup constant (B_1) of 1 and 10 [37].

Tabbara et al. [37] investigated the effect of the initial droplet diameter on the breakup characteristics and the evaporation of water droplets. Within this study four parent diameters were investigated 50 μm, 100 μm, 200 μm and 500 μm. Figure 2-20 shows the time taken to complete breakup with varying parent droplet diameter (50 – 500 μm) and varying breakup constant (B_1) of 1 and 10. The breakup constant is defined within Chapter 3 and is required in the WAVE secondary breakup model (equation 3.55). It was seen that the time taken for the 50 μm parent droplet to completely

breakup varies between 2.2 μs and 16.5 μs . Larger droplets take a greater time to shed all of their mass for instance for a parent droplet of 500 μm it takes a time from 17 μs and 115 μs for the droplet to completely breakup. Therefore, it was seen that the time taken for the parent droplet to complete breakup increased as the parent droplet diameter increased from 50 μm to 500 μm . Additionally, an increase in the breakup constant from 1 to 10 resulted in an increase in the time for the droplet to completely breakup.

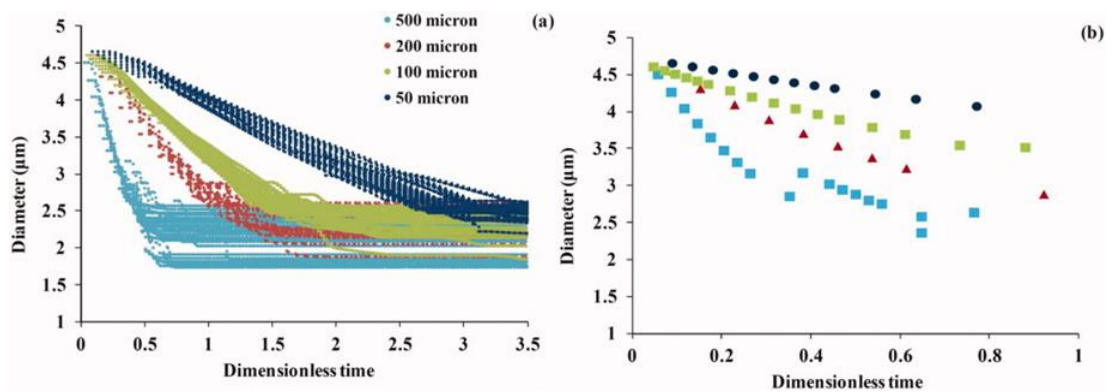


Figure 2-21: Child droplet sizes for different initial parent droplets (a) and filtered results containing only initial primary child droplets (b) [37].

Figure 2-21 shows the change in child droplet diameter with time with varying parent droplet diameters (50 – 500 μm). It can be seen that as the initial parent droplet size is increased from 50 to 500 μm , the average primary child droplet size decreases. For a 500 μm parent droplet diameter the minimum droplet size is around 2.3 μm . While for the 50 μm parent droplet diameter the minimum droplet size is around 4.1 μm .

Figure 2-22 shows the time taken for droplets of diameters varying from 2 – 10 μm to shed 10 % of their mass from vaporization or completely breakup. In figure 2-22 it can be seen that as the droplet diameter increases the time taken for the droplets to vaporize 10 % of their mass increases rapidly. It is well known that small droplets have the greatest contribution to vaporization due to their large surface area to volume

ratio. Vaporization occurs on the surface of droplets and hence small droplets can vaporize more readily. It can also be seen that the breakup time increases drastically for droplet diameters within the range of 2.5 μm – 3 μm . At droplet sizes within this range vaporization is the main factor that drives the disintegration of droplets. Therefore, it can be seen that the mechanism contributing to droplet disintegration is heavily dependent on the droplet diameter. Disintegration of small droplets occurs due to vaporization of the droplets while large droplet disintegration occurs due to breakup of the large droplets into smaller droplets.

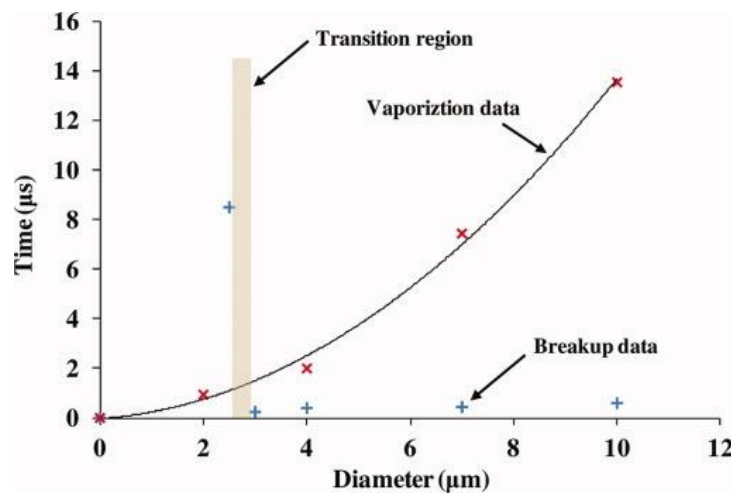


Figure 2-22: Time taken for droplet of varying sizes to shed 10% of their original mass by vaporization and breakup [37].

This type of study is sufficient for a generic understanding of the effect of injecting liquid feedstock into a SHVOF thermal spray system. However, there are a number of limitations with the discrete particle model employed within this study; for one liquid feedstock is less commonly injected into a combustion chamber through the use of an atomizer in SHVOF. More commonly liquid feedstock forms a jet which undergoes primary breakup. Another limitation of this study is that the study is conducted at standard temperature and pressure rather than SHVOF conditions which may affect the dynamics of the breakup and evaporation.

2.8.2 Effect of Type of Injection

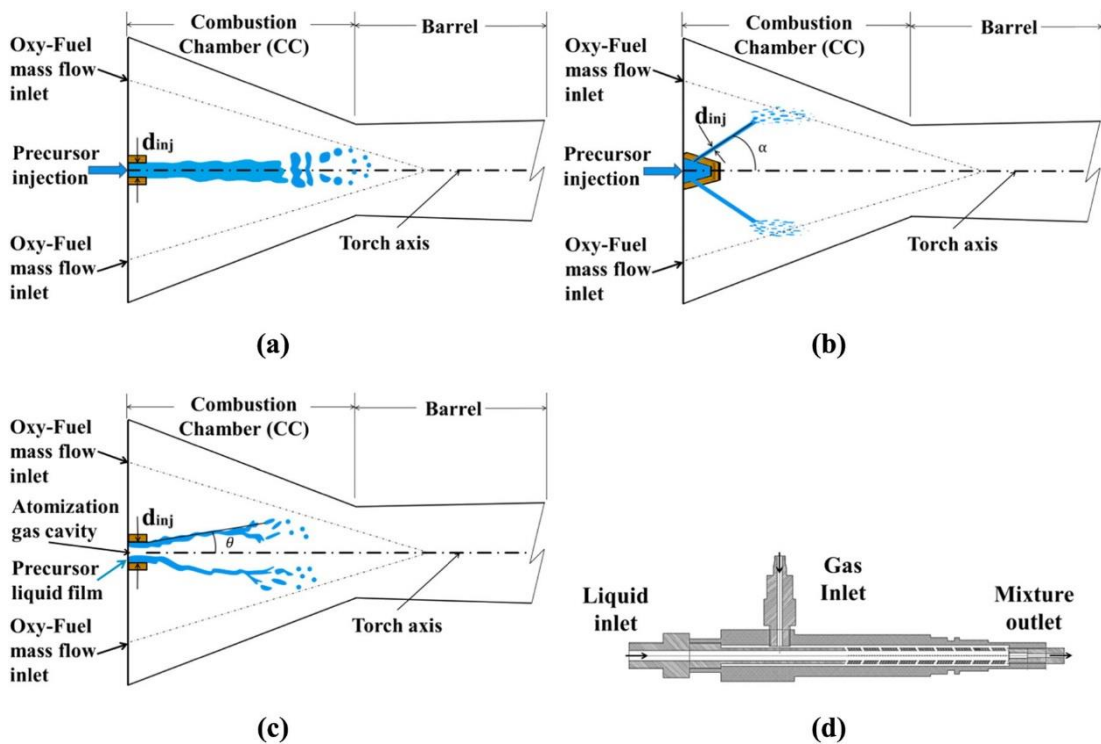


Figure 2-23: Different Injection types for liquid feedstocks (a) surface-type injection (STI) (b) group-type injection (GTI) (c) effervescent-type injection (ETI), and (d) design of effervescent-type injection-nozzle [68].

Mahrukh et al. [69] investigated the effect of different injection models for the DPM single component droplet injection. The thermophysical properties of the suspension were determined from curve fitted correlations for the specific heat, density, viscosity, surface tension and thermal conductivity. The approach employed to model the suspension thermophysical properties did not account for the effect of evaporation on the suspension composition. This study looked at three different injection types; group injection surface injection and effervescent injection as can be seen by figure 2-23. In this study the effect of the particles on the liquid properties was accounted for through established correlations. Values for the specific heat, density, viscosity and thermal conductivity for the liquid and solid properties were calculated using a volume average

of the two components for the density and specific heat. Brinkman's modification of Einstein's formulae for the relationship of the volume fraction of particles within a suspension was used to calculate the viscosity of the suspension. The various models to determine the viscosity that are employed within suspension thermal spray literature are outlined and discussed within section 2.9.2. Bruggeman's [70] formula for the thermal conductivity was used to calculate the effect of the particles on the thermal conductivity.

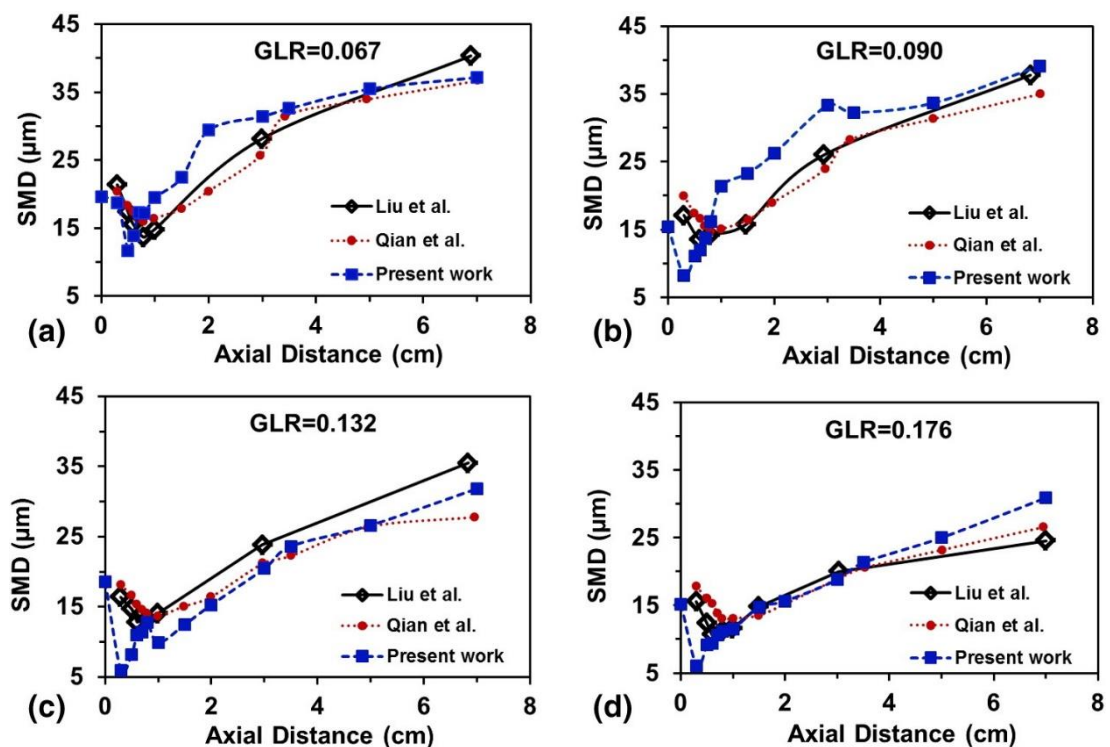


Figure 2-24: Comparison of the predicted results at varied GLR with Liu et al. and Qian et al. (a) 0.067, (b) 0.090, (c) 0.132, and (d) 0.176 [69].

Mahruk et al. [68] compared the Sauter mean diameter (SMD) of water droplets exiting an effervescent injector into atmosphere at varying gas-to-liquid mass flow rate ratios (GLR) to experimental measurements collected by Liu et al. [71] and numerical data from Qian et al. [72] & [73]. The Sauter diameter of a droplet is defined as the diameter of a sphere that has the same volume/surface area ratio as a droplet of

interest. The Sauter mean diameter is the mean Sauter diameters from many droplets considered. It can be seen from figure 2-24 that the model employed by Mahrukh et al. [68] compared well to the experimentally and numerically values of the SMD at GLR varying from 0.067 – 0.0176.

Table 2-3: Summary of injection conditions for different cases studied by [68]

Injection types				
Case 1 → Without Droplets, only combustion gas flow characteristics				
Case 2.1 → Surface-type injection, angle of injection 0°.				
Group type injection		Effervescent type injection		
Case	Angle of injection	Case	Spray half angle	GLR
Case 2.2	5°	Case 3.1	4°	0.095
Case 2.3	10°	Case 3.2	6°	0.190
Case 2.4	15°	Case 3.3	8°	0.285
Case 2.4	20°			

Mahrukh et al. [68] then went onto investigate what effect the injection angle had on SHVOF thermal spray process for different injection types. Table 2-3 shows a summary of the conditions investigated within the study. Initially the angle of injection was varied from 0° - 20° for the group type injection. The effect of the angle of injection on the droplet evaporation, ethanol mass fraction, and droplet SMD were investigated as shown in figure 2-25. It can be seen from figure 2-25 (a) that the rate of evaporation increases as the angle of injection increases from 5° to 15°. As the angle of injection increases further from 15° to 20° a decrease in the maximum evaporation rate is observed.

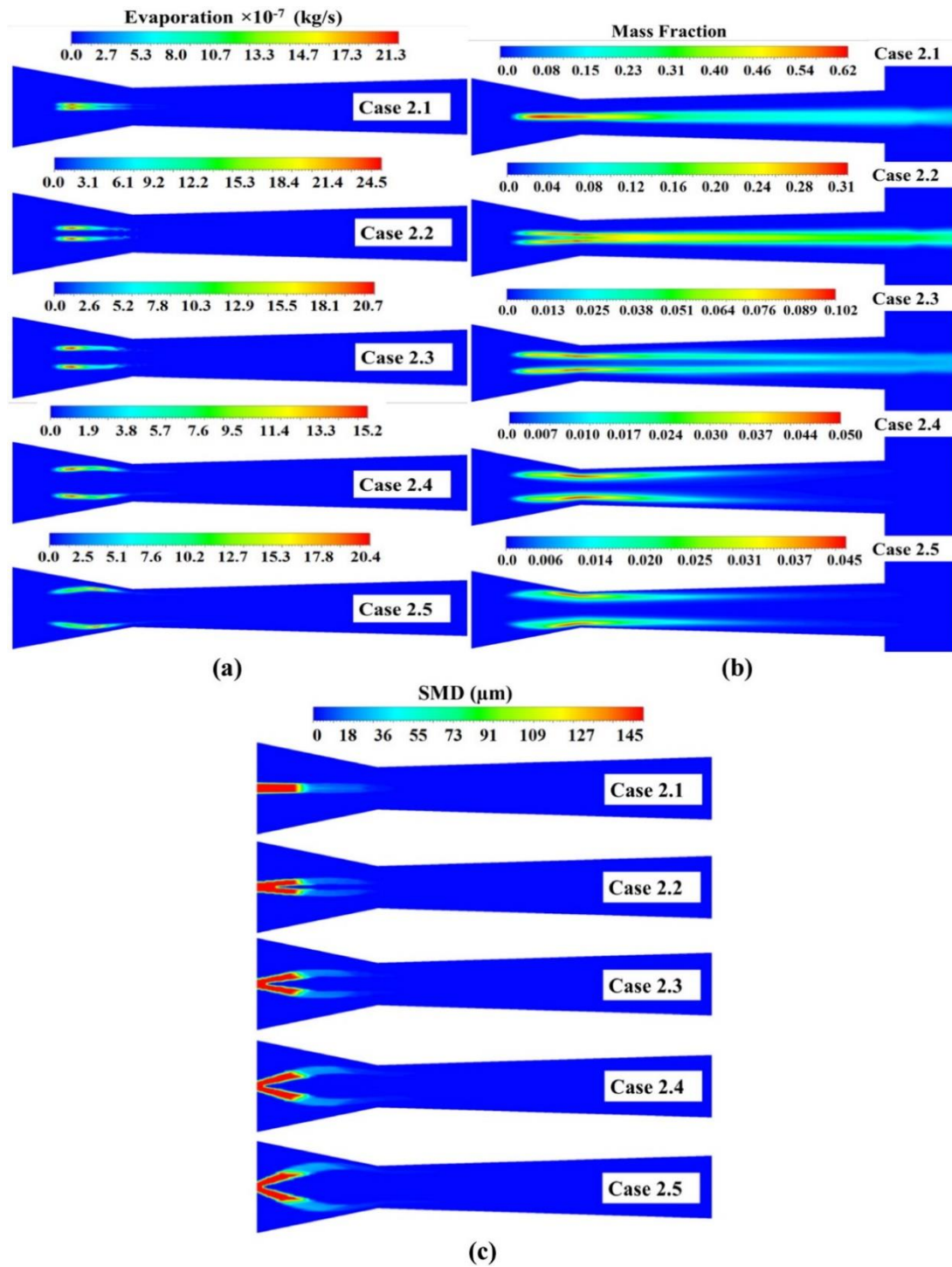


Figure 2-25: (a) evaporation rate, (b) mass fraction of ethanol and (c) SMD of the ethanol droplets at different injection angles for a group type injector [68].

The increase in the evaporation rate with the increase in the angle of injection up to 15 degrees is further demonstrated by the ethanol mass fraction contours shown in figure 2-25 (b). As the droplets evaporate an increase in the mass fraction of ethanol

is seen and then as the ethanol reacts with unreacted oxygen the mass fraction of ethanol decreases. For angles of injections within the range of 0° - 10° the ethanol is still present even beyond the torch exit. With the smaller angle of injection, the combustion of ethanol is delayed due to incomplete evaporation within the nozzle. At large angles of injection (15° - 20°) it can be seen that the ethanol is fully consumed within the nozzle. This is due to the ethanol evaporating more readily at higher injection angles.

Figure 2-25 (c) shows the effect of the angle of injection on the droplet SMD. Increasing the angle of injection increases droplet dispersion within the combustion chamber. Effective dispersion of droplets results in more effective heating, evaporation and combustion of ethanol within the droplets. However, increasing the angle of injection up to 20° results in collision of particles within the combustion chamber walls. Collision of particles with the combustion chamber walls will result in deposition of solid particles to the walls of the combustion chamber which in turn will cause blockages within the nozzle.

Figure 2-26 shows the (a) evaporation rate, (b) mass fraction of ethanol and (c) SMD of the ethanol droplets at different GLR for an effervescent type injector. Figure 2-26 (a) shows a decrease in the SMD with an increasing GLR, this suggests that increasing the GLR improves the atomization of droplets, however, this reduction in the SMD is quite small. It can be seen by comparing figures 2-25 (c) and 2-26 (a) that the ETI results in more rapid atomization of the droplets at the injection in comparison to the GTI. Smaller droplets benefit from more rapid evaporation due to their higher surface area to volume ratio. As the half angle increases the droplets cannot penetrate the core of the combustion chamber. Hence, the lower rate of evaporation is observed for the ETI when compared to the GTI as the droplets cannot enter the hottest region of the

combustion chamber. The effect of the angle of injection on the evaporation rate is augmented by the increase in the evaporation rate with an increase in the GLR. Figure 2-26 (c) shows a lower ethanol mass fraction in the barrel section with an increase in the GLR. The ethanol is completely evaporated and was burned before the torch exit. Unfortunately, the effect of the GLR and injection angle were not investigated independently. Therefore, it is difficult to understand how much of the effect is due to the varying GLR and how much is due to the varying angle of injection.

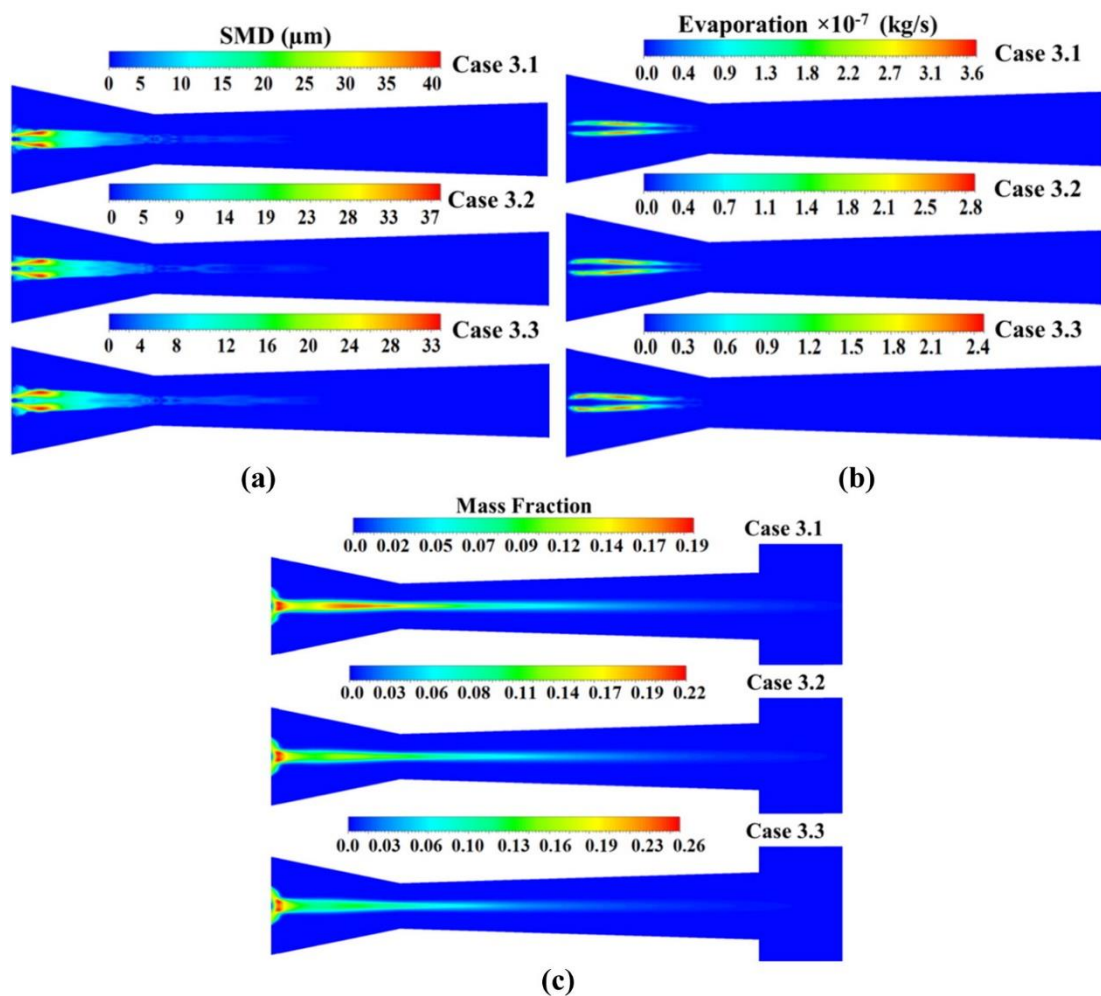


Figure 2-26: (a) evaporation rate, (b) mass fraction of ethanol and (c) SMD of the ethanol droplets at different GLR for an effervescent type injector [68].

2.8.3 Comparison of Numerical Model to Accuraspray G3

More recent studies in modelling suspension thermal spray process have looked to model the suspension as a multicomponent droplet [74] & [75]. This approach models the droplet very similar to a pure liquid droplet however the material properties are modified such that they account for the effect of the particles on the overall droplet properties. This approach also models an additional scalar to account for the mass fraction of the individual constituents within the droplets as evaporation of the liquid component occurs. This modelling approach addresses some of the issues such as accounting for the effect of the evaporation of the liquid on the suspension properties.

Jadidi et al. [20] modelled the injection of a suspension comprised of ethanol, ethylene-glycol and mullite using a multicomponent DPM framework into the DJ2700 nozzle. The ensembled average inflight particle velocity and temperature were compared to experimental measurements obtained from Accuraspray G3. A detailed outline of the operating principles of Accuraspray is given in chapters 2.10 and 6.1. Figures 2-27 and 2-28 show a comparison of the ensembled average inflight particle velocity and temperature numerical model to Accuraspray G3 measurements respectively. This study demonstrated that there was a significant under prediction in the gas temperatures by around 500 K. Within this study the Ranz - Marshal correlation was employed to determine the heat transfer coefficients. Currently within SHVOF thermal spray modelling the Ranz-Marshal correlation has been the only model employed to determine the heat transfer coefficients. Alternative models exist within literature for application to high Mach flows and the effectiveness of different models to determine the heat transfer coefficient may address this underprediction.

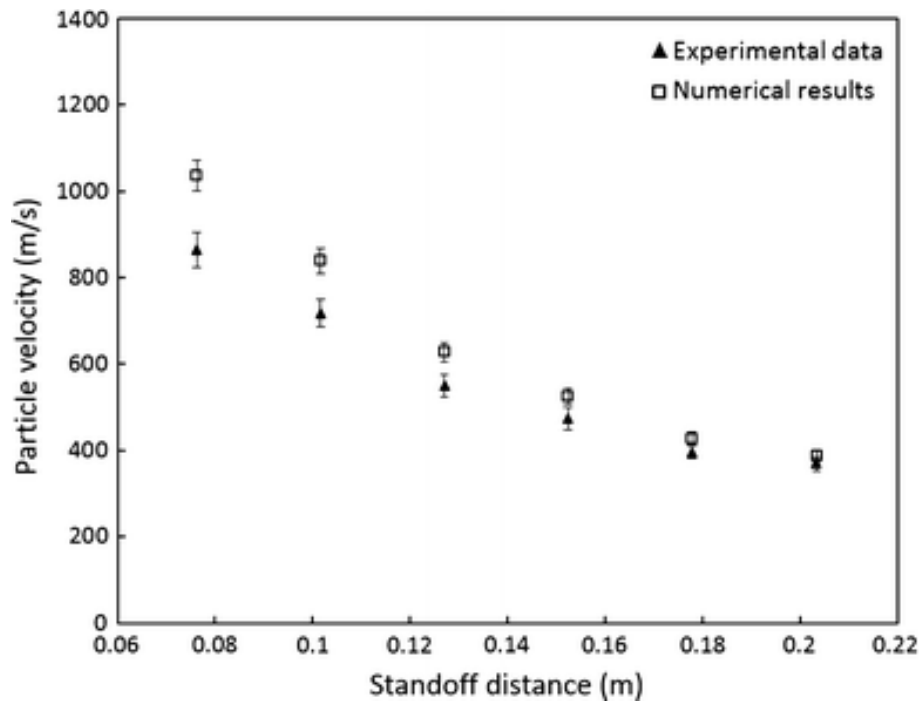


Figure 2-27: Comparison of numerical modelling data to Accuraspray G3 measurements for the inflight particle velocities [20].

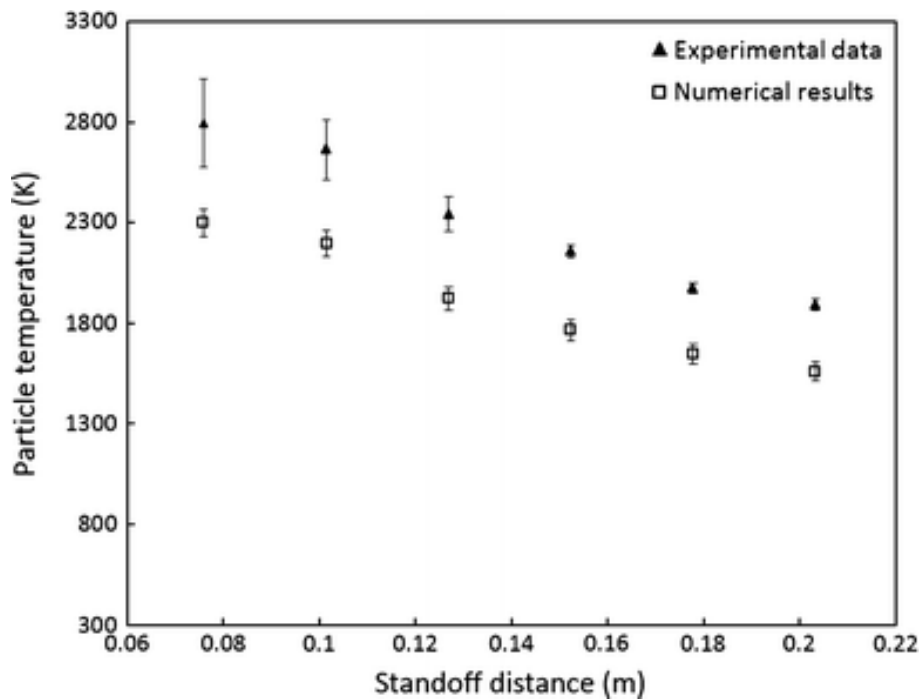


Figure 2-28: Comparison of numerical modelling data to Accuraspray G3 measurements for the inflight particle temperatures [20].

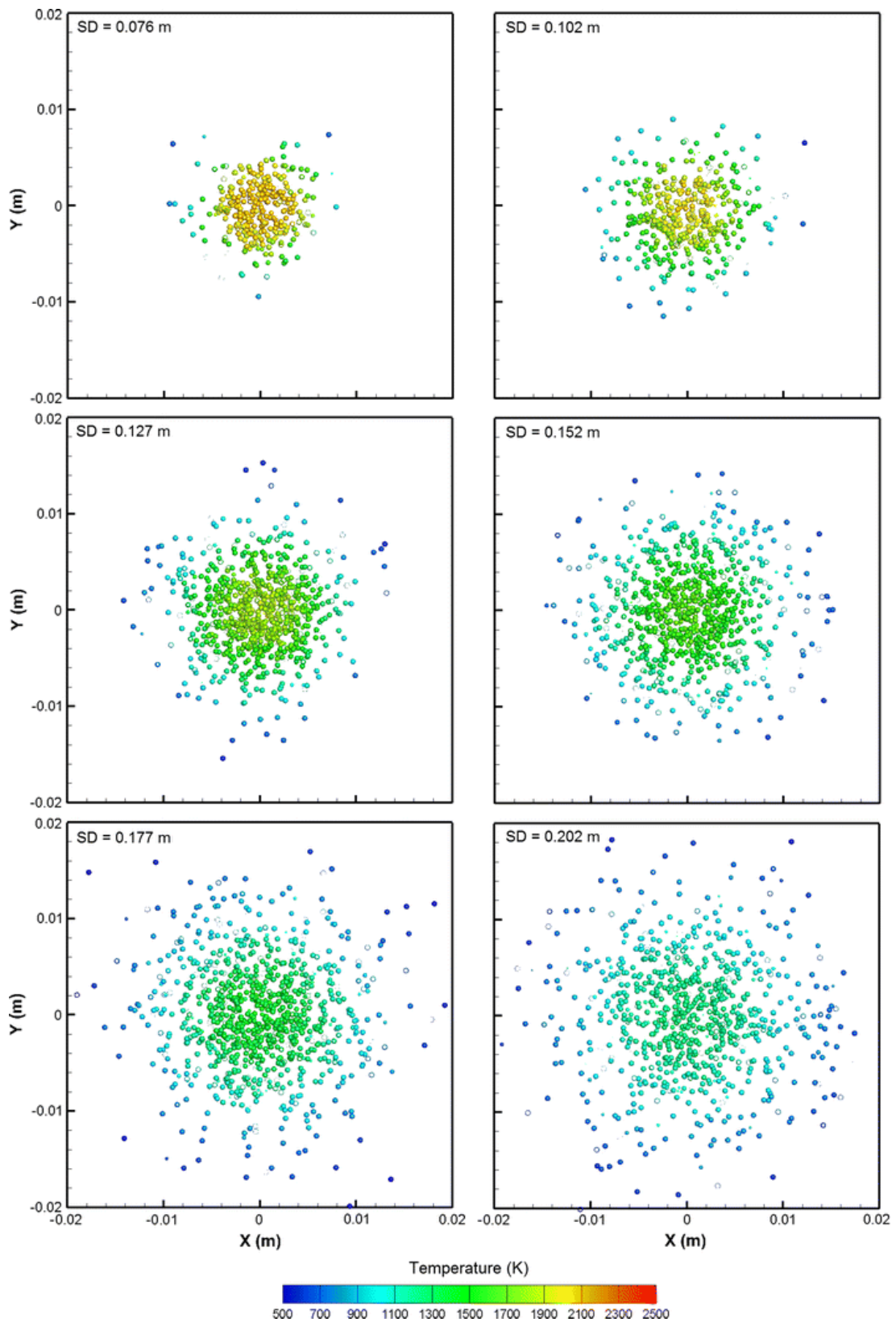


Figure 2-29: Particle temperature and spatial distributions at different standoff distances (SOD) [20].

Additionally Jadidi et al. [20] investigated the effect of the standoff distance on the spatial distribution of particles. The correlation given by equation 2.14, where $S.D$ represents the standoff distance and D_{spray} represents the cross-sectional diameter of spray particles. The usefulness of such a correlation is questionable as the correlation may model the spread of particles at the operating conditions employed within this numerical study, however, this correlation does not account for other factors which will affect the spatial distribution of particles. There are other factors that effect of the spatial distribution of particles, such as the flow Mach number, turbulent kinetic energy of the jet and the dissipation rate, which would affect the spread of the particles.

$$D_{spray} = 0.55(S.D)^{1.6} + 0.006 \quad (Eq\ 2.14)$$

2.8.4 Effect of Substrate Geometry

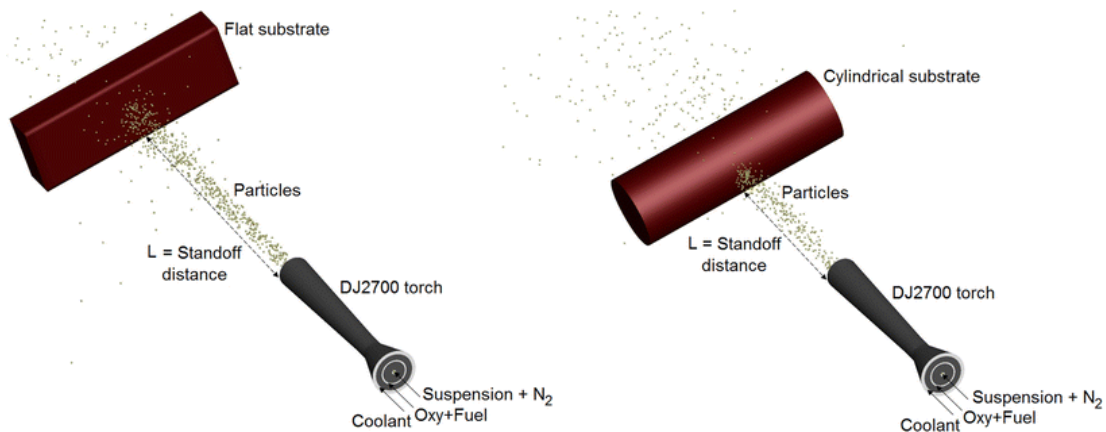


Figure 2-30: Substrate geometries investigated (left) flat substrate and (right) cylindrical substrate [60].

Jadidi et al. [60] looked at including the effect of the substrate of the gas phase and particles. In this study a flat substrate and cylindrical substrate geometries were

investigated which can be seen in figure 2-30. The effect of the substrate geometry and the standoff distance on the centreline velocity were investigated.

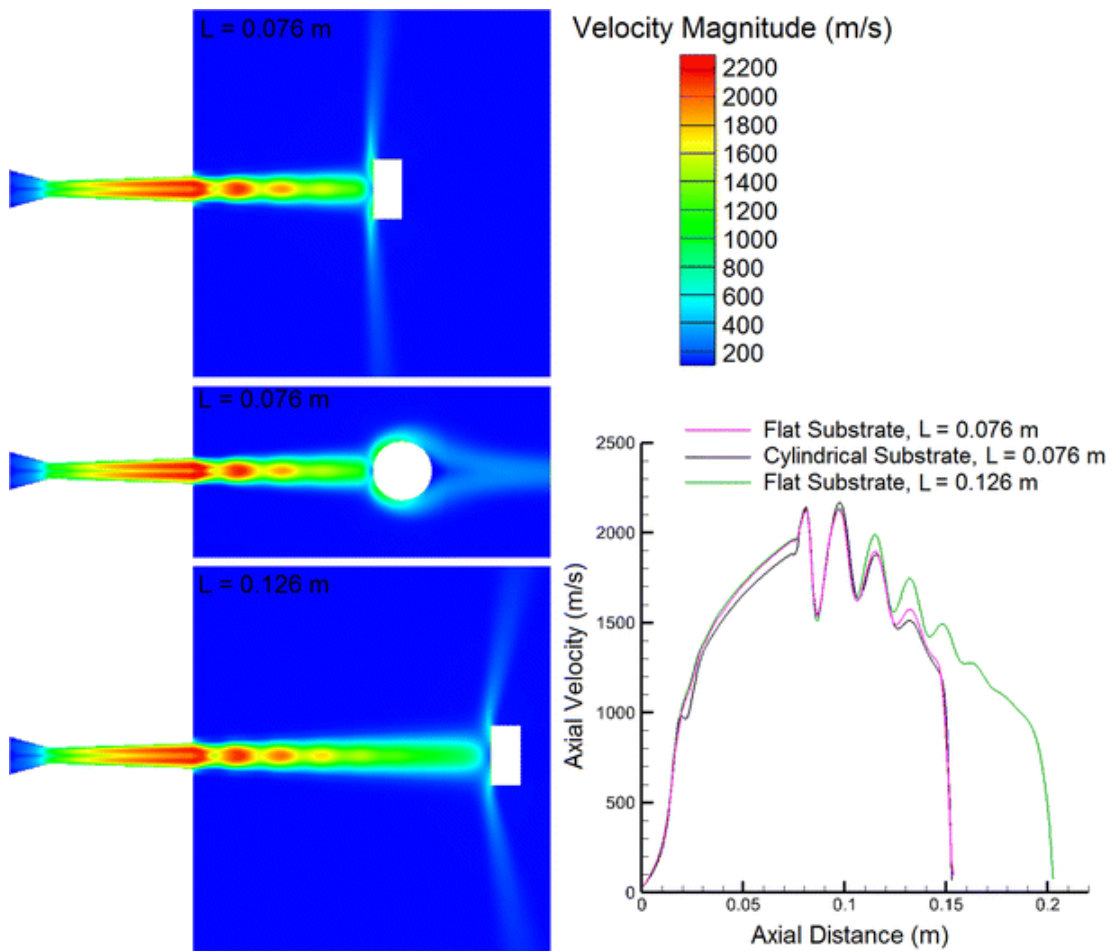


Figure 2-31: Effects of substrate shape and location on gas velocity magnitude: velocity contours (left) and along centreline (right) [60].

Figure 2-31 shows the effect of the substrate shape and the substrate location on the velocity magnitude and centreline velocity magnitude. It can be seen from figure 2-31 that the substrate geometry does not significantly influence the centreline velocity as a very similar velocity profile is seen for the flat and cylindrical substrates at the same

standoff distance. However, it can be seen that the location of the substrate significantly impacts the velocity within the free jet. As the standoff distance increases from 76 mm to 126 mm the number of shock waves increases from 4 to 6 respectively. Additionally, as the standoff distance increases from 76 mm to 126 mm the velocity magnitude at any given point along the centreline is greater for the standoff distance of 126mm. It can be seen that a bow shock forms close to the substrate which results in a pressure increase and a velocity decrease. As the standoff distance increases, the strength of the bow shock decreases. It was seen that the bow shock was more prevalent for the cylindrical substrate with the same standoff distance than the flat substrate.

The ratio of particles which impacted the substrate to the total number of particles injected were investigated for the two geometries. Figure 2-32 shows the effect of substrate shape and standoff distance on suspension/particle trajectory, velocity magnitude, and temperature. It was seen from calculating the ratio of total particles to the number of particles that impact the substrate that at a fixed standoff distance ($L = 0.076$ m) the striking rate for a flat substrate was greater than that of the cylindrical substrate. Additionally, it can be seen from figure 2-32 that many of the particles follow the gas phase streamlines and do not impact on the substrates. Comparing the number of particles that deviate away from the substrate at $L = 0.076$ m, it can be seen that, compared to flat substrate, more fine particles get diverted close to the cylindrical substrate. It was suggested that particles that move close to the jet centreline are less influenced by the bow shock that forms in front of the substrate. Particles that are deviated away from the centreline, are less likely to impact the substrate.

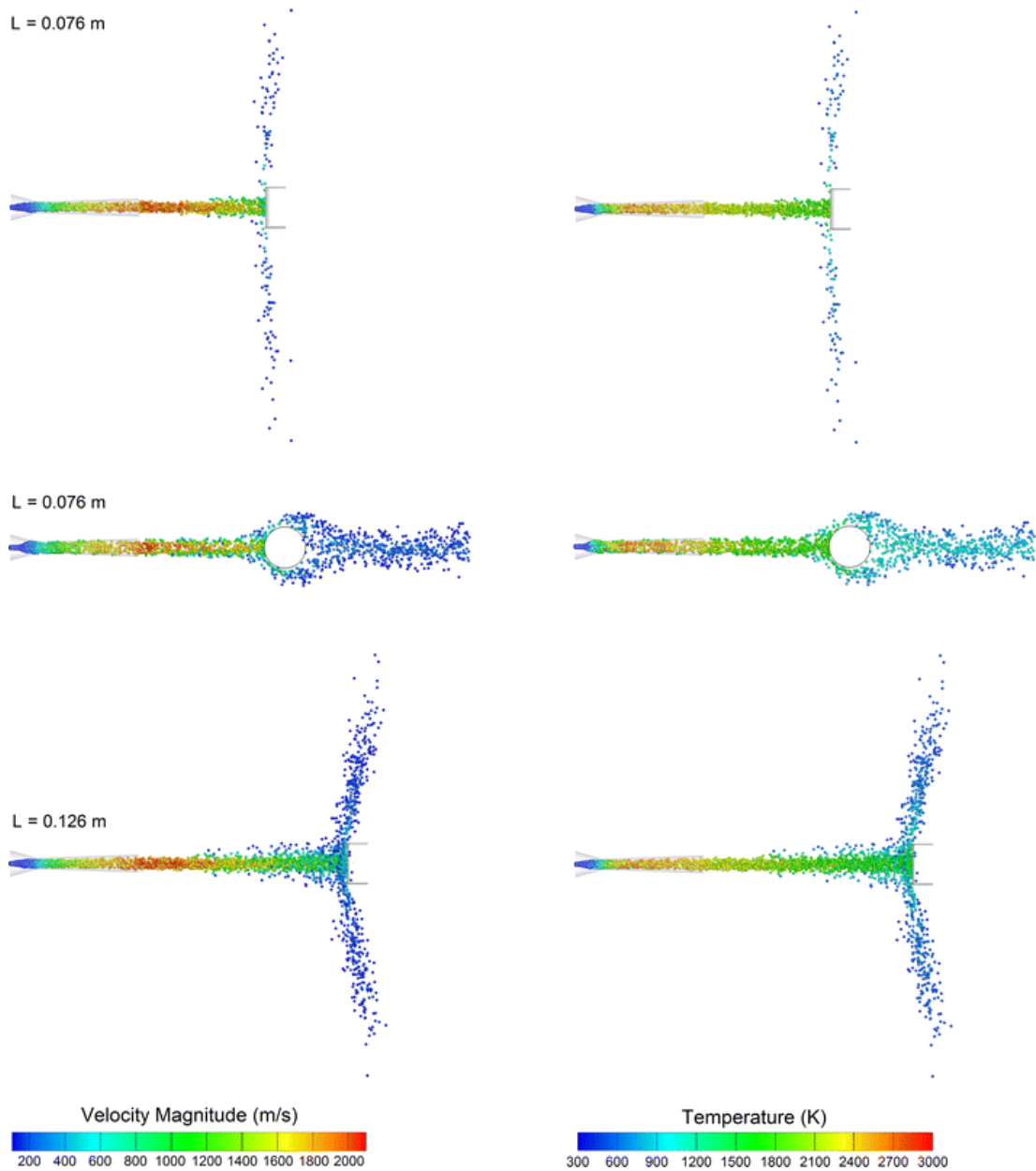


Figure 2-32: The effect of substrate shape and standoff distance (L) on suspension/particle trajectory, velocity magnitude, and temperature [60].

Figure 2-33 shows a distribution of the particle landing location for a flat substrate at two standoff distances (0.076 m and 0.0126 m) and a cylindrical substrate a standoff distance of 0.076 m. It can be seen by comparing the particle landing distribution for a flat substrate at the two standoff distances, at the shorter standoff distance of 0.076

m the landing location of the particles is clustered around the centre of the flat plate ($S/d_w = 0.5$). Additionally, comparing the landing location of particles impacting a flat substrate and a cylindrical substrate at the same standoff distance (0.076 m) the effect of the substrate geometry on the landing location of the particles can be evaluated. From figure 2-33 it can be seen that the landing location of the particles is cluster around the centre of the substrate to a greater degree for a flat substrate than a cylindrical substrate. From both figure 2-32 and figure 2-33 it is can be seen that both the substrate geometry and the standoff distance have a significant influence on how often particles impact the substrate and where the particles impact the substrate.

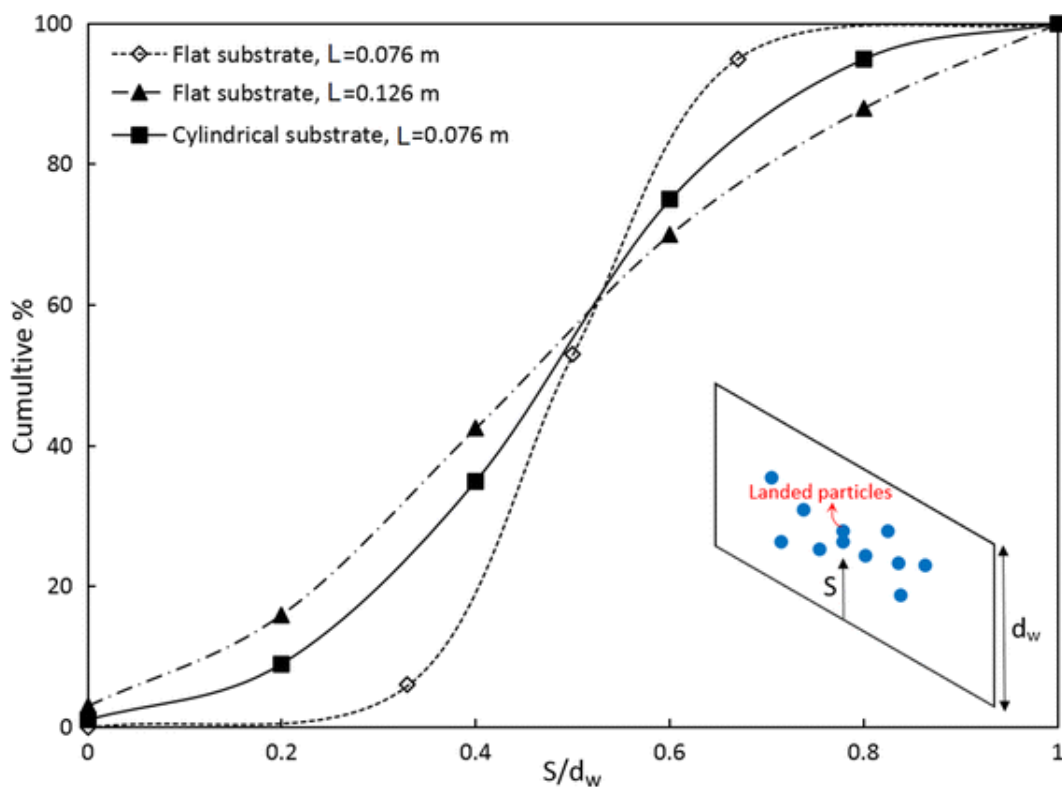


Figure 2-33: Particle landing location distributions for various substrates and standoff distances [60].

Table 2-4: Summary of numerical modelling approaches employed within SHVOF thermal spray (ordered by date of publication)

Author	Turbulence Model	Combustion Model	Multiphase Model	Drag Coefficient	Nusselt Correlation	Primary Breakup	Secondary Breakup
Dongmo et al. 2009 [76]	Realizable k-ε	Eddy Dissipation Model	Single component DPM	Crowe	Ranz-Marshall	-	TAB
Dongmo et al. 2009 [77]	Realizable k-ε	Eddy Dissipation Model	Single component DPM	Crowe	Ranz-Marshall	-	TAB
Taleby et al. 2012 [78]	Realizable k-ε	Eddy Dissipation Model	Single component DPM	Morsi and Alexander drag model [79]	Ranz-Marshall	-	-
Tabbara et al. 2012 [37]	Realizable k-ε	Eddy Dissipation Model	Single component DPM	Spherical	Ranz-Marshall	-	WAVE
Gozali et al. 2013 [80]	Realizable k-ε	Eddy Dissipation Model	Single component DPM	Spherical	Ranz-Marshall	-	WAVE

Gozali et al. 2014 [59]	Realizable k-ε	Eddy Dissipation Model	Multicomponent DPM	Spherical	Ranz-Marshall	-	TAB
Gozali et al. 2015 [81]	Realizable k-ε	Eddy Dissipation Model	Single component DPM	Spherical	Ranz-Marshall	-	TAB
Mahrukh et al. 2016 [69]	Realizable k-ε	Eddy Dissipation Model	Single component DPM	Non-spherical	Ranz-Marshall	-	TAB
Mahrukh et al. 2016 [68]	Realizable k-ε	Eddy Dissipation Model	Single component DPM	Non-spherical	Ranz-Marshall	-	TAB
Jadidi et al. 2016 [20]	Realizable k-ε	Eddy Dissipation Model	Multicomponent DPM	Crowe	Ranz-Marshall	-	TAB
Jadidi et al. 2018 [60]	Realizable k-ε	Eddy Dissipation Model	Multicomponent DPM	Crowe	Ranz-Marshall	-	TAB

2.9 Modelling Suspension Plasma Spray Thermal Spray

There are several similarities and differences between SHVOF thermal spray and suspension plasma spray (SPS). For instance, the most notable similarity is that both use a liquid feedstock to inject sub-micron particles into the flow field. The most notable differences are that SPS thermal spray utilises the energy generated from the formation of plasma instead of combustion like with SHVOF thermal spray. Additionally, within SHVOF thermal spray suspension is injected within the combustion chamber as opposed to SPS thermal spray where an external injection is utilised. Therefore, SPS thermal spray provides a useful body of literature to address challenges faced within SHVOF thermal spray.

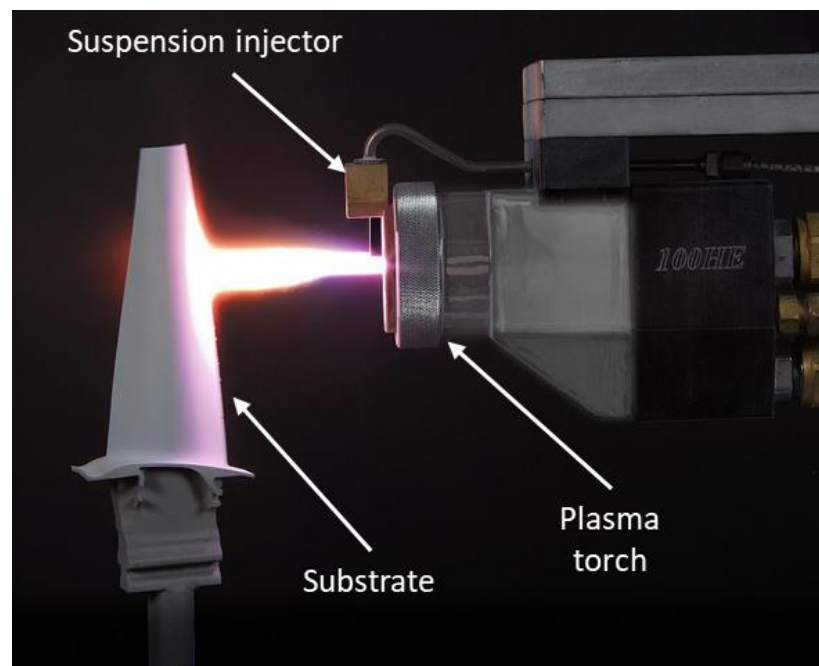


Figure 2-34: Suspension plasma torch in operation coating a turbine blade [82]

Suspension plasma spray (SPS) thermal spray is a process where liquid feedstock is injected into a plasma jet emitted from a plasma torch. The plasma jet is generated by ionising a gas with a high atomic weight (Ar, N₂) mixed with a gas with a high thermal conductivity (H₂, He) [83]. Further discussion and information on the fundamental

principles behind the plasma torches used within SPS thermal spray can be found in [84]. The gas temperature and velocities within SPS thermal spray can reach up to 10000 K and 1000 m/s within the core of the torch. Therefore, gas temperatures within SPS thermal spray well exceeds SHVOF thermal spray. Within SPS thermal spray suspension is radially injected into the plasma jet, a suspension plasma torch in operation is shown in figure 2-34, where the jet undergoes primary breakup, secondary breakup and the liquid within the suspension is vaporized. SPS thermal spray produces coatings with a higher porosity than SHVOF thermal spray due to the lower impact velocity of particles [85].

2.9.1 Effect of Injection Conditions

Jabbari et al. [75] investigated the effect of the injection velocity, injection location and the angle of injection on the on the inflight particle characteristics for suspension plasma spray. Table 2-5 shows a summary of the injection conditions investigated within this study [75].

Table 2-5: Summary of Injection Conditions Investigated

Case Number	Velocity (m/s)	Axial Distance (mm)	Injector angle (°)
1	12.9	7	14
2	25.7	7	14
3	38.6	7	14
4	25.7	1	0
5	25.7	17	14

To validate the numerical model; the effect of the turbulence model was compared to experimental and numerical data available within SPS thermal spray literature as shown in figure 2-35. It can be seen from figure 2-35 that the RSM model provides the most agreement to the experimental measurements. Additionally, jet penetration was compared to experimental data obtained from high-speed imaging of the suspension injection into the plasma jet as shown in figure 2-36. It can be seen that the numerical measurements compare relatively well to the experimental data as shown in figure 2-36. It was suggested that the underestimation associated with the numerical simulations could be the result of neglecting the primary breakup modelling. To model the primary breakup, methods such as volume of fluid (VOF) are required. The VOF model, however, requires a mesh of the order of the liquid and particle structures to accurately resolve the droplet and particles within the flow and hence is more computationally expensive.

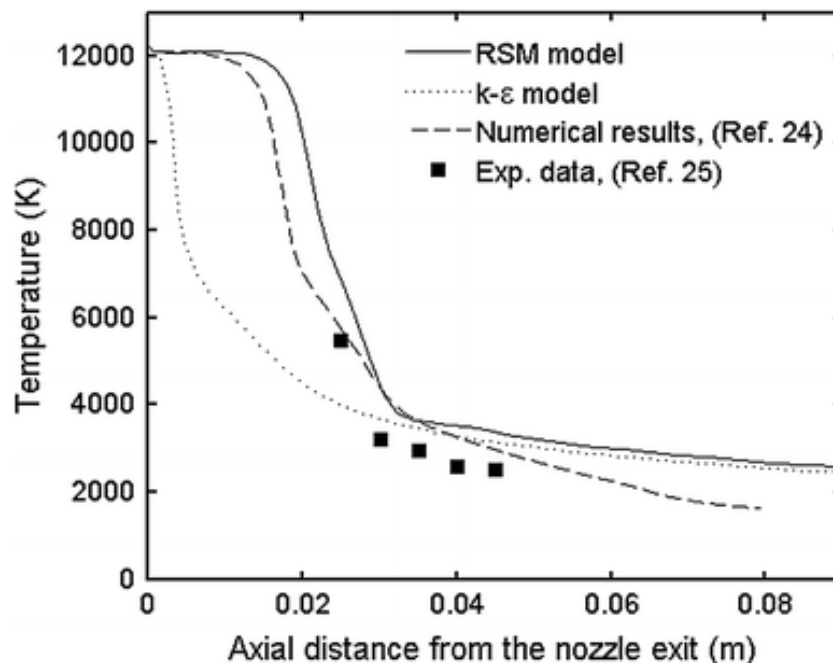


Figure 2-35: Comparison between centreline temperature profiles obtained by RSM and standard $k-\epsilon$ models with experimental and numerical data [75].

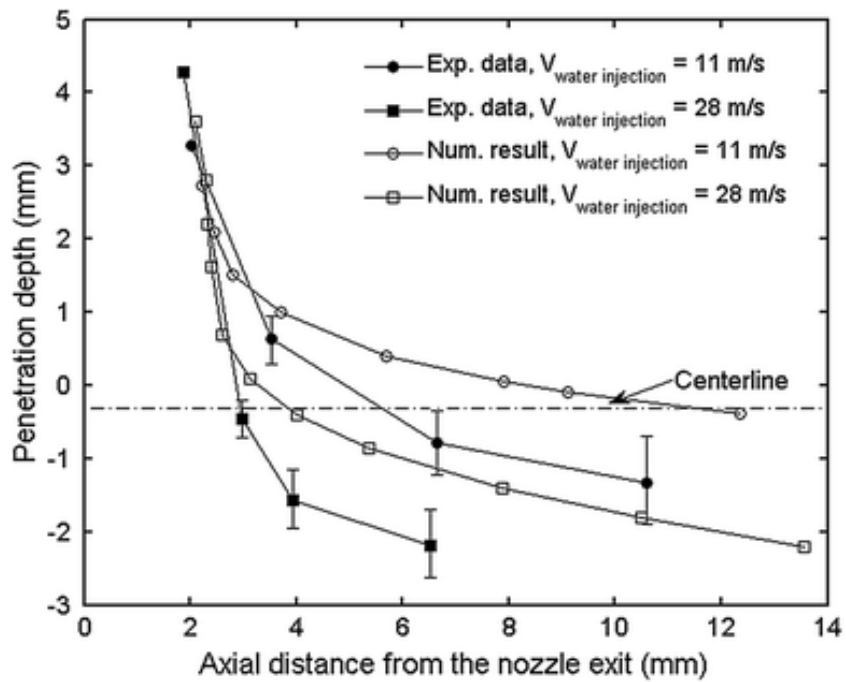


Figure 2-36: Comparison of Jet Penetration between the numerical model and experimental measurements [75].

Figure 2-37 shows the effect of the suspension injection velocity on the gas axial velocity with varying injection velocity of 12.9, 25.7 and 38.6 m/s. It can be seen from figure 2-37 that as the injection velocity increases, the penetration in the plasma plume increases and the gas velocity in this region decreases due to excessive momentum exchange. Figure 2-38 shows the effect of the suspension injection velocity on the gas temperature with varying injection velocity of 12.9, 25.7 and 38.6 m/s. It can be seen from figure 2-38 that as the injection velocity increases, the penetration in the plasma plume increases and the gas temperature in this region decreases due to excessive momentum exchange.

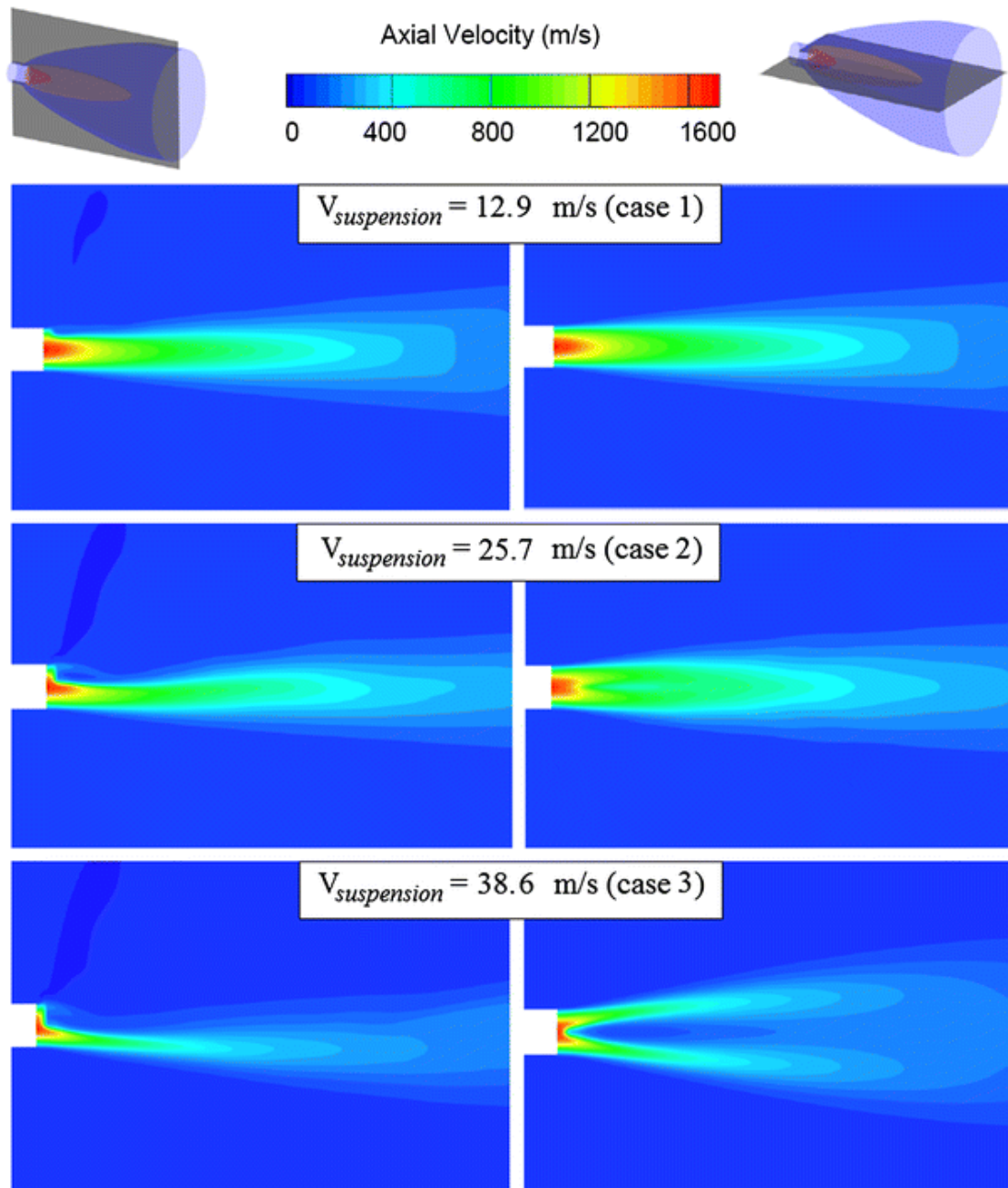


Figure 2-37: Effect of suspension injection velocity on the axial gas velocity, left hand side is side view pictures (symmetry plane) and right hand side is top view pictures [75].

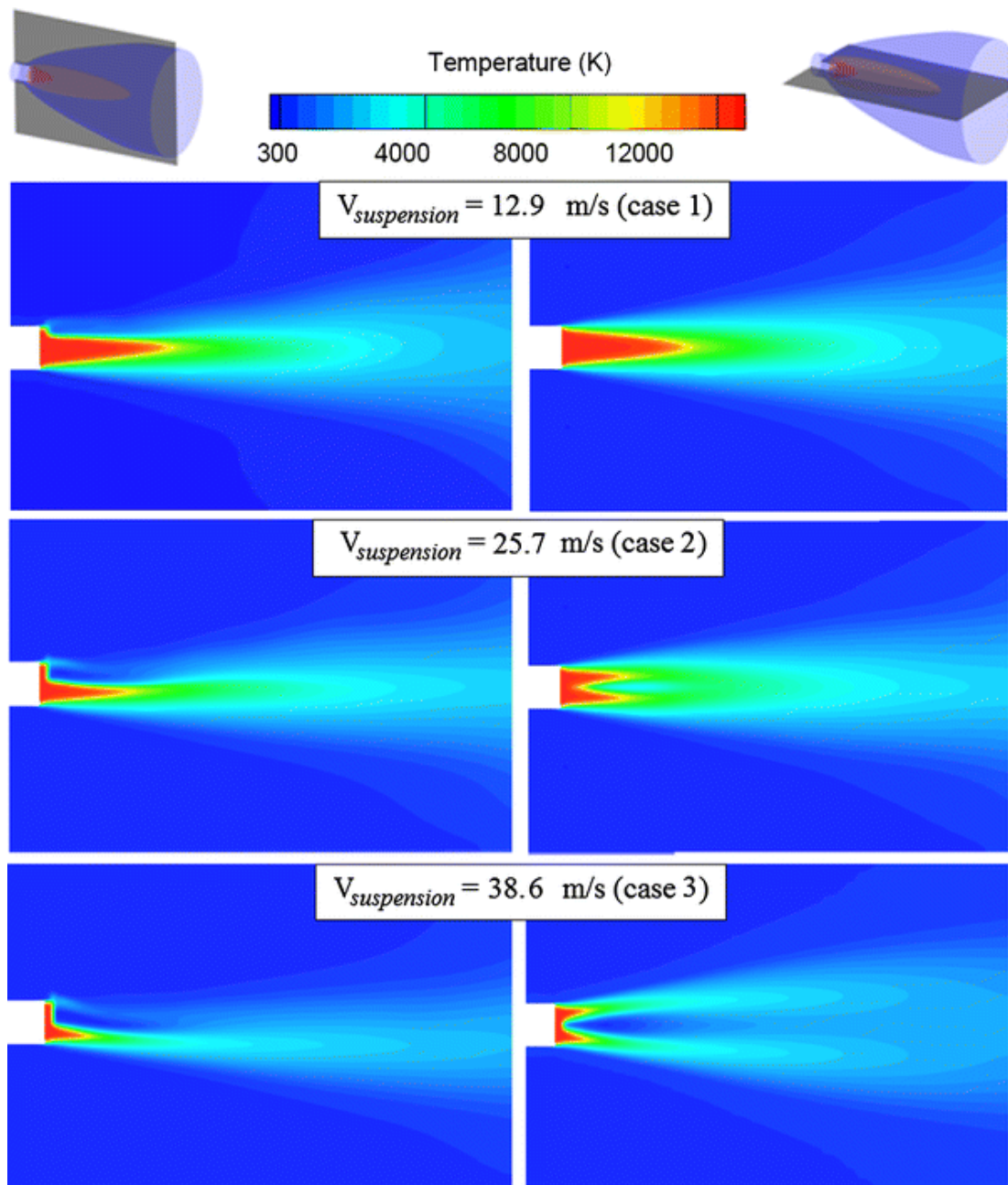


Figure 2-38: Effect of suspension injection velocity on gas temperature, left hand side is side view pictures (symmetry plane) and right hand side is top view pictures

[75].

Figures 2-39, 2-40 and 2-41 show the cumulative particle-size distribution, particle temperature and particle velocity as a function of particle counts (%) respectively at different locations from the nozzle exit. It was stated within the study that varying the standoff distance from 40 mm to 60 mm did not have a significant impact on the particle size and temperature. In contrary it was shown from figure 2-41 that at a standoff distance of 40 mm that a large number of particles reach a velocity of greater than 400 m/s. As the standoff distance increases fewer particles exceed a velocity of 400 m/s. Therefore, increasing the stand-off distance from 40 mm to 60 mm will result in an increase in the number particles with a lower velocity. The lower particle velocity will result in an increase in the porosity of the coating.

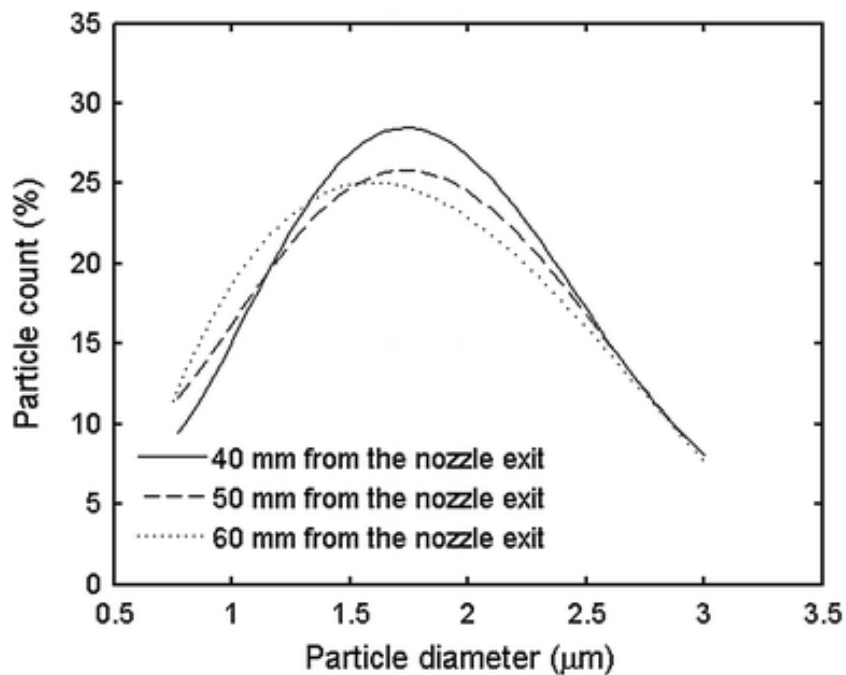


Figure 2-39: Particle-size distributions at different distances from the nozzle exit.

For injection velocity of 25.7 m/s [75].

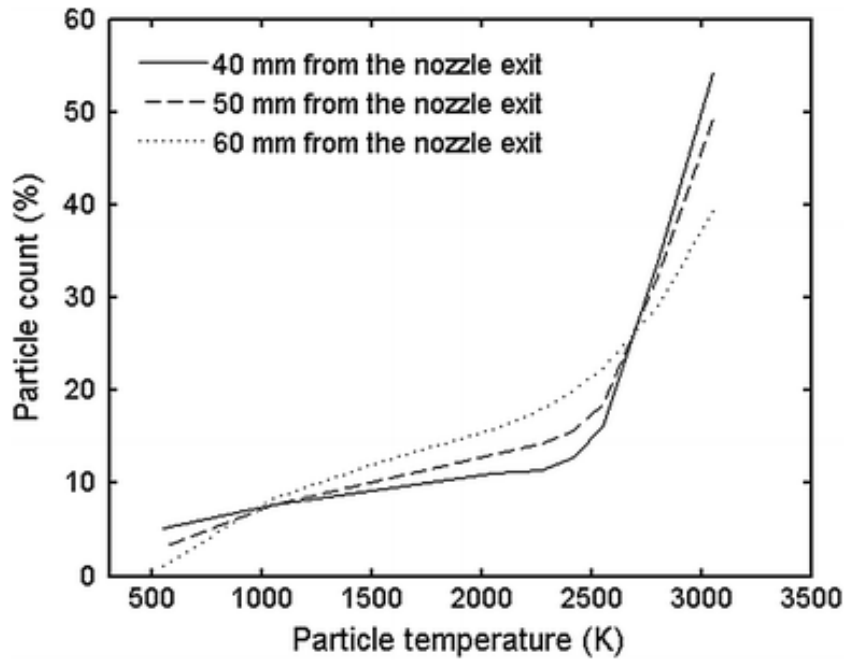


Figure 2-40: Particle-temperature distributions at different distances from the nozzle exit. For injection velocity of 25.7 m/s [75].

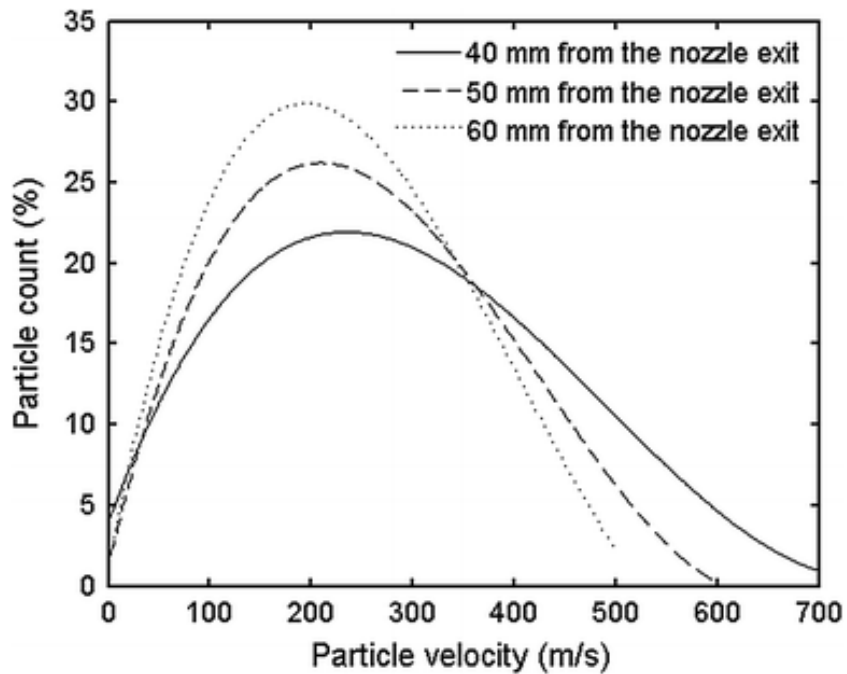


Figure 2-41: Particle-velocity distributions at different distances from the nozzle exit. For injection velocity of 25.7 m/s [75].

Figure 2-42 shows the effect of suspension injection angle and its location on the gas phase temperature. Although the suspension injection angle and location for cases 2 and 4 are different, the location where suspension interacts with the plasma plume is the same for both cases. It can be seen from figure 2-42 that if the suspension injector is near the gun exit and its angle is toward the gun, the suspension penetration depth and hence the velocity and temperature of the particles are higher.

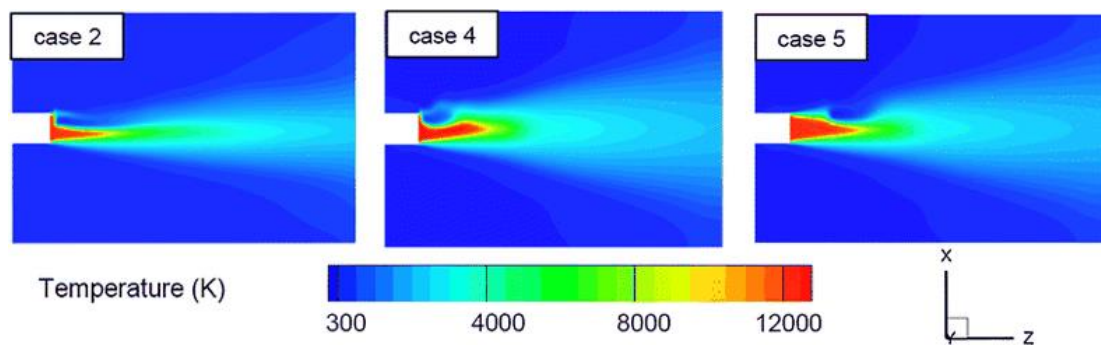


Figure 2-42: The effect of suspension injector location and angle on the gas temperature (14° , 0° , and 14° , from left to right, respectively). (7, 1, and 17 mm, from left to right, respectively) [75].

For SHVOF thermal spray, the suspension is typically injected axially into the combustion chamber due to the enhanced heat and momentum transfer to the suspension with this type of injection. Hence, all numerical modelling studies of SHVOF thermal spray have utilised an axial injection into the combustion chamber. However, there are scenarios where a radial injection into the jet like that employed within SPS thermal spray may be advantageous over an axial injection. For example, injecting oxygen sensitive materials radially into the free jet will reduce the exposure time of particles to oxygen. Therefore, a radial injection outside of the nozzle would be preferred over an axial injection into the combustion chamber.

2.9.2 Effect of Suspension Viscosity Model

Farrokhpanah et al. [74] compared the effect of different suspension viscosity models, for application to SPS thermal spray. The various suspension models were compared to experimental measurements of the suspension viscosity with varying particle concentration. Within this investigation, various models for the suspension viscosity were investigated as shown in equations 2.15 – 2.20. Equation 2.15 gives the relative viscosity of the suspension which is defined by the ratio of the suspension viscosity, μ_{eff} , to the liquid viscosity, μ_{liquid} .

$$\mu_r = \frac{\mu_{eff}}{\mu_{liquid}} \quad (Eq\ 2.15)$$

Equation 2.16 provides the Thomas model for the suspension viscosity where ϕ is defined by the solid volume fraction, $A = 0.00273$ and $B = 16.6$ [86].

$$\mu_r = 1 + 2.5\phi + 10.5\phi^2 + Ae^{B\phi} \quad (Eq\ 2.16)$$

Equation 2.17 provides the model proposed by Toda et al. [87].

$$\mu_r = \frac{1 + 0.5(1 + 0.6\phi)\phi - \phi}{(1 - \phi - 0.6\phi^2)^2(1 - \phi)} \quad (Eq\ 2.17)$$

Additional models such as that proposed by Krieger et al. [88] provide the suspension viscosity in terms of the maximum packing fraction ϕ_m that is given by the maximum solid volume fraction that can be achieved by adding particles within the suspension and the intrinsic viscosity given by $[\mu]$.

$$\mu_r = \left(1 - \frac{\phi}{\phi_m}\right)^{[\mu]\phi_m} \quad (Eq\ 2.18)$$

Equation 2.19 provides the model proposed by Dabak et al. [89] where N is an empirical constant which is taken as 2.0 for high shear rates.

$$\mu_r = \left(1 + \frac{|\mu|\phi}{N \left(1 - \frac{\phi}{\phi_m} \right)} \right)^N \quad (Eq 2.19)$$

Equation 2.20 provides the model proposed by Horri et al. [90] developed to provide better matching to experimental measurements at high solid volume fractions. K refers to an empirical constant to be modified to match experimental measurements.

$$\mu_r = 1 + 2.5\phi + K\phi \left(\frac{\phi}{\phi_m - \phi} \right)^2 \quad (Eq 2.20)$$

Figure 2-43 compares the different suspension viscosity models to experimental measurements for a YSZ and water suspension. It can be seen in figure 2-43 that all the models give a good prediction of the suspension viscosity at low solid contents. However, at high solid contents the models produce a poor prediction. The model proposed by Horri et al. [90] provides the best prediction for the suspension viscosity.

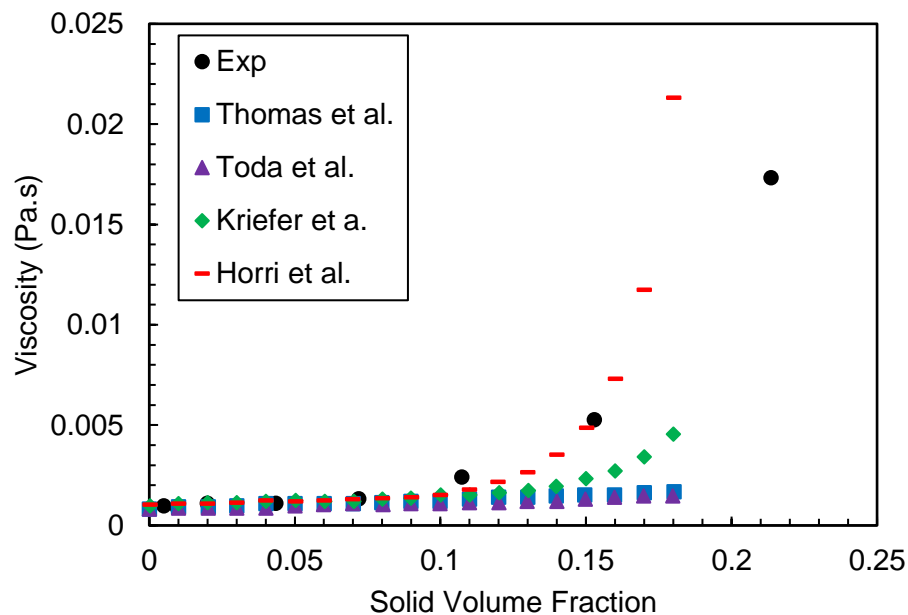


Figure 2-43: Comparison of different suspension viscosity model to experimental data [74].

2.9.3 Modelling Primary Breakup Within SPS

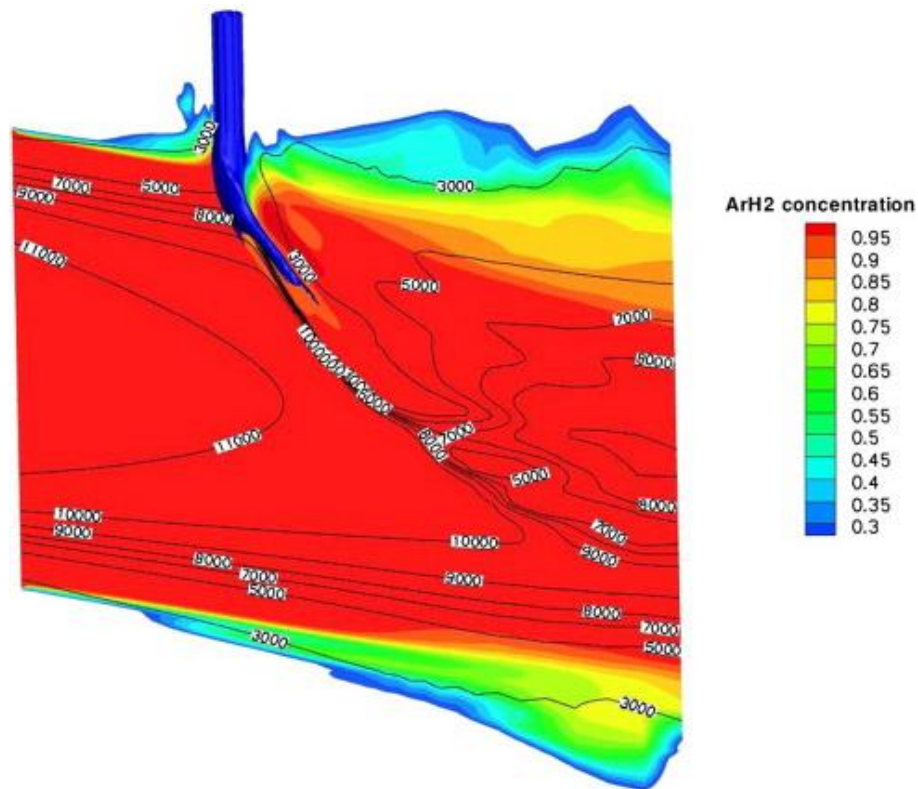


Figure 2-44: Interaction of a liquid column with an Ar-H₂ plasma crossflow using the VOF model [22].

Caruyer et al. [22] modelled the interaction of a droplet and a liquid jet with a plasma crossflow as shown in figures 2-44 and 2-45. Caruyer et al. [22] employed the VOF model to model the multiphase nature of the flow. Within this investigation the primary breakup of the liquid jet and the secondary breakup of a droplet within the crossflow was captured by resolving the interface between the two phases and hence is able to capture a wider range of physics over the DPM model. The study employed a mesh of 25 million cells and a time step of 1×10^{-8} s which makes this approach very computationally expensive with current computing capabilities. A very fine mesh is required to resolve the small droplet structures that form however an alternative approach to modelling the droplets formed from primary breakup is to couple the VOF

model to a DPM model so small droplets can be modelled using a mesh independent approach. This allows for a significantly coarser mesh to be employed and a significant reduction in the computational cost.

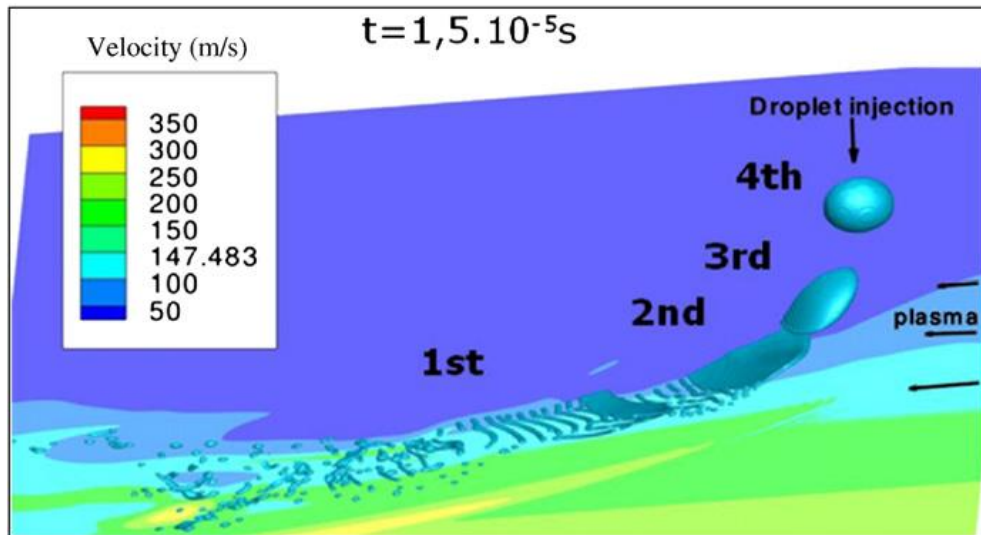


Figure 2-45: Interaction of a droplet with an Ar-H₂ plasma crossflow using the VOF model [22].

Additionally, Meillot et al. [91] employed the VOF model to capture the interaction between a liquid jet and a plasma crossflow as shown in figure 2-46. Within this study Meillot et al. [91] employed a mesh of 16 million cells and a time step of $1 \times 10^{-8} \text{ s}$. The numerical model was compared to low-resolution high-speed imaging as shown in figure 2-47. The numerical model showed good qualitative agreement to the breakup models as compared to the high-speed imaging. This approach demonstrates a significant improvement in the primary breakup regions over the DPM model. However, the VOF model requires a significant increase in the mesh density and computational resources.

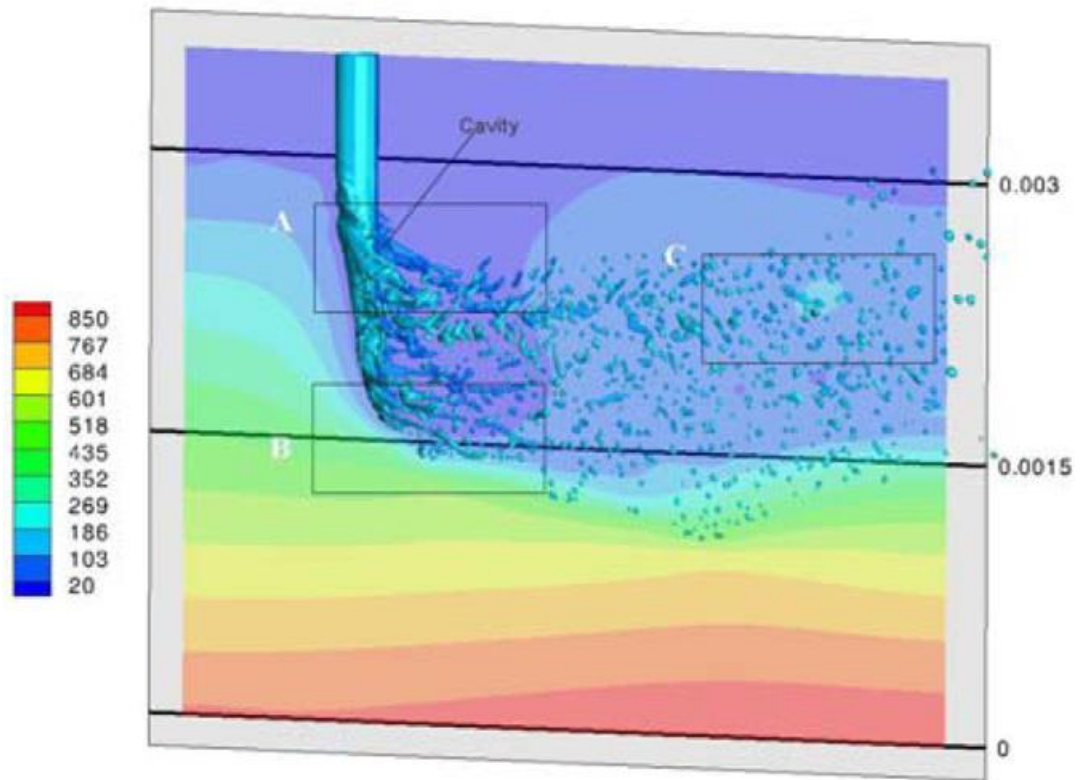


Figure 2-46: Interaction of a liquid column with a Ar-H₂ plasma crossflow using the VOF model [91].

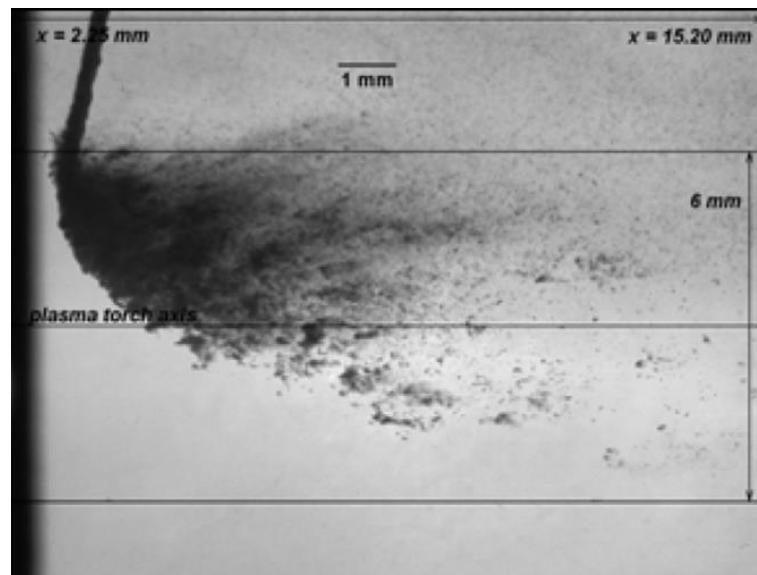


Figure 2-47: Shadow photographs of a continuous water jet interacting with a dc plasma flow [91].

2.10 Developments Within Multiscale Multiphase Models

Multiphase flows are challenging and computationally expensive to model due to the wide range of length scales of multiphase structures. For example, when modelling the jet breakup of a liquid jet exiting a nozzle structures near the inlet of the nozzle are of the order of the diameter of the nozzle. Far from the nozzle droplet sizes are of the order of micrometres. There are a wide range of multiphase models available within commercial CFD solvers such as Ansys Fluent that differ in approach to modelling the multiphase nature as outlined below:

- Eulerian model – The Eulerian model is the most complex multiphase model available. The model solves “ n ” set of continuity and momentum conservation equations for “ n ” phases [92].
- Volume of Fluid (VOF) –The VOF framework is an interphase tracking method that solves a shared set of mass and momentum conservation equations with an additional scalar equation for the volume fraction of each of the phases [93].
- Mixture Model – The mixture model solves a shared a shared set of mass and momentum conservation equations with an additional scalar equation for the volume fraction of each of the phases. In addition to this an additional algebraic equation for a velocity slip between the phases [94].
- Discrete Phase Model (DPM) – The DPM framework is a particle tracking model that treats the multiphase structures as single spherical point entities. Conservation equations for the momentum and energy equations are solved for to determine the particles position, velocity and temperature [95].

Within recent years there has been a growing body of literature looking to couple various multiphase models to overcome some of the practical limitations in the individual models [96], [97], [98], [99] & [100]. There has been a growing body of literature implementing a coupled VOF and DPM framework in modelling breakup of jets and formation of films onto the surface of walls through droplet impingement. In doing so the large-scale structures such as the liquid core, ligaments and the film are modelled using the VOF model and the small-scale droplets formed are then transferred and modelled using the DPM framework. Resolving the small-scale structures using a VOF framework requires a significant computational cost. The small scale droplets can be modelled at a much lower computational cost using a DPM framework.

Early attempts to couple VOF model with the DPM model had to address the criteria of conversion of droplets from a VOF framework to a DPM framework. Grosshans et al. [101] utilised a “coupling layer” where VOF droplets are converted into DPM droplets as they pass through a plane known as the coupling layer. One of the challenges in employing a coupled VOF and DPM model for breakup investigations is to address the issue that arises from the different mesh requirements within the VOF and DPM framework. With the implementation of a coupling layer suitable meshes can be employed within the respective zones. For the VOF framework mesh should be of an order of magnitude smaller than the droplets. Whilst for the DPM framework the mesh should be of an order larger than the droplets. The coupling layer approach however is significantly more expensive than alternative approaches. Adeniyi et al. [100] developed a coupled DPM to VOF framework for bearing chamber applications using the commercial CFD code Ansys Fluent. Within this implementation droplets were modelled using the DPM framework and the film formation of the bearing

chamber walls were modelled using the VOF framework. The criteria for conversion between DPM and VOF was the proximity of DPM droplets to the interface. Tomar et al. [102] employed a two-way coupled VOF and DPM framework to model jet breakup. The conversion of VOF droplets to DPM droplets was determined by the diameter of the VOF droplets. If the droplets were smaller than the specified diameter then the droplets would convert to DPM. This approach can offer greater savings in computational cost over the coupling layer method as the droplets can be switched from a VOF framework to a DPM framework as soon as the droplets are formed. The conversion of droplets from DPM to VOF was based on the proximity of the droplets to an interface. If the droplets are close enough to an interface the DPM droplet will be deleted and a spherical secondary phase structure is patched in its location. Kim et al. [103] & [104] employed a coupled VOF and DPM approach to model the atomization of fuel within a gas turbine injector. Within this study droplets were converted from a VOF framework to a DPM framework if two criteria were met. The first criteria are based on the droplet volume if the droplets are smaller than the specified volume the droplets were converted from VOF to DPM. The second criteria are based upon the droplet sphericity if the droplets are sufficiently spherical the droplets are converted from VOF to DPM. The numerical prediction of the SMD from the coupled VOF and DPM model compared well against the experimental measurements. Shinjo et al. extended the application of the coupled VOF and DPM model to include the effects of combustion [105], [106] & [107] for a diesel jet. Shinjo et al. investigated four cases: diesel jet in cold flow, diesel jet in hot flow, with the inclusion of a single step reaction and finally the inclusion of a multistep reaction. The multistep reaction demonstrated good agreement in predicting the ignition delay with existing literature.

2.11 Diagnostic Techniques for SHVOF and SPS Thermal Spray

Suspension thermal spray is a challenging process to control due to the range of parameters that affect the deposition of particles onto the substrate of the coating. Coating deposition is affected by the gas flow rate, suspension flow rate, suspension composition, nozzle geometry, fluctuations at the gas and suspension inlets and standoff distance to name a few. The inflight particle velocities and temperatures however are amongst the most important parameters that can control the coating deposition, coating microstructure and hence the properties of the coating [108].

Table 2-6: Comparison of DPV-2000 and Accuraspray-G4 particle diagnostic systems

	DPV-2000	Accuraspray G3
Measurement Volume	1.4 mm ² x 1.9 mm	(Cylinder) diameter 3 mm x length 25 mm
Velocity Measurement	Single Particle Method	Time of Flight
Temperature Measurement	Two-colour Pyrometry	Two-colour Pyrometry
Diameter Measurement	Emission	-

Various diagnostic systems have been developed for thermal spray using conventional powdered feedstock which include DPV 2000 and Accuraspray. The diagnostic systems measure the inflight particle velocity, temperature and diameter. Diagnostic systems play provide an invaluable tool to validate numerical models. Table 2-6 compares the two most common commercially available diagnostic systems; DPV-2000 with Accuraspray G3 [18]. The most notable differences between DPV and Accuraspray are that DPV employs a single particle measurement technique whilst

Accuraspray employs an ensembled average method. For application to suspension thermal spray only the Accuraspray diagnostic system can measure the submicron and nanoparticles that are present within SHVOF thermal spray.

2.11.1 Accuraspray Diagnostic System

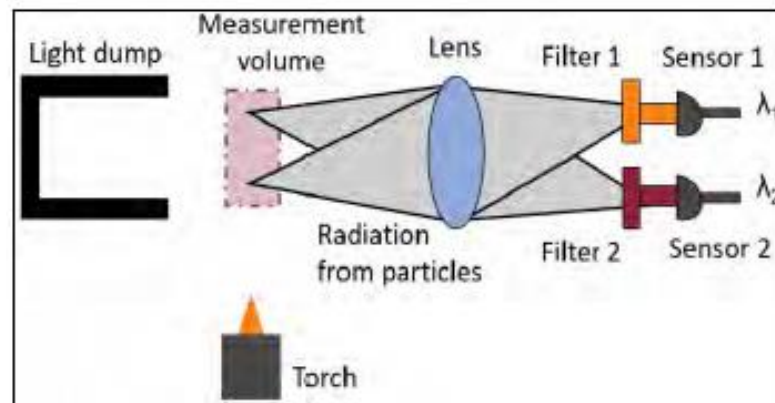


Figure 2-48: Pyrometer for characterization of the particles configured with a double-point measurement of Accuraspray G3 [108].

The Accuraspray diagnostic system measures particle velocities and temperatures based upon an ensembled averaged method. The particle velocities and temperatures are calculated using a time of flight and a two colour pyrometry method respectively. The Accuraspray diagnostic system is the only system commercially available that is able to measure particle velocities and temperatures for particles that range in size from submicron to nano as is the case with SHVOF thermal spray. Further discussion on the Accuraspray technique is provided within Chapter 6. Akbarnozari et al. [108] modified the Accuraspray G3 system which is based upon measuring the intensity of radiation at two locations and at two wavelengths, as shown in figure 2-46, to improve temperature measurements.

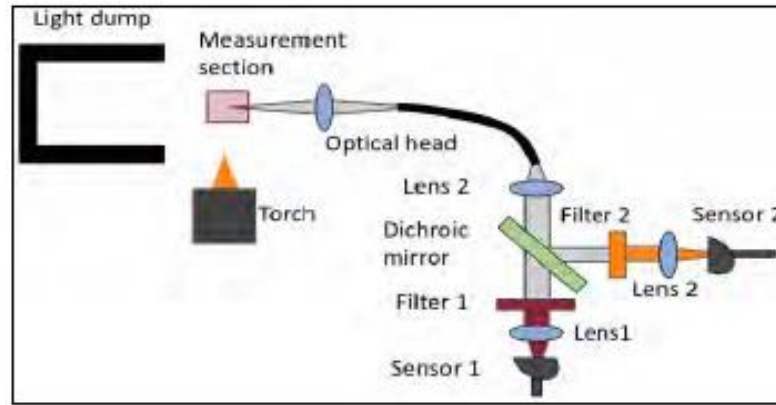


Figure 2-49: Pyrometer for characterization of the particles configured with a single-point measurement of Accuraspray 4.0 [108].

Akbarnozari et al. [108] modified the Accuraspray G3 system to measure the radiation intensity at a single point and at two wavelengths (Accuraspray G4) as shown in figure 2-47. Temperature and velocity predictions from the modified Accuraspray system were compared to the Accuraspray G3 system for SPS thermal spray at various standoff distances, plasma torch power and suspension feed rates. Scanning electron microscope (SEM) images of the microstructure were taken at the various conditions investigated. It was seen that the temperature and velocity predictions from the modified Accuraspray G4 system correlated better to changes in the microstructure of the coating. Additionally, Akbarnozari et al. successfully measured particle velocities and temperatures for SPS thermal spray and SHVOF thermal spray for a number of different particle materials.

2.12 Summary of Literature Review

In summary it can be seen that an extensive body of literature surrounding SHVOF thermal spray and the underlying physical processes that govern SHVOF thermal spray has accumulated. The literature surrounding combustion, primary breakup, secondary breakup and evaporation of suspension droplets has been studied. There are a number of studies relevant to SHVOF thermal spray that have been studied within this literature review from the field of modelling HVOF thermal spray. For investigations include evaluating the effect of the combustion model, assessing the effect of numerical scheme and determining the effect of the equivalence ratio. The investigations outlined are all important questions that must be considered within SHVOF thermal spray and have been investigated to some degree within HVOF thermal spray literature.

A review of the numerical investigations within SHVOF thermal spray literature have been outlined. Investigations have focused on what effect the droplet injection velocity, droplet injection diameter, injector type, substrate geometry have on SHVOF thermal spray. Additionally, investigations have compared the numerical models employed within SHVOF thermal spray to ensembled average measurements of particle velocity and particle temperature to evaluate the model accuracy.

Finally, the literature surrounding SPS thermal spray has been studied due to the wide overlap between SPS and SHVOF thermal spray. From the SPS thermal spray literature an understanding of different injection methods has been presented. SPS thermal spray literature looks to build upon current modelling methods by accounting for the primary breakup of the liquid / suspension jet which has currently not been addressed within SHVOF thermal spray modelling investigations.

2.13 Thesis Organisation

The current scope of the present thesis is focused around improving the understanding of SHVOF thermal spray. Current nozzles employed within SHVOF thermal spray have been developed for powder feedstock. Hence there is an insufficient understanding on what effect the nozzle geometry has on the SHVOF thermal spray process. There are a number of different nozzles available commercially which vary by combustion chamber length, barrel length and the total length of the nozzle. Chapter 4 evaluates what effect the combustion chamber length, barrel length and the total length have on the gas flow, suspension evaporation and the inflight particle velocities and temperatures.

Within SPS it is common practice to inject the suspension radially outside of the flame. However, a radial injection outside of the flame is not often seen within SHVOF thermal spray. For some cases a radial injection of suspension may be beneficial. For example, oxygen sensitive materials such as graphene oxidize and degrade when exposed to oxygen at high temperatures for prolonged durations of time. Therefore, a radial injection of suspension may improve the quality of the coating due to the shorter exposure time to oxygen at high temperatures. Additionally, a shrouding system is designed that allows for a radial injection of suspension as well as preventing mixing of ambient oxygen into the jet. Chapter 5 investigates what effect an injection radially into the free jet has on the inflight particle condition. This thesis also builds upon the current modelling approaches employed within SHVOF thermal spray literature. Chapter 5 compares two approaches to modelling the combustion reaction for SHVOF thermal spray. One approach employs a global mechanism and another approach employs a robust reaction mechanism. The gas temperatures are then compared to the theoretical adiabatic flame temperature for the two approaches employed.

Additionally, it was discussed within the literature review that the current numerical models for the heat transfer to suspension under-predict the particle temperatures by as much as 500 K in comparison to Accuraspray measurements. Currently to model the heat transfer coefficient within suspension high velocity oxy fuel thermal spray the Ranz - Marshal correlation is used. The Ranz - Marshal correlation was developed for spray dryers which operate at very low velocities and temperatures in comparison to SHVOF thermal spray. Chapter 6 evaluates more appropriate correlations for the heat transfer coefficient to address the current under-prediction observed within the numerical modelling.

Finally, this thesis looks to address a current limitation within suspension high velocity oxy fuel thermal spray modelling. Current numerical models employed within SHVOF thermal spray ignore the primary breakup of the jet. SPS thermal spray has employed the volume of fluid framework to model the primary breakup of suspension into a plasma jet however, this approach is very computationally expensive. Chapter 7 models the primary breakup using the volume of fluid framework and then models the droplets formed using a discrete phase model framework. This approach will allow for a significantly lower computational cost over the full volume of fluid framework and a drastic increase in the fidelity over the discrete phase model framework. Chapter 7 also looks at what effect the injection Weber number has on the primary breakup of the jet and its dynamics.

Chapter 3: Numerical Modelling

The commercial CFD solver Ansys Fluent V19.3 (Pennsylvania, USA) has been employed to model the SHVOF thermal spray system. This chapter provides a comprehensive overview of the principles for modelling the fluid flow within SHVOF thermal spray and specifically those which have been employed within this thesis. The models to describe the mass conservation, momentum conservation, turbulence, compressibility, combustion, multiphase flows and the phase change are outlined in detail within this section. Additionally, the numerical algorithm that is employed within Ansys Fluent is also provided.

3.1 Basic Fluid Flows

To model any flow using the finite volume method within CFD the mass and momentum conservation equations must be solved for. The mass and momentum conservation equations are given by equations 3.1 and 3.2 respectively. The density is given by ρ , the time is given by t , $\vec{u} = (u, v, w)^T$ refers to the velocity vector, p , refers to the static pressure, g refers to the gravitational acceleration and I refers to the unit tensor. The stress tensor, $\bar{\tau}_{ij}$, in the momentum equation is defined by equation 3.3

Mass Conservation Equation:

$$\frac{\partial \rho}{\partial t} + \nabla \cdot \rho \vec{u} = 0 \quad (\text{Eq 3.1})$$

Momentum Conservation Equation:

$$\frac{\partial \rho}{\partial t} + \nabla \cdot (\rho \vec{u} \vec{u}) = -\nabla p + \nabla \cdot (\bar{\tau}_{ij}) + \rho g \quad (\text{Eq 3.2})$$

$$\bar{\tau}_{ij} = \mu \left[(\nabla \vec{u} + \nabla \vec{u}^T) - \frac{2}{3} \nabla \cdot \vec{u} I \right] \quad (Eq 3.3)$$

Compressible effects are encountered in gas flows that are characterised by high velocities and/or in flows where there are large pressure and temperature variations. Compressible flows experience large variations within the fluid density. An additional equation for the density must be solved to account for the density variations within the flow which is given by the ideal gas law (equation 3.4). Within the ideal gas law, p_{op} refers to the operating pressure, R refers to the universal gas constant, M_w refers to the molecular weight and T refers to the temperature. The temperature is determined by the energy equation given by equation 3.5. The effective conductivity is given by k_{eff} , \vec{j}_j refers to the diffusion flux for species j and S_h refers to the heat source term that accounts for heat transfer between continuous flow and discrete flow.

Ideal Gas Law:

$$\rho = \frac{p_{op} + p}{\frac{R}{M_w} T} \quad (Eq 3.4)$$

Energy Equation:

$$\frac{\partial \rho E}{\partial t} + \nabla \cdot (\rho \vec{u} E + p) = \nabla \cdot \left(k_{eff} \nabla T - \sum_j h_j \vec{j}_j + (\bar{\tau}_{eff} \cdot \vec{u}) \right) + S_h \quad (Eq 3.5)$$

3.2 Turbulence Modelling

In SHVOF thermal spray the flow is turbulent in nature, there is no exact definition for turbulence. Turbulent flows display certain characteristics; they are random, diffusive, and highly dissipative. The Reynolds number, Re , can be used to predict if the flow is turbulent in nature [109]. The Reynolds number is given by equation 3.6 where U refers to the characteristic flow velocity, L refers to the characteristic flow length scale and μ refers to the dynamic viscosity.

$$Re = \frac{\rho UL}{\mu} \quad (Eq\ 3.6)$$

Turbulence is challenging to models as turbulent flows operate over a wide range of length and time scales [109]. The largest of the length scales are referred to as integral length scales, l_0 , the smallest length scales are referred to as the Kolmogorov length scales [110], η , which are given by equation 3.7 and 3.8 respectively. The largest time scales are referred to as large eddy turnover time, t_L , and the smallest time scales are referred to as the time scale for small eddies, t_η , which are given by equation 3.9 and 3.10 respectively. The turbulent kinetic energy per unit mass is given by, k , ε refers to the turbulent dissipation rate and ν refers to the kinematic viscosity. The wide range of length and time scales make turbulence very computationally expensive to model [111].

$$l_0 \propto \frac{k^{3/2}}{\varepsilon} \quad (Eq\ 3.7)$$

$$\eta = \left(\frac{\nu^3}{\varepsilon}\right)^{1/4} \quad (Eq\ 3.8)$$

$$t_L = \frac{L}{U} \quad (Eq\ 3.9)$$

$$t_\eta = \left(\frac{\nu}{\varepsilon}\right)^{\frac{1}{2}} \approx \frac{\nu L}{U^3} \quad (\text{Eq 3.10})$$

Turbulence modelling can be characterised by how much of the flow is modelled and resolved [112]. As more of the flow is resolved the fidelity of the turbulence model increases, however the computational expense also vastly increases. A direct numerical simulation (DNS) approach to account for the effects of turbulence resolves the entirety of the flow. The Reynolds averaged Navier-Stokes (RANS) methods model much of the flow and resolve the remainder of the flow scales. Scale resolving simulations (SRS) such as the large eddy simulation (LES) approach resolve the large-scale structures and model the small-scale structures. Figure 3-1 illustrates the fundamental concepts behind the DNS, RANS and LES models.

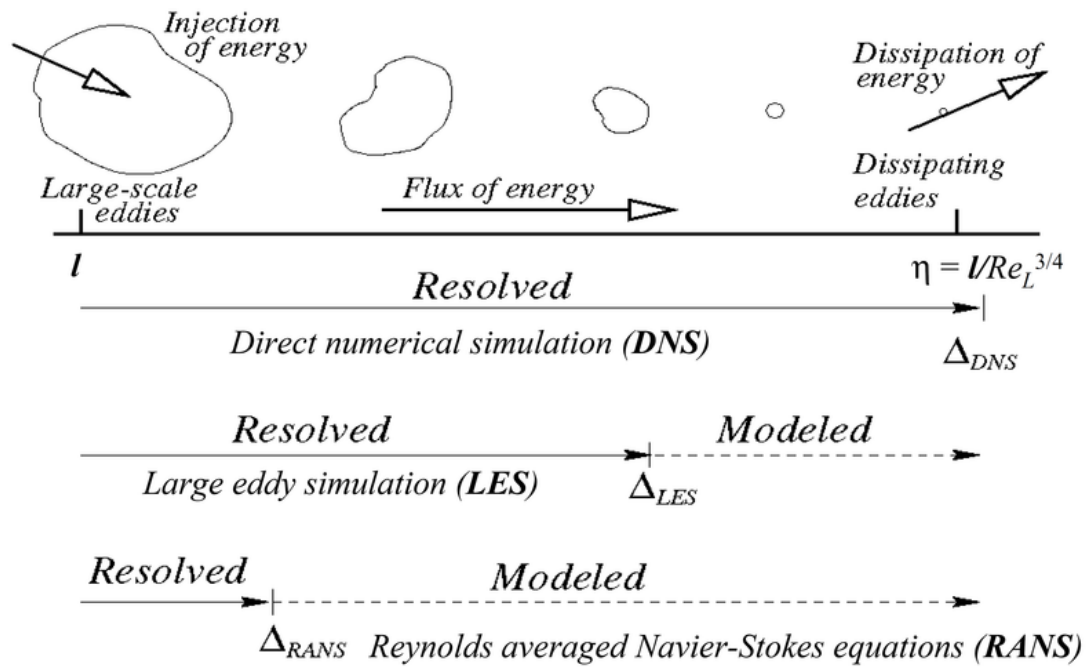


Figure 3-1: Fundamental concepts behind the RANS, LES and DNS turbulence models [113].

3.2.1 LES Models:

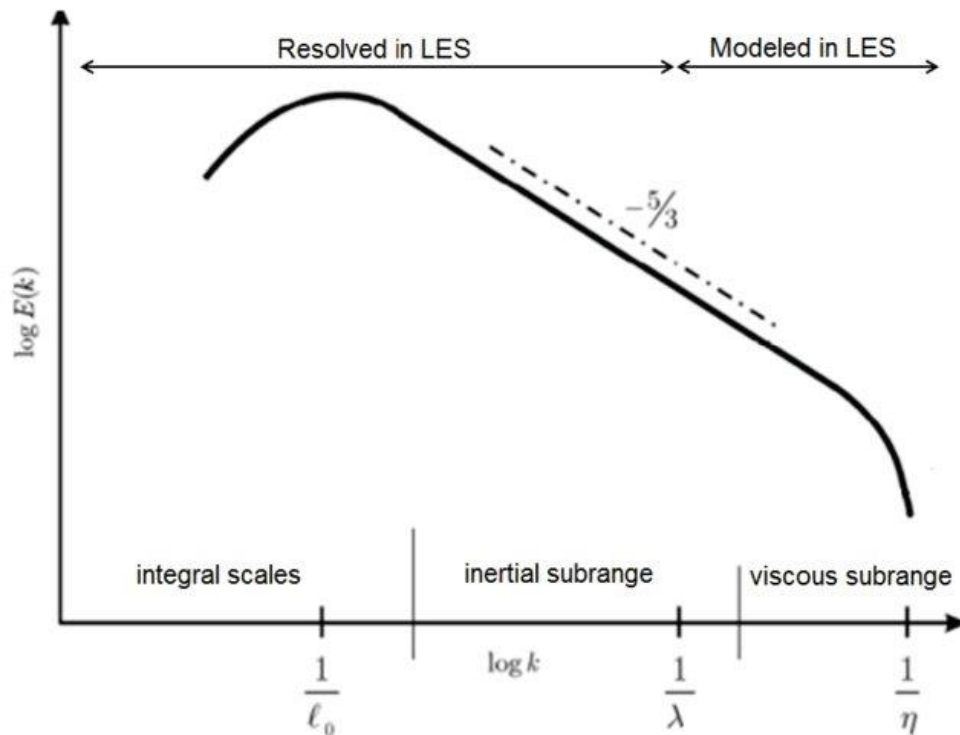


Figure 3-2: Energy Spectrum in turbulent flows [114].

In turbulent flows energy is cascaded down from large scale structures to small scale structures [114]. The energy spectrum shows the energy distribution over the entire range of turbulent scales as shown in figure 3-2. The large eddies carry most of the energy and the small eddies carry a smaller proportion of the energy. From this it is assumed that the large-scale structures have a larger contribution to the bulk properties of the flow. Therefore, it is more important to accurately model the large-scale structures than the small-scale structures.

An instantaneous property, φ , can be decomposed into the sum of a filtered component, $\tilde{\varphi}$, and a fluctuating component, φ' , as shown in equation 3.11. A filter is applied to the Navier-Stokes equations to separate the resolved scales from the unresolved scales, the filtered variable is given in equation 3.12. The filter function is given by, $\bar{G}(x, x')$ and D refers to the fluid domain. The discretization employed

within the finite volume method implicitly provides the filtering operation as shown in equation 3.13. It is implied within equation 3.13 that the filter takes the form within equation 3.14. The filtered forms of the continuity equation and Navier Stokes equations are given by equation 3.15 and 3.16 respectively [115].

$$\varphi = \tilde{\varphi} + \varphi' \quad (Eq\ 3.11)$$

$$\tilde{\varphi}(x) = \int_D \varphi(x') \bar{G}(x, x') dx' \quad (Eq\ 3.12)$$

$$\tilde{\varphi}(x) = \frac{1}{V} \int_D \varphi(x') dx' \quad (Eq\ 3.13)$$

$$\bar{G}(x, x') = \begin{cases} \frac{1}{V}, & x' \in v \\ 0, & x' \text{ otherwise} \end{cases} \quad (Eq\ 3.14)$$

$$\frac{\partial \tilde{u}_i}{\partial \tilde{x}_i} = 0 \quad (Eq\ 3.15)$$

$$\frac{\partial \tilde{u}_i}{\partial t} + \frac{\partial \tilde{u}_i \tilde{u}_j}{\partial \tilde{x}_j} = -\frac{1}{\rho} \frac{\partial \tilde{p}}{\partial \tilde{x}_i} - \frac{\partial \tau_{ij}}{\partial \tilde{x}_j} + \nu \frac{\partial^2 \tilde{u}_i}{\partial \tilde{x}_i \partial \tilde{x}_i} \quad (Eq\ 3.16)$$

A closure for the filtered Navier Stokes equations is required for the sub grid scale (SGS) tensor, τ_{ij} . The SGS tensor represents the effect of the small-scale structures on the large-scale flow. The SGS tensor is modelled in LES using SGS models while all the other terms are resolved. The Boussinesq approximation, given by equation 3.17, can be applied to provide closure to the LES filtered equations. The unit tensor is given by δ_{ij} and μ_t refers to the turbulent viscosity.

$$\tau_{ij} - \frac{1}{3} \tau_{kk} \delta_{ij} = \mu_t \left(\frac{\partial \bar{u}_i}{\partial x_j} + \frac{\partial \bar{u}_j}{\partial x_i} \right) \quad (Eq\ 3.17)$$

There several different SGS models available, the Wall-Adapting Local Eddy-Viscosity (WALE) model has been employed within chapter 7. The WALE model

offers a few advantages over other SGS models for example the model returns the correct wall asymptotic (y^3) behaviour for wall bounded flows unlike the Smagorinsky model [116] & [117].

The wall-adapting local eddy (WALE) viscosity is defined by Equation 3.18. The mixing length scale for the sub grid scales, L_s , and the rate of strain tensor, S_{ij} , are given by equations 3.19 and 3.20 respectively. Within equation 3.18 for the mixing length scale is given by L_s , the von Karman constant is given by κ , d refers to the distance to the closest wall, C_w refers to the wale constant and $V^{1/3}$ refers to the cube root of the cell volume. The wale constant varies within the literature where the published value for the constant takes the value of $C_w = 0.50$ while other studies have shown superior performance of the model with a value of $C_w = 0.325$.

$$\mu_t = \rho L_s^2 \frac{(S_{ij}^d S_{ij}^d)^{\frac{3}{2}}}{(\bar{S}_{ij} \bar{S}_{ij})^{\frac{5}{2}} + (S_{ij}^d S_{ij}^d)^{\frac{5}{4}}} \quad (Eq\ 3.18)$$

$$L_s = \min\left(\kappa d, C_w V^{\frac{1}{3}}\right) \quad (Eq\ 3.19)$$

$$S_{ij}^d = \frac{1}{2}(\bar{g}_{ij}^2 + \bar{g}_{ji}^2) - \frac{1}{3}\delta_{ij}\bar{g}_{kk}^2 \quad (Eq\ 3.20)$$

$$\bar{g}_{ij} = \frac{\partial \bar{u}_i}{\partial x_j} \quad (Eq\ 3.21)$$

3.2.2 RANS Models:

An instantaneous variable, $\varphi(x, t)$, can alternatively be decomposed into a mean component, $\bar{\varphi}(x)$, and fluctuating component, $\varphi'(x, t)$, as shown by equation 3.22. The mean property of the flow is defined by equation 3.23 [118]. This decomposition can be applied to the variables in the Navier-Stokes equations, producing the Reynolds averaged Navier-Stokes equations which are given by equation 3.24.

$$\varphi(x, t) = \bar{\varphi}(x) + \varphi'(x, t) \quad (\text{Eq 3.22})$$

$$\bar{\varphi}(x) = \lim_{T \rightarrow \infty} \frac{1}{T} \int_t^{t+T} \varphi(x, t) dt \quad (\text{Eq 3.23})$$

$$\frac{\partial \bar{u}_i}{\partial t} + u_j \frac{\partial \bar{u}_i}{\partial x_j} = -\frac{\partial \bar{p}_i}{\partial x_i} + \nu \frac{\partial^2 \bar{u}_i}{\partial x_i \partial x_j} - \frac{\partial \overline{u'_i u'_j}}{\partial x_j} \quad (\text{Eq 3.24})$$

Within the RANS equations all the terms except the stress tensor term can be resolved. Turbulence modelling implements a model for the stress tensor to provide closure the RANS equations. The Boussinesq approximation provides closure to the RANS equations and is given by equation 3.25. The turbulent viscosity can then be determined from a turbulence model.

$$\overline{u'_i u'_j} = \mu_t \left(\frac{\partial \bar{u}_i}{\partial x_j} + \frac{\partial \bar{u}_j}{\partial x_i} \right) - \frac{2}{3} \left(\rho k + \mu_t \frac{\partial \bar{u}_k}{\partial x_k} \right) \delta_{ij} \quad (\text{Eq 3.25})$$

Typically, in SHVOF thermal spray the realizable k -epsilon model is employed to model the turbulence [28]. The realizable k -epsilon model provides a robust far wall treatment of the flow and allows for the use of wall functions which reduces computational costs. The realizable k -epsilon model solves two transport equations for the turbulent kinetic energy per unit mass, k , and the dissipation rate, ε , which are

given by equations 3.26 and 3.27 respectively. The dilatation in compressible turbulence, Y_M , accounts for the compressibility effects on the overall dissipation rate and G_k represents the generation of turbulent kinetic energy due to the average velocity gradients. The turbulent Prandtl numbers for k and ε are given by σ_k and σ_ε respectively. The turbulent Prandtl number for k and the turbulent Prandtl number for ε take the value of 1.0 and 1.2, respectively. C_1 and C_2 are constants for the realizable k-epsilon model, the constant C_1 is determined by equation 3.28 and the constant C_2 takes the value of 1.9.

$$\frac{\partial \rho k}{\partial t} + \frac{\partial}{\partial x_j} (\rho u_j k) = \frac{\partial}{\partial x_j} \left[\left(\mu + \frac{\mu_t}{\sigma_k} \right) \frac{\partial k}{\partial x_j} \right] - \rho \varepsilon + G_k - Y_M \quad (\text{Eq 3.26})$$

$$\begin{aligned} \frac{\partial \rho \varepsilon}{\partial t} + \frac{\partial}{\partial x_j} (\rho u_j \varepsilon) \\ = \frac{\partial}{\partial x_j} \left[\left(\mu + \frac{\mu_t}{\sigma_\varepsilon} \right) \frac{\partial \varepsilon}{\partial x_j} \right] + \rho C_1 S \varepsilon - \frac{\rho C_2 \varepsilon^2}{k + \sqrt{\nu \varepsilon}} \end{aligned} \quad (\text{Eq 3.27})$$

$$C_1 = \max \left[0.43, \frac{\frac{k}{\varepsilon} \sqrt{2 S_{ij} S_{ij}}}{\frac{k}{\varepsilon} \sqrt{2 S_{ij} S_{ij}} + 5} \right] \quad (\text{Eq 3.28})$$

3.2.3 Turbulent Boundary Layer

The fluid directly adjacent to the wall is at rest which gives rise to the no slip boundary condition employed at the walls to model the flow. The boundary layer is defined by the region where the flow transitions from rest to the free stream velocity. Within the boundary layer the flow transitions from laminar to turbulent. Near the wall the flow is laminar, further from the wall the flow transitions from laminar to turbulent and far from the wall the flow is turbulent which is shown in figure 3-3.

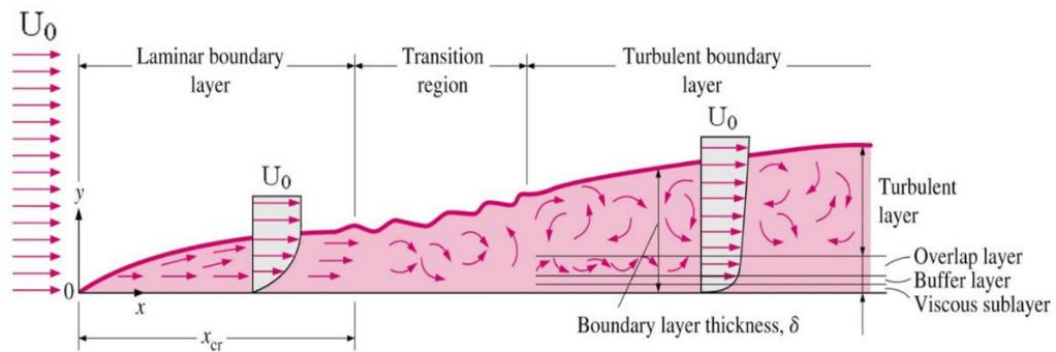


Figure 3-3: Development of the boundary Layer [119].

Extra consideration must be employed when considering the boundary layer within turbulence models. If the mesh is well resolved within the viscous laminar region (viscous sub layer) the boundary layer can be fully resolved. This however requires for the first node from the wall to be placed at a $y^+ \approx 1$ and for 10 cells to lie within the buffer and sublayer. The definition of the y^+ is given by equation 3.29, where y refers to the distance from the wall, ν refers to the kinematic viscosity, the wall shear stress is given by τ_w and the friction velocity, u_τ , is given by equation 3.30.

$$y^+ = \frac{yu_\tau}{\nu} \quad (Eq\ 3.29)$$

$$u_\tau = \sqrt{\frac{\tau_w}{\rho}} \quad (Eq\ 3.30)$$

Alternatively, the boundary layer can be modelled where a much coarser mesh can be applied to reduce the computational cost of accounting for the effects of the boundary layer. Further from the wall within the fully turbulent region the nondimensional velocity takes the form of a log law as shown in figure 3-4. A wall function taking the form of the log law can be employed at the wall to model the boundary layer. For the log law to be valid the first cell off the wall must lie within the fully turbulent region which occurs at $30 < y^+ < 300$. Ideally the mesh should be either coarse enough to lie within the fully turbulent region or fine enough to lie within the laminar region. The first node off the wall should avoid being placed within the buffer layer $5 < y^+ < 30$. However Ansys Fluent can accommodate cells that lie within the buffer layer [62].

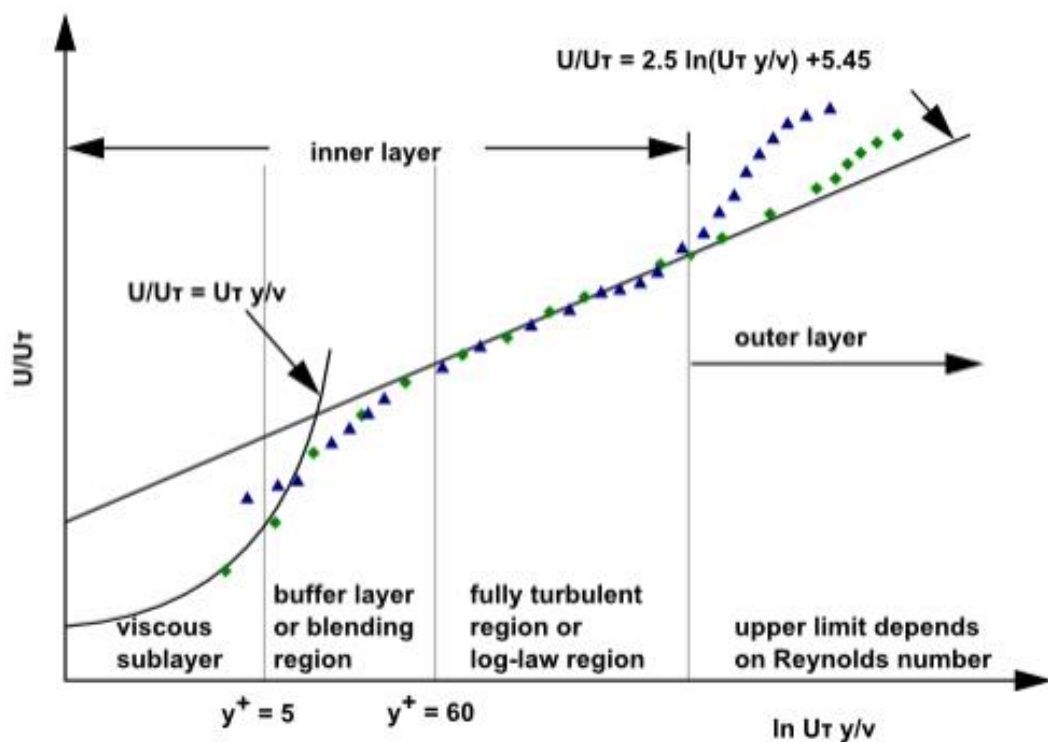


Figure 3-4: Subdivisions of the near wall region [62].

3.3 Combustion Modelling

Most common approach to modelling combustion within the SHVOF literature are to employ a species transport model that accounts for the convection, diffusion and reaction of all the species considered. The species transport model is given by equation 3.31, where i refers to the index of the species, Y_i refers to the mass fraction of species i , J_i refers to the mass diffusion flux of species i , R_i refers to the rate of production of species i from reactions that may take place and S_i refers to the source of species i from phase change.

$$\frac{\partial \rho Y_i}{\partial t} + \nabla \cdot (\vec{u} Y_i) = -\nabla \cdot \vec{J}_i + R_i + S_i \quad (\text{Eq 3.31})$$

For “ N ” number of species present within the fluid “ $N-1$ ” species equations are solved for. The sum of all of the species mass fractions totals 1.0 as implied in equation 3.32 which offers an additional equation.

$$\sum_{i=0}^N Y_i = 1.0 \quad (\text{Eq 3.32})$$

The mass diffusion flux term in equation 3.31 represents the diffusion of species that arises due to species and temperature gradients. For turbulent flows the mass diffusion term is determined by equation 3.33. Where $D_{i,m}$ represents the mass diffusion coefficient of species i , Sc_t represents the turbulent Schmidt number which takes the value of 0.7 and $D_{T,i}$ represents the thermal (Soret) diffusion coefficient of species i .

$$\vec{J}_i = -\left(\rho D_{i,m} + \frac{\mu_t}{Sc_t}\right) \nabla Y_i - D_{T,i} \frac{\nabla T}{T} \quad (\text{Eq 3.33})$$

Within SHVOF the reactants undergo combustion and there is a consumption and production of species. To model the consumption and production of species as a result of combustion the rate of reaction must be determined. There are a number of models

available to determine the rate term; within this thesis the eddy dissipation model and the eddy dissipation concept have been employed. Chapter 5 compares the temperature and species fraction predictions by both of these models.

Eddy Dissipation Model

For turbulent reacting flows the rate of reaction is limited by the turbulent mixing and hence the turbulent chemistry interactions (TCI) must be considered. For turbulent premixed combustion the reaction rate is limited by the mixing of hot reactant products with the cold premixed fuel and oxygen. Therefore, under the assumption that the combustion is limited by the mixing; the kinetic rates can be neglected as they are assumed to be instantaneous. The eddy dissipation model determines the rate of production of species, i , due to reaction, r , and the rate, $R_{i,r}$, is given by the limiting term of the two following expressions within equations 3.34 and 3.35 [120]. The mass fraction of any product species is given by Y_p , Y_R refers to the mass fraction of a particular reactant $v'_{i,r}$ refers to the stoichiometric coefficient for reactant i in reaction r . A and B are constants which take the values of 4.0 and 0.5 respectively.

$$R_{i,r} = v'_{i,r} M_{w,i} A \rho \frac{\varepsilon}{k} \min \left(\frac{Y_R}{v'_{R,r} M_{w,R}} \right) \quad (Eq\ 3.34)$$

$$R_{i,r} = v'_{i,r} M_{w,i} A B \rho \frac{\varepsilon}{k} \frac{\sum_P Y_P}{\sum_j^N v''_{j,r} M_{w,j}} \quad (Eq\ 3.35)$$

Eddy Dissipation Concept

The Eddy Dissipation Concept (EDC) is an extension to the EDM model to account for detailed reaction mechanisms in turbulent combustion flows [121] & [122]. The EDC model assumes the reaction occurs in small turbulent structures, which are typically much smaller than the computational grid. The model distinguishes the cell into two subzones: the reacting fine structures and the surrounding fluid. The reaction is confined to the fine scale structures which is treated as being adiabatic, isobaric, plug flow reactors (PFR). Turbulent mixing transfers mass and energy from the fine structures to the surrounding fluid [123] & [124]. The length scale of the fine structures, ξ^* , is given by equation 3.36. The volume fraction constant C_ξ is taken as a value of 2.1377. The volume fraction of the fine scale is given by the cube of the length scale of fine structures. Species are assumed to react over the time scale given in equation 3.37. The time scale constant is given by C_τ which takes the value of 0.4082. Assuming the reaction occurs only within the fine structures the net reaction rate is determined by equation 3.38 [125]. The fine-scale species mass fraction of species i after reacting over the time τ^* is given by Y_i^* .

$$\xi^* = C_\xi \left(\frac{\nu \varepsilon}{k^2} \right)^{\frac{1}{4}} \quad (Eq\ 3.36)$$

$$\tau^* = C_\tau \left(\frac{\nu}{\varepsilon} \right)^{\frac{1}{2}} \quad (Eq\ 3.37)$$

$$R_i = \frac{\rho \xi^*}{\tau^* [1 - (\xi^*)^3]} (Y_i^* - Y_i) \quad (Eq\ 3.38)$$

3.4 Multiphase Modelling

This sub-chapter outlines the fundamental principles for the VOF, DPM and coupled VOF and DPM frameworks that have been employed within this thesis. Chapters 4, 5 and 6 employ the DPM model and chapter 7 employs the coupled VOF and DPM model for the suspension.

3.4.1 Discrete Particle Model

The discrete particle model (DPM) is a droplet tracking method for discrete multiphase entities such as droplets and particles. The droplets are modelled as point entities which assumes no internal gradients. The discrete phase is modelled using a mass and momentum conservation and is coupled to the gas phase through source terms within the governing equations as shown in figure 3-5 [126].

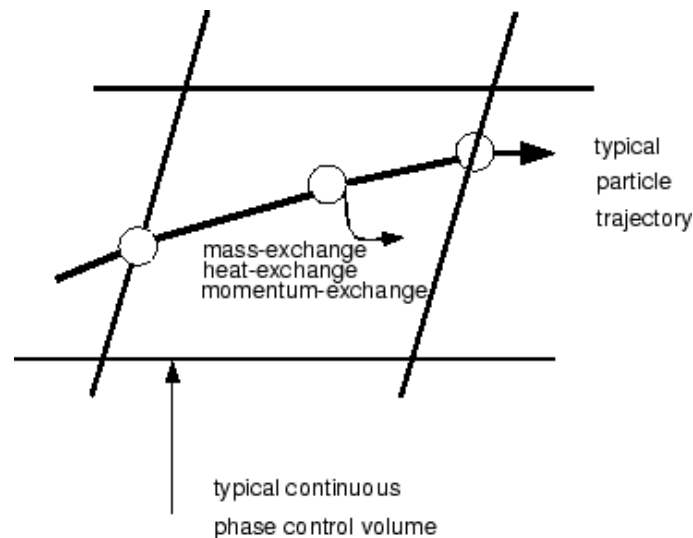


Figure 3-5: Heat, Mass, and Momentum Transfer Between the Discrete and Continuous Phases [62].

The motion of the droplets is given by Newton's second law, equation 3.39. the mass of the particle is given by m_p , u_p refers to the velocity of the particle, t refers to the time, A_p refers to the surface area of the particle, ρ_g refers to the density of the

continuous phase and u_g refers to the velocity of the continuous phase. The drag coefficient, c_D , is given by the drag law of Crowe et al. [127] which accounts to the Mach number effects on the drag coefficient. The drag coefficient is given by equation 3.40. The incompressible drag coefficient is given by, C_{D0} , Re_d refers to the particle Reynolds number, Ma refers to the Mach number and γ refers to the ratio of specific heat capacities.

$$m_p \frac{du_p}{dt} = \frac{1}{2} c_D \rho_g A_p (u_g - u_p) |u_g - u_p| \quad (Eq 3.39)$$

$$c_D = 2 + (C_{D0} - 2) e^{-3.07\sqrt{\gamma} \frac{1+Re_d(12.278+0.548Re_d)Ma}{1+11.278Re_d} \frac{Ma}{Re_d}} + \frac{5.6/(1+Ma)}{\sqrt{\gamma}Ma} e^{-\frac{Re_d}{2Ma}} \quad (Eq 3.40)$$

To model the effects of turbulent dispersion on the particle trajectories the discrete random walk model has been employed. The discrete random walk (DRW) model includes the effect of instantaneous turbulent velocity fluctuations, u' , on the particle trajectories using a stochastic method. The instantaneous velocity field, u , that accounts for turbulent fluctuations is given by equation 3.41 where \bar{u} refers to the time averaged velocity.

$$u = \bar{u} + u' \quad (Eq 3.41)$$

In the discrete random walk model, the fluctuating velocity components are initially calculated, this value is used for a time interval equal to that of the characteristic time scale. Their random value is kept constant over an interval of time given by the characteristic lifetime of the eddies. The integral time scale, T_L , for the k -epsilon model is given by equation 3.42.

$$T_L = 0.30 \frac{k}{\varepsilon} \quad (Eq 3.42)$$

The interaction of particles and turbulent eddies is characterised by a fluctuating velocity, u' , and a time scale, τ_e . The fluctuating velocity is a constant over the lifetime of the turbulent eddies and the distributing of turbulent fluctuations follows a Gaussian distribution.

$$u' = \zeta \sqrt{\overline{(u')^2}} \quad (Eq\ 3.43)$$

Equation 3.43 is used to determine the fluctuating velocity, ζ , refers to the normally distributed random fluctuations and the second term on the right-hand side refers to the RMS of the velocity fluctuations. The RMS of the velocity fluctuations, assuming an isotropic flow, relates to the turbulent kinetic energy through equation 3.44. The characteristic lifetime of the eddy is given by equation 3.45.

$$\sqrt{\overline{(u')^2}} = \sqrt{\overline{(v')^2}} = \sqrt{\overline{(w')^2}} = \sqrt{\frac{2k}{3}} \quad (Eq\ 3.44)$$

$$\tau_e = 2T_L \quad (Eq\ 3.45)$$

The particle temperature, T_p , can be determined from equation 3.46 where c_p refers to the specific heat capacity of the particle and h_{fg} refers to the latent heat. The heat transfer coefficient, h , is computed using a Nusselt number correlation. There are numerous Nusselt number correlations available within mass and heat transfer literature. This chapter discusses three applicable Nusselt number correlations and chapter 6 evaluates the effectiveness of these correlations for SHVOF thermal spray.

$$(m \cdot c_p)_p \frac{dT_p}{dt} = hA_p(T_g - T_p) - \frac{dm}{dt} h_{fg} \quad (Eq\ 3.46)$$

The Ranz - Marshall Nusselt number correlation is the most popular correlation employed to determine the heat transfer coefficient to solid spherical particle or droplets [128] & [129]. The Ranz - Marshall correlation was developed from droplet

evaporation experiments at low Reynolds numbers and low Mach numbers for application to spray drying. Experiments to determine the heat transfer coefficient and the evaporation rate of droplets were conducted at varying Reynolds numbers from 0 – 200. The Ranz - Marshall correlation for the Nusselt number is given by equation 3.47. The particle diameter is given by, d_p , the thermal conductivity of the continuous phase is given by, k_∞ and Pr refers to the Prandtl number of the continuous phase [62]. The Prandtl number is defined as the ratio of the momentum diffusivity to thermal diffusivity as given by equation 3.48. Within equation 3.48 the dynamic viscosity and thermal conductivity is given by μ and k respectively.

$$Nu = \frac{hd_p}{k_\infty} = 2.0 + 0.6Re_d^{1/2}Pr^{1/3} \quad (Eq\ 3.47)$$

$$Pr = \frac{c_p\mu}{k} \quad (Eq\ 3.48)$$

There are several flaws with the Ranz-Marshall correlation, for example the correlation does not account for the Mach number effects on the heat transfer to particles. Kavanau et al. [130] and Drake et al. [131] have investigated the effect of the Mach number on the heat transfer coefficient within subsonic and supersonic flow respectively. From the experimental studies conducted from both Kavanu et al. and Drake et al. It was shown that the Nusselt number varies greatly with the Mach number. The Ranz - Marshall correlation is unable to account for the effect of the Mach number on the heat transfer coefficient. An alternative Nusselt number correlation to the Ranz-Marshall correlation which has been applied to cold spray and high velocity oxy fuel thermal spray however has not yet been employed within SHVOF thermal spray provides the Nusselt number as a function of the Mach number. The compressible correlation accounts for the Mach number effects on the Nusselt number and is given by equation 3.49.

$$Nu = 2.0 + 0.4Re_p^{0.5} Pr^{1/3} \exp(0.1 + 0.872 Ma) \quad (Eq 3.49)$$

The effects of rarefaction can play a significant role within flows and the Knudsen number, Kn , can be used to evaluate the effects of rarefaction. The Knudsen number is defined as the ratio of the molecular mean free path length, Λ , to the physical length and is given by equation 3.50. As the Knudsen number increases the effects of rarefaction become significant and non-continuum effects must be considered [27].

$$Kn = \frac{\Lambda}{d_p} \approx \sqrt{\frac{\pi\gamma}{2}} \left(\frac{Ma}{Re_p} \right) \quad (Eq 3.50)$$

Kavanau et al. [130] derived the heat transfer coefficient of spherical particles within the slip flow regime which accounts for the Mach number and Knudsen number effects on the Nusselt number. They derived a Nusselt number correlation for application to particles within a rarefied gas flow and looked to fit their Nusselt correlation to particles within a rarefied subsonic flow. The Kavanau correlation is given by equation 3.51; where the incompressible Nusselt number is given by, Nu_0 .

$$Nu = \frac{Nu_0}{1.0 + 3.42Nu_0 \frac{Ma}{Re_p Pr}} \quad (Eq 3.51)$$

Droplets in a high-speed gas flow break up into smaller droplets, this process is known as secondary breakup. There are a number of different secondary breakup models available, each of which are suitable for a different Weber numbers. The TAB breakup model is suitable for low speed and low Weber number sprays. The WAVE model is suitable for sprays where the Weber number exceeds 100. The KHRT breakup model is an additional breakup model suitable for Weber numbers exceeding 100.

The wave secondary breakup model assumes the breakup time and droplet sizes are related to the fastest growing Kelvin-Helmholtz instability on the droplet surface [37]

& [132]. The child droplet diameter is assumed to be proportional to the wavelength of the fastest growing instabilities as given by equation 3.52. where B_o is a model constant which is set to 0.61. The maximum growth rate, Ω , and its wavelength, Λ , is given by equation 3.53 and 3.54 respectively. The gas Weber number is given by, We_g , Ta refers to the Taylor number and Oh refers to the Ohnesorge number.

$$r = B_o \Lambda \quad (Eq\ 3.52)$$

$$\Omega = \frac{(0.34 + 0.38We_g^{0.5})}{(1 + Oh)(1 + Ta^{0.6})} \left(\frac{\rho_1 a^3}{\sigma} \right) \quad (Eq\ 3.53)$$

$$\Lambda = 9.02a \frac{(1 + 0.45Oh^{0.5})(1 + Ta^{0.7})}{(1 + 0.8We_g^{1.67})^{0.6}} \quad (Eq\ 3.54)$$

The rate of change of the parent droplet diameter, a , is given by equation 3.55 and the breakup time for the droplet, τ_p , is given by equation 3.56. The radius of the droplet is given by, r and B_1 refers to a model constant and is set to the value 1.73.

$$\frac{da}{dt} = - \frac{a - r}{\tau_p} \quad (Eq\ 3.55)$$

$$\tau_p = \frac{3.726B_1 a}{\Lambda \Omega} \quad (Eq\ 3.56)$$

The Kelvin-Helmholtz Rayleigh-Taylor (KHRT) secondary breakup model builds upon the WAVE model by combining the effects of the aerodynamic forces due to the Kelvin – Helmholtz instability with the acceleration of droplet ejection into the freestream due to the Raleigh – Taylor instabilities. To model the liquid core in the near nozzle injection, a Levich core length, L , is applied that only allows breakup due to Kelvin-Helmholtz wave growth, which is given by equation 3.57. The Levich constant is given by, C_L , d_o refers to the diameter of the nozzle.

$$L = C_l d_0 \sqrt{\frac{\rho_l}{\rho_g}} \quad (Eq 3.57)$$

Both mechanisms model the secondary breakup by tracking wave growth on the surface of the droplet, with breakup occurring due to the fastest growing instability. The frequency of the fastest growing wave is given by equation 3.58 where g_t refers to the acceleration of the droplet in its direction of travel. The corresponding wave number, K_{RT} , is given by equation 3.59. Breakup occurs after Raleigh Taylor waves have been growing for a time larger than the breakup time, τ_{RT} . The breakup time is given by equation 3.60 where C_τ refers to the Rayleigh-Taylor breakup time constant which takes the value of 0.50. The radius of the child droplet, r_c , is given by equation 3.61 where C_{RT} refers to the breakup radius constant which takes the value of 0.1.

$$\Omega_{RT} = \sqrt{\frac{2 \left(g_t (\rho_p - \rho_g) \right)^{\frac{3}{2}}}{3\sqrt{3}\sigma(\rho_p + \rho_g)}} \quad (Eq 3.58)$$

$$K_{RT} = \sqrt{\frac{-g_t(\rho_p - \rho_g)}{3\sigma}} \quad (Eq 3.59)$$

$$\tau_{RT} = \frac{C_\tau}{\Omega_{RT}} \quad (Eq 3.60)$$

$$r_c = \frac{\pi C_{RT}}{K_{RT}} \quad (Eq 3.61)$$

As the suspension droplet temperature increases above the liquid components' vaporization temperature there is mass transfer from the droplet to the gas due to vaporization. Vaporization occurs when the droplet temperature, T_p , is greater than the constituent vaporization temperature, T_{pap} , and below its boiling point, T_b , given in equation 3.62. For processes where there is convection of the evaporating material from the droplet surface to the bulk gas flow, Stephan flow, the mass transfer rate

increases. The convection – diffusion vaporization model proposed by Miler and Sazhin accounts for the effect of Stephan flow on the mass transfer rate, which is given by equation 3.63 and 3.64. Where m_p refers to the mass of the droplet, k_c refers to the mass transfer coefficient and B_m refers to the Spalding mass number. The Spalding mass number is given by equation 3.64. The vapour mass fraction at the surface is given by, $Y_{i,s}$, vapor mass fraction in the bulk gas is given by $Y_{i,o}$.

$$T_{vap} \leq T_p < T_{bp} \quad (Eq\ 3.62)$$

$$\frac{dm_p}{dt} = k_c A_p \rho \ln(1 + B_m) \quad (Eq\ 3.63)$$

$$B_m = \frac{Y_{i,s} - Y_{i,o}}{1 - Y_{i,s}} \quad (Eq\ 3.64)$$

Boiling occurs when the droplet temperature exceeds that of its boiling point, equation 3.65. The mass transfer rate from the droplet to the bulk gas is given by the d^2 law which is given by equation 3.66. The specific heat capacity of the continuous phase is given by $c_{p,\infty}$ and h_{fg} refers to the latent heat.

$$T_{vap} \leq T_p < T_{bp} \quad (Eq\ 3.65)$$

$$\frac{d(d_p)}{dt} = \frac{4k_c}{\rho_p c_{p,\infty} d_p} (1 + 0.23\sqrt{Re_d}) \ln \left(1 + \frac{c_{p,\infty}(T_\infty - T_p)}{h_{fg}} \right) \quad (Eq\ 3.66)$$

To account for the melting of the solid particles an effective specific heat capacity model can be employed. The effective specific heat capacity method adjusts the specific heat capacity to account for the latent heat of fusion required to melt solid material. The effective specific heat capacity, $c_{p,eff}$, is calculated using equation 3.67 [133] & [134]. The specific heat capacity of the material in its solid phase is given by

$c_{p(s)}$ and $c_{p(l)}$ refers to the specific heat capacity of the material in its liquid phase and L refers to the latent heat of fusion required to melt the material.

$$c_{p,eff} = \begin{cases} c_{p(s)}, & T < T_1 \\ \frac{1}{2} \left(\frac{L}{T_2 - T_1} + c_{p(s)} + c_{p(l)} \right), & T_1 \leq T < T_2 \\ c_{p(l)}, & T \geq T_2 \end{cases} \quad (Eq 3.67)$$

3.4.2 Volume of Fluid Model:

The volume of fluid (VOF) method looks at locating the interface between two phases. The VOF model solves the volume fraction, ϕ_q , equation for phase q within the computational domain. Within each cell the sum of the volume fraction for all the phases must sum to 1.0. At cells where the volume fraction lies within $0 < \phi < 1$ an interface reconstruction method is employed to map the interface. The volume of fraction equation is solved which is given by equation 3.68.

$$\frac{\partial \phi_q}{\partial t} + U \cdot \nabla \phi_q = 0 \quad (Eq 3.68)$$

The VOF model requires a mesh fine enough to resolve the structures, one of the challenges is the interface is constantly moving. Hence, a static mesh of uniform density will require a significant computational cost. Methods can be employed to improve the interface reconstruction; one such method is to employ a dynamic mesh refinement algorithm. Dynamic mesh refinement looks to refine the mesh density around the interface as the solution changes as can be seen in figure 3-6.

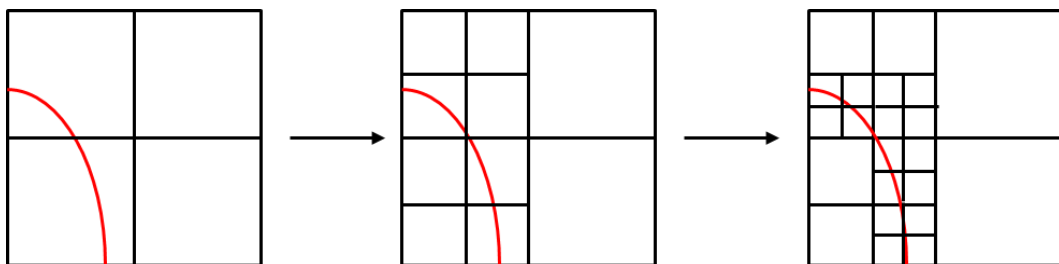


Figure 3-6: Dynamic mesh refinement using a cut cell method.

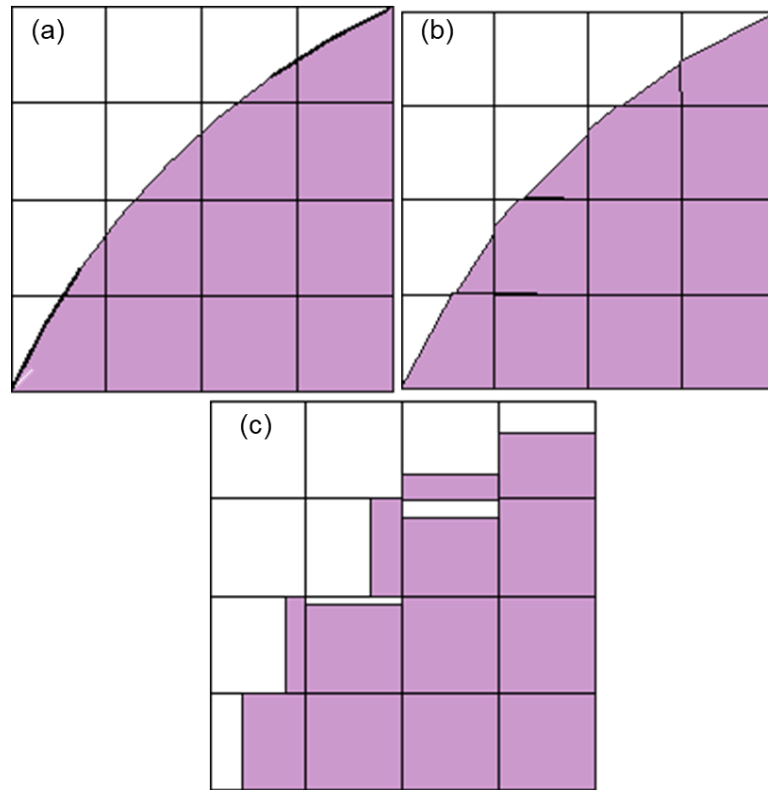


Figure 3-7: (a) Actual interface, (b) geo-reconstruct scheme and (c) donor acceptor scheme.

There are several numerical schemes available to reconstruct the interface between the two phases. One of the challenges with VOF is ensuring a suitable scheme is employed to accurately model the interface. Figure 3-7 shows comparison of the geo-reconstruct and the donor acceptor scheme to the actual interface. The geo-reconstruct scheme employs a piecewise linear interpolation of the interface which provides the most accurate re-construction of the interface. The geo-reconstruct scheme is however significantly more computationally expensive than alternative approaches. The donor acceptor scheme identifies cells that lie on the interface known as donor cells. Neighbouring cells referred to as the acceptor cells are then filled with fluid equalling to the amount of fluid identified from the donor cells. This method is employed to reduce the numerical diffusion along the interface.

3.4.3 Coupled Volume of Fluid and Discrete Particle Model

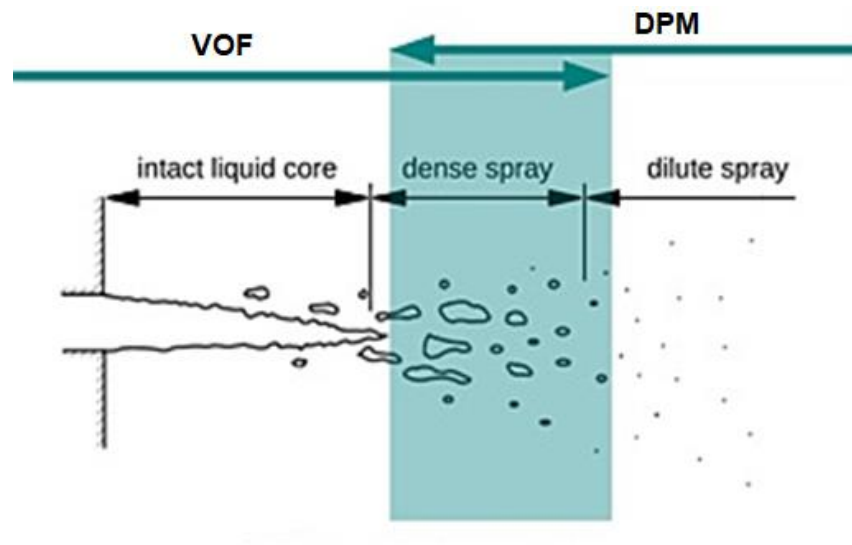


Figure 3-8: A Coupled VOF and DPM Model for Jet Breakup [135].

A coupled VOF and DPM framework can be employed to provide a high fidelity and cost-effective approach to model entire range of multi-phase structures. Large scale structures can be resolved to a high fidelity using a VOF framework. Small droplet structures that are formed from the primary breakup are converted from a VOF framework to a DPM framework where they are modelled at a lower computational cost. The DPM model allows for a robust and inexpensive treatment of small droplet structures as these droplets are treated as point entities. The modelling of a liquid jet breakup using a coupled VOF and DPM framework is illustrated within figure 3-8.

As the suspension is injected into the combustion chamber; it forms a jet which is modelled using a VOF framework. Ligaments form on the surface of the jet and detach from the jet forming small droplets. Once the ligaments detach from the jet and form into droplets, they are converted from a VOF framework to a DPM framework. The cells containing the liquid phase are patched with the gas phase to allow conservation of the volume fraction equation [136] & [137]. A droplet with the equivalent mass,

diameter, average temperature, average velocity and average species components is then injected at that same location. A source term is implemented within the mass and momentum conservation equations to account for the mass transfer between the continuous phase and the discrete phase. If an adaptive mesh refinement is employed the mesh adaption is re-coarsened

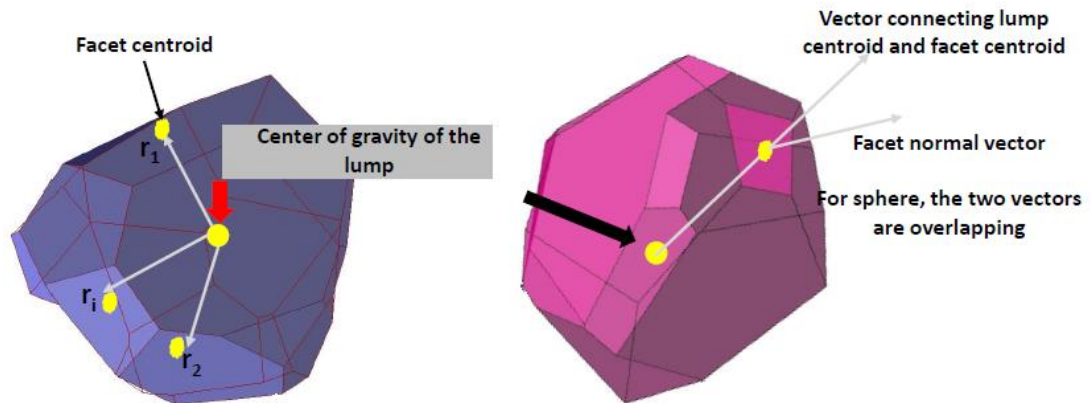


Figure 3-9: Droplet normalized radius standard deviation [left] and average radius surface orthogonality [right] [126].

To allow for a coupling of the VOF and DPM models a switching condition is required to determine which multiphase structures will be converted from a VOF framework to a DPM framework. Within Ansys Fluent a lump detection algorithm is employed to identify droplet structures which are suitable for conversion. The geometric properties of the liquid structures, such as the droplet normalized radius standard deviation and average radius surface orthogonality are evaluated as shown in figure 3-9. If the droplets are smaller than the set radius for conversion and more spherical than the set measure of sphericity the droplets are converted from a VOF framework to a DPM framework.

3.5 Numerical Algorithm

To solve the governing equations the segregated pressure-based solver has been employed within chapters 4 - 6. The segregated solver has been employed due to the low computational cost required for this solution method. With this approach the velocity components and the pressure are solved sequentially, then additional scalar equations for the energy, species and turbulence equations are solved for.

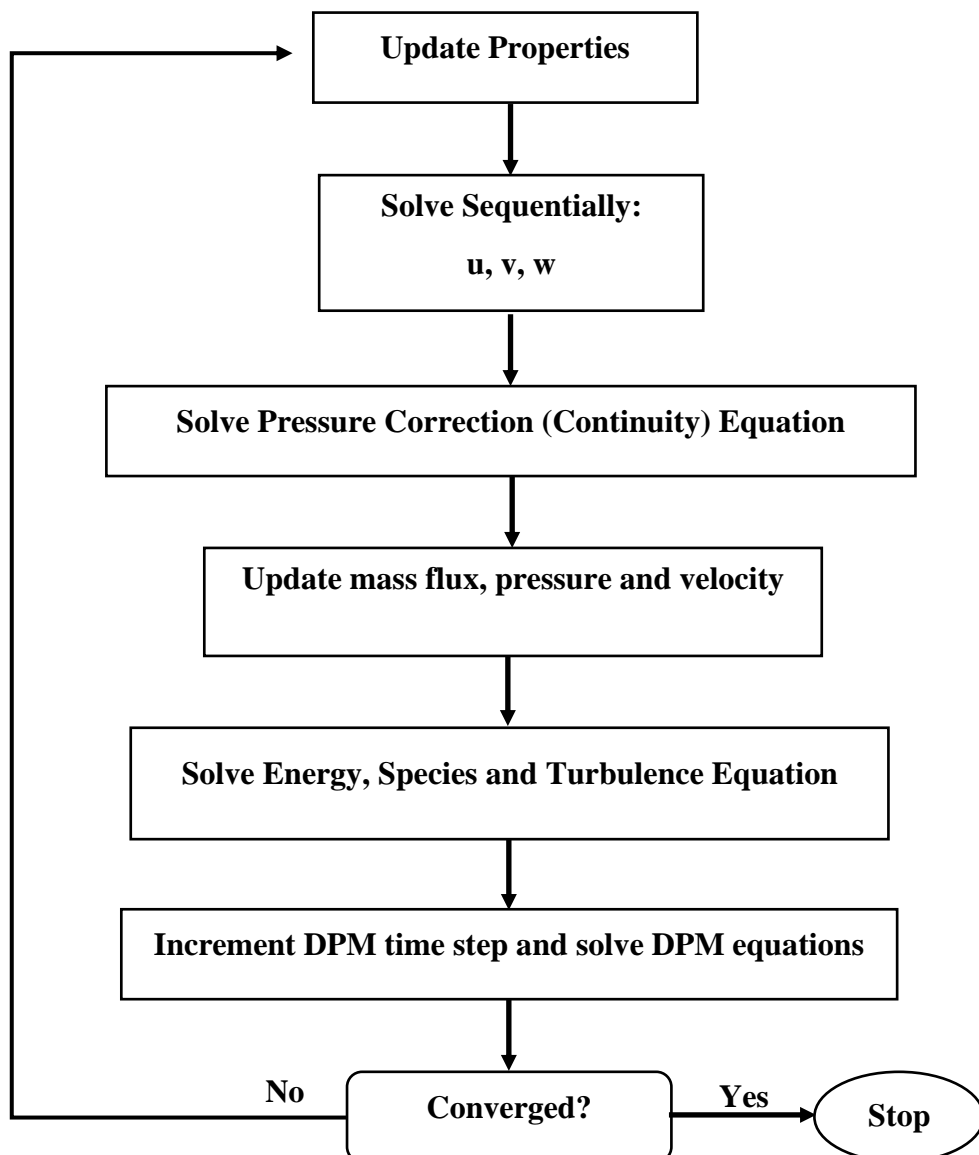


Figure 3-10: Segregated Pressure Based Solution Algorithm

With the SIMPLE algorithm an initial condition is specified for the governing variables, from the initial conditions the gradient terms are calculated. The discretised forms of the momentum equation are then solved for to determine an intermediate velocity field and the mass fluxes are calculated from this velocity field. The calculated mass flux does not satisfy the continuity equation and a mass flux correction is applied such that the updated mass flux satisfies the continuity equation. With the SIMPLE algorithm the mass flux correction, J'_f , is given by equation 3.69 where p'_{c0} and p'_{c1} represent the cell pressure correction either side of the cell faces and d_f is a function of the momentum equation coefficients. The updated mass fluxes now satisfy the continuity equation. The simple algorithm substitutes the mass flux correction equations into the discretised continuity equations to obtain a pressure correction value that satisfies the continuity equation. Once the pressure correction is calculated the pressure field and the face fluxes are corrected. Figure 3-10 outlines the segregated solution algorithm [138].

$$J'_f = d_f(p'_{c0} - p'_{c1}) \quad (Eq\ 3.69)$$

Issues arose with the segregated solution algorithm in preventing solution divergence when modelling the combustion chamber in chapter 7. Alternatively, the momentum equations and the pressure-based continuity equation can be solved for simultaneously. The additional scalar equations are solved for sequentially once the pressure and velocity components are solved for. This is referred to as the coupled solver; the solver allows for a large time step to be employed. In this study the solver was found to be more robust and stable. The coupled algorithm requires fewer iterations to reach convergence however is more computationally expensive. In the coupled algorithm the fully implicit coupling is attained through an implicit discretization of pressure gradient terms in the momentum equations, and an implicit discretization of the face

mass flux. Figure 3-11 outlines the coupled solution algorithm employed to solve the set of governing equations. In chapter 7 of this thesis where the combustion chamber has been modelled using a coupled VOF and DPM framework the coupled solver has been employed.

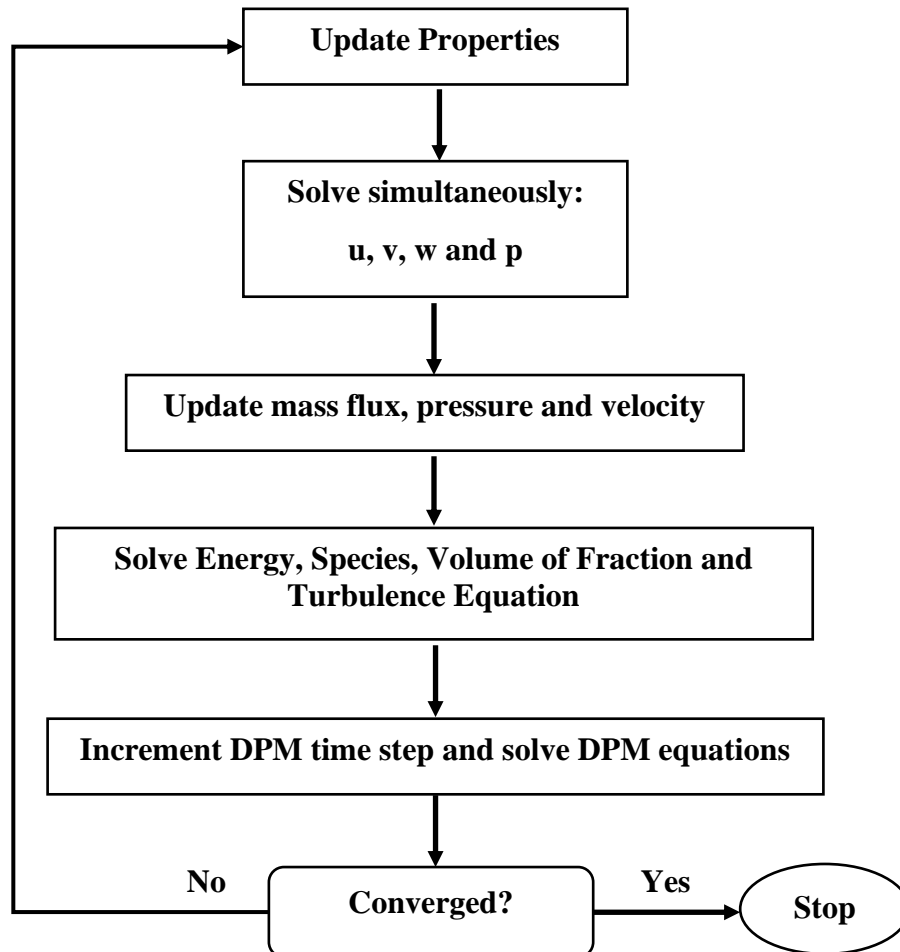


Figure 3-11: Coupled Pressure Based Solution Algorithm

The various numerical methods that have been employed are outlined within this chapter. Further discussion on the accuracy and the fidelity of the numerical methods is provided in the subsequent chapters. The accuracy of the numerical approaches are compared to experimental measurements obtained using high speed imaging, time of flight measurements, two colour pyrometry measurements and experimental measurements from the literature.

Chapter 4: Investigation into the Effect of the Nozzle Geometry onto the Gas, Suspension and Particle Dynamics

4.1 Introduction:

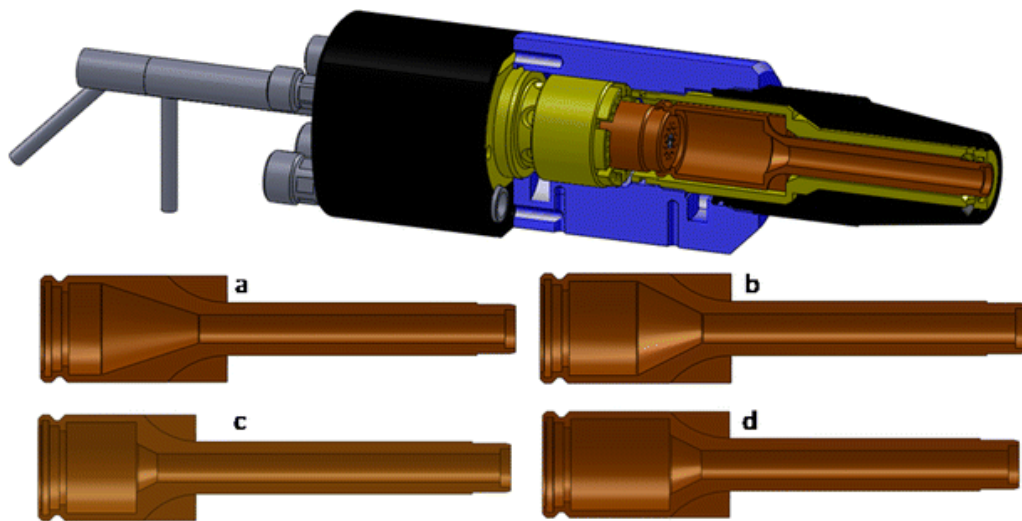


Figure 4-1: TopGun SHVOF gun with different nozzle types (a) and (b) for low melting temperature materials; (c) and (d) for high melting temperature materials

There are many suppliers for commercial thermal spray hardware; GTV is one of the largest thermal spray suppliers and manufacturers on the market. GTV offer a range of SHVOF guns which include TopGun, JP5000 and Jet Kote to name a few [139]. In addition to the range of SHVOF guns supplied by GTV they offer a range of nozzle geometries for their guns. Figure 4-1 shows a cross section of the inside of the TopGun SHVOF gun and four commercially available nozzles [15]. Currently there is no general consensus as to which case each nozzle is best suited when it comes to suspension spray. Most nozzles were developed for conventional size HVOF powders, as opposed to suspensions. Understanding the effect that the nozzle geometry has on

the gas temperature, gas velocity, gas pressure, particle temperature and the particle velocity will allow for better control and predictability of coating properties. An understanding of the effect of geometrical parameters will allow for optimization of next generation nozzles for suspension feedstock as opposed to optimising for powdered feedstock.

4.2 SHVOF Nozzle Geometries

The nozzles in SHVOF thermal spray gun are comprised of a combustion chamber followed by a barrel as shown in figure 4-2. The region connecting the combustion chamber and the barrel is referred to as the throat. The premixed fuel and oxygen are injected into the combustion chamber through a set of circular inlets that span circumferentially around the combustion chamber. The suspension is injected into the centre of the combustion chamber with an injector. The suspension is injected into the centre of the combustion chamber with an injector.

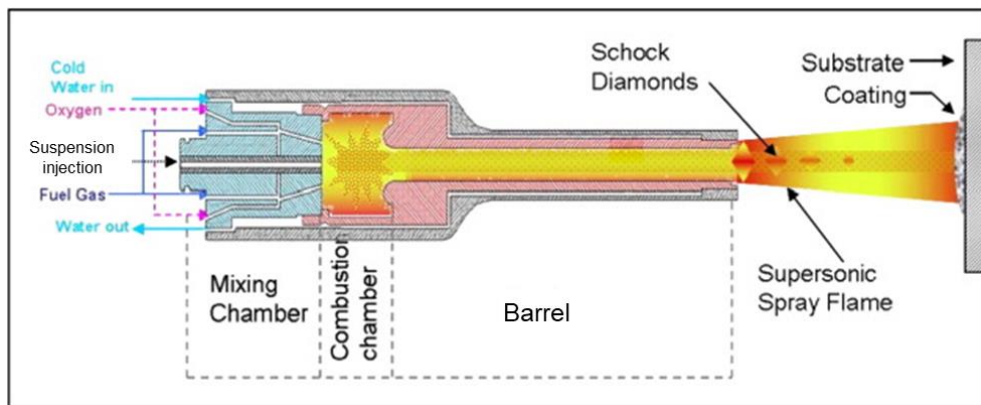


Figure 4-2: Suspension high velocity oxy fuel thermal spray torch design for the TopGun system [139].

The length of the combustion chamber, barrel length and the total nozzle length are the main parameters that vary from nozzle to nozzle from commercial suppliers. The nozzles follow a naming convention and the nozzle is named by three numbers, the numbers refer to the combustion chamber length, the total length and finally the barrel

diameter, respectively. For example, the 30-135-8 nozzle has a 30 mm long combustion chamber, a total length of 135 mm and a barrel diameter of 8mm. The 0-78-8 nozzle has been named accordingly as this nozzle is a convergent barrel nozzle as opposed to a nozzle with a discrete combustion chamber as seen in the other three nozzles. This chapter compares investigates the gas dynamics, evaporation rate, average inflight particle velocity and temperature for four commercially available nozzles shown in figure 4-3. The four nozzle geometries have been used as it allows for an evaluation of the effect of the combustion chamber length while maintaining a constant total nozzle length by comparing the 30-135-8 nozzle with the 22-135-8 nozzle. It allows for a comparison of the effect of the total nozzle length by comparing the 135 mm nozzles with the 78 mm nozzles. Finally, it allows for an evaluation of the effect of having a discrete combustion chamber by comparing the 12-78-8 nozzle with the 0-78-8 nozzle. These are the main parameters that vary between different nozzles available from commercial thermal spray suppliers.

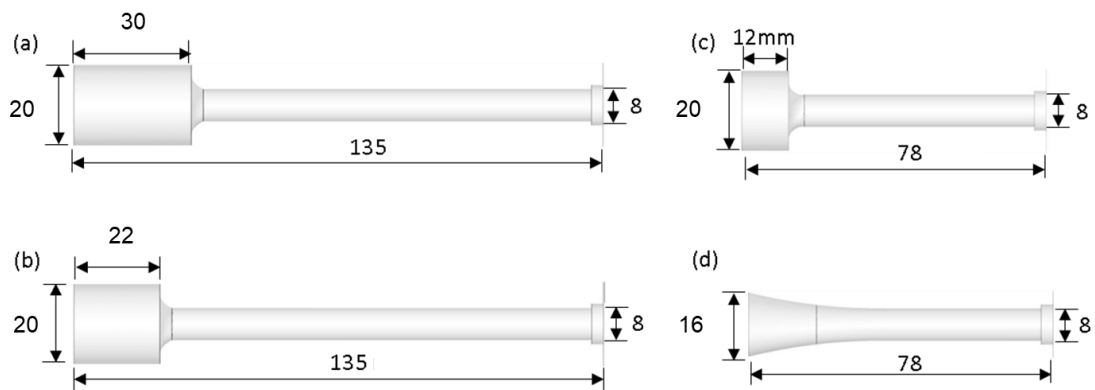


Figure 4-3: Nozzle geometries evaluated within this study (a) 30-135-8, (b) 22-135-8 (c) 12-78-8 and (d) 0-78-8 nozzle

4.3 Modelling Methodology

A fully structured 2-D axi-symmetric mesh is used to model the geometry. 2D axis-symmetric investigations have been used in a wide range of SHVOF thermal spray studies [68], [140] & [77] as they can provide an in depth understanding of the process with very low overhead in the computational cost for the numerical model. The premixed fuel and oxygen are injected into the combustion chamber through an inlet with a diameter of 1 mm located at distance of 4 mm away from the axis of symmetry. A description of the boundary conditions is given in table 4-1. The gas phase is solved for using a QUICK scheme for the convective terms. The QUICK scheme has been employed as this numerical scheme shows good agreement with the location of the shocks [69] when compared with alternative numerical schemes available and experimentally obtained measurements from imaging data as outlined within the literature review, section 2.7.2. The numerical modelling approach employed within this study is very similar to numerical models from the literature that have been validated using experimental data obtained from the literature or from Accuraspray measurements [20], [68] & [69].

To model the gas phase the following compressible governing equations are solved for; mass conservation, momentum conservation, ideal gas law, energy conservation, species conservation and the realizable $k-\varepsilon$ turbulence model with the enhanced wall function. The governing equations outlined above are provided within section 3.1 – 3.3. Combustion is modelled using a species transport model and the eddy dissipation model [61] for the hydrogen combustion. The combustion reaction employed within this study is a single step global reaction that accounts for the formation of dissociated species. The coefficients can be determined via a chemical equilibrium Gordon and McBride [141]. The coefficients for the combustion reaction are determined from the

approach outlined in section 2.2. The suspension is injected using a two-way coupled discrete particle model using a multicomponent injection. A suspension comprised of 80 % water and 20 % Cr₂O₃ is injected axially into the combustion chamber.

Table 4-1: Table of the boundary conditions.

Specified Boundary Condition	Values
Total Gas Flow Rate	0.0059 Kg/s
Outlet Condition	1 atm
Equivalence Ratio	1
Suspension Flow Rate	50 ml/min
Wall Boundary Condition	0 m/s

4.4 Mesh Independence and Convergence

A mesh independence study has been conducted to ensure a mesh independent solution the centreline velocity is evaluated at grid spacings of 0.5mm, 0.25mm and 0.125mm. Figure 4-4, 4-5, 4-6 and 4-7 show the centreline velocity at the three mesh sizes for the 30-135-5, 22-135-8, 12-78-8 and the 0-78-8 nozzles respectively. Table 4-2 outlines the cell spacing for the three meshes employed for the four nozzle geometries investigated. Mesh M1, M2 and M3 refers to a base cell spacing of 0.5 mm, 0.25 mm and 0.125 mm respectively. The wall normal cell spacing for all three meshes has been kept constant to maintain a y^+ of 4.5 for all three meshes. The wall normal spacing has been chosen to ensure that the wall can be resolved using the enhanced wall

functions available within Ansys Fluent and as outlined within section 3.2.3. The cell spacing far from the nozzle outlet has been kept to 5 times the base mesh cell spacing. A coarser mesh has been employed far from the nozzle exit due to the smaller gradients that occur within this region of the flow. The coarser cell spacing allows for a reduction in the cell count and consequently a reduction in the computational cost of the numerical model.

Table 4-2: Summary of mesh features for meshes considered within the mesh independence test for the 30-135-8, 22-135-8, 12-78-8 and 0-78-8 nozzles.

Mesh	Base Mesh Size	y+
M1	0.500 mm	4.5
M2	0.250 mm	4.5
M3	0.125 mm	4.5

It can be seen from figures 4-4, 4-5, 4-6 and 4-7 that there is a difference between the velocity profiles within the combustion chamber and at the shocks when reducing the base size from 0.50 mm to 0.25 mm when comparing meshes M1 and M2. The base meshes with a cell size of 0.5 mm are unable to capture the final two – three shock waves. However, reducing the base mesh size further from 0.25 mm to 0.125 mm when comparing meshes M2 and M3 there is no further change in the solution. Hence, mesh independence is seen with a base mesh size of 0.25 mm. Figure 4-8 shows the meshes for the four nozzle geometries investigated with a truncated domain. .

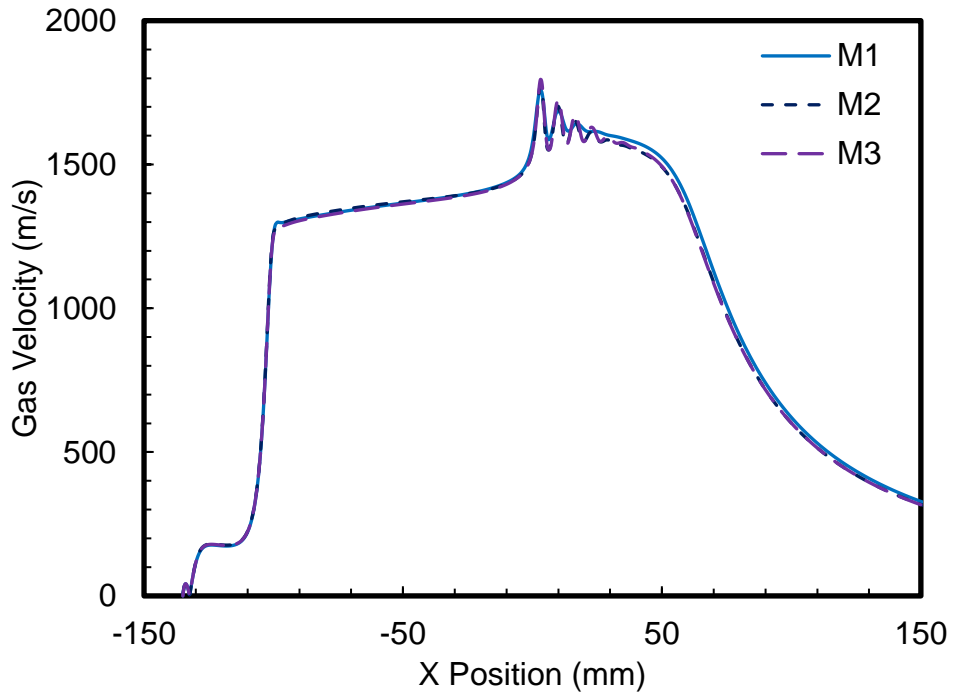


Figure 4-4: Centreline velocity magnitude for the 30-135-8 nozzle at three base cell spacings.

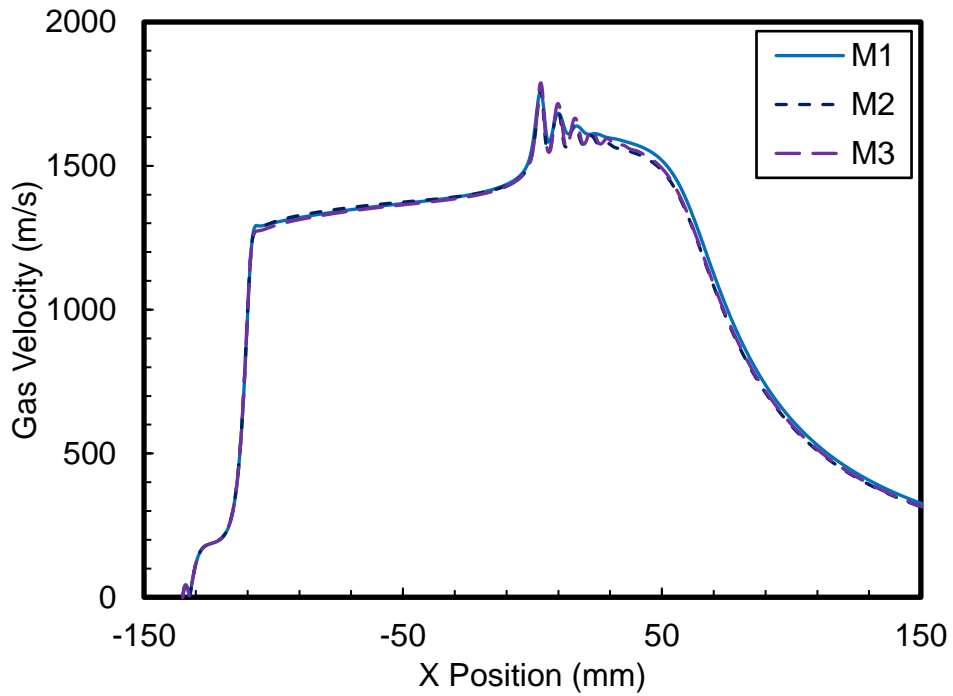


Figure 4-5: Centreline velocity magnitude for the 22-135-8 nozzle at three base cell spacings.

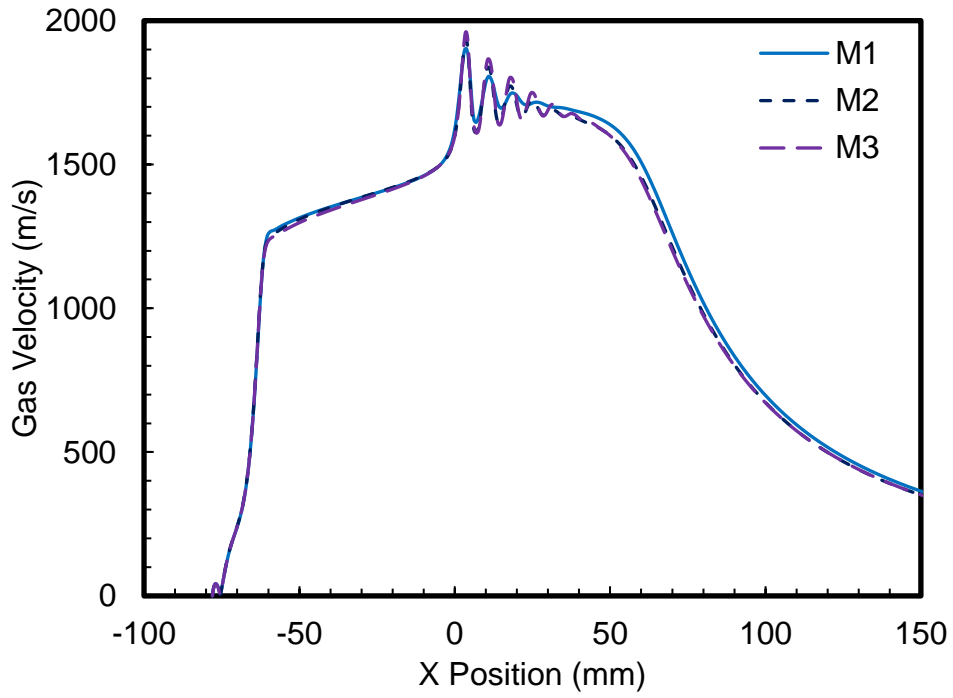


Figure 4-6: Centreline velocity magnitude for the 12-78-8 nozzle at three base cell spacings.

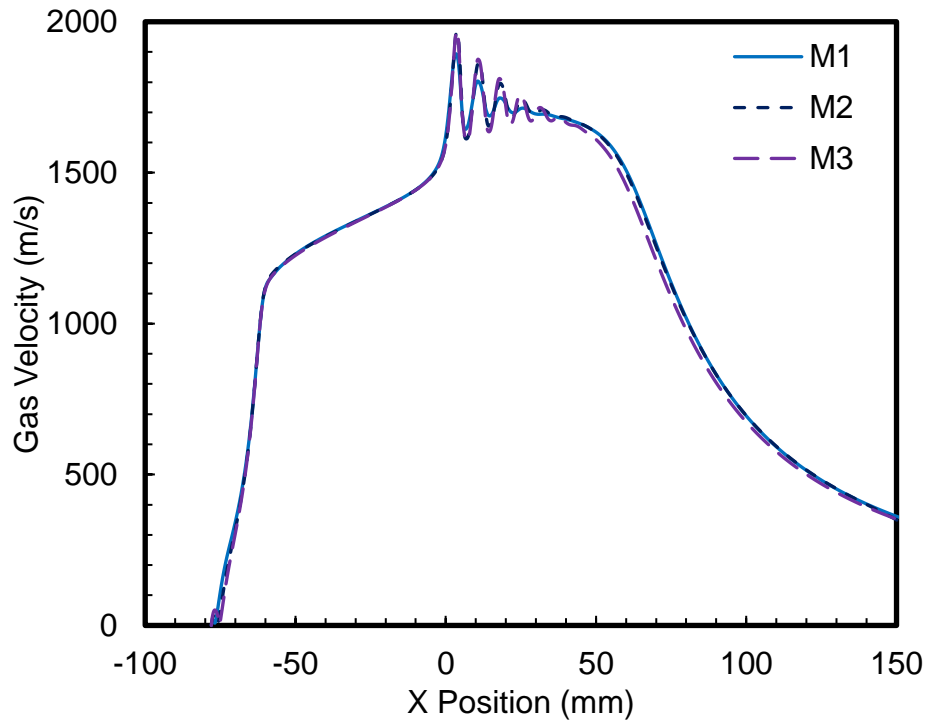


Figure 4-7: Centreline velocity magnitude for the 0-78-8 nozzle at three base cell spacings.

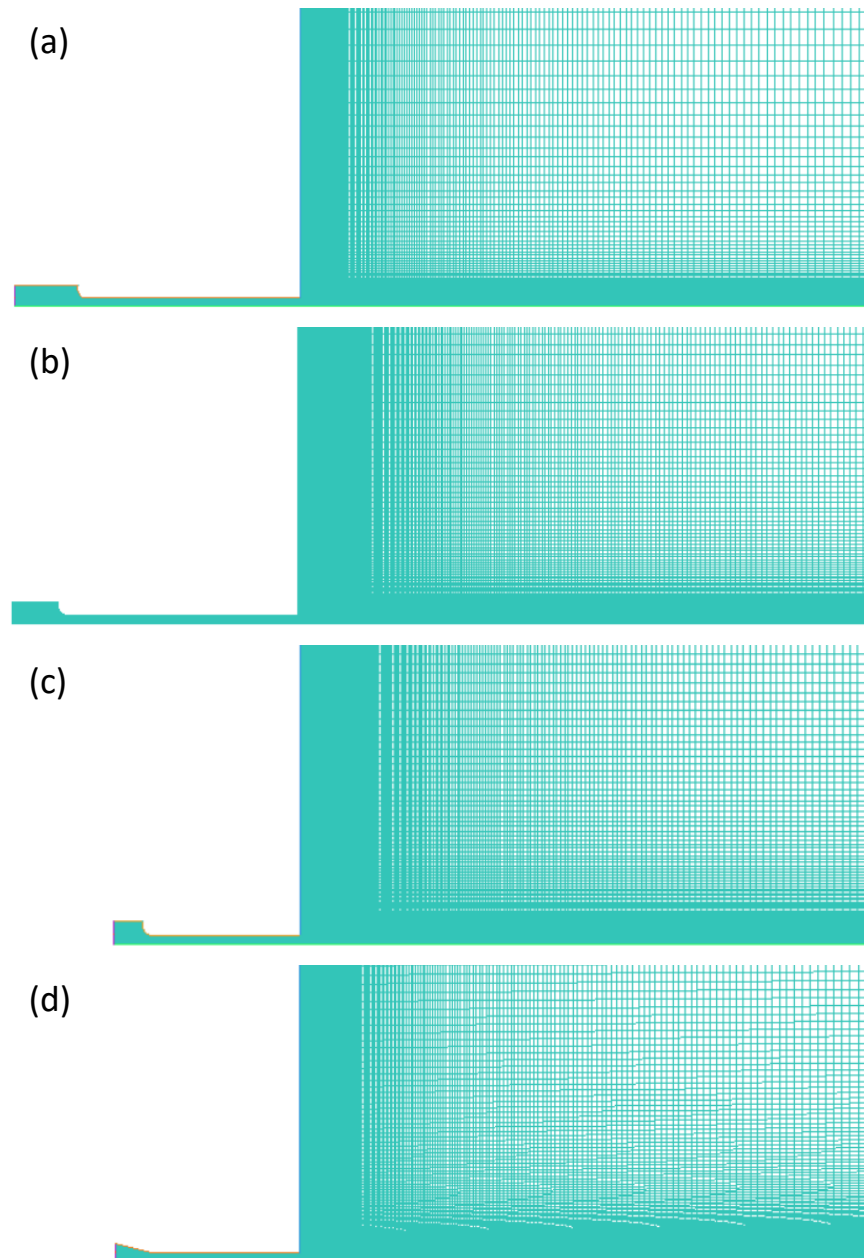


Figure 4-8: Mesh for the four nozzle geometries considered (a) 0-78-8, (b) 12-78-8, (c) 22-135-8 and (d) 30-135-8 nozzles.

To ensure convergence two criteria were examined; the residuals and monitor points. Convergence was obtained when the residuals fell to below $1e-05$ for the continuity equation, $1e-05$ for the momentum equations, $1e-05$ for the RANS equations and $1e-06$ for the energy and species equations. The monitor points were used to examine the local velocity and temperature within the domain. When no further change in the solution was observed, the solution was said to be converged.

4.5 The Effect of the Nozzle Geometry on the Gas Velocity

Optimum design of any nozzle employed within SHVOF thermal spray will ideally operate at the highest velocity achievable to ensure maximum momentum from the gas phase to the suspension and particles within the suspension. Particles that impact the substrate with a higher velocity will have an increased inter laminar adhesion and better adhere to the substrate. The increase in the particle velocity will also form denser coatings with a lower porosity [142]. One way to increase the particle velocity at impact is to ensure that the nozzles operate at a higher gas velocity. Figure 4-9 compares the centre line gas velocity magnitude for the four nozzles with and without a suspension injection.

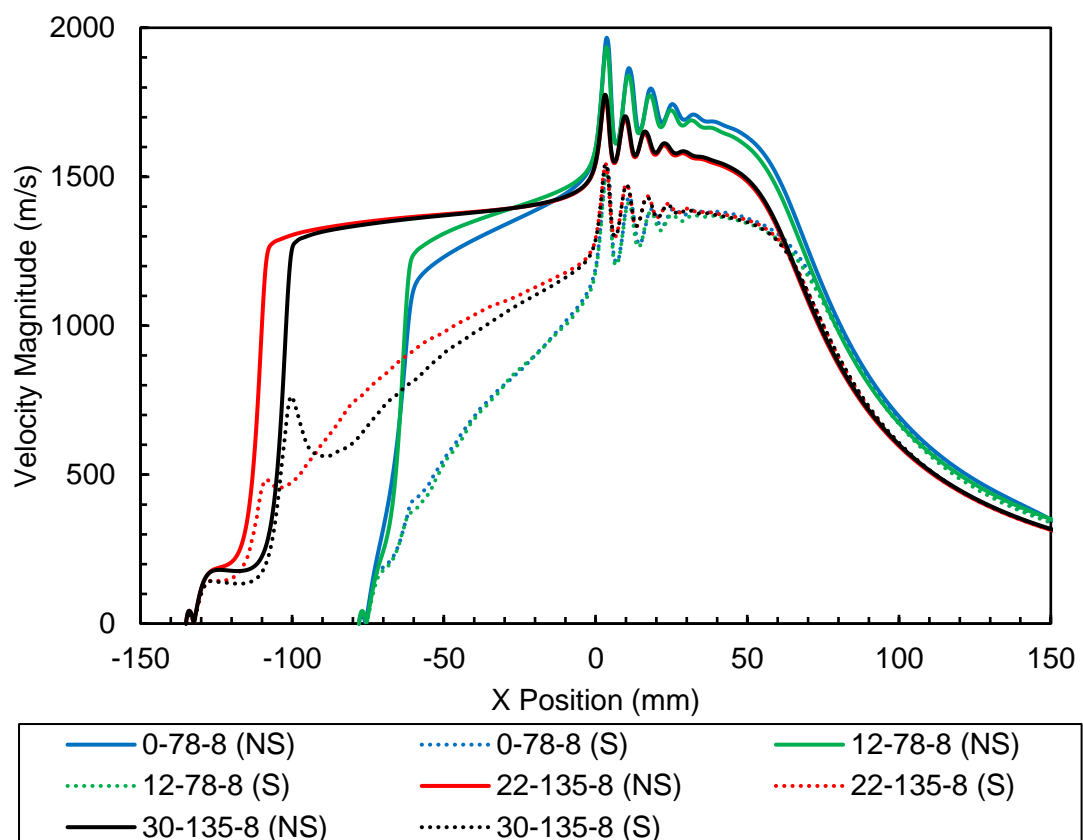


Figure 4-9: Centreline gas velocity for the 30-135-8, 22-135-8, 12-78-8 and 0-78-8 nozzles, (NS) No Suspension and (S) Suspension.

Figure 4-9 shows that the nozzles designed with a longer combustion chamber have a higher velocity at the exit of the combustion chamber. For example, the flow exits the combustion chamber of the 12-78-8 mm nozzles with a velocity of 1225 m/s while the flow exits the combustion chamber of the 30-135-8 nozzle at 1290 m/s. An increase in the combustion chamber length of 18 mm results in an increase in the gas velocity at the exit of the combustion chamber by 65 m/s.

It can also be seen from figure 4-9 that the two shorter 78 mm length nozzles operate at a significantly higher velocity before the suspension is injected in the barrel exit and the free jet. For example, at a standoff distance of 50 mm from the nozzle exit the 135 mm nozzle operate at a velocity of approximately 1450 m/s while the 78 mm nozzles operate at a velocity of approximately 1600 m/s. A reduction in the nozzle length of 57 mm results in an increase in the gas velocity by 150 m/s at the standoff distance considered. Once the suspension is injected the combustion chamber, the 135 mm nozzles operates at a higher gas velocity than the 78 mm nozzles up to a distance of 60 mm into the free jet. For example, at the nozzle exit the 135 mm nozzles operate at a velocity of approximately 1200 m/s while the 78 mm nozzles operate at a velocity of approximately 1100 m/s.

$$St = \frac{\rho_p d_p^2 U_{g,b}}{18\mu_g L} \quad (Eq\ 4.1)$$

Suspension particle trajectories and profiles follow the velocity profile of the gas closely due to the size of the particle low mass inertia of the particles. The Stokes number characterises the particle – fluid interactions within particle laden flows [143], the Stokes number is defined as the ratio of the particle to eddy response times [144]. The Stokes number is given by equation 4-1 [145] where the particle density is given by, ρ_p , the particle diameter is given by, d_p , the bulk flow gas velocity is given by $U_{g,b}$,

the gas viscosity is given by, μ_g , and the characteristic length scale of the flow is given by L . The particle stokes number within SHVOF can range from the order of 1 to 100 depending on the particle diameter. Within the barrel of the nozzle the characteristic length scale is given by the barrel diameter and when considering the interaction between the particles and the substrate the characteristic length scale refers to the length scale of the substrate. Due to the very small diameter and therefore the low Stokes number of particles within SHVOF thermal spray the particles will match the flow profile very closely. The higher gas velocity in the barrel and near the nozzle exit for the longer 135 mm nozzles will result in higher particle velocities in these regions. Far from the nozzle exit the gas velocity for the 135 mm nozzles and the 78 mm nozzles are identical so there will be little to no variation in the particle velocity between these nozzles far from the nozzle exit.

4.6 The Effect of the Nozzle Geometry on the Gas Pressure

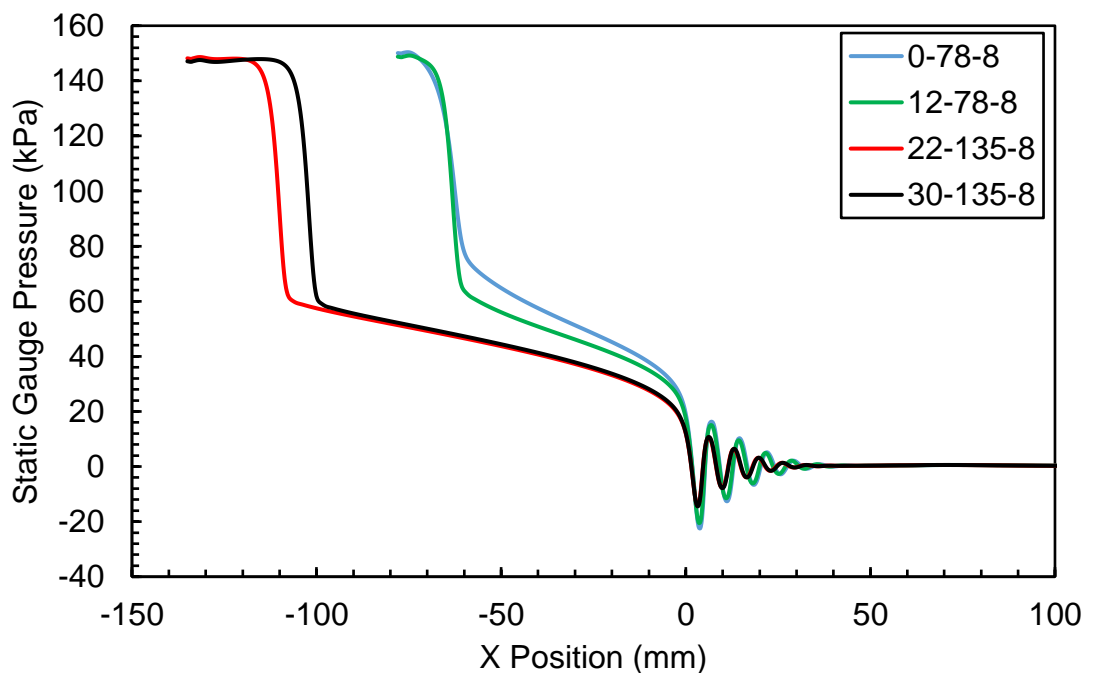


Figure 4-10: Centreline static gas pressure for the 30-135-8, 22-135-8, 12-78-8 and 0-78-8 nozzles.

Figure 4-10 compares the centre line static gas pressure for the four nozzles without a suspension injection. Figure 4-10 shows a higher gas pressure for the shorter 78 mm nozzles at the nozzle exit in contrast to the 135 mm nozzles. As the flow travels down the barrel, frictional forces cause the pressure to drop. The longer 135 mm nozzles experience a higher pressure drop than the 78 mm nozzles due to the longer barrel length. It can be seen that the 30-135-8 nozzle experiences a pressure drop of 54 kPa from the barrel entrance to the exit, while the 12-78-8 nozzle experiences a pressure drop of 51 kPa. Due to the higher pressure at the nozzle exit for the 78 mm nozzles the magnitude of the resultant shock waves are greater than that of the longer 135 mm nozzles. The flow is therefore able to expand to a greater degree which results in a higher gas velocity. As is demonstrated by comparing the gas velocity for the same two nozzles within the free jet, at 50 mm from the nozzle exit the 12-78-8 mm nozzle operates at 110 m/s greater velocity than the 135 mm nozzle.

The flow at the exit of all four nozzles is under-expanded as the pressure at the outlet exceeds the atmospheric pressure. This condition gives rise to the shock diamonds seen within the free jet. The shocks produced within the free jet produce an inefficient mechanism to convert the gas pressure into kinetic energy within the jet. Korpla et al. [146] designed and modelled a De Laval then compared the gas velocity to the typical barrel nozzle design for HVOF thermal spray. The De Laval nozzle was designed to ensure ideally expanded flow at the nozzle exit and preventing the formation of shocks at the nozzle exit to allow for efficient transfer of gas pressure to kinetic energy. Lee et al. [147] also varied the nozzle geometry to optimise the expansion of the flow at the exit of the nozzle aerosol deposition. Korpla et al. and Lee et al. demonstrated that optimising the nozzle can produce significantly higher gas velocities up to 400 m/s with the nozzle ideally expanded. Next generation of SHVOF thermal spray nozzles

could look to ensure ideally expanded conditions at the exit for a range of operating conditions. This may lead to more efficient conversion of gas pressure to kinetic energy may allow for higher gas velocities, higher particle velocities and hence denser coatings with a lower porosity. The nozzles will however only be ideally expanded for the operating conditions employed to optimise the nozzle. Therefore, moving away from these conditions will result in under-expanded or over-expanded flow.

4.7 The Effect of the Nozzle Geometry on the Gas Temperature

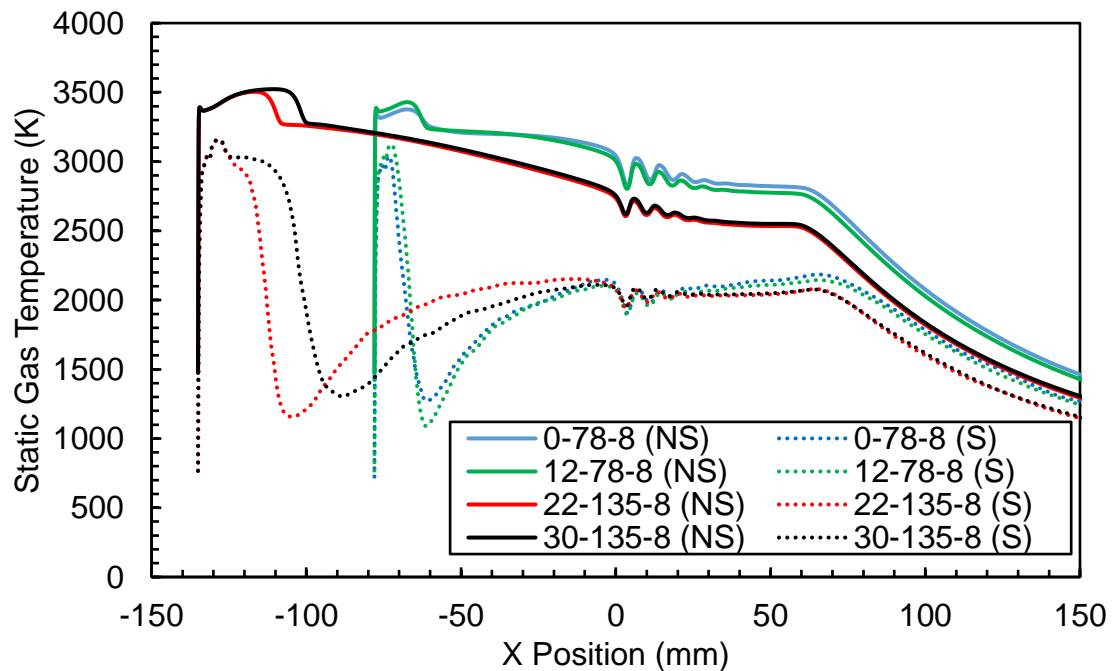


Figure 4-11: Centreline static gas temperature for the 30-135-8, 22-135-8, 12-78-8 and 0-78-8 nozzles, (NS) No Suspension and (S) Suspension.

Tan et al. [94] has shown that particles with a higher temperature prior to impact require a lower critical velocity to successfully deposit onto the substrate. Therefore, particles with a higher temperature prior to impact are more likely to deposit onto the substrate. Nozzles designed within SHVOF thermal spray should look to maximise the temperature of particles prior to impacting the substrate. Figure 4-11 compares the centre line static gas temperature for the four nozzles with suspension (S) and without

suspension (NS) injected into the combustion chamber. It can be seen from figure 4-11 that before any suspension is injected into the combustion chamber the longer 135 mm nozzles operate at a higher temperature than the 78 mm nozzles within the combustion chamber and the nozzle throat. Both 78 mm nozzles have a shorter combustion chamber, as the flow travels through the combustion chamber the pressure drops, velocity increases and the temperature increases. This effect is greater as the combustion chamber length increases. However, within the barrel and the free jet region the shorter 78 mm nozzles operate at a higher temperature than the 135 mm nozzles. Additionally, it can be seen that after the suspension is injected into the combustion chamber there is a significant drop in the gas temperature within throat and the barrel of the nozzle. The largest drop in gas temperature is seen in the 12-78-8 nozzle and the smallest drop in the gas temperature is seen in the 30-135-8 nozzle. The 12-78-8 nozzle experiences a temperature drop of 2100 K whilst the 30-135-8 nozzle experiences a temperature drop of 1900 K. Within the nozzle it can be seen that the 135 mm nozzles operate at a higher gas temperature than the 78 mm nozzles. Beyond the nozzle exit it is seen that the 78 mm nozzles operate at a higher gas temperature than the 135 mm nozzles. The difference is however much smaller in the free jet in comparison to the gas temperature without any suspension injected into the nozzle.

4.8 Effect of the Nozzle Geometry on the Evaporation of Suspension

Nozzles that operate with a suspension feedstock injection must ensure efficient and effective vaporization of the liquid within the suspension. The current understanding employed to develop the nozzles for SHVOF has been built upon optimising the nozzles for powdered feedstock. Nozzles designed for suspension feedstock must ensure the liquid is readily vaporised so that the particles have sufficient time to be

heated to impact the substrate in a molten state. Figure 4-12 compares the centre line evaporation rate for the 30-135-8, 22-135-8, 12-78-8 and 0-78-8 nozzle.

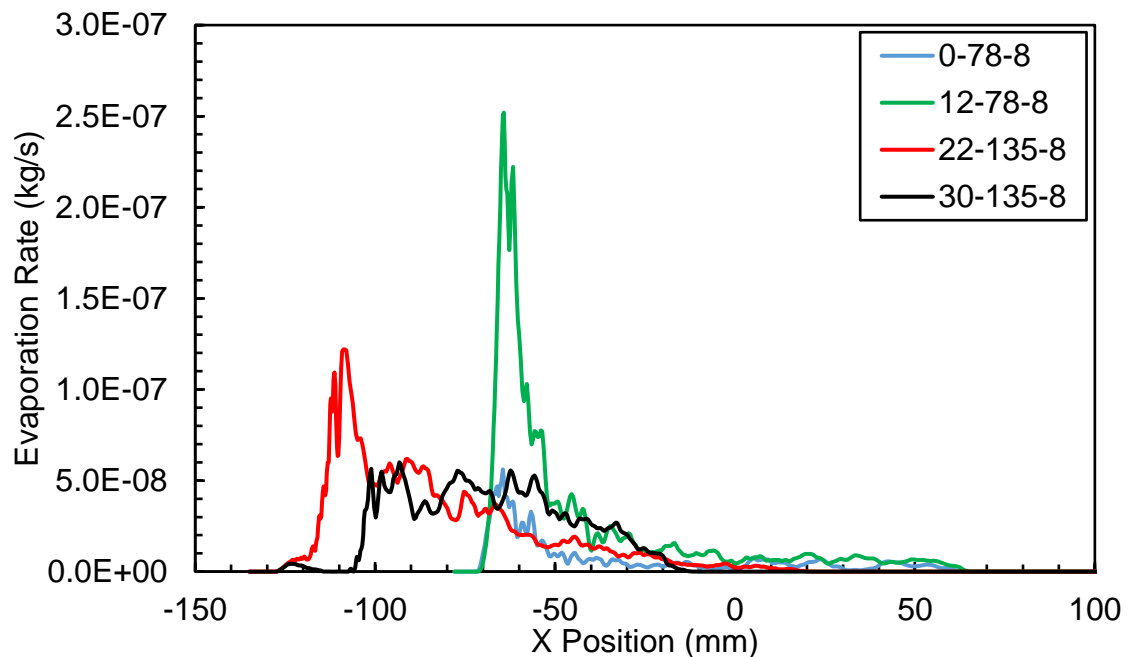


Figure 4-12: Centreline evaporation rate for the 30-135-8, 22-135-8, 12-78-8 and 0-78-8 nozzles.

It is seen from figure 4-12 comparing the evaporation rate profile for the two 78 mm length nozzles with the 135 mm nozzles, the suspension vaporization continues to 70 mm beyond the nozzle exit for the 78 mm nozzles. For the 135 mm nozzles vaporization commences much closer to the nozzle exit. For the SHVOF thermal spray process it is desired that the suspension vaporizes as soon as possible. This allows for maximum duration of time that the particles are heated allowing for particles to impact the substrate in their molten state.

It can also be seen from figure 4-12 by comparing the three nozzles with a discrete combustion chamber; the nozzles with a shorter combustion chamber experience a higher maximum evaporation rate. The maximum evaporation rate occurs within the throat of the nozzle This is a result of the pressure drop within the throat of the nozzle

which allows suspension to vaporise more readily. With a smaller combustion chamber the suspension droplets have spent a lower duration of time before they reach the nozzle throat, there is more moisture is available within the suspension droplets to vaporize within the throat.

4.9 Effect of the Nozzle Geometry on the Inflight Particle Velocities

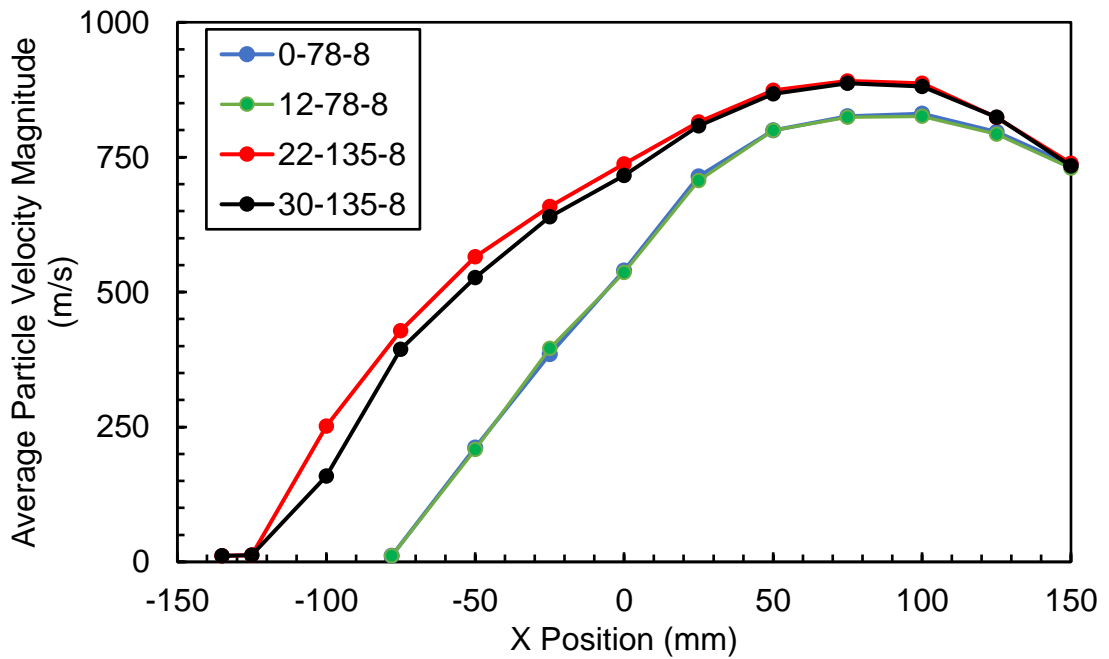


Figure 4-13: Average particle velocities for the 30-135-8, 22-135-8, 12-78-8 and 0-78-8 nozzles.

Figure 4-13 compares the average particle velocity for the 30-135-8, 22-135-8, 12-78-8 and the 0-78-8 nozzle. The 0 mm position on the x-axis refers to the nozzle exit for all four of the nozzles. Figure 4-13 shows that for all four nozzles the maximum particle velocity is reached at a standoff distance of approximately 75 – 100 mm. This is in line with experimental observations where the samples are sprayed at a standoff distance of 85 mm [24]. It can also be seen that the 135 mm nozzles accelerate particles to a significantly higher velocity than the 78 mm nozzles. Comparing the average particle velocity at the nozzle exit the 135 mm nozzles accelerate the particles to

approximately 220 m/s greater velocity than the 78 mm nozzles. With a longer nozzle, the particles experience a greater time within the flow before they reach the exit of the nozzle. This greater residence time within the gas allows for greater acceleration and hence a higher particle velocity.

4.10 Effect of the Nozzle Geometry on the Inflight Particle Temperatures

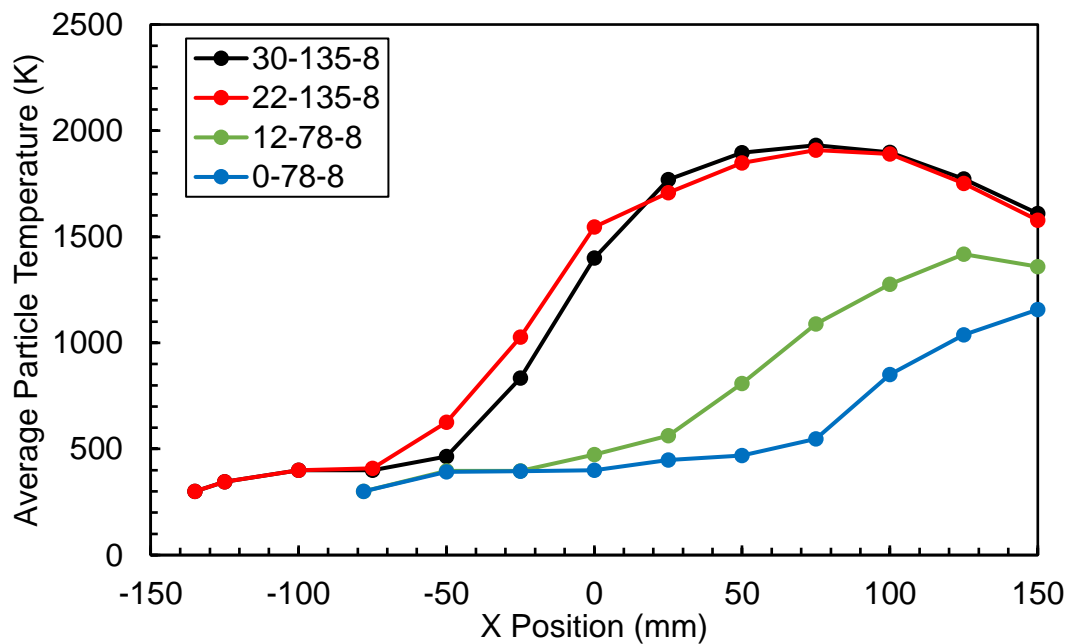


Figure 4-14: Average particle velocities for the 30-135-8, 22-135-8, 12-78-8 and 0-78-8 nozzles.

Figure 4-14 compares the average particle temperature for the 30-135-8, 22-135-8, 12-78-8 and 0-78-8 nozzles. From figure 4-14 it can be seen that for the 135 mm and 78 mm nozzles; the maximum particle temperature is reached at a standoff distance of approximately 50 - 75 mm and 100 - 125 mm respectively. With the shorter 78 mm nozzles particles still contain moisture well into the free jet unlike the 135 mm nozzles. Therefore, the particles reach their maximum temperature further into the free jet and require a greater standoff distance to maximise the particle temperatures. It can also

be seen that the 135 mm nozzles heat the particles to a significantly higher temperature than the 78 mm nozzles. Comparing the average particle temperature at the nozzle exit the 30-135-8 nozzle the particles temperature approximately 800 K greater than for the 12-78-8 nozzle. With a longer nozzle, the particles experience a greater time within the flow before they reach the exit of the nozzle. This greater residence time within the gas allows for greater heating of the particles which results in a higher particle temperature.

It can be seen by comparing the average particle temperature for the 12-78-8 and the 0-78-8 nozzles the convergent barrel nozzle design (0-78-8) results in a lower particle temperature in comparison to the discrete combustion chamber design. This is a result of the lower evaporation rate with the convergent barrel nozzle (0-78-8) in comparison to the nozzles with a discrete combustion chamber (12-78-8) nozzle. With a higher evaporation rate the suspension vaporises sooner and particles can be heated sooner, this results in a higher particle temperature.

There are numerous nozzles available from commercial SHVOF suppliers and this investigation has compared four nozzles to understand the effect of the combustion chamber length, barrel length and the total length of the nozzle. Next generation of SHVOF thermal spray nozzles should look to maximise the gas velocities, gas temperatures and the duration the particles are heated and accelerated to allow for particles to impact the substrate with the maximum velocity and temperature. All the nozzles considered from GTV are under-expanded at the typical operating conditions. The next generation of SHVOF thermal spray nozzles could optimise the nozzle geometry to ensure the nozzles are ideally expanded at the nozzle exit. As this shown to provide more efficient conversion of the gas pressure into kinetic energy and therefore higher gas velocities within cold spray and HVOF thermal spray.

4.11 Summary

In summary it can be seen that the nozzle geometry has a significant impact on the gas and particle dynamics. The aim when designing the nozzle geometry is to ensure that the particles can reach higher velocities and higher temperatures which ensures that the particles will adhere well to the substrate and form a coating with a low porosity. Comparing the gas dynamics between various nozzles it is shown that the shorter (78 mm) nozzles operate at a higher velocity and temperature within the free jet in comparison to the longer (135 mm) nozzles. A reduction in the nozzle length of 57 mm results in an increase in the gas velocity by 150 m/s at the standoff distance considered. Additionally, the reduction in the total nozzle length from 135 mm to 78 mm resulted in an increase in the gas temperature of 300 K before any suspension is injected. However, it is also seen that with the longer nozzles; the liquid component of the suspension is completely vaporized within the nozzle in comparison to the shorter nozzles where the suspension commences vaporization well into the free jet. This allows for a greater duration of particle heating and acceleration which results in a higher particle velocity and temperature. Therefore, the higher gas velocity and temperature that the shorter nozzles operate at do not translate directly into higher particle velocities and temperatures respectively. When optimising the nozzle length, it must be ensured that particles spend a sufficient duration of time within the flow to be adequately heated and accelerated. Additionally, the nozzle length must be optimised to maximise the gas flow velocity and temperature.

Chapter 5: Development of a Hybrid Nozzle for Oxygen Sensitive Materials

5.1 Introduction

In the current SHVOF thermal spray, suspension is injected axially into the combustion chamber. There is a significant body of modelling and experimental literature investigating the effect of different parameters for axial injections of suspension within the combustion chamber [69], [81]. However, there are certain cases where the quality of the coating as well as the efficiency of deposition or the functionality of the coating can be significantly enhanced through a radial injection of suspension outside of the nozzle. Oxygen sensitive materials such as graphene nanoplatelets (GNPs), carbon nanotubes and fullerene oxidise and degrade when heated and exposed to oxygen for significant durations of time at high temperatures. A radial injection with a shrouding environment of suspension can reduce in-flight time and therefore allow for their deposition [16].

Typically, within SHVOF thermal spray, there has been little success in deposition of coatings using a radial injection of suspension as opposed to SPS where this injection method has been more successful. The reason for this is that in SPS gas temperatures can be anywhere up to 5 times higher than that in SHVOF and hence gas densities are significantly lower. The lower gas densities allow for the suspension to penetrate the cross flow more readily. Additionally, within SHVOF thermal spray the gas is operating at supersonic velocities as opposed to SPS thermal spray where the gas velocities are subsonic and hence significantly lower. The major hurdle in radial injection for SHVOF thermal spray is to provide the liquid jet with sufficient

momentum to penetrate into the centre of the gas jet whilst ensuring that there is not an excessive loss in heat and momentum. Hence this chapter employs a CFD methodology to understand and optimise the radial injection of suspension into a HVOF crossflow.

Shrouding for HVOF thermal spray has been developed to deposit oxygen sensitive materials, as the shroud prevents mixing of ambient air with the HVOF jet and therefore reduces the oxygen content within the jet [17], [148]. There are two types of shrouding often used within thermal spray a physical barrier shroud and a gas shroud. the physical barrier shroud cases the thermal spray jet with an enclosure to prevent mixing of air into the jet. A gas shroud is used to inject an inert gas shroud around the jet to delay the mixing of ambient oxygen into the gas shroud [149]. A combination of shrouding the HVOF jet and a radial injection of suspension into a HVOF jet provides two major benefits. It allows for a reduction in mixing of oxygen from the atmosphere into the HVOF jet with a reduction in the inflight time of oxygen sensitive particles to allow for deposition of coatings with pristine properties. A hybrid nozzle is designed within this this chapter; a hybrid nozzle is referred to the system that combines an axial injection of suspension or powder feedstock, a physical shrouding system, a gas shrouding system with a radial injection within the shroud is shown in figure 5-1. This nozzle design has been developed to deposit two feedstock materials with drastically different properties and sensitivities to oxygen. Murray et al. [150] sprayed an alumina and graphene nanocomposite coating using a suspension which consisted of 0.257% GNPs by weight and 25.443% alumina, with the remainder deionised water. The suspension was injected axially into the combustion chamber and a coating was deposited onto a substrate. It was shown that the coating demonstrated a two order of magnitude reduction in the specific wear rate for the alumina/GNP composite in

comparison to an equivalent alumina coating. Employing a hybrid nozzle to inject a separate alumina and GNP suspension will accommodate for the drastically different sensitivities to oxygen and thermal requirements for the alumina and the GNPs and improve the efficiency of deposition of GNPs. Injecting the GNPs outside of the nozzle radially into the HVOF jet will allow for less oxygen entrainment and a shorter exposure to oxygen at high temperature for the GNPs. Whilst allowing for sufficient heating and melting for the axially injected alumina.

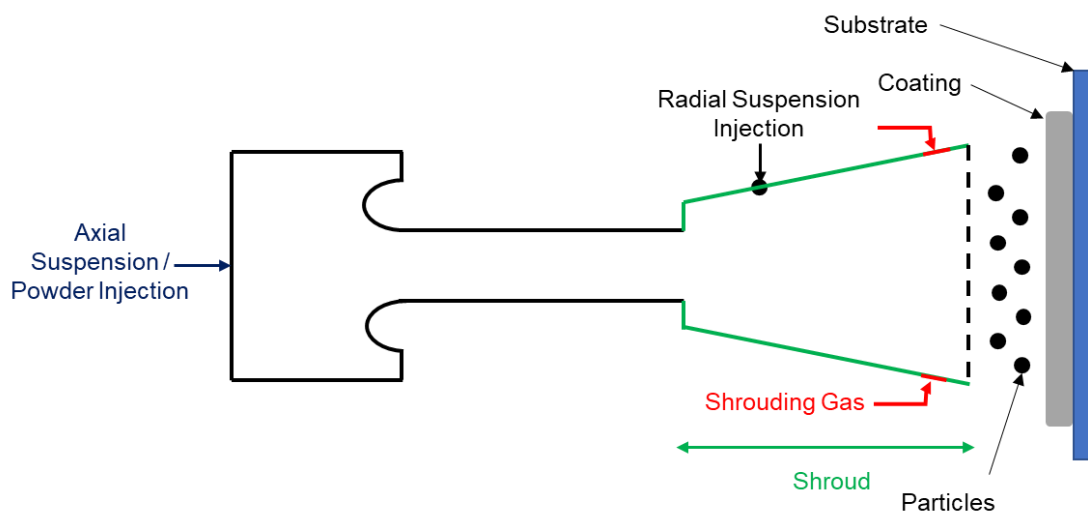


Figure 5-1: Hybrid nozzle design for SHVOF thermal spray (not drawn to scale).

This chapter compares the single step reaction mechanism employed with the eddy dissipation model with a multi-step reaction mechanism with the eddy dissipation concept model (section 5.4). The effect of suspension flow rate, injection angle and the diameter of the injector are investigated to determine suitable injection conditions for the suspension within the shroud. The numerical model is compared to experimental observations obtained from high-speed imaging without the shrouding attachment. A hybrid nozzle is designed and modelled within this chapter that incorporates a radial injection of suspension into the shroud. The effect of the expansion of the shroud and the shrouding gas flow rate on the flow field is

investigated to minimise oxygen entrainment and maximise suspension penetration into the crossflow.

5.2 Modelling Methodology

The premixed hydrogen and oxygen are injected into the combustion chamber using an annular inlet with a width of 1 mm located 4 mm from the centreline of the combustion chamber. The centreline of the nozzle is indicated by the blue line in figure 5-2. A steady state gas flow field is established before injecting any suspension. To model the gas phase the continuity, momentum conservation, ideal gas law, energy conservation, species fraction and the realizable k- ϵ turbulence model with an enhanced wall function are solved for using the SIMPLE algorithm; the governing equations for which are described in chapter 3, sections 3.2 – 3.4 .

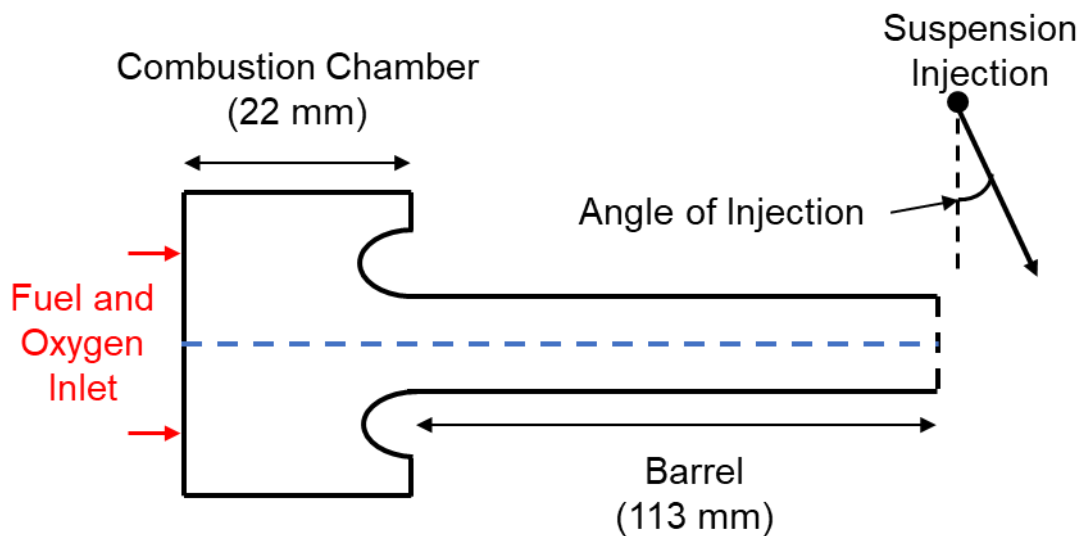


Figure 5-2: Schematic of computational domain (Not drawn to scale).

The suspension is injected using a two-way coupled multicomponent DPM model. The DPM model has been employed within this study as it has shown adequate agreement with experimental data with a radial injection for SPS thermal spray [151]. The DPM model has robust secondary breakup, evaporation models and is computationally

efficient. A cone injection is employed consisting of 20 particle streams, a cone angle of 1 degree has been calculated based upon Ranz et al. [152]. A Two-way turbulence coupling, secondary breakup and the pressure dependent boiling models have been employed. The unsteady discrete phase is solved for once with every 10 gas phase iterations with a DPM time step of 1×10^{-5} s. The DPM time step has been chosen such that DPM particles move forward no more than one cell on average. The inverse distance node-based averaging is employed to distribute the DPM source term amongst neighbouring cells [153], [154]. The boundary conditions for the gas phase and the discrete phase are given in table 5-1. The wall temperature boundary condition is based on prior models employed within the literature [20], [140] & [60]. Figure 5-2 outlines a schematic of the radial injection of suspension into the HVOF jet.

Table 5-1: Table of the boundary conditions employed.

Surface	Value	Temperature (K)
Total Gas Flow Rate	5.9×10^{-3} kg/s	300
Outlet Condition	Pressure Outlet	300
Equivalence Ratio	1	
Suspension Flow Rate	50 - 300 ml/min	300
Wall Boundary Condition	No-slip	500

5.3 Mesh Independence and Convergence

The mesh employed within this study is a fully structured mesh generated by the multi blocking method using Ansys ICEM. A mesh independence study has been conducted to ensure a mesh independent solution; the centreline velocity is evaluated at three grid spacings. The meshes are named M1 M2 and M2 of which correspond to a base cell spacing of 0.125mm, 0.25mm and 0.5mm. The call spacing in the free jet far from the nozzle exit is around 5 times that of the base cell spacing which is employed to drastically reduce the mesh count and to reduce computational cost in regions where there are small changes in the flow gradients. A non-dimensional wall normal cell spacing of 4.5 has been used for all the meshes. This ensures the enhanced wall treatment can be used for the boundary layer treatment. Table 5-2 summarises the characteristic features of the meshes employed within the mesh independence study. Figure 5-3 show the centreline velocity and temperature at the three mesh sizes. It can be seen that decreasing the base cell spacing from 0.25 mm to 0.125 mm bares no change in the solution. However, increasing the base cell spacing from 0.250 mm to 0.500 mm there is a change in the amplitude of the shocks and in the gas velocity within the combustion chamber.

Table 5-2: Summary of mesh features for meshes considered within the mesh independence.

Mesh	Base Mesh Size	y+
M1	0.125 mm	4.5
M2	0.250 mm	4.5
M3	0.500 mm	4.5

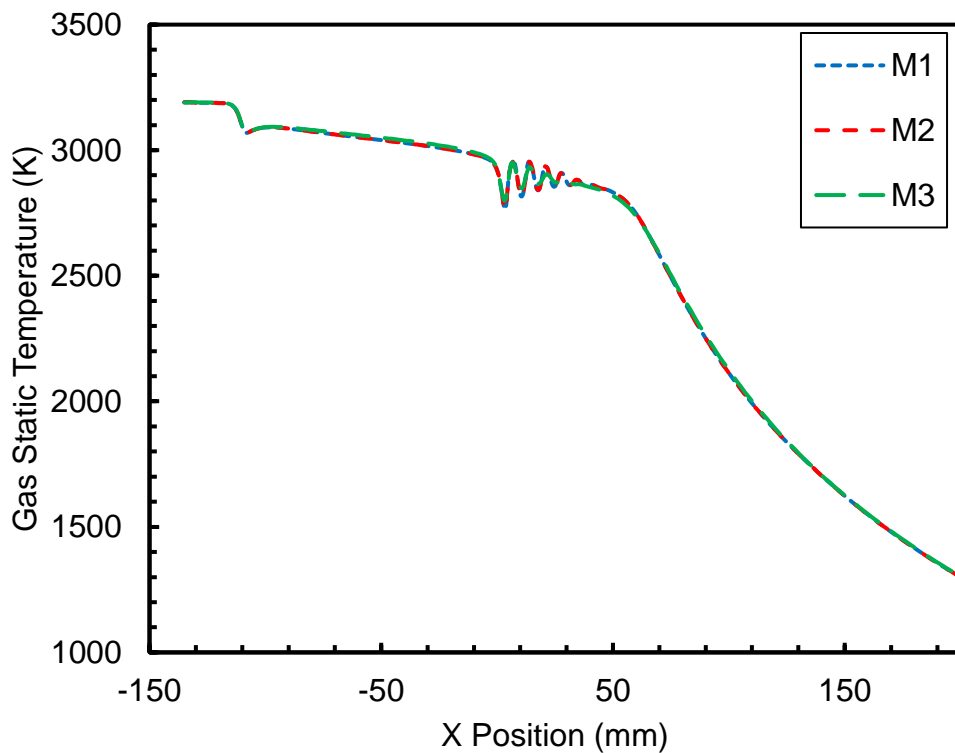
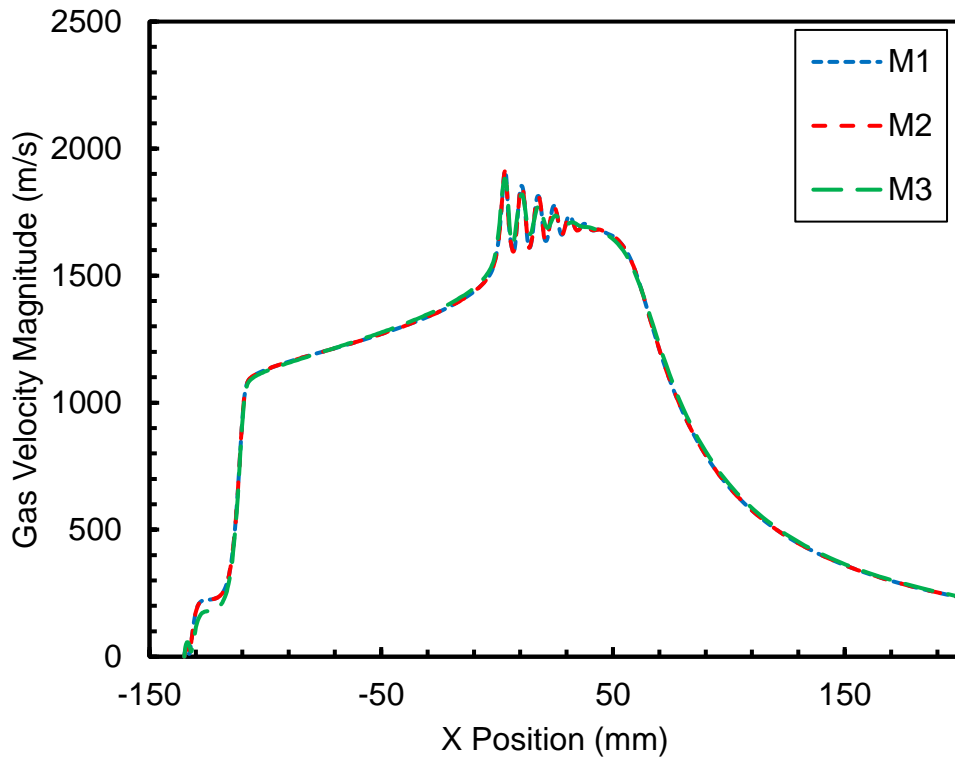


Figure 5-3: Centreline velocity magnitude (Top) and static gas temperature (Bottom) on three different mesh densities (M1, M2 and M3).

Figure 5-4 shows the mesh used with no shroud attachment and a cross-section of the mesh at the nozzle outlet. The domain consisted of a cylinder 400 mm long and a diameter 400 mm wide. The mesh independence study was conducted for the single-phase solution. The mesh resolution in the centre of the fluid domain where the gas jet, shock waves and suspension jet injection are located is much finer than the rest of the fluid domain. Whilst near the outer region of the domain the mesh resolution is much coarser. Sufficient resolution is required in all three special directions to ensure the jet penetration can be accurately modelled; any lack of resolution will affect the jet penetration into the crossflow. To ensure convergence the residuals and monitor points within the domain were evaluated. Convergence was obtained when the residuals fell to below $1e-05$ for the continuity momentum and RANS equations and $1e-06$ for the energy and species equations. The monitor points were used to examine the local velocity and temperature within the domain. When no further change in the solution occurred, the solution was said to be converged.

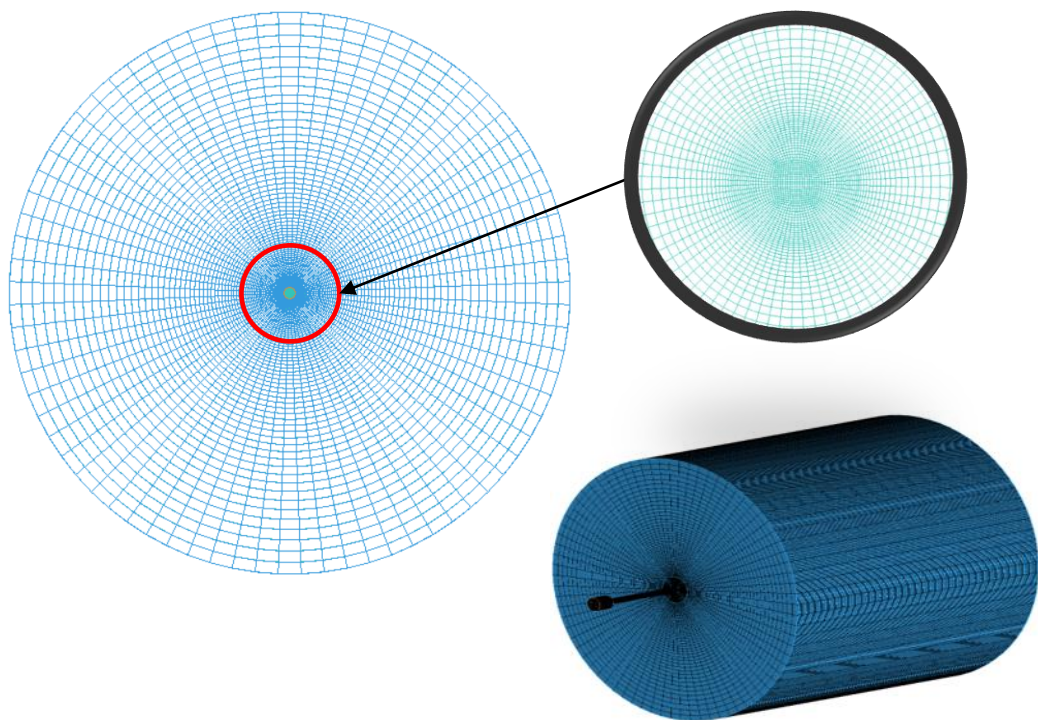
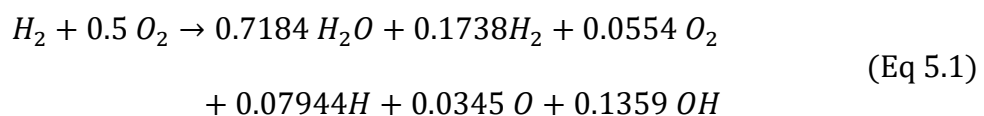


Figure 5-4: Mesh employed for study with no shroud attachment.

5.4 Comparison of Combustion Model

In SHVOF thermal spray the Eddy Dissipation Model (EDM) model with a global single step reaction mechanism is the sole approach employed to model the combustion reaction. There are a number of flaws with this prior modelling approach. The combustion process is governed by a vast number of sub-reactions simplifying these reactions to a single step global reaction will inherently suffer from errors. Typically to determine the global reaction mechanism the composition of products is determined from equilibrium calculations based upon the average temperature and pressure within the combustion chamber. The composition does not account for local variations of temperature and pressure which will affect the species generated from the combustion reaction.

The Eddy dissipation concept (EDC) is an extension to EDM model that can incorporate detailed chemical reaction mechanisms. The EDC model considers the interactions of the combustion chemistry with the effects of turbulent mixing and has been applied to a wide range of applications [155], [156]. The EDM model with a single step reaction mechanism is compared to the Eddy Dissipation Concept (EDC) model with a robust reaction mechanism to evaluate the accuracy of the EDM model with the single step reaction mechanism. The global reaction mechanism employed for the EDM model is given by equation 5.1, the reaction is rounded to 4 decimal places. Figures 5-5 compares the centreline static gas temperature using the EDC model and the EDM model.



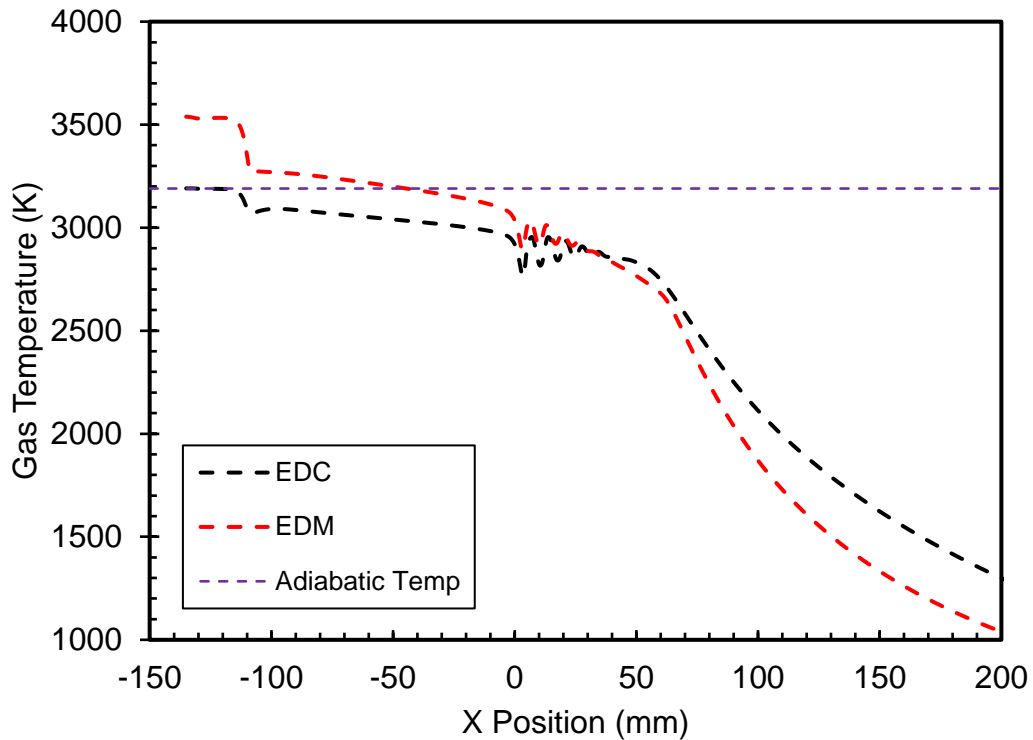


Figure 5-5: Comparison of the centreline static gas temperature using the EDC and EDM combustion model with the adiabatic flame temperature.

From figure 5-5 it can be seen that a combustion chamber temperature of 3550 K is calculated from the EDM model and the single step reaction mechanism. The adiabatic flame temperature within the combustion chamber is calculated as 3200 K from software Gordan and McBride (NASA CEA) [35] at the combustion chamber pressure of 2.6 bar and an equivalence ratio of 1. The EDM model therefore over predicts the combustion chamber temperature in comparison to the adiabatic flame temperature by 350 K. Additionally, it can be seen that a combustion chamber temperature of 3200 K is calculated from the EDC model, this matches the adiabatic flame temperature 3200 K and does not suffer from this over prediction in the gas temperature. It can also be seen that there is a significant difference between the slopes of the temperature curves in the free jet. This is a result of ambient oxygen mixing and further reacting with the gas jet, the detailed reaction mechanism can resolve these reactions in greater

detail than the global reaction mechanism which is solely determined to approximate the reaction within the combustion chamber as reported within Emami et al. [156]. The over prediction in the gas temperature affects many aspects of the flow such as the gas density, the gas velocity, evaporation rates of suspension, particle temperature and the particle velocities. The EDC provides a significant improvement in the calculation of the gas temperature within the combustion chamber as opposed to the EDM model currently employed in literature.

Figures 5-6 compares the centreline species mass fraction calculated from the EDC model and the EDM model for (a) H₂, (b) O₂ and (c) H₂O. It can be seen from figure 5-6 (a) that the EDC model predicts a significantly higher mass fraction of hydrogen and oxygen within the nozzle. The EDM model predicts a hydrogen mass fraction of 13 % while the EDC model predicts a hydrogen mass fraction of 24 % within the entrance of the combustion chamber. From figure 5-6 (a) it can also be seen that there are large regions where the hydrogen mass fraction remains constant with the EDM model as is seen from 100 mm from the nozzle exit (inside of the nozzle) to 40 mm from the nozzle exit (within the free jet). This is not physically plausible as any unreacted hydrogen will react with intermediate species such as O and OH radicals.

It can be seen from figure 5-6 (b) that the EDC model predicts an oxygen mass fraction of 0 % while the EDM model predicts a oxygen mass fraction of 7 % within the combustion chamber entrance. Additionally, it can be seen from figure 5-6 (c) that the EDM model predicts a water mass fraction of 80 % while the EDC model predicts a water mass fraction of 75 % within the combustion chamber. The EDM model predicts higher conversion of hydrogen into the combustion products which results in the over prediction in the combustion chamber temperature when compared to the adiabatic flame temperature. The single step reaction does not account for factors such as the

combustion chamber geometry, the level of turbulence, local pressure and local temperature variations within the combustion chamber. All of which significantly impact the combustion reaction and the species formed from the combustion reaction. Resolving the reaction mechanism for hydrogen combustion using a detailed reaction mechanism allows for a better prediction of the species composition within the combustion chamber which does not result in the over-prediction in the combustion chamber temperature as seen with the global single step reaction mechanism.

The EDC model with the reaction mechanism employed is significantly more computationally expensive than the EDM model with the global mechanism as the reaction mechanism employed requires the calculation of twenty reaction rates as opposed to one reaction rate. The computational cost of determining the reaction rates can be reduced by employing techniques such as chemistry agglomeration and in-situ adaptive tabulation (ISAT) [157]. Chemistry agglomeration lumps cells together with a similar species composition and temperature. The reaction rate for the lumped cells is then determined collectively rather than calculating the reaction rates individually. The ISAT tabulation reduces the computational cost by storing the values for the reaction rates within a lookup table. If the inputs differ by a small value which is set by the solver then the reaction rate is looked up from the ISAT table however if the inputs differ significantly then the reaction rates are recalculated. The gas temperature affects much of the flow characteristics the EDC model has been used within this study due to the superior performance of this model compared to the EDM model despite its higher computational cost.

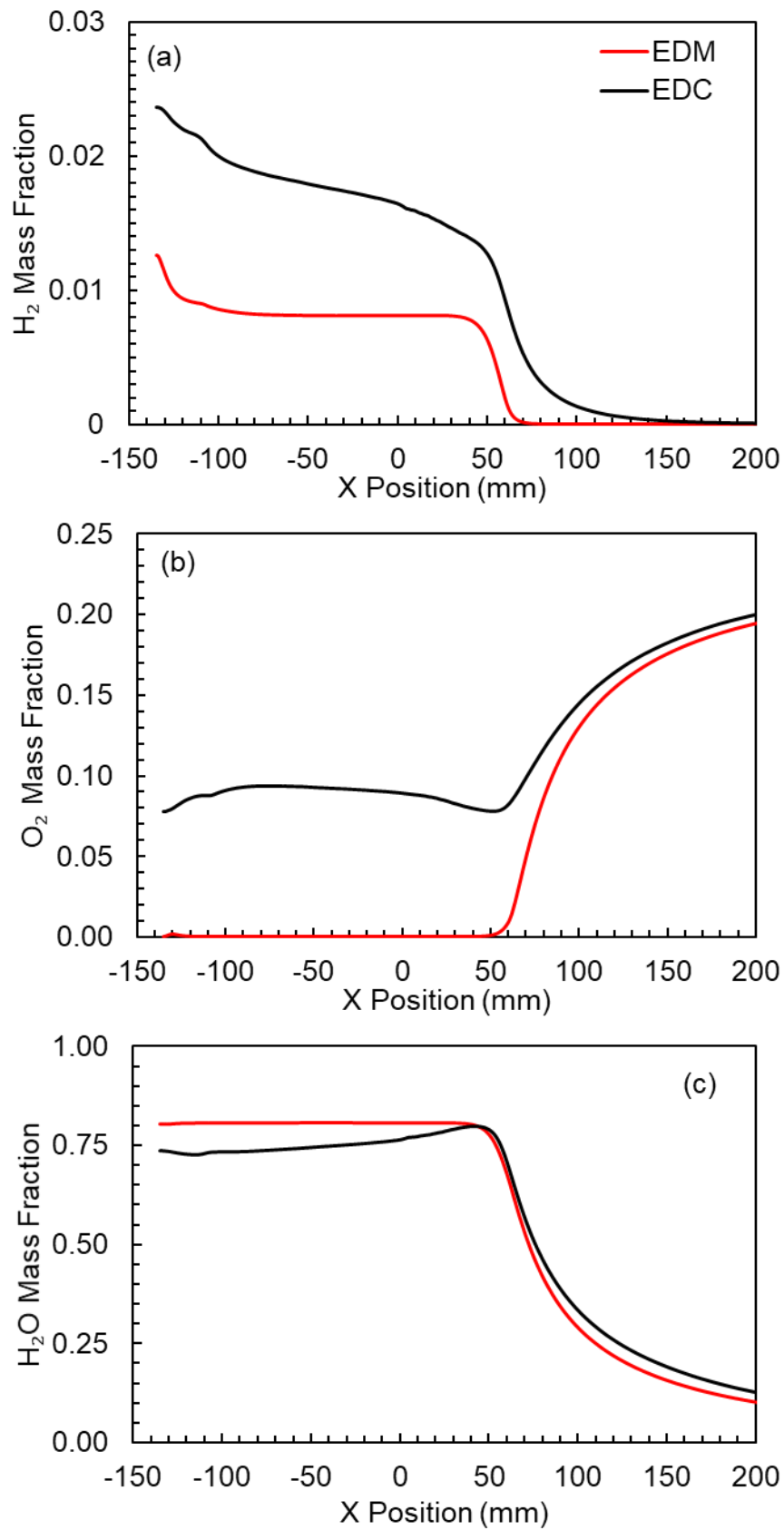


Figure 5-6: Effect of the combustion model on the prediction of the centreline species mass fraction plots for (a) H₂, (b) O₂ and (c) H₂O

5.5 High Speed Imaging of Suspension Injection

Comparisons against experimental measurements provide an invaluable tool to evaluate the accuracy of the numerical model. High speed imaging has been used in a wide range of applications to allow for a comparison of numerical models with experimental observations. For example radial injection of suspension is very common in suspension plasma spray (SPS); shadowgraphy is often used in SPS to validate the numerical models [75] & [158]. Shadowgraphy is a flow visualisation technique that allows for the identification of the characteristic features of the flow in a fluid medium with a varying density [159]. The fluid density is a function of the refractive index and a shadow is formed because the light rays are refracted. The position on where the undeflected ray would arrive now remains dark and where the deflected ray arrives appears brighter than the surrounding environment [159].

The Phantom V12 (Ametek, Pennsylvania, USA) high-speed CCD camera with the sigma 70 – 300 mm F4-5.6 lens was used to capture images of the suspension injection within this investigation. The image resolution with this setup is 10 px/mm and an exposure time of 1 ms was used [16]. The camera was placed in view of the suspension injection 0.45 m in front of the spray gun, and the lighting system is used to provide back illumination. The lighting was placed 0.6 m behind the glass panel and was angled such that the lighting provided maximum contrast to the suspension injection. A panel of glass was placed in front of the camera to protect the camera from damage. A white background was placed 0.3 m behind the thermal spray system to allow for a contrast between the liquid jet and the background as shown in figure 5-7.

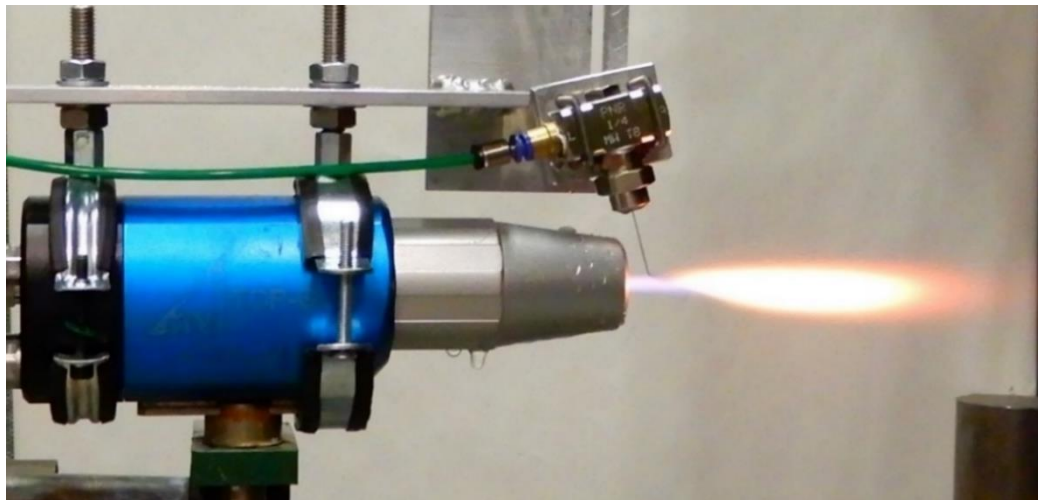
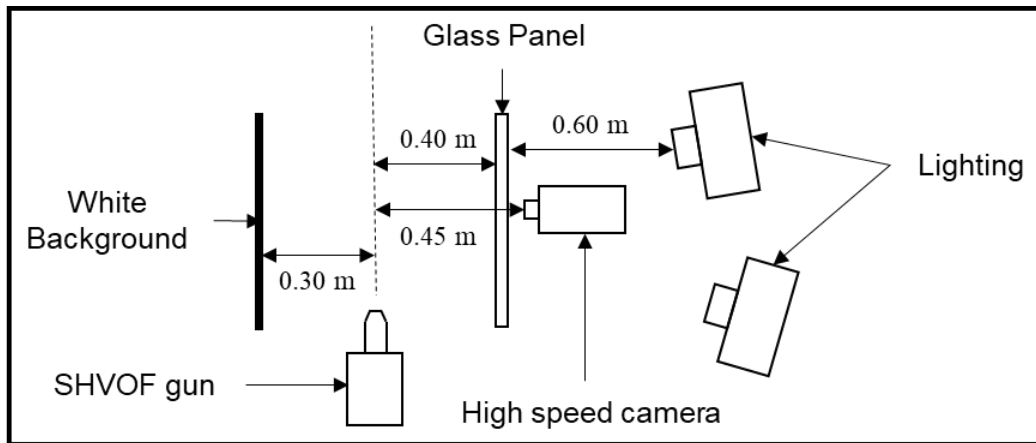


Figure 5-7: Schematic of experimental set up of high-speed camera and lighting system to image the radial injection of suspension.

A flame of 75 kW was obtained as this flame power allowed for a supersonic flame which is the characteristic feature of SHVOF thermal spray [26]. A higher flame power was avoided as very high gas velocities would prevent any suspension from penetrating the gas jet at all. A liquid jet of suspension made up of suspension 14 weight percent Al_2O_3 and water was then injected radially into the flame at a distance of 10 mm downstream from the nozzle exit and 22 mm above the centreline. The downstream distance is based on optimisation studies using high speed imaging conducted by Venturi et al. [16] The distance above the centreline does not affect the flow dynamics of the suspension injection. The mass flow rate was monitored via a flow rate meter to ensure the desired flow rate of 50 ml/min, 100 ml/min, 150 ml/min,

200 ml/min, 250 ml/min and 300 ml/min. The suspension was injected using a commercial XMW 4001 T8 1/4" air atomising nozzle (PNR, UK) used without the air, the injector design is shown in figure 5-8. This corresponds to pure liquid injector with an internal duct diameter of 0.45 mm. The custom atomizer holder attachment allowed for the choice of the injection angle as well as the axial and radial location of the atomizer [16]. The suspension feed rate was controlled by varying the air pressure in the feedstock chamber and measured using an ES-Flow low-flow ultrasonic flowmeter (Bronkhorst Ltd., UK).

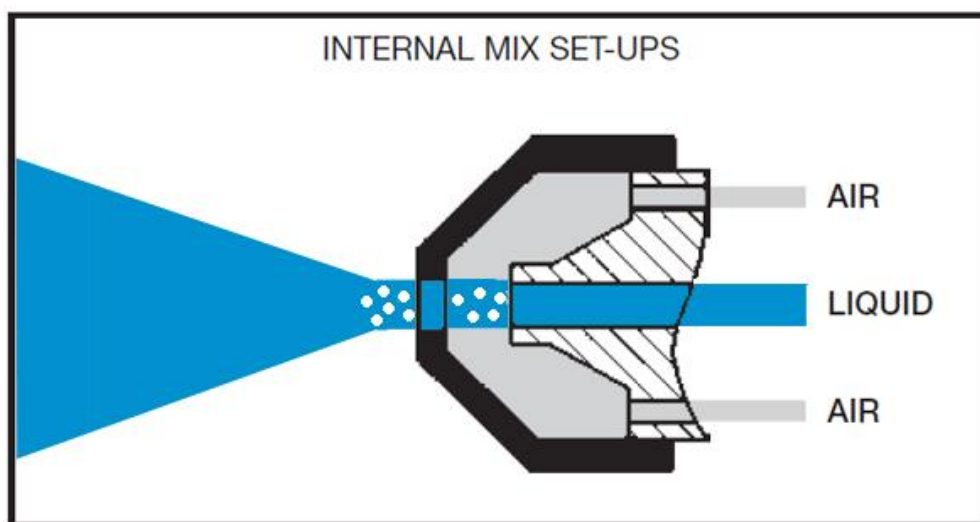


Figure 5-8: Design of injector used for a radial injection of suspension into the HVOF jet [160].

A background image was taken without any injection of suspension to allow the removal of the background from the images. Once the suspension injection flow rate matched the desired flow rate a series of pictures were taken at a frame rate $\sim 5 \times 10^2$ per second and the images were processed using "Image J" (NIH, Maryland, USA) to remove the background. The raw images are converted to a binary image by applying a threshold value of 22% within ImageJ [158]. The distance of the breakup from the jet axis and the windward trajectory was extracted from the images.

5.6 Comparison of Numerical Model to High Speed Imaging

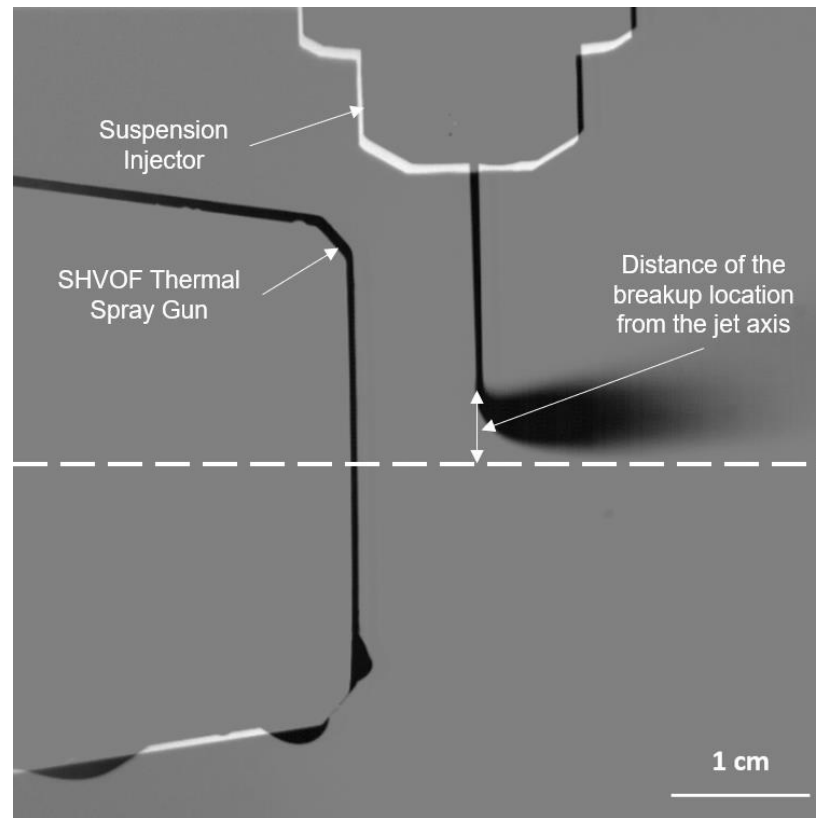


Figure 5-9: Image of a radial injection of suspension into the flame with the distance of penetration and breakup from the jet axis outlined.

The location of breakup and the windward trajectory for the suspension into the flame is examined experimentally using high speed imaging, the location of the breakup is illustrated in figure 5-9. The breakup location and the windward trajectory are obtained from the high-speed images taken of the suspension injection into the HVOF crossflow at flow rates varying from 50 ml/min – 300 ml/min. The location of the breakup and the windward trajectories obtained are compared to the numerical model to evaluate the accuracy of the numerical model employed. Figure 5-10 (a), (b), (c), (d), (e) and (f) show the processed high speed images taken for a radial injection of suspension at a volume flow rate of 50, 100, 150, 200, 250 and 300 ml/min respectively.

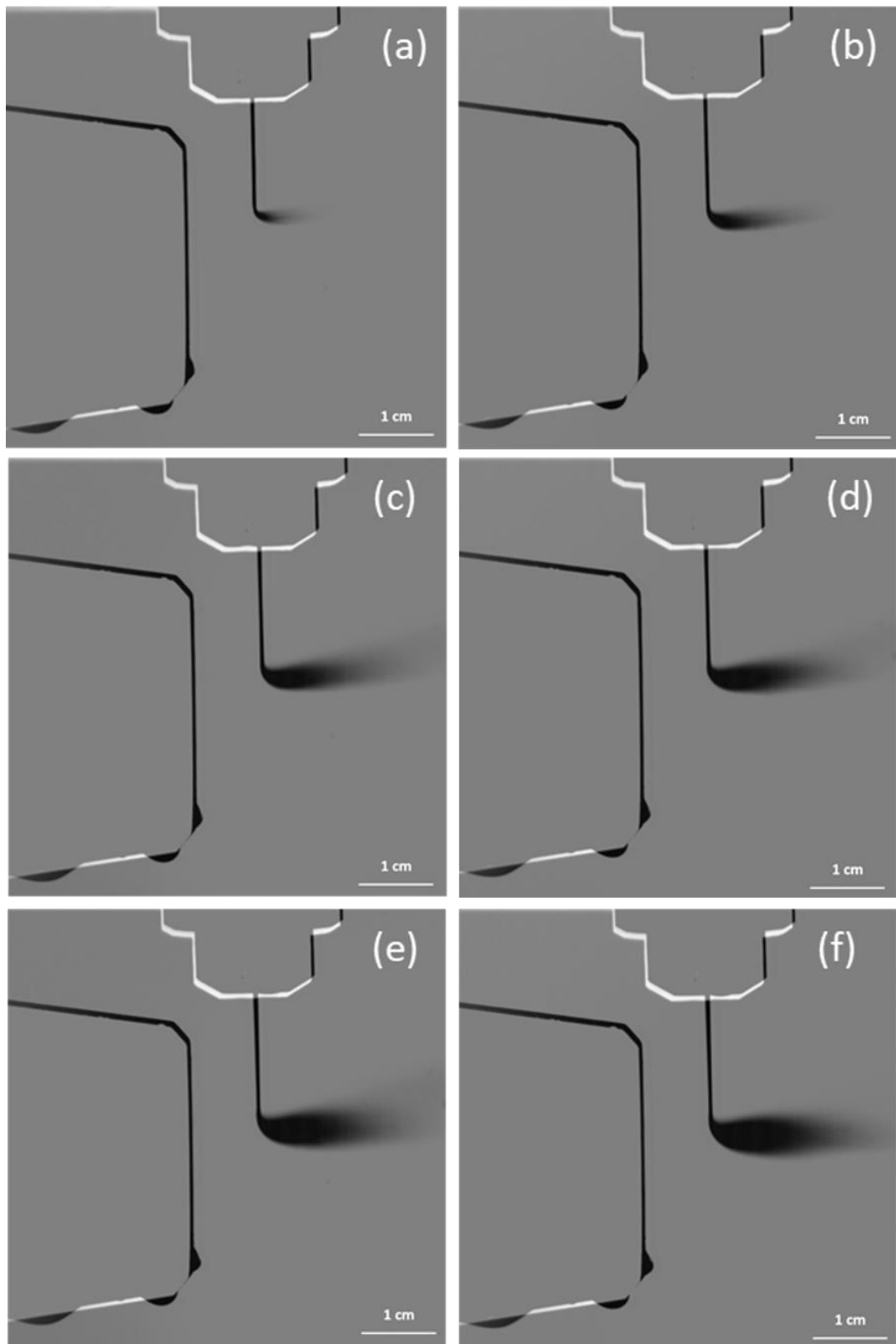


Figure 5-10: Image of radial injection of an Al_2O_3 and water suspension into a 75 kW flame with varying liquid injection flow rates of (a) 50 ml/min, (b) 100 ml/min, (c) 150 ml/min, (d) 200 ml/min, (e) 250 ml/min and (f) 300 ml/min.

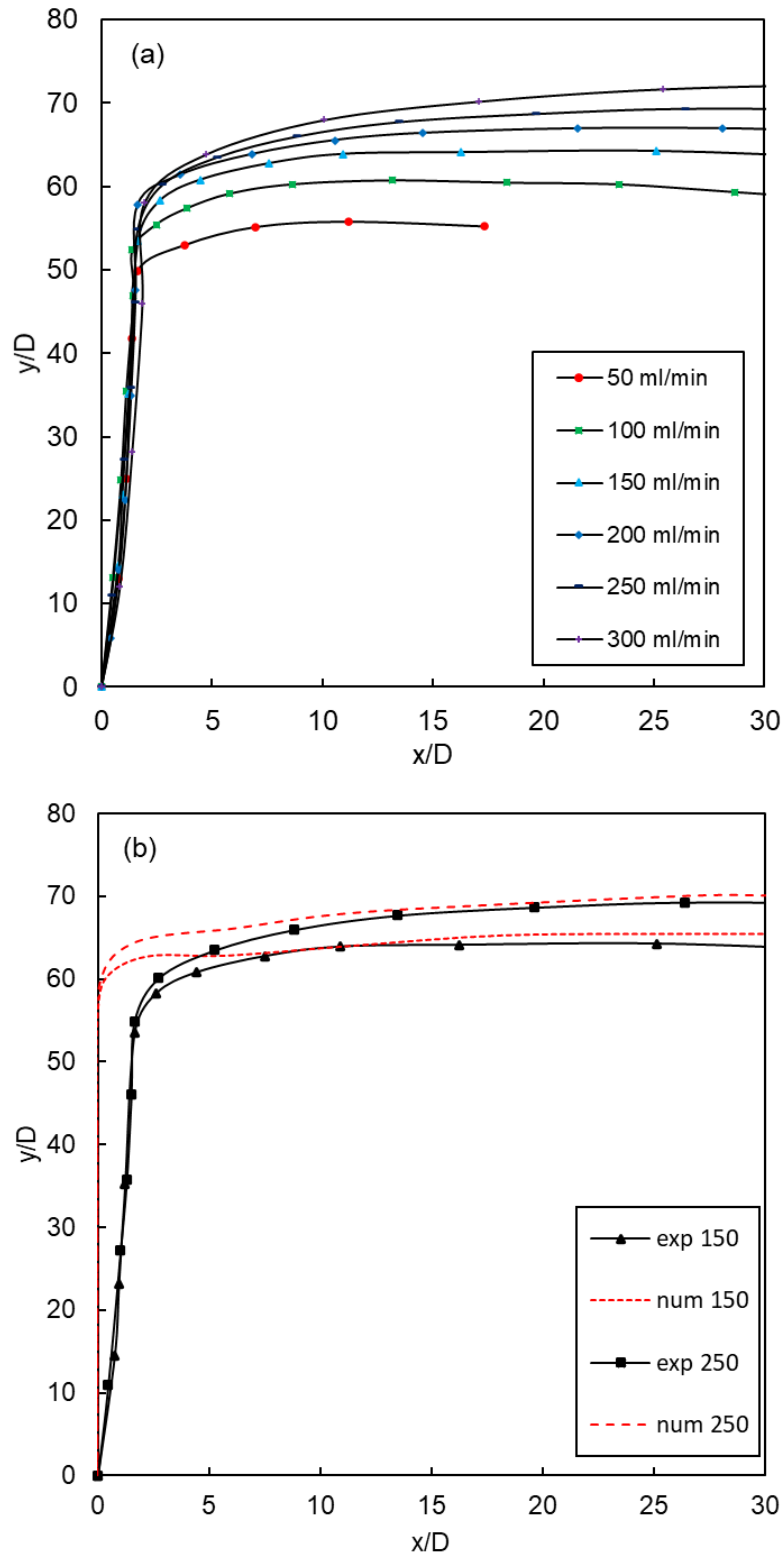


Figure 5-11: (a) Experimental values of the windward trajectories for suspension flow rates of 50 – 300 ml/min, (b) Comparison of experimentally obtained values of the windward trajectories to CFD for flow rates of 150 ml/min and 250 ml/min.

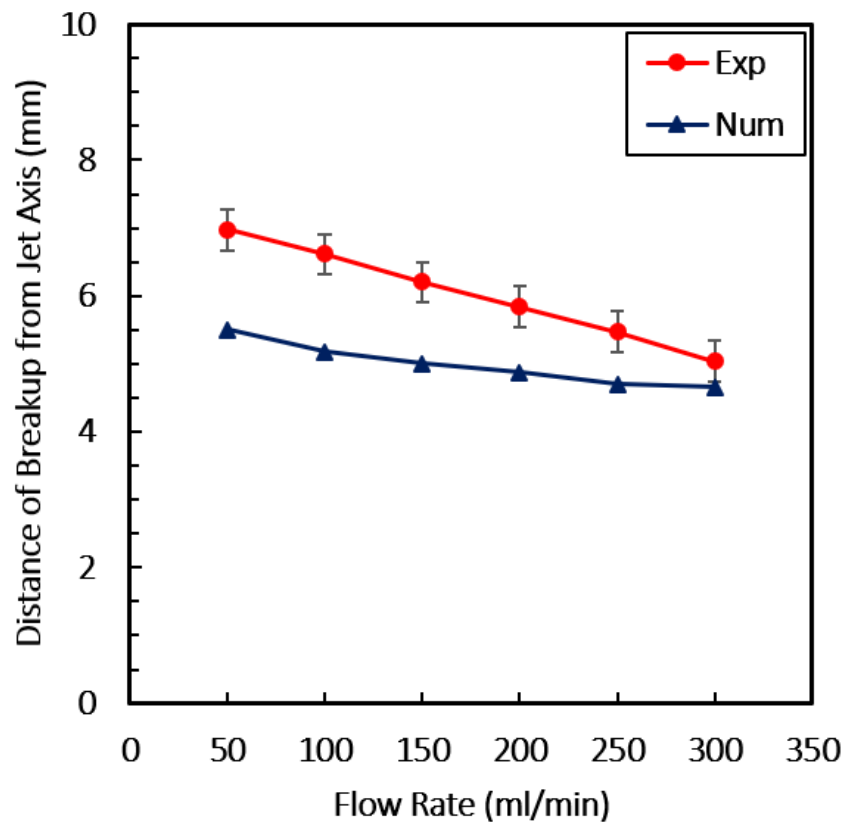


Figure 5-12: Comparison of experimental values of the jet breakup distance from the centreline to the numerically obtained values from CFD.

To validate the model, numerical values of the location of the breakup of the jet from the centreline and the windward jet trajectory are compared with experimental measurements. The windward trajectories are measured from the windward edge of the injector orifice. Figures 5-11 (a) plots the jet windward trajectories at suspension flow rates of 50 ml/min – 300 ml/min; it can be seen as suspension flow rate increases the jet penetrates further in to the HVOF flame. Figures 5-11 (b) compare the jet trajectories predictions from the numerical model against that of experimental measurements at 150 ml/min and 250 ml/min. It can be seen that the jet trajectory prediction matches very well to the experimental measurements within the plume region of the flow. Figures 5-12 compare the prediction of the location of the breakup of the suspension jet from the numerical model to the experimental measurements at

varying flow rates. Figure 5-12 shows an improved agreement between the numerical model and the experimental observed value of the location of the breakup as the suspension flow rate increases. As the suspension flow rate increases the difference between experimental measurement and numerical values becomes smaller. At a flow rate of 50 ml/min there is a difference in the distance of the jet breakup from the centreline of 1 mm and at 300 ml/min there is a discrepancy of 0.2 mm between the numerical and experimental measurement. Which corresponds to a percentage difference of 17.4 % and 4 % at 50 ml/min and 300 ml/min respectively.

The “blob” method has been employed to model the injection of suspension into the HVOF crossflow. It simplifies the jet to an injection of discrete droplets with a diameter equivalent to the injector diameter. The suspension undergoes secondary breakup, evaporation, heating and acceleration due to the HVOF crossflow. The model provides good agreement with experimental measurements for the windward trajectory and the breakup location from the centreline. The windward trajectory predictions match the experimental measurements in the plume region. The difference between the location of the breakup predicted numerically and obtained through experimental measurements can differ by as low as 4% with the model employed. Improvements over this modelling approach can be obtained by resolving the primary breakup of the liquid jet. For this interface resolving methods such as the volume of fluid (VOF) [161], [162] or a level-set (LS) [163], [164] approach is required. These methods are significantly more computationally expensive as a mesh of an order finer than the breakup structures is required and suitable time steps to ensure model stability are required.

5.7 Investigation into the Effect of Suspension Flow Rate

The particles must penetrate into the centre of the jet to ensure the particles are sufficiently heated and accelerated upon impacting the substrate. The suspension flow rate must carefully be considered to ensure the suspension can penetrate into the crossflow. Figures 5-13 show a centre plane contour of the gas velocity with varying suspension volume flow rate from 50 ml/min to 300 ml/min. Figures 5-14 show the centreline gas velocity magnitude as the suspension flow rate is varied from 50 ml/min to 300 ml/min. It can be seen that as the suspension flow rate increases up to 100 ml/min the centreline gas velocity is near identical to the gas velocity without any suspension injection. This suggests that up to 100 ml/min there is little penetration of the suspension into the crossflow as there is little momentum transferred from the gas flow. With further increases in the suspension flow rate above 100 ml/min, the centreline velocity of the gas jet reduces significantly. This suggests there is greater penetration of suspension into the crossflow at higher flow rates and therefore greater transfer of momentum which reduces the gas velocity.

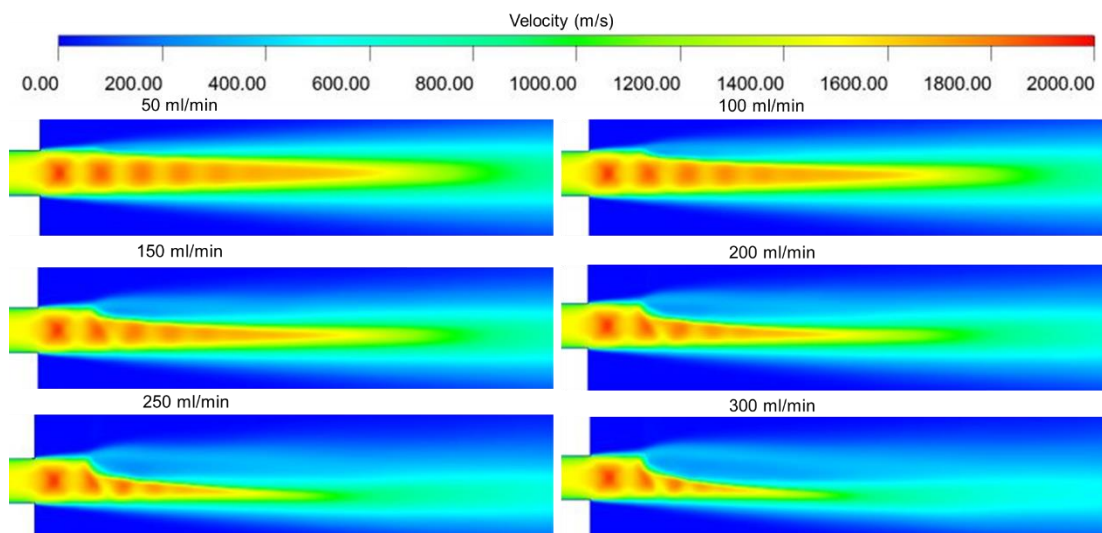


Figure 5-13: Centre plane contour of the gas velocity magnitude with varying suspension flow rates of 50, 100, 150, 200, 250 and 300 ml/min.

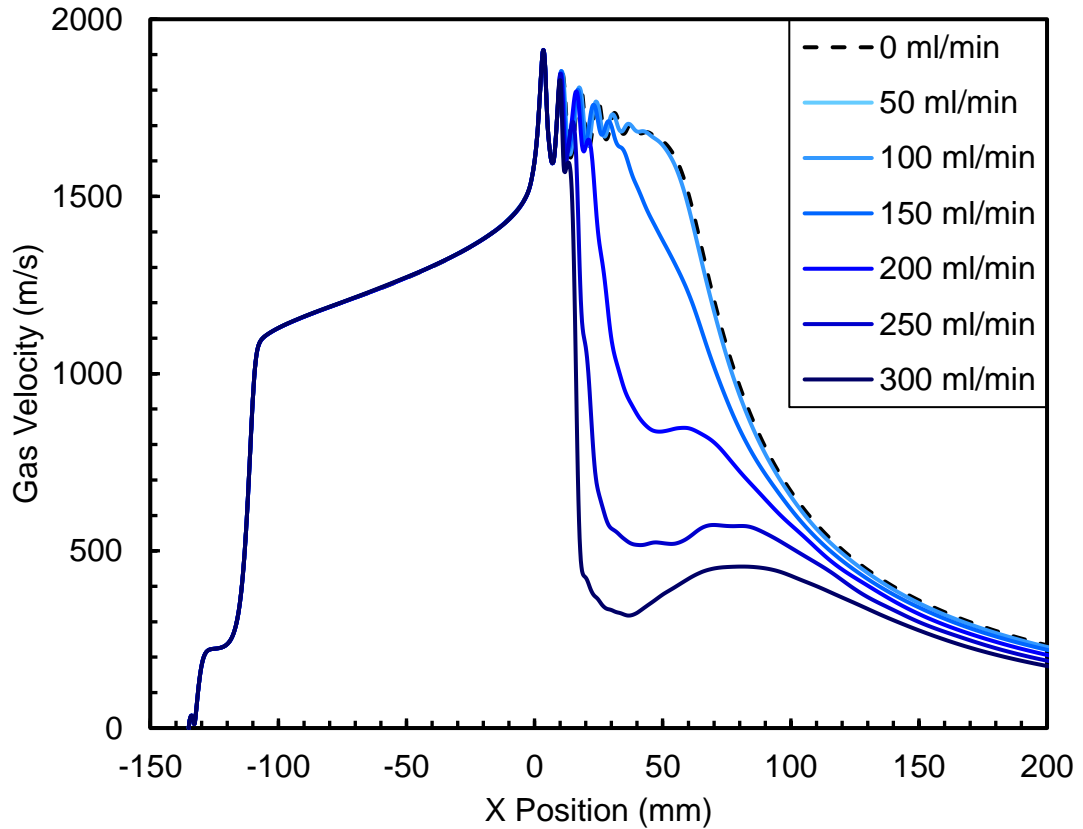


Figure 5-14: CFD prediction of the centre line plots of the gas velocity magnitude with varying suspension flow rate.

When injecting suspension into a HVOF crossflow the suspension is introducing a significant quantity of water into the flame. This liquid that is injected into the flame will significantly cool the HVOF jet. The effect of the suspension flow rate on the gas temperature therefore must be considered. Figures 5-15 show a centre plane contour of the gas temperature with the suspension flow rate varying from 50 ml/min to 300 ml/min. Figures 5-16 show the centreline static gas temperature as the suspension flow rate is varied from 50 ml/min to 300 ml/min. Figures 5-16 show that low suspension flow rates up to 100 ml/min have little effect of the suspension injection on the static gas temperature. As the suspension flow rate increases the temperature decrease in the free jet region reduces significantly. A maximum temperature decrease of approximately 1800 K occurs at a flow rate of 300 ml/min.

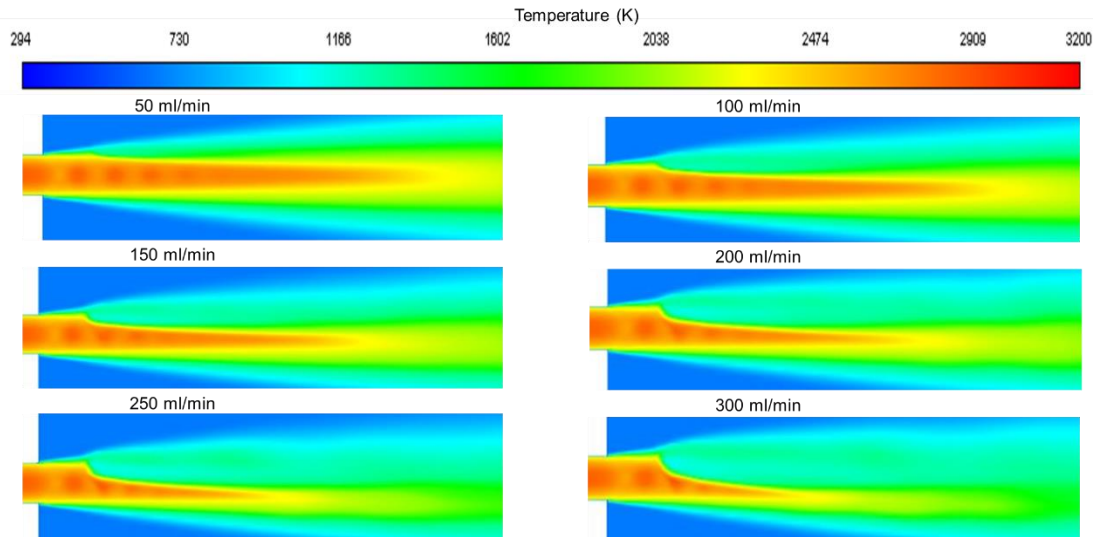


Figure 5-15: Centre plane contour of the static gas temperature with varying suspension flow rate from 50, 100, 150, 200, 250 and 300 ml/min.

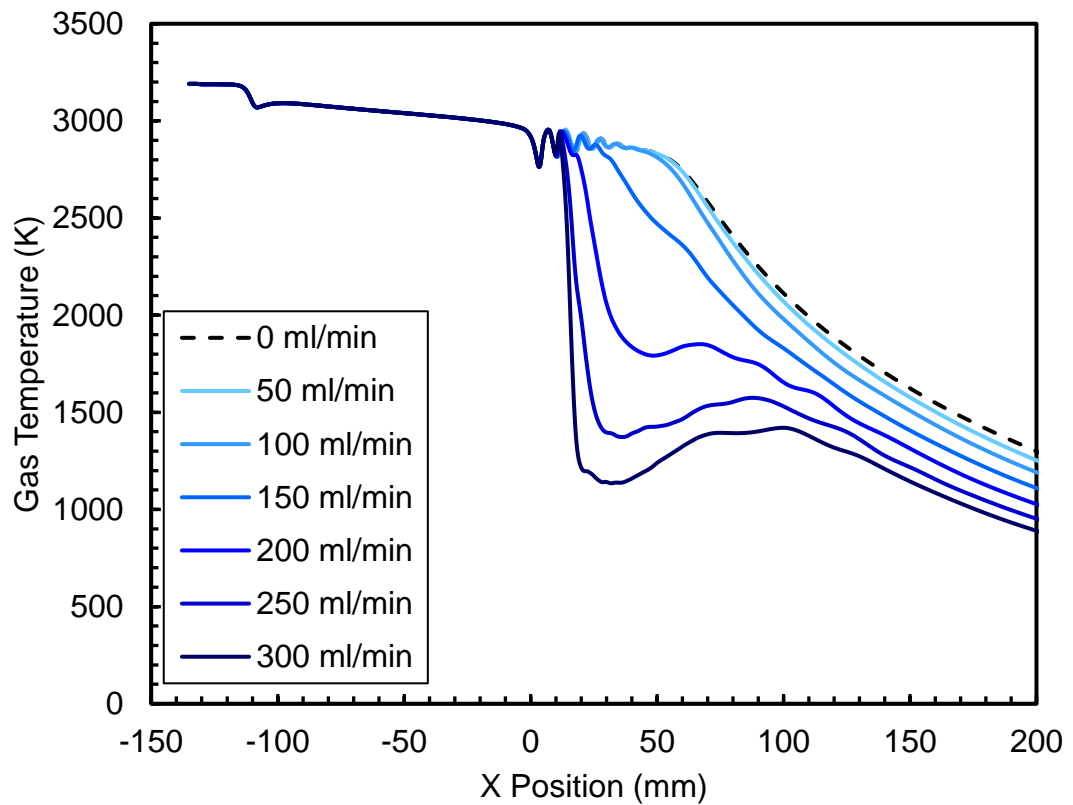


Figure 5-16: CFD prediction of the centre line plots of the static gas temperature with varying suspension flow rate.

There are two shock wave structures that form in the free jet with a radial injection of suspension into a HVOF crossflow; the oblique shock that forms from the expansion of gas at the nozzle exit and the bow shock that forms from the interaction between the liquid jet injection and the supersonic crossflow [165]. A bow shock occurs upstream of the front of a blunt object when the upstream flow velocity exceeds Mach 1 [166]. Figures 5-17 shows a centre plane contour of the Mach number at varying suspension flow rates from 50 ml/min to 300 ml/min. From figure 5-17 it can be seen that a bow shock forms in the location of the penetration of the suspension jet within the supersonic region of the flow. At low suspension flow rates, the effect of the suspension injection is small due to the low penetration of the suspension jet into the suspension crossflow. As the suspension flow rate increases the suspension is able to penetrate deeper into the crossflow. The bow shock trails the suspension injection in the windward direction. A black and white colour scale has been used as it provided more suitable contrast that clearly defined the shock wave structures within the flow.

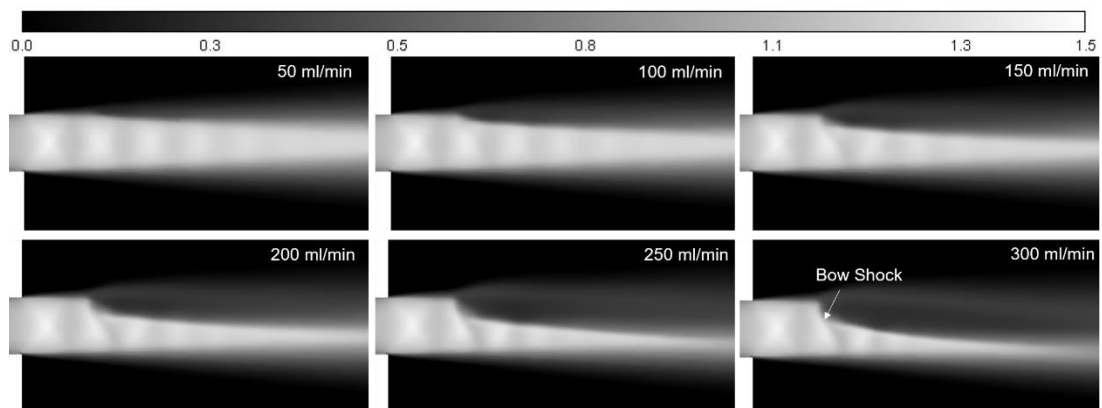


Figure 5-17: Plots of the Mach number with varying suspension flow rate from 50 - 300 ml/min displaying a bow shock preceding the suspension injection.

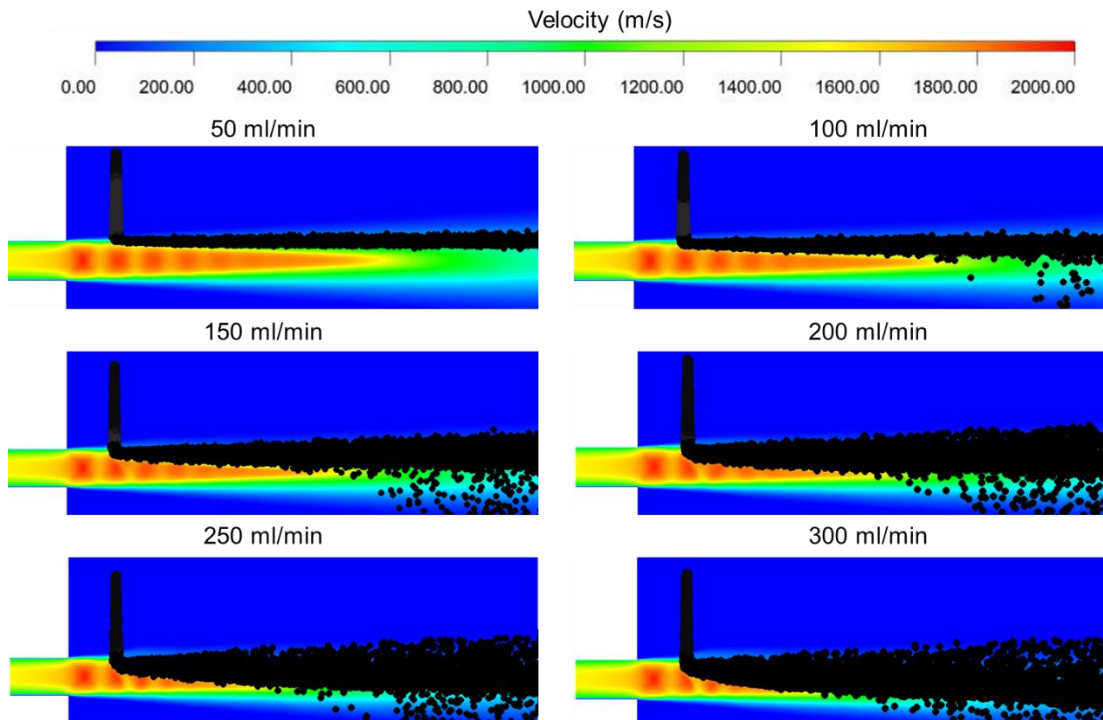


Figure 5-18: Suspension injection within the gas jet for varying suspension flow rate of 50, 100, 150, 200, 250 and 300 ml/min.

Ensuring the suspension effectively penetrates the HVOF crossflow is essential to ensure effective heat and mass transfer to the suspension. This ensures particles impact the substrate with an adequate velocity and temperature to well adhere to the substrate. Figure 5-18 shows the injection of suspension into the flame and the particle locations within the gas jet for varying suspension flow rate of 50 ml/min to 300 ml/min. It can be seen that as the suspension flow rate increases the droplets penetrate further into the gas stream. It is reported in literature that for a liquid jet in a crossflow; penetration of the liquid jet into the gas jet requires the dynamic pressure of the liquid jet to exceed that of the gas jet as indicated by equation 5.2 [167]. The higher velocity (flow rate) of the suspension results in greater penetration into the crossflow.

$$\rho_l u_l^2 > \rho_g u_g^2 \quad (\text{Eq 5.2})$$

Figures 5-19 show the suspension particle velocities at a downstream distance of 85 mm from the nozzle exit at varying suspension flow rates from 50 ml/min to 300 ml/min. The particle velocity scatter plots are capped at 800 m/s for all results as very few particles reach this velocity and only for certain suspension injection conditions. The inflight particle conditions were evaluated at a plane 85 mm downstream of the nozzle exit as this is the typical standoff distance for axially injected suspension. Nanoparticles have low mass and thermal inertia due to their size. The gas velocities and temperatures drop off significantly beyond 85 mm hence particles decelerate and cool rapidly in this region.

It can be seen, as the suspension flow rate is increased to 200 ml/min, there is an increase in the maximum particle velocity. As the suspension flow rate is increased from 50 ml/min to 200 ml/min the maximum particle velocity increases from 450 m/s to 950 m/s. When the suspension flow rate increases from 50 ml/min to 200 ml/min the higher penetration of the suspension results in a higher maximum particle velocity. However, when the suspension flow rate is increased further from 200 ml/min to 300 ml/min the maximum velocity of the particles then begins to decrease from 950 m/s to 500 m/s. As the suspension flow rate increases further the significant reduction in the gas velocity results in the lower maximum particle velocity. A greater quantity of suspension is injected into the gas jet and the suspension is removing a great deal of the momentum from the gas jet. Hence, the optimum flow rate to maximise particle velocities at the standoff distance of 85 mm from the gas nozzle exit lies within the region of 150 – 200 ml/min. It can be seen that the plots within figure 5-19 have a lack of symmetry. This may be improved by increasing the number of DPM particle injections however this will drastically increase the computational cost of the numerical model as a result.

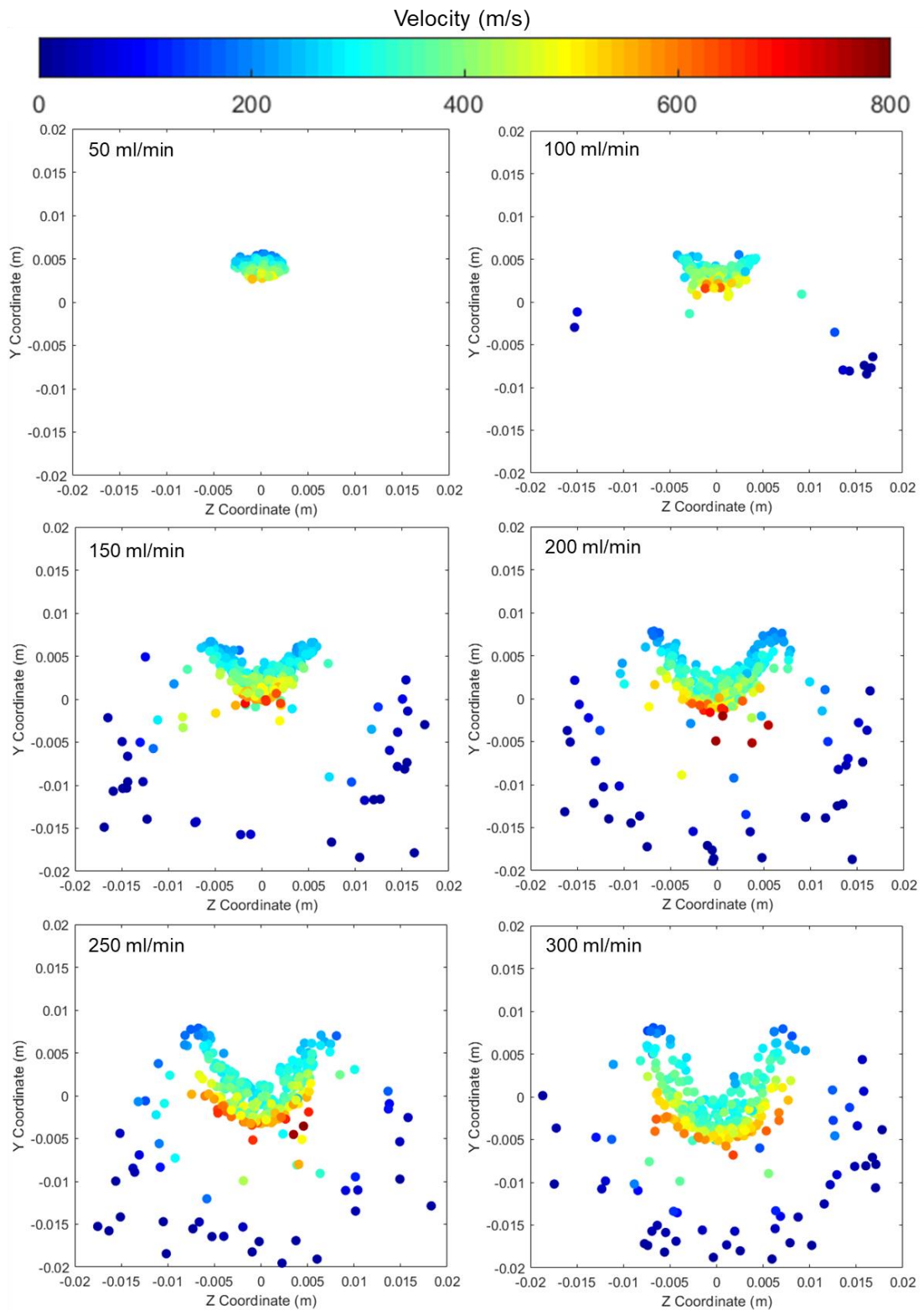


Figure 5-19: Suspension particle velocities at standoff distance of 85 mm; varying suspension flow rate of 50, 100, 150, 200, 250 and 300 ml/min.

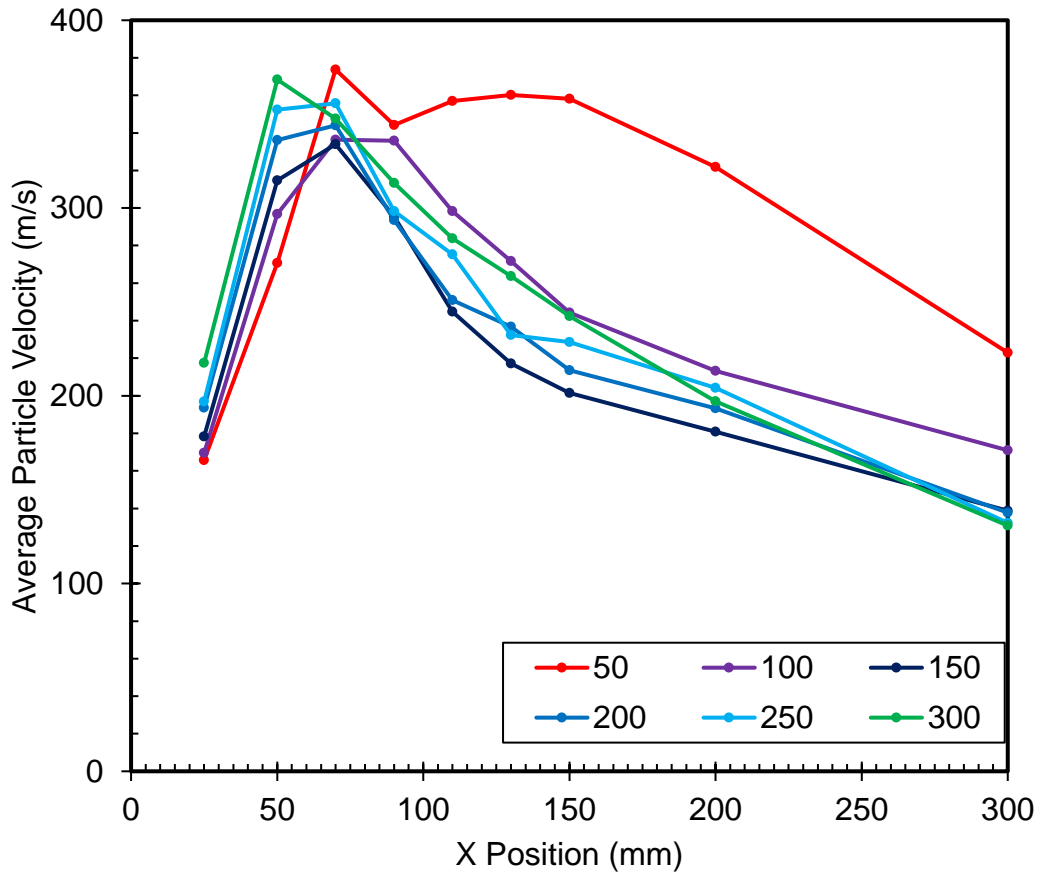


Figure 5-20: Average inflight particle velocities at the suspension flow rates of 50, 100, 150, 200, 250 and 300 ml/min.

Figure 5-20 shows the average inflight particle velocity for the suspension flow rates investigated. It can be seen that as the suspension flow rate increases the average velocity of the particles increases up to 50 mm downstream from the nozzle exit. A high suspension flow rate allows for greater penetration which enhances heat transfer to the suspension. Moisture can evaporate more effectively from the suspension which reduces the suspension droplets mass. The lighter suspension droplets can be accelerated to higher velocities as they occupy higher velocity regions of the jet. Further downstream the particle velocities are a function of the penetration of the jet, the mass of the suspension particles and the gas velocity. As the particles decelerate the rate of deceleration is dependent on the mass of the particles. At lower suspension

flow rates, the particles have a higher mass, the particles decelerate at a lower rate due to the higher moisture content. Additionally, heavy particles are less susceptible to turbulent fluctuations, the heavier particles do not stray out of the gas jet to any great degree. The particles continue to accelerate whilst at higher suspension flow rates particles decelerate as they travel out of the gas jet. Finally, at high suspension flow rates the gas velocity is lower due to the greater momentum transfer to the particles at high suspension flow rates. These three effects combined determine the particle velocity far from the injection location.

Figures 5-21 show the suspension particle temperatures at standoff distance of 85 mm for a varying suspension flow rate of 50 ml/min to 300 ml/min. It can be seen that as the suspension flow rate is increased from 50 ml/min to 300 ml/min a greater proportion of particles are heated. It can also be seen that as the suspension flow rate increases from 50 ml/min to 150 ml/min the maximum particle temperature increases from 400 K to 2000 K. As the suspension flow rate increases above 150 ml/min the maximum temperature the particles reach reduces significantly. As the suspension flow rate increases from 150 ml/min to 300 ml/min the maximum particle temperature decreases from 2000 K to 1450 K. With the increase in the suspension flow rate particles are able to penetrate deeper into the gas jet. This allows for greater heat transfer to the particles and hence the maximum particle temperature increases up to a flow rate of 150 ml/min. However, as the suspension flow rate increases further the addition of more suspension into the gas removes greater quantities of heat from the gas jet which results in the lower temperatures of the gas jet. This can be seen with the increase of the suspension flow rate from 150 ml/min to 300 ml/min. The melting temperature of Al_2O_3 is 2072 K [168] therefore excessively high suspension flow rates prevent particles from being heated sufficiently to become near molten.

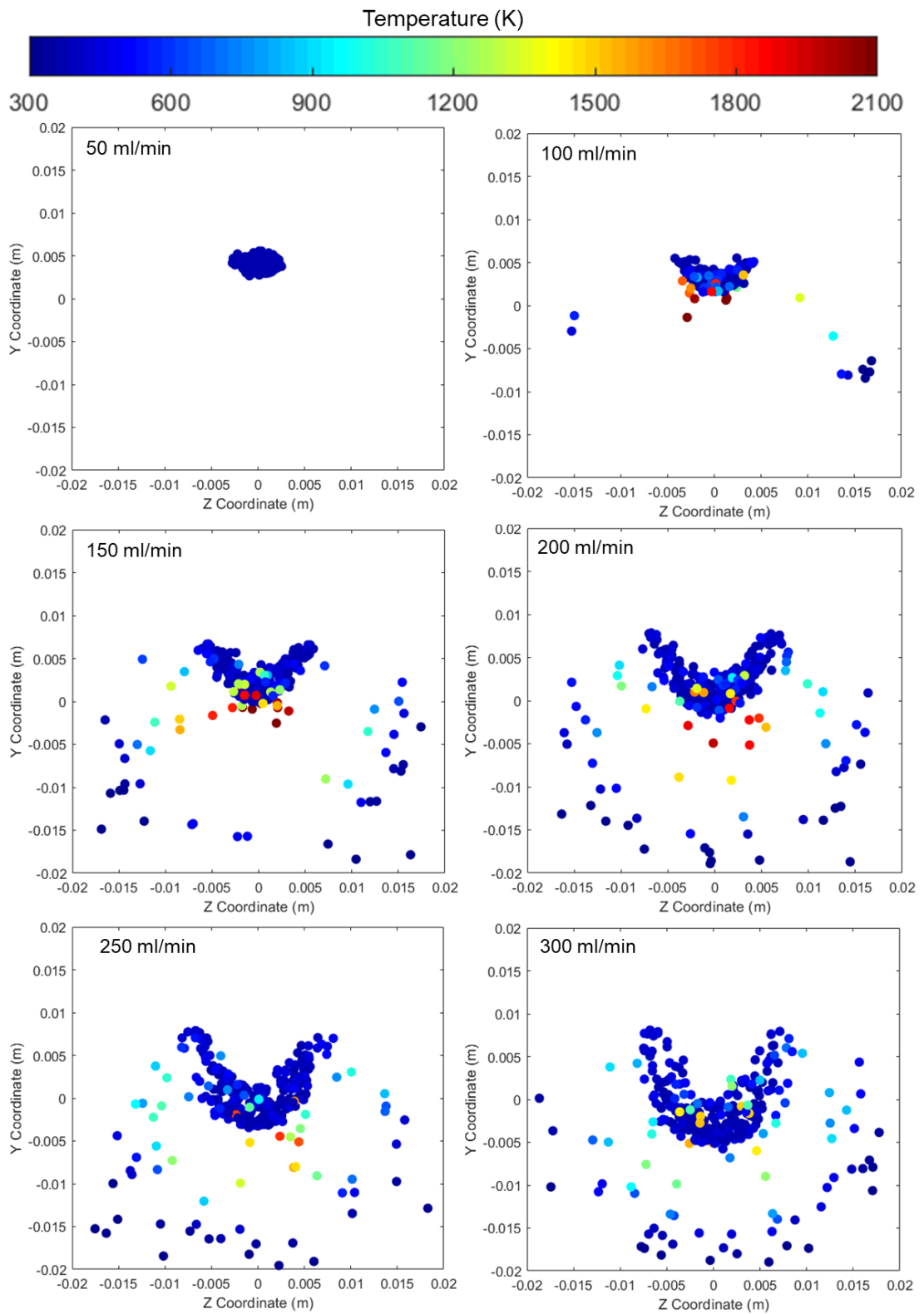


Figure 5-21: Particle temperatures at standoff distance of 85 mm for a varying suspension flow rate of 50, 100, 150, 200, 250 and 300 ml/min.

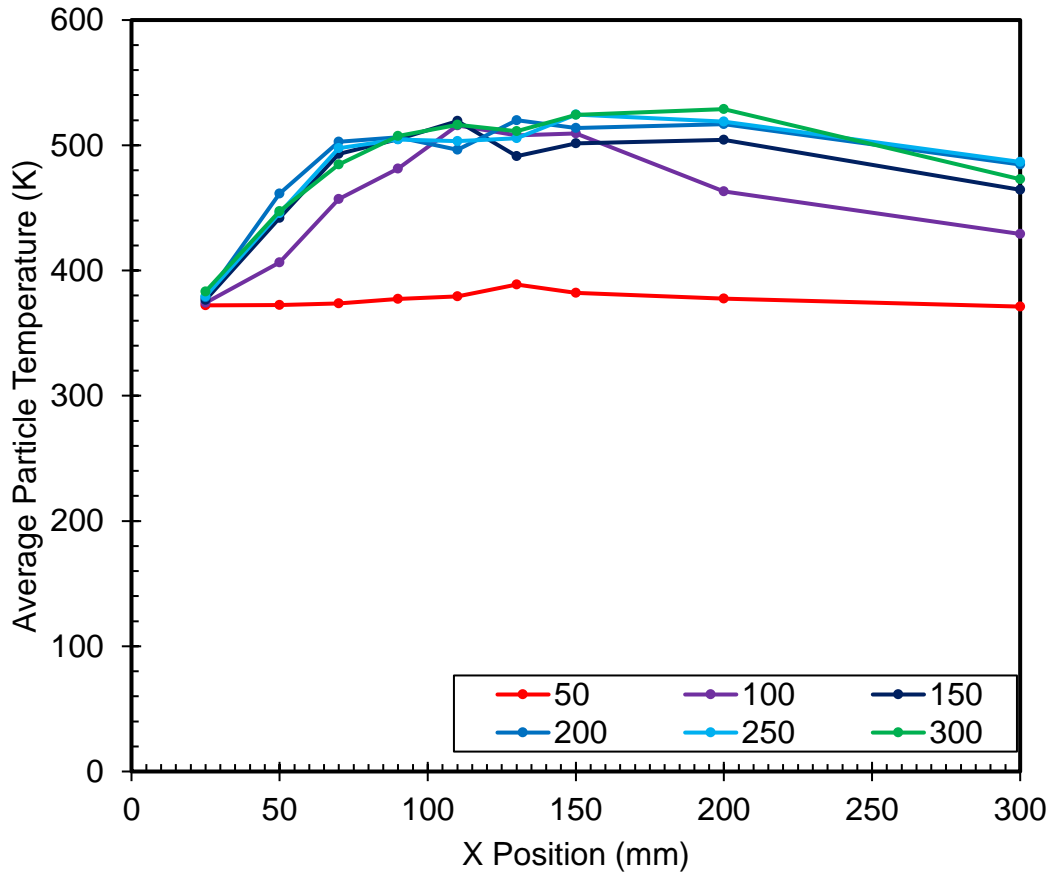


Figure 5-22: Average inflight particle temperature at for the suspension flow rates of 50, 100, 150, 200, 250 and 300 ml/min.

Figure 5-22 shows the average inflight particle temperature at varying suspension volume flow rates from 50 ml/min, to 300 ml/min. In general, it can be seen that increasing the suspension flow rate from 50 ml/min to 300 ml/min results in a higher average particle temperature further downstream from the nozzle exit around the region of 150 mm, with the highest average particle temperature occurring at 300 ml/min and the lowest occurring at 50 ml/min. As the suspension flow rate increases more particles are able to reach closer to the centreline and undergo more effective heating this results in an increase in the average particle temperature.

It can be seen that as the suspension flow rate increases the particles become more scattered. Improved heat transfer at higher suspension flow rates results in lighter

particles due to greater evaporation of the liquid component within the suspension. Lighter particles move out of the gas jet easily due to the turbulent nature of the flow. As the particles move out of the jet they cool and decelerate rapidly due to their low thermal and mass inertia. Ensuring these particles do not stray out of the flow can significantly improve in-flight particle characteristics.

A major challenge in radial injection SHVOF thermal spray is ensuring that the suspension can sufficiently penetrate the gas jet. It is concluded that a high injection velocity is required to allow for a greater penetration of suspension. A high penetration of the suspension is required to maximise heat and momentum transfer to the particles. The injection velocity can be increased by increasing the suspension flow rate. This, however, results in greater removal of heat and momentum from the flame due to the increase in the quantity of suspension injected into the flame and hence excessively increasing the suspension flow rate reduces the maximum velocity and temperature the particles are able to obtain. Operating at low suspension flow rates does not significantly impact the gas velocity or the gas temperature. However, the low suspension penetration at low flow rates results in low particle velocities and temperatures. As the flow rate decreases the jet penetration decreases which allows for fewer particles to be heated and accelerated as the proportion of particles that reach the centre of the gas jet decreases. Optimizing the suspension injection flow rates involves maximising the suspension penetration into the flame without removing excessive heat and momentum from the flame. An optimum flow rate to maximise particle temperatures lies within the range of 100 ml/min to 150 ml/min for this case as this suspension flow rate leads to particles that are molten upon impact and looks to maximise the proportion of particles that are heated. The optimum suspension flow rate to maximise particle velocities lies within the range of 150 – 200 ml/min.

5.8 Investigation into the Effect of Angle of Injection

The angle of injection into the HVOF cross flow must be considered to determine how the injector should be angled within the shroud. Using a 100 ml/min flow rate the suspension injection angle has been varied. Three injection angles are considered: an angle of positive 15 degrees, 0 degrees and negative 15 degrees. A positive injection angle occurs with the suspension injection angled in the direction of the gas flow. A negative injection angle is defined as the liquid jet travelling in the direction opposing the gas flow. Figure 5-23 show the average velocity of particles at various standoff distances for the three injection angles investigated. It can be seen that as the angle of injection varies from the positive value of + 15 degrees to - 15 degrees the velocity of the particles decreases. With a positive injection angle, particles are given an initial velocity in the direction of the flow. Hence, a positive injection angle results in a higher inflight particle velocity due to the higher initial X velocity in the flow direction. A maximum difference in the average particle velocity of 125 m/s occurs between a negative injection of 15 degrees and a positive injection of 15 degrees at the location of 125 mm from the nozzle exit.

Figure 5-24 shows the average inflight temperature of particles for the three injection angles investigated. It can be seen from figure 5-24 that as the angle of injection varies from the negative value of 15 degrees to the positive value of 15 degrees, the average temperature of the particles decreases. With a negative injection angle, particles must be decelerated and then be accelerated in the direction of the flow. This allows for the particles to spend a greater duration of time within the flame and hence allow for greater heating of the particles. A maximum difference in the average particle temperature of 100 K occurs between a negative injection of 15 degrees and a positive injection of 15 degrees at the location of 150 mm from the nozzle exit.

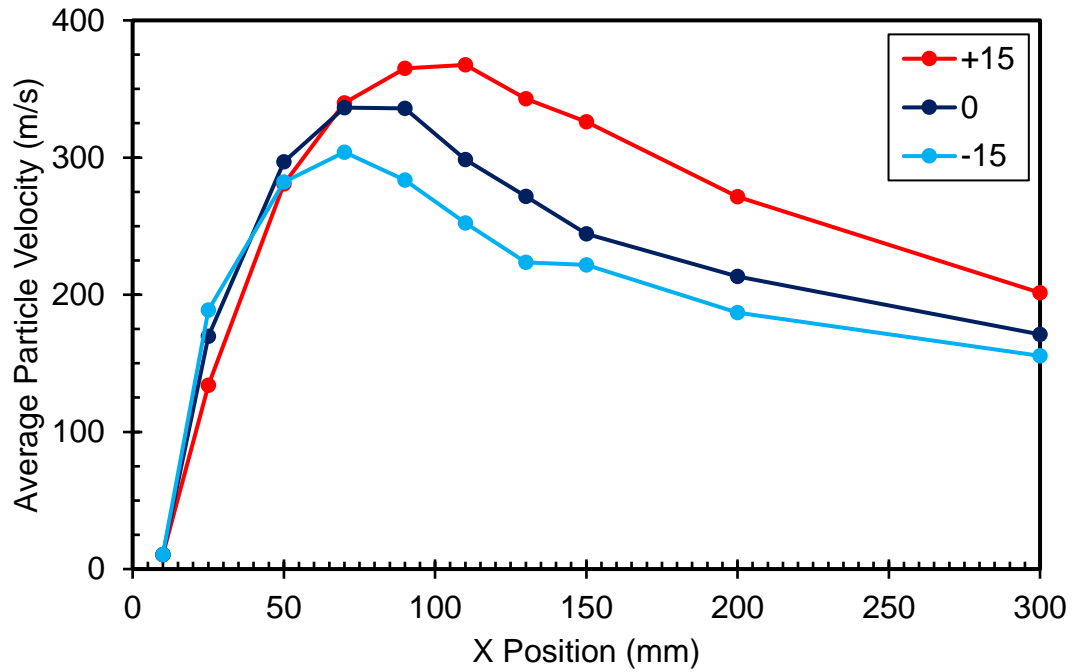


Figure 5-23: Average inflight particle velocity for the injection angle of +15, 0 and -15 degrees at a flow rate of 100 ml/min.

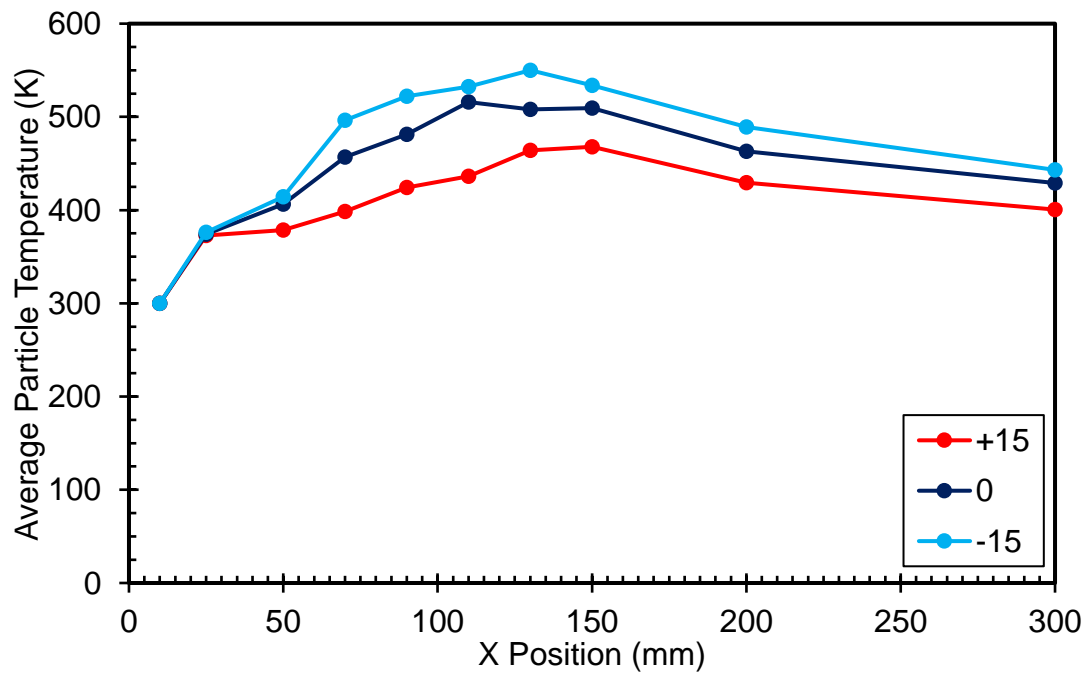


Figure 5-24: Average inflight particle temperature for the injection angle of +15, 0 and -15 degrees at a flow rate of 100 ml/min.

Varying the angle of injection can significantly influence the in-flight particle conditions. There are situations where particles may benefit from a negative, a positive and a perpendicular injection. With a positive angle of injection suspension droplets are given a larger initial velocity in the direction of the gas flow, hence particles have a higher inflight velocity. Particles with a low melting temperature will benefit from a positive injection as particles will impact the substrate with a higher impact velocity. With a negative injection angle, the suspension droplets initial velocity opposes the gas jet. The suspension droplets must first be decelerated and then accelerated in the direction of the gas flow. Droplets and particles spend a greater duration of time within the flame and therefore higher particle temperatures are seen for a negative injection angle. A negative injection will benefit particles with a higher melting temperature allowing particles to spend a greater duration of time within the flame resulting in higher temperature upon impacting the substrate. With Al_2O_3 based suspension the high melting point of the particles and low sensitivity to oxygen at high temperatures makes a negative injection angle beneficial. This results in greater heating of particles to increase the quantity of molten inflight particles.

5.9 Investigation into the Effect of the Injector Diameter

An evaluation of the effect of the diameter of the injector within the shroud must be considered to optimise the injector diameter. In this investigation three injector diameters were considered, a flow rate of 100 ml/min and an angle of negative 15 degrees have been used. The negative angle of injection is used for this investigation due to the higher article temperatures, Al_2O_3 has a high melting temperature of 2072°C particles will therefore benefit from the negative injection angle. The injector diameter was varied at 0.3 mm, 0.45 mm and 0.6 mm. Figures 5-25 show the particle velocities at a standoff distance of 85 mm from the nozzle exit for varying injector diameters of

0.3 mm, 0.45 mm and 0.6 mm. It can be seen that as that as the diameter of the injector decreases, the maximum velocity the particles can increases. With the injector diameter of 0.3 mm particles reach a maximum velocity of 900 m/s, as the injector diameter increases to 0.6 mm the maximum particle velocity reduces to 500 m/s.

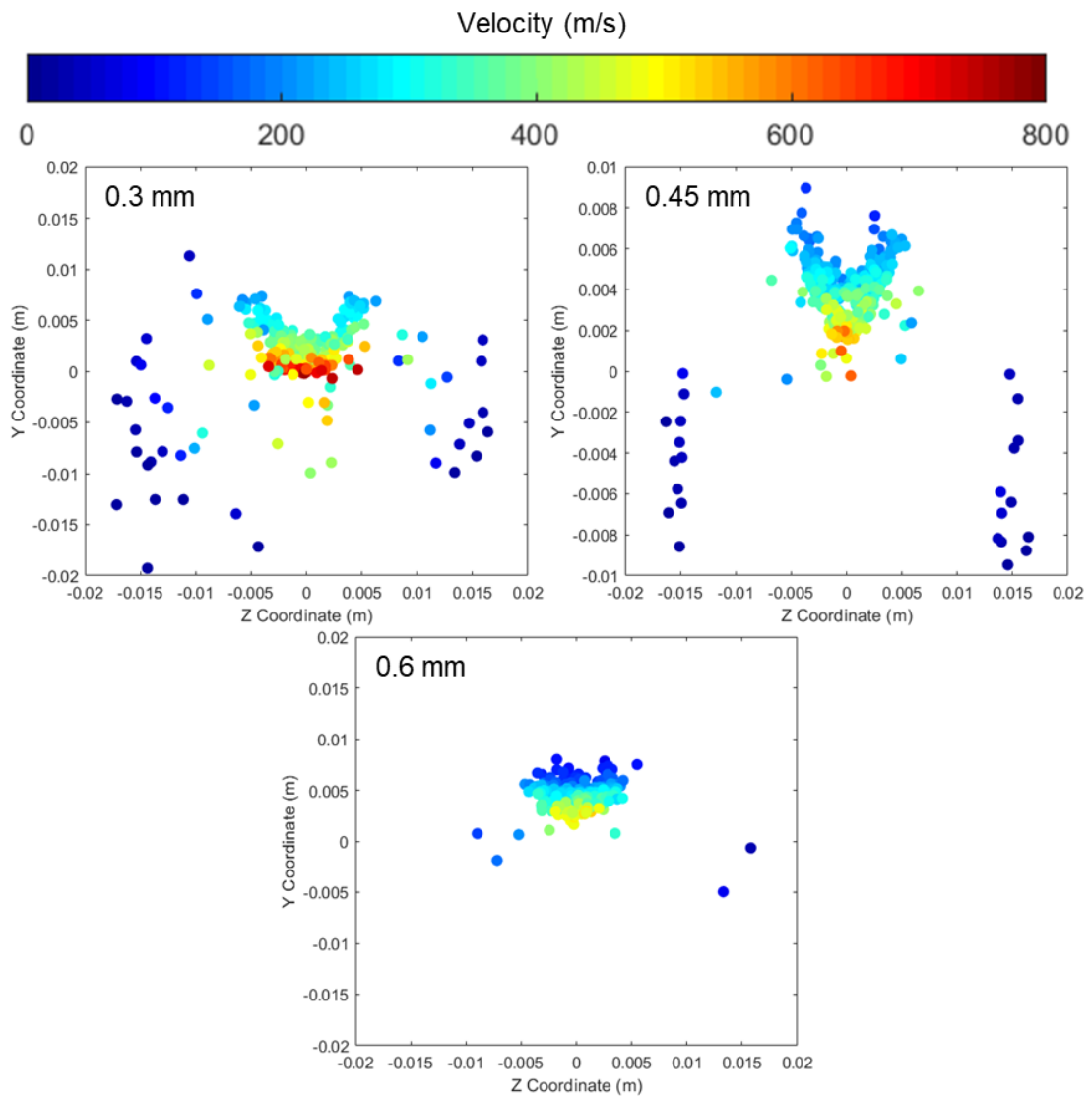


Figure 5-25: Suspension particle velocities at standoff distance of 85 mm for a varying diameter of injection of 0.3 mm, 0.45 mm and 0.6 mm.

Figure 5-26 shows the average inflight particle velocities for the varying injector diameters of 0.3 mm, 0.45 mm and 0.6 mm. From figure 5-26 it can be seen that decreasing the injector diameter from 0.6 mm to 0.3 mm the maximum average particle

velocity increases from 240 m/s to 440 m/s. It can be seen that downstream from the injection location that the average particle velocity for the 0.6 mm injector exceeds the 0.3 mm injector at a location of 200 mm from the nozzle exit. For a smaller injector diameter, the particles at a given flow rate will have a higher injection velocity. The higher injection velocity will allow for a greater penetration of suspension which enhances heat and momentum transfer to the droplets. Particles will be lighter due to the greater proportion of liquid vaporised. Lighter particles have a small mass inertia and decelerate more rapidly for the smaller injector diameter.

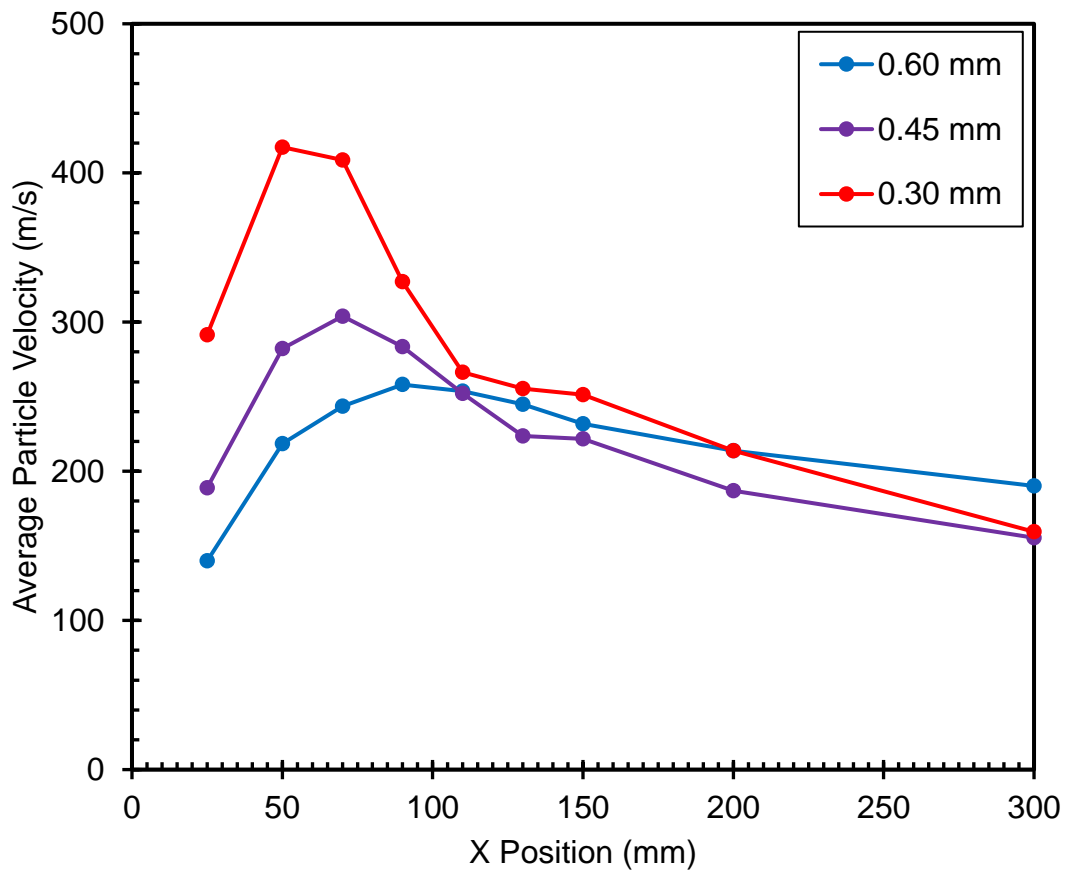


Figure 5-26: Average inflight particle velocity for a varying diameter of injection of 0.3mm, 0.45mm and 0.6mm.

Figure 5-27 shows the particle temperature at a standoff distance of 85 mm from the nozzle exit for varying injector diameters of 0.3 mm, 0.45 mm and 0.6 mm. It can be

seen from figure 5-27 that as the diameter of the injector reduces, there is a greater number of particles that are heated. Figure 5-28 shows the average inflight particle temperatures for the varying injector diameters of 0.3 mm, 0.45 mm and 0.6 mm. It is seen that as the injector diameter decreases the maximum temperature the particles have reached increases. As the higher velocity allows greater penetration of suspension into the gas jet. Therefore, particles are exposed to higher gas temperatures which result in the higher particle temperatures.

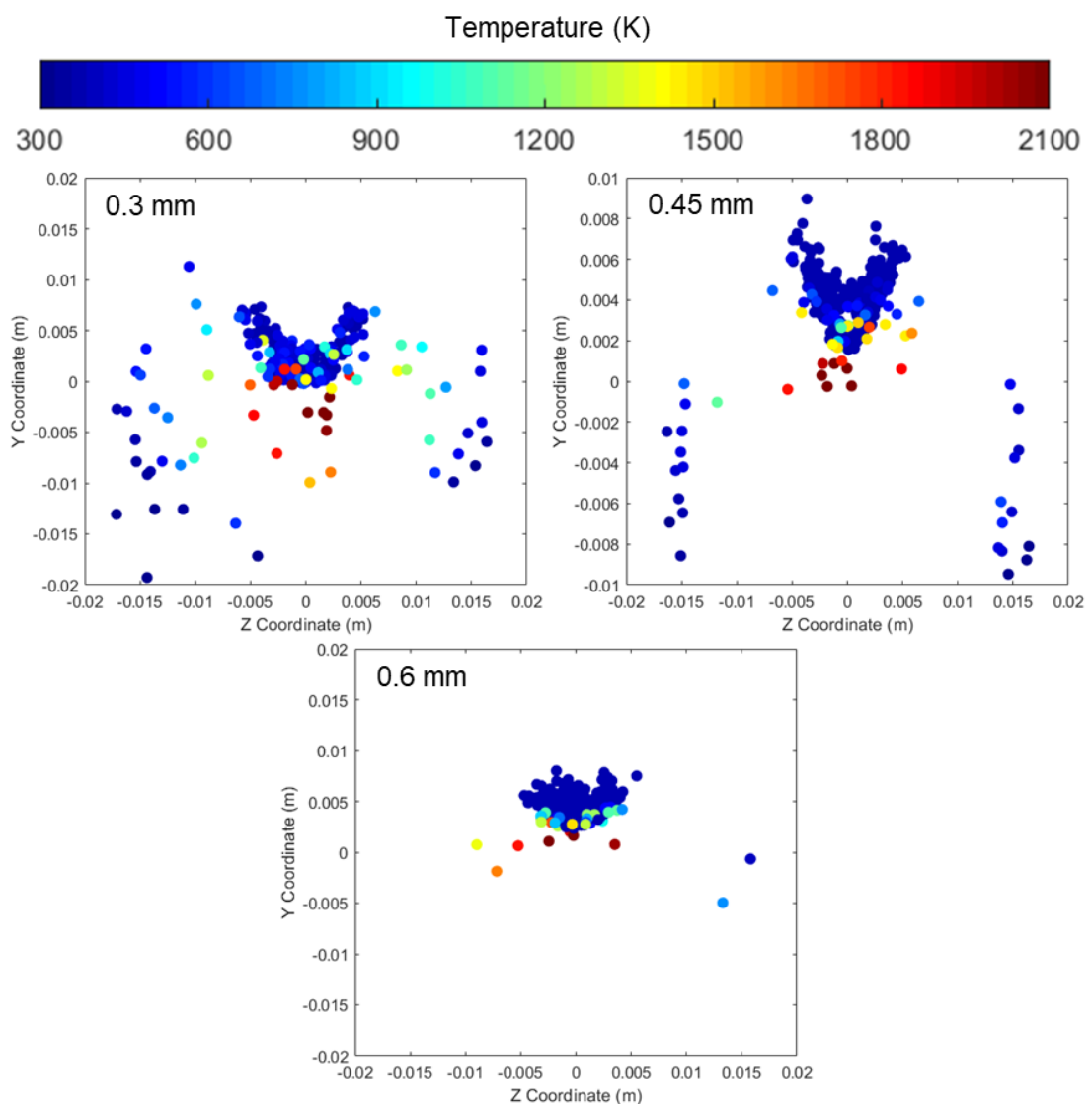


Figure 5-27: Suspension particle temperatures at standoff distance of 85 mm for a varying diameter of injection of 0.3mm, 0.45mm and 0.6mm.

From figures 5-25 and 5-27 it can be seen that at a smaller injector diameter, particles stray out of the jet more readily. With a higher velocity injection, the larger radial component of the velocity as well as the lighter particle mass due to greater liquid evaporation is resulting in particles exiting the gas jet. As the particles exit the jet the particles quickly lose their heat and momentum due to their low mass and thermal inertia. Ensuring particles remain within the gas jet is a challenge that will need to be addressed when injecting suspension radially for SHVOF thermal spray.

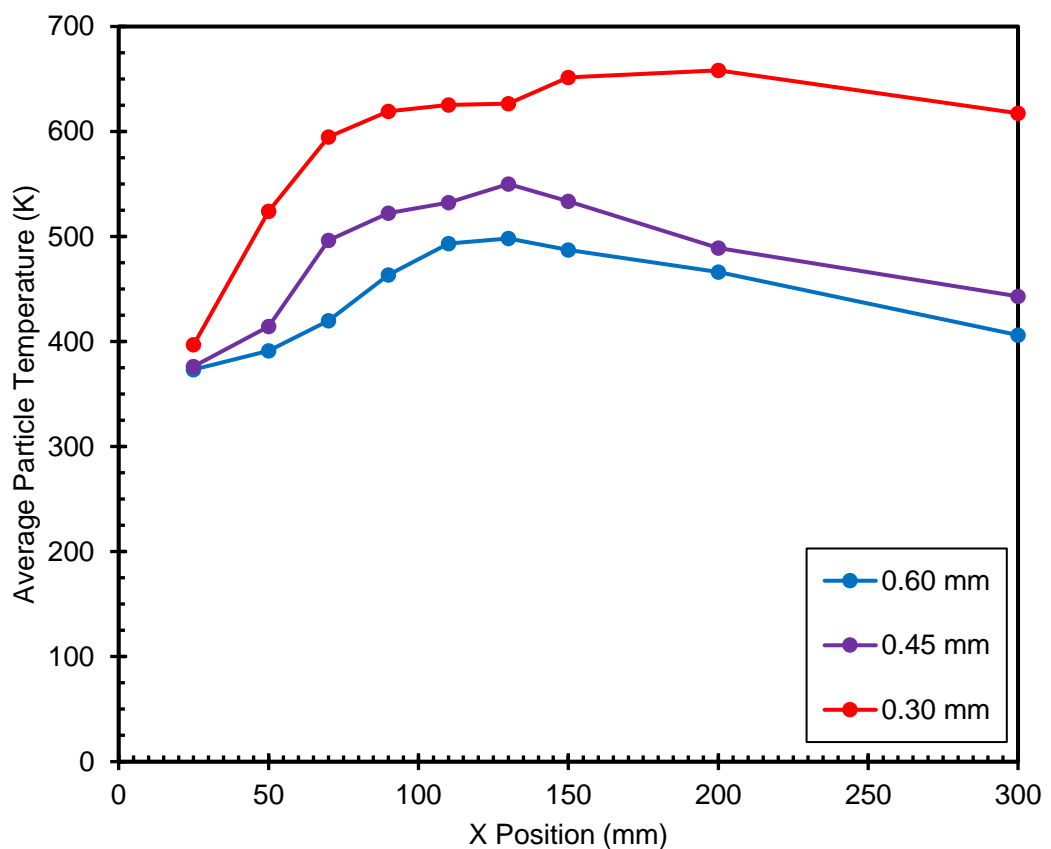


Figure 5-28: Average inflight particle temperature for a varying diameter of injection of 0.3mm, 0.45mm and 0.6mm.

The injection velocity for the suspension exiting the injector is dependent on the suspension flow rate and the injector diameter. It has been shown that increasing the suspension flow rate results in greater penetration of the suspension into the gas jet

due to the higher injection velocity. The injection velocity can also be increased by reducing the injector diameter at a fixed flow rate. The higher injection velocity of the suspension with a smaller diameter injector increases the penetration of the suspension into the gas jet. Which significantly increases the proportion of particles heated without capping the maximum velocity and temperature the particles can obtain. Reducing the diameter of the injector comes with its own limitations as the injector is more prone to clogging as the diameter shrinks. The minimum injector diameter that does not enable clogging should be employed within the shroud. The shroud will look to spray a range of materials the injector diameter will therefore be different depending upon the material sprayed. GNP's for example are a flat planar structure with a nominal thickness of 6-8 *nm* and an average width of 5 μm (15-20 layers) and therefore, GNP's will be prone to clogging [16]. GNP's will require a larger injector than Al_2O_3 considered within this study. Having a removeable injector will allow for the injector to be individually optimised to each material sprayed.

5.10 Effect of Shrouding Expansion Ratio on Gas Dynamics

The purpose of a shroud within thermal spray is to prevent mixing of atmospheric oxygen with the gas jet. The shroud attaches onto the end of the HVOF gun to create an inert atmosphere within the shroud to enhance the deposition of oxygen sensitive materials. The shroud designed within this chapter also allows for a location to radially inject suspension into the crossflow; the shroud also employs a shrouding gas to delay the mixing of ambient oxygen with the jet. Figure 5-1 shows the hybrid nozzle designed and modelled within this chapter. The total length of the shroud design is kept constant at 75 mm. The total length of 75 mm is specified so that the radial injection of suspension and an axial injection of powder or suspension feedstock can simultaneously be sprayed to deposit composite coatings. A composite coating is

formed from two different materials which can offer enhanced properties over coatings produced from the individual materials [150]. A hybrid nozzle will enhance the deposition of oxygen sensitive materials as the nozzle combines an axial injection into the combustion chamber and a radial injection into the shroud. A composite coating can be deposited using the hybrid nozzle by simultaneously axially injecting suspension or powder typically a ceramic such as Cr_2O_3 or Al_2O_3 into the combustion chamber and radially injecting suspension containing GNP's into the shroud. The axially injected material spends a greater duration of time within the flow to allow for greater heating of particles. This ensures the particles are sufficiently molten upon impacting the substrate. The radially injected material spends a shorter time within the flow and undergoes less heating within the flow this reduces oxidation and degradation at high temperatures of oxygen sensitive. Kinoshita et al. [169] demonstrate that a distance of 5 – 10 mm is required from the end of the shroud and the substrate. Larger distances than 10 mm demonstrated poor coating structures and an increased oxide content within the coating. Typically for suspension axially injected a standoff distance of 85 mm is used [170]. Employing a shroud length of 75 mm allows for typical standoff distances for axially injected SHVOF thermal spray to be used with the shroud.

The effect of the diameter at the exit of the shroud on the air entrainment, gas velocity and gas temperature within the shroud are investigated to determine the optimum expansion ratio for the shroud. Three diameters are investigated are 24 mm, 28 mm and 32 mm at the shroud exit. The diameters at the exit are chosen from modelling investigations undertaken for SPS thermal spray by Jankovic et al. [171]. Jankovic et al. investigated the effect of the angle of shrouding for a shrouding attachment developed for SPS thermal spray. It was seen for a shroud with an angle greater than 7 degrees air entrainment rapidly increases. Below 7 degrees there was very little air

entrainment seen within the shroud. The flow conditions investigated by Jankovic et al. were subsonic as SPS thermal spray operates at subsonic conditions. Within SHVOF thermal spray the flow operates at supersonic conditions the effect of the shroud diameter is investigated within this chapter to see if similar behaviour is seen at supersonic conditions. Three diameters are investigated within this study of 24 mm, 28 mm and 32 mm correspond to a shrouding angle of 7.5 degrees, 10.5 degrees and 13.5 degrees respectively. Figure 5-29 shows the effect of the shroud exit diameter on the oxygen mass fraction within the shroud. From figure 5-29 it can be seen that the expansion ratio significantly reduces the oxygen content within the shroud which is introduced by air entrainment into the shroud. The shroud with a diameter of 32 mm at the exit allows for a significant amount of air entrainment into the centre of the shroud which compromises the integrity of the inert atmosphere. The shroud with a diameter of 28 mm at the exit allows for small amount of air entrainment into the should near the exit of the shroud. The shroud with a diameter of 24 mm at the exit does not allow for any air entrainment into the shroud.

Matthews et al. [149] outlined three mechanisms for oxide formation from the thermal spray process. The first refers to oxide introduces within the coating from the initial feedstock. The second refers to the oxides deposited from inflight particles that have oxidised during flight due the exposure to the oxygen within the jet. The third refers to the oxidation of the coating post deposition, molten splats on the surface of the coating are exposed to oxygen within the air. The molten splats oxidise and introduce oxides into the coating during the spay process. The purpose of the shroud is to minimise mixing of atmospheric oxygen into the jet. This in turn minimises oxides introduced into the coating through the second mechanism. The 24 mm shroud allows for no oxygen entrainment into the shroud and hence the 24 mm shroud exit diameter

provides the optimum condition for spraying oxygen sensitive materials as it maintains an inert environment. The results within this study match well to those seen by Jankovic et al. there is very little to no air entrainment seen an exit diameter of 24 mm which corresponds to a shroud angle of 7.5 degrees. Increasing the exit diameter to 32 mm which corresponds to a shroud angle of 13.5 degrees significant air entrainment is seen into the shroud.

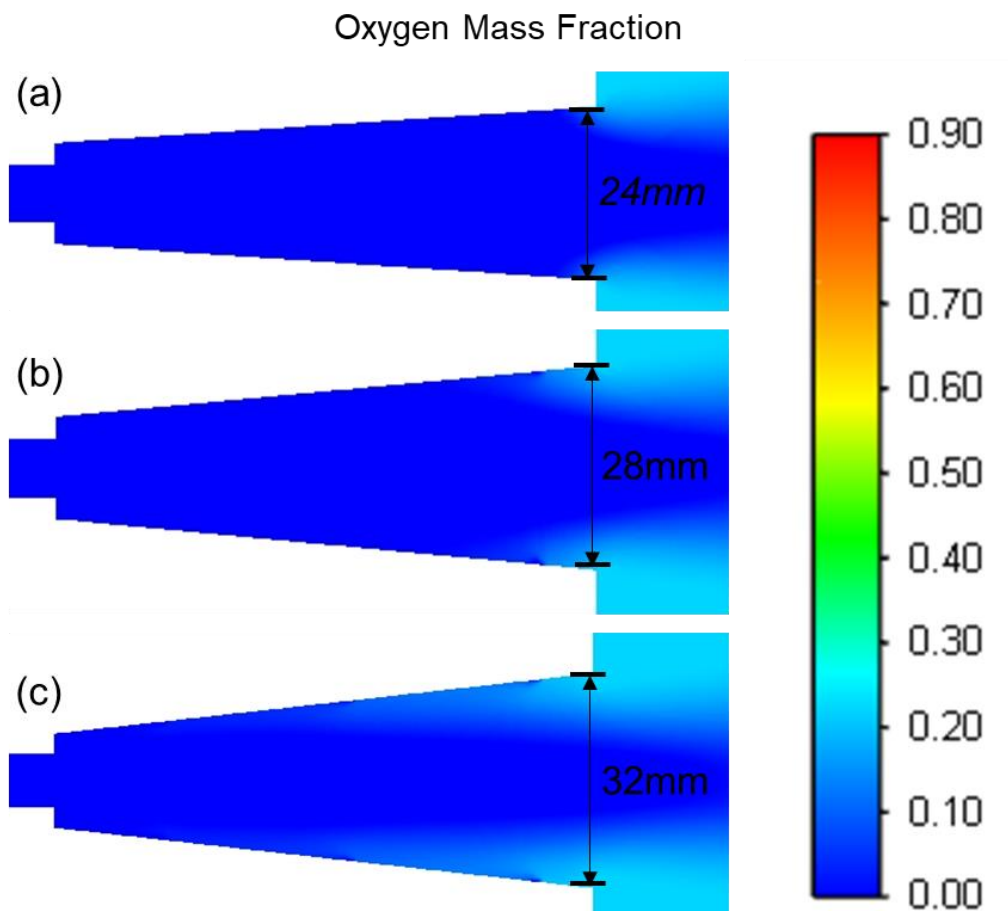


Figure 5-29 (a), (b) and (c): Effect of the shroud exit diameter on oxygen mass fraction within the shroud (a) 24 mm, (b) 28 mm and (c) 32 mm (no suspension)

In addition to preventing mixing of ambient oxygen into the HVOF jet, the effect of the diameter at the shroud exit on the gas velocity and gas temperature is considered. Figures 5-29 shows what effect of the shroud diameter at the exit has on the gas

velocity. It can be seen from figure 5-29, in the shock region the shroud amplifies the gas velocity locally in comparison to the flow field without a shroud. Additionally, it can be seen that as the diameter at the shroud exit reduces from 32 mm to 24 mm the maximum velocity increases locally by an additional 400 m/s. The greater velocity within the shock region for the 24 mm shroud will inhibit the penetration of suspension droplets in comparison to the shrouds with a larger diameter at the shroud exit. The higher gas velocity results in a higher dynamic pressure of the HVOF crossflow [167]. Far away from the shock region the reverse trend holds true, as the diameter at the shroud exit decreases the gas velocity decreases also. The higher gas velocity in this region with the larger shroud diameter at the exit will result in a higher particle impact velocity and hence particles will be more likely to deposit onto the substrate.

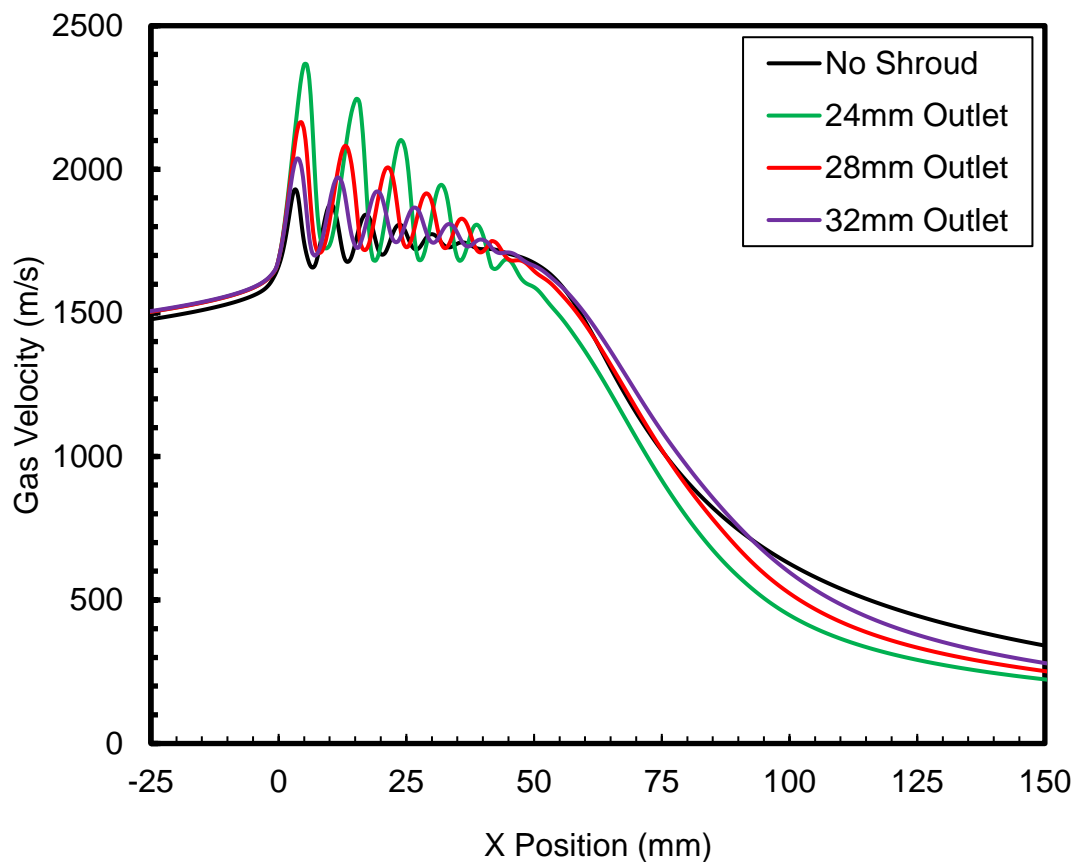


Figure 5-30: Effect of shroud expansion ratio onto the gas velocity.

A radial injection of suspension has been widely used to deposit coatings within SPS thermals spray due to the high gas temperatures within SPS thermal spray. The high gas temperatures result in lower gas densities which allow for the suspension to readily penetrate the crossflow into the SPS jet [167]. Figure 5-30 show the effect of the shroud exit diameter onto the gas static temperature. It can be seen from figure 5-30 that the gas flow operates at a higher temperature without a shroud attachment in and near the shock region. Additionally, it can be seen that as the shroud diameter at the exit increases from 24 mm to 32 mm the gas temperature decreases by as much as 300 K within the shock region. Downstream from the shock region the reverse trend holds true, the addition of a shroud attachment results in an increase in the gas temperature. The shroud attachment delays mixing of cold air from the atmosphere with the jet allowing for a greater temperature beyond the shock region. The 32 mm shroud exit diameter allows for the mixing of air within the shroud whilst the 24 mm nozzle allows for mixing of air furthest downstream from the shroud exit. As the mixing of cold air from the atmosphere occurs further downstream with the shortest shroud exit the cold air mixes into the jet later. Therefore, as the diameter at the shroud exit decreases there is an increase in the gas temperature. However, the difference between the various shroud configurations is no larger than 100 K.

There are two considerations that must be met when choosing the shroud geometry for a shroud that allows for a radial injection. the first is that the shroud should minimise the mixing of atmospheric oxygen with the jet. The second is that the shroud geometry should be optimised to maximise penetration of the suspension into the jet. The 24 mm shroud allows for no air entrainment it however operates at a higher velocity where the suspension penetrates into the jet. This will reduce penetration of suspension into the jet and reduce the efficiency of deposition. The 34 mm shroud allows for

significant air entrainment into the shroud and hence will result in significant oxidation of particles within the shroud. The 32 mm shroud has a locally lower velocity where the suspension will penetrate than the smaller shroud exit diameters allowing for the greatest penetration of the suspension into the jet. The 28 mm shroud allows for a compromise where there is little air entrainment within the shroud and the velocity where the suspension will penetrate is locally lower allowing for greater penetration of suspension into the jet.

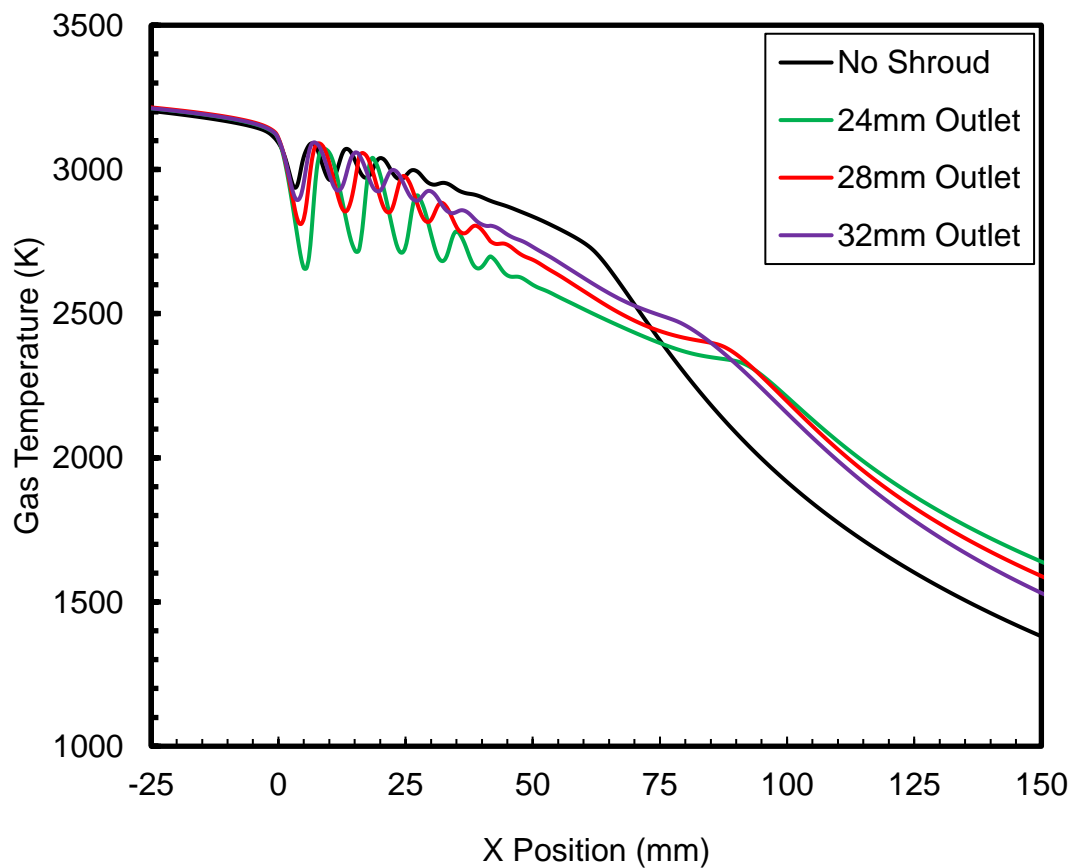


Figure 5-31: Effect of shroud expansion ratio onto the gas temperature.

5.11 Effect of Shrouding Gas on the Entrainment Within the Shroud

There are two types of shrouds that have been employed within the thermal spray literature. The first is a solid barrier shroud that has been discussed and modelled within section 5.10. The second type of shroud employed within thermal spray is a gas shroud of inert gas; typically, the gas used is nitrogen or argon. The purpose of the gas shroud is to act as a barrier to air penetration into the thermal spray jet. The inert gas delays the mixing of the air with HVOF or plasma jet [149]. This investigation looks at introducing an inert gas shroud with the solid barrier shroud to delay the mixing of oxygen with the HVOF jet and considering the effect of the addition of an inert gas shroud to the gas dynamics. The 28 mm shroud exit has been employed within this study to investigate if the air entrainment into the shroud can be reduced. The 28 mm shroud exit diameter design allows for a lower velocity and a higher temperature near the injection location over the shroud with a 24 mm diameter. It is well understood that a lower gas velocity within the crossflow will allow for suspension to penetrate more readily as shown within equation 5.2. Hence this design will allow for suspension to penetrate more readily into the crossflow over the 24 mm exit diameter. This design allows for oxygen to enter into the shroud and this investigation looks to vary the flow rate to prevent any air entrainment into the shroud by varying the shrouding gas flow rate.

The inert gas is injected using an annular inlet to simplify the geometry to allow for a structured mesh to be employed. The designed shroud will use a set of circular holes spaced uniformly around the circumference of the shroud. The diameter of the holes will match the annular width employed within this study. The modification to the inlet geometry will introduce some modelling errors however, it is a well-established practise to simplify the geometry for simpler meshing requirements. Simplifying the

inlet configuration has been employed in a range of SHVOF thermal spray modelling studies to simplify the fuel inlet within the combustion chamber [20], [60]. The inert gas inlet is located 7.5 mm from the shroud outlet and has a width of 1 mm. Four flow rates for the inert gas of 0 g/s, 1 g/s, 2 g/s and 3 g/s are considered, the inert gas used within this study is nitrogen.

Figure 5-32 shows the oxygen mass fraction within the shroud at varying shrouding gas flow rates of 0 g/s, 1 g/s, 2 g/s and 3 g/s. It can be seen that at flow rates up to 1 g/s gas the air can entrain into the shroud introducing oxygen into the shroud. The oxygen introduces compromises the inert atmosphere which will degrade and oxidise the oxygen sensitive material injected into the shroud. As the shrouding gas mass flow rate increases above 2 g/s there is no air entrainment into the shroud. This will improve the deposition of oxygen sensitive materials as oxygen is prevented from mixing into the shroud from the atmosphere. The optimum shrouding gas mass flow rate is between 2 g/s and 3 g/s as this flow rate prevents air entrainment into the shroud. Jankovic et al. [171] and the results shown in section 5.10 show that for shrouding angles large than ~ 7 degrees air entrainment rapidly increases. However, from this study it can be seen that the shrouding gas allows for larger shroud angles to be employed. within this study air entrainment can be prevented into a shroud with a shrouding angle of 10.5 degrees with a shrouding gas mass flow rate of 2 g/s

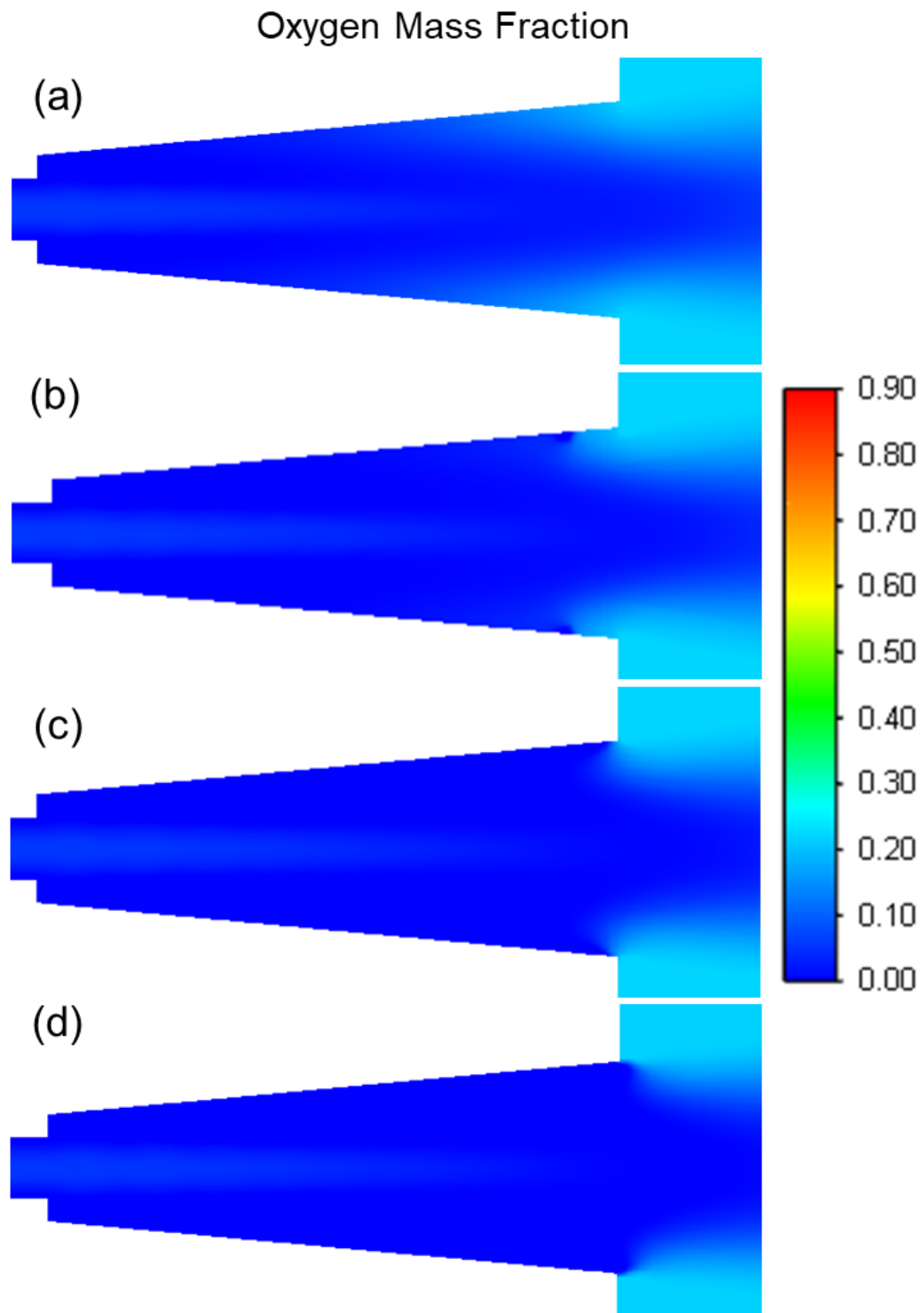


Figure 5-32: Oxygen mass fraction within the shroud at varying shrouding gas flow rates of (a) 0 g/s, (b) 1 g/s, (c) 2 g/s and (d) 3 g/s

In addition to preventing mixing of ambient oxygen into the HVOF jet, the effect of the shrouding gas mass flow on the gas velocity and gas temperature is considered. The shrouding gas should not adversely affect the gas velocity or the gas temperature. Figure 5-33 shows the effect of gas shrouding mass flow rate on the centreline gas velocity within the shroud. Figure 5-34 shows the effect of gas shrouding mass flow rate on the centreline gas temperature within the shroud. It can be seen from figures 5-33 and 5-34 that as the shrouding gas mass flow rate increases up to 3 g/s there is very little to no change on the centreline gas velocity and gas temperature. Therefore, the shrouding gas does not negatively impact the flow field by excessively decelerating or cooling the gas jet.

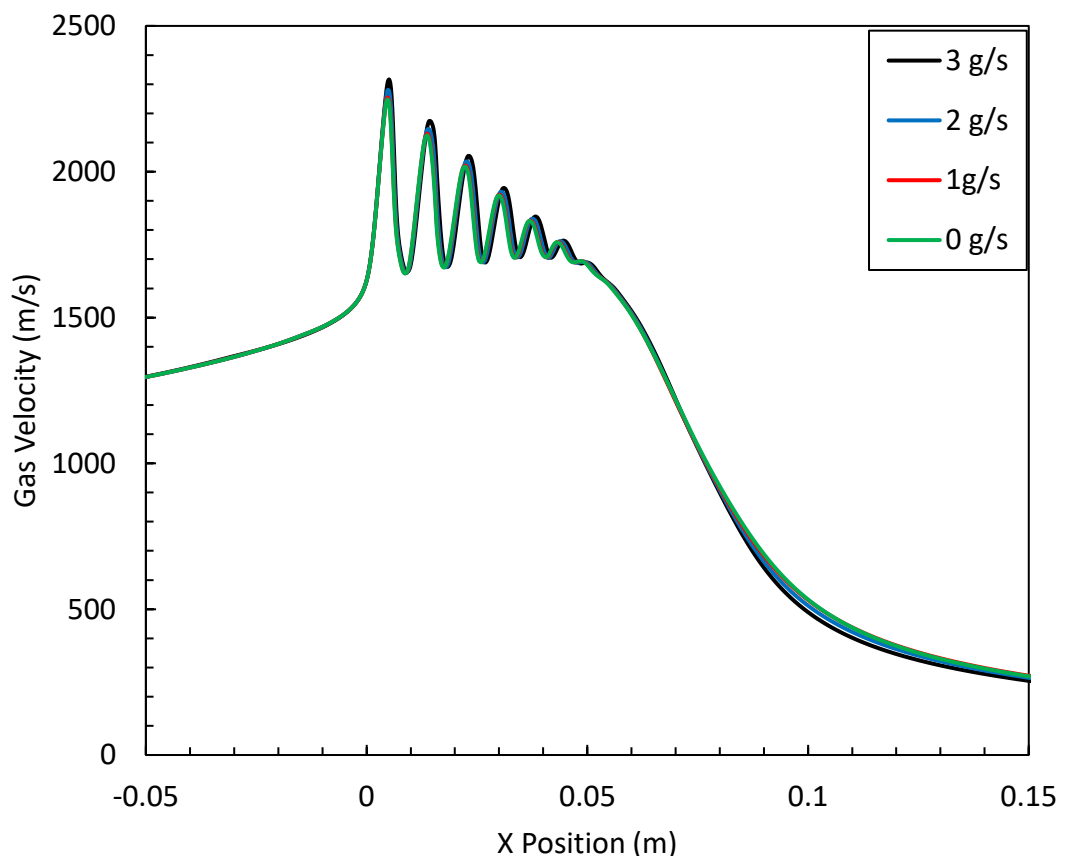


Figure 5-33: Effect of gas shrouding mass flow rate on the centreline gas velocity within the shroud.

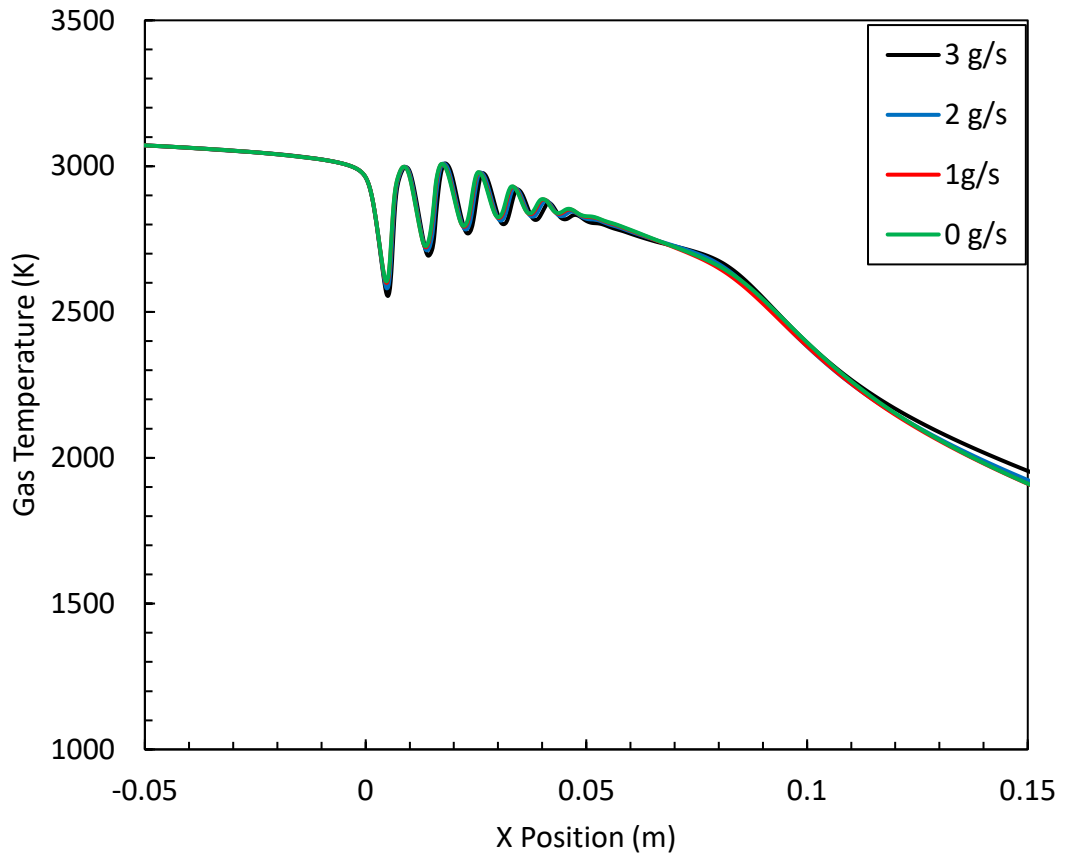


Figure 5-34: Effect of gas shrouding mass flow rate on the centreline gas temperature within the shroud.

From the CFD analysis and a review of relevant literature a shrouding attachment has been designed and manufactured. A divergent shroud has been utilised to minimise deposition of suspension on the shroud walls. A divergent shroud expands towards the outlet of the shroud which increases the distance the particles need to travel before they can impact the walls of the shroud. The further the particles have to travel out of the centre of the jet the greater deceleration the particles will experience. The particles will be less likely to have the sufficient momentum or the critical velocity to successfully bond to the walls of the shroud. This will prevent particles from depositing onto the shroud walls and from the should clogging. A shroud exit diameter of 28 as reducing the diameter of the shroud at the exit to 24 mm results in higher gas

velocities and lower gas temperatures in the shock region. The suspension is injected into the shock region and the higher gas velocity and lower gas temperature reduces suspension penetration due to the higher dynamic pressure of the cross flow which the suspension must overcome. Additionally, the shroud with a diameter of 28 mm operates at higher velocities than the 24 mm beyond the shroud exit and hence will result in greater deposition of particles onto the substrate due to the higher gas velocity. The 28 mm shroud however allows for air entrainment into the shroud which is not seen with a smaller shroud exit diameter of 24 mm.

A shrouding gas is employed to prevent air entrainment in shroud designs with a shrouding angle larger than 7 degrees. The shroud angle used within the shroud designed within this thesis is 10.5 degrees. With no shrouding gas air entrains into the shroud, the air entrainment into the shroud can be prevented by introducing an inert shrouding gas. A flow rate of 2 g/s prevents any air entrainment into the shroud for the 28 mm nozzle which ensures an optimum environment for depositing oxygen sensitive materials. Larger shrouding angles allow for a lower velocity and a higher temperature near the injection location. Both conditions improve suspension penetration into the jet.

The downstream location of the suspension injector was determined from experimental investigations using high speed imaging conducted by Venturi et al. [16]. Venturi et al. investigated the effect of the distance of the injector from the nozzle exit has on suspension vaporization and breakup using high speed imaging found that a distance of 10 mm from the nozzle exit was most effective at ensuring effective vaporization of the suspension. Hence within the shroud the injector is located at 10 mm from the nozzle exit. A perpendicular, positive 15 degrees and negative 15 degrees injection has been utilised within the shroud. The downstream injection allows for

particles to reach higher gas velocities due to the higher initial velocity component in the crossflow direction which is useful for low melting point materials. The upstream injection allows for particles to reach a higher temperature which is useful for materials with a higher melting temperature. Three removeable injectors are located within the shroud such that the injectors can be switched out such that the diameter of the injector can be modified as this study has shown that decreasing the injector diameter increases suspension penetration. However, some materials may block the injector readily as the injector diameter becomes small. Hence, this injector diameter can be increased to determine the minimum size that does not promote clogging.

A modular shroud design has been employed for the shroud to allow for ease of maintenance and to avoid welding of the shroud. The shroud has 4 modules: the inner cone, the gas injection jacket, the GTV Topgun holder and the injector. The inner cone has been modelled within this chapter and the geometry of the inner cone has been determined from the results of this chapter. There are holes within the inner cone to allow for an inert gas injection for the shrouding gas. The gas injection jacket surrounds the inert gas inlet and provides a location to inject and feed inert gas into the shroud. The GTV Topgun holder is an attachment that mounts the shroud onto the end of the GTV Topgun. The geometry of this module is constraint by the geometry of the GTV Topgun housing as the holder should ensure a tight fit between the shroud and the GTV Topgun. The final module for the injector allows the injectors to insert into the inner cone to provide an injection location. This module provides a water jacket around the inner cone to allow for cooling of the water jacket. The cooling geometry was designed and optimised by internal analysis conducted by Dr. Federico Venturi. The CAD designs of the shroud and the 4 modules with the assembly drawings can be found in Appendix I.

5.12 Effect of Shrouding on Inflight Particle Dynamics

For particles to deposit onto the substrate they must become sufficiently heated, melted and impact the substrate at a velocity greater than the critical velocity [94]. Figure 5-35 evaluates the average particle velocity with and without the shroud predicted from the numerical model. For both injections, the suspension is injected radially at a location of 10 mm downstream from the nozzle exit at a flow rate of 100 ml/min at an angle of negative 15 degrees with an injector diameter of 0.3 mm. The injection conditions employed were employed to maximise particle temperatures. It can be seen from figure 5-35 that the addition of a shroud attachment results in lower average particle velocities. There is a maximum difference of approximately 100 m/s between particle velocities with and without the shroud attachment. Both with and without the shroud attachment show a similar trend for the average inflight particle velocity. The velocity increases up to 50 mm from the nozzle exit. Beyond this there is decay of particle velocities downstream from 50 mm. Beyond 50 mm from the nozzle exit there is a significant drop in the gas velocity as shown in figure 5-30. Suspension particles have a low mass inertia and hence the particles decelerate rapidly with the gas flow.

Figure 5-36 evaluates the average particle temperature with and without the shroud attachment. It can be seen from figure 5-33 that up to 150 mm from the nozzle exit the addition of the shroud results in a small reduction in the particle temperatures. However, beyond 150 mm the shroud attachment results in significantly higher particle temperatures. At a standoff distance of 150 mm the gas temperature is approximately 200 K – 300 K greater with the shroud attachment as shown in figure 5-31. The shroud attachment delays the mixing of colder gases from the atmosphere with the HVOF jet. the mixing of cold gas with the jet results in the decrease in the gas temperature within the free jet. The addition of the shroud allows for particle temperatures to increase up

to a distance of 250 mm from the nozzle exit. Whilst without the shroud particle temperatures begin to decrease at distances greater than 150 mm from the nozzle exit. The maximum difference occurs at 250 mm from the nozzle exit where the shroud allows particles to reach a temperature of 350 K higher than without the shroud attachment. Axially injected suspension is typically sprayed at 85 mm due to the sharp decrease in the gas velocity and temperature seen above this standoff distance. The critical velocity decreases with the particle temperature at impact [94]. Therefore, particles sprayed with the shroud will require a lower velocity for successful deposition onto the substrate. Further studies will have to be conducted for the optimum standoff distance for an axially injected suspension with a shroud attachment. Finally, studies will need to look into the optimum standoff distance for the hybrid nozzle which employs both an axially injected suspension into the combustion chamber and a radially injected suspension into the shroud.

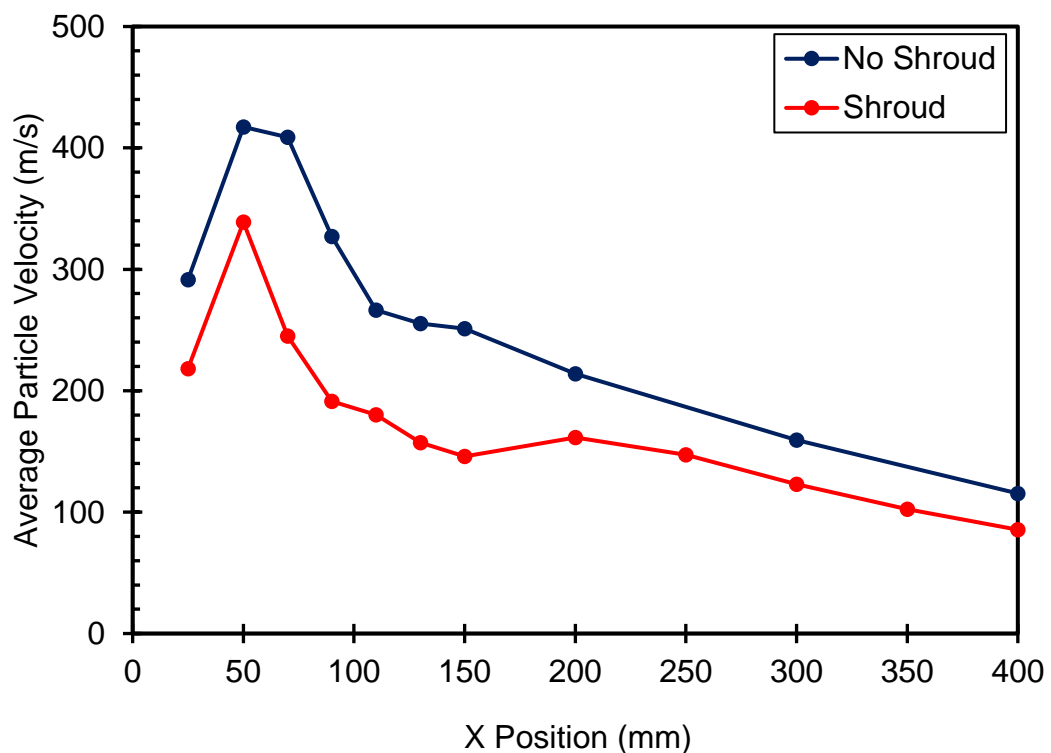


Figure 5-35: Effect of shroding on average inflight particle velocities

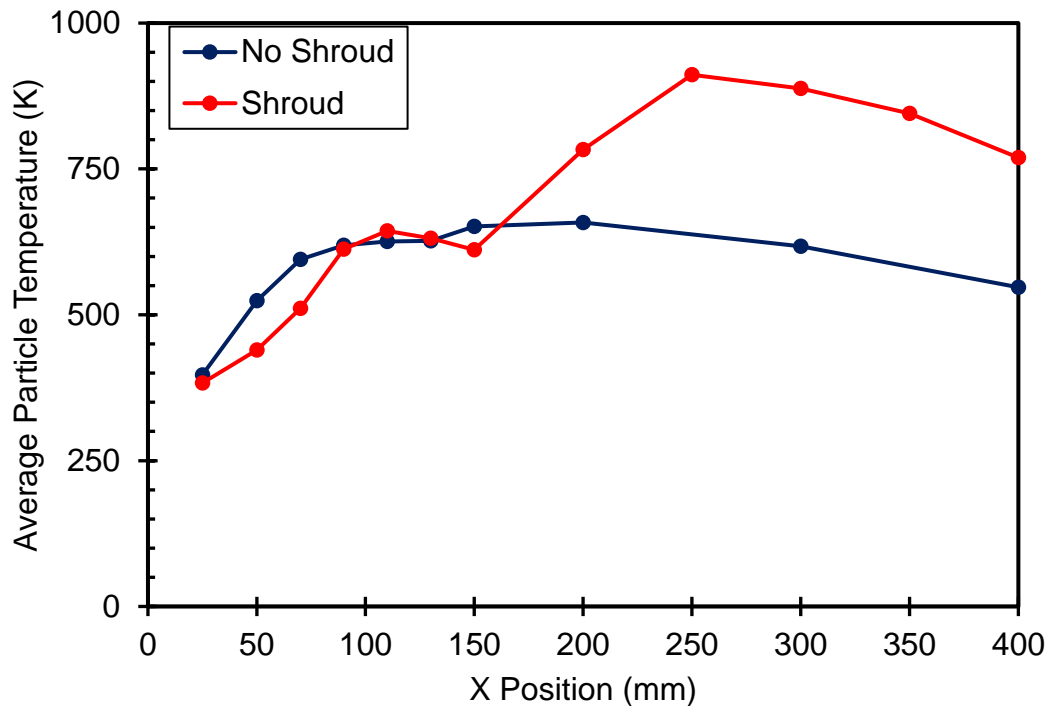


Figure 5-36: Effect of shroding on average inflight particle temperatures

To evaluate the optimum standoff distance for the shroud the particle velocity and particle temperatures at various standoff distances must be evaluated. Figure 5-37 shows that inflight particle velocities at a standoff distance of (a) 85 mm, (b) 105 mm, (c) 125 mm, (d) 145 mm, (e) 165 mm and (e) 185 mm from the nozzle exit. From figure 5-37 it can be seen that up to a standoff distance of 145 mm the particle velocity increases. There are more particles that can reach a velocity of approximately 700 m/s. With the sharp drop in gas velocity beyond 50 mm from the nozzle exit as seen in figure 5-33 particles can more readily penetrate into the centre of the jet. The gas velocity drops from 1500 to 300 m/s from a standoff distance of 50 mm to 140 mm respectively. Large droplets with un-vaporized suspension can maintain their momentum and also further into the centre jet as the gas velocity decreases. However, as standoff distance increases from 145 mm to 185 the maximum velocity particles

can reach decreases from 700 m/s to approximately 430 m/s. The continuing drop in gas velocity results in deceleration of droplets for two reasons. Firstly, the gas velocity decreases below the particle velocity hence particles decelerate. Secondly, as the larger suspension particles spend longer within the flow more and more of their liquid is vaporized, they become lighter. These droplets are unable to maintain their momentum and hence particle velocity decreases. This reduction in velocity is likely to result in coatings with a higher porosity. Hence the optimum standoff distance to maximise the inflight particle velocity with the shroud attachment is 145 mm from the gun nozzle exit. The standoff distance with the shrouding attachment is greater than that employed without a shroud attachment, typical standoff distances for axial injections of suspension lie at 85 mm from the nozzle exit.

Figure 5-38 shows that inflight particle temperature at a standoff distance of (a) 85 mm, (b) 105 mm, (c) 125 mm, (d) 145 mm, (e) 165 mm and (e) 185 mm from the nozzle exit. It can be seen from figure 5-38 that at a standoff distance of 85 mm very few particles are heated to temperatures of excess of 2000 K. As the standoff distance increases from 85 mm to 125 mm there is a greater number of particles that reach a temperature of an excess of 2000 K. As the standoff distance increases further from 125 mm to 185 mm there is a significant reduction in the maximum particle temperature. the maximum particle temperature decreases from 2200 K to 1600 K. The gas temperature with the shroud attachment can be as large as 300 K greater than without the shroud attachment. The gas jet cools further downstream due to the delayed mixing with cooler ambient oxygen allowing particles to maintain high temperatures for a greater duration of time. The optimum standoff distance that would maximise average particle velocities and temperatures with the shroud attachment would lie in the region of 125 mm – 145 mm.

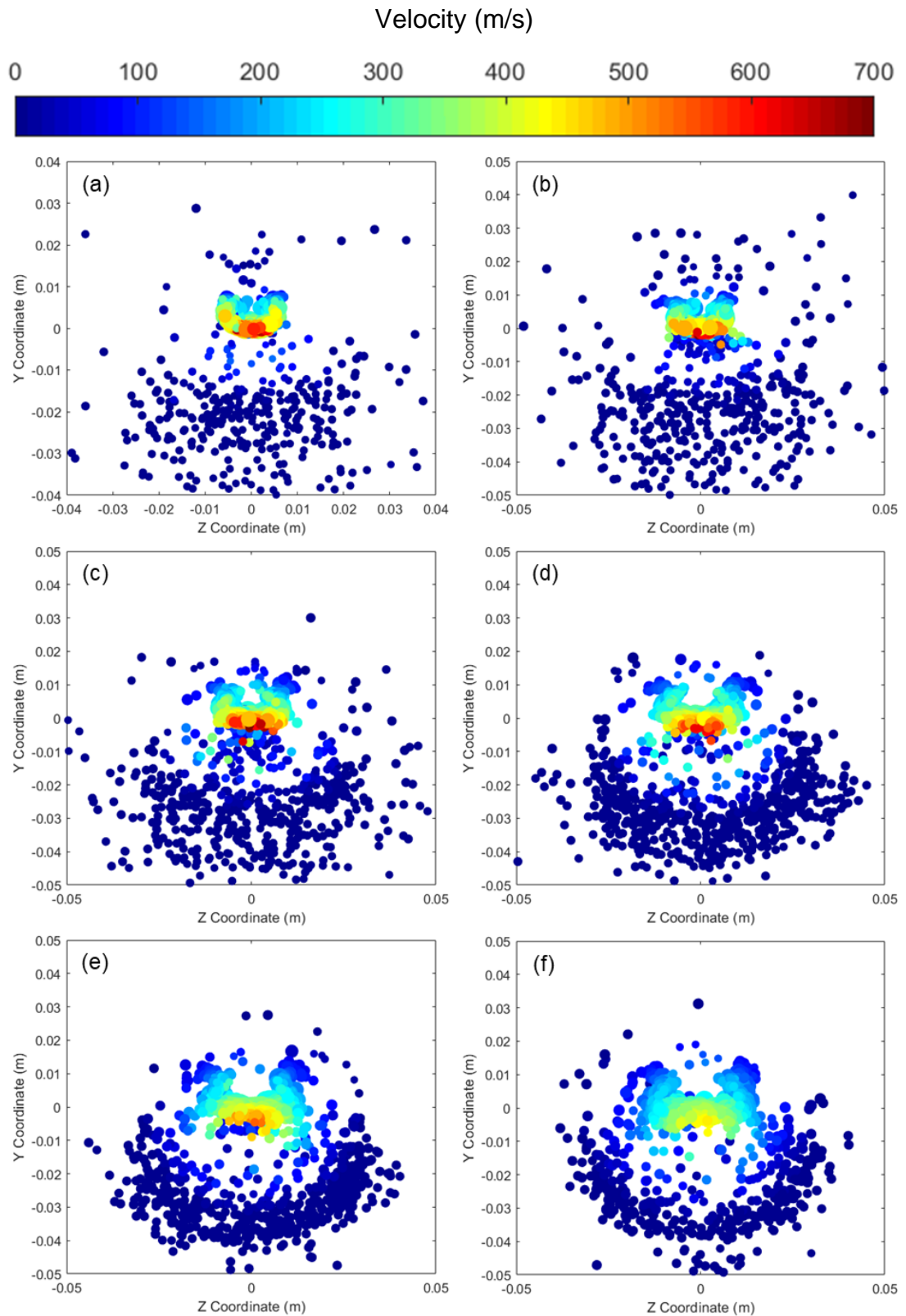


Figure 5-37: Effect of distance from the nozzle exit (standoff distance) on inflight particle velocities with a shroud attachment (a) 85 mm, (b) 105 mm, (c) 125 mm, (d) 145 mm, (e) 165 mm and (e) 185 mm.

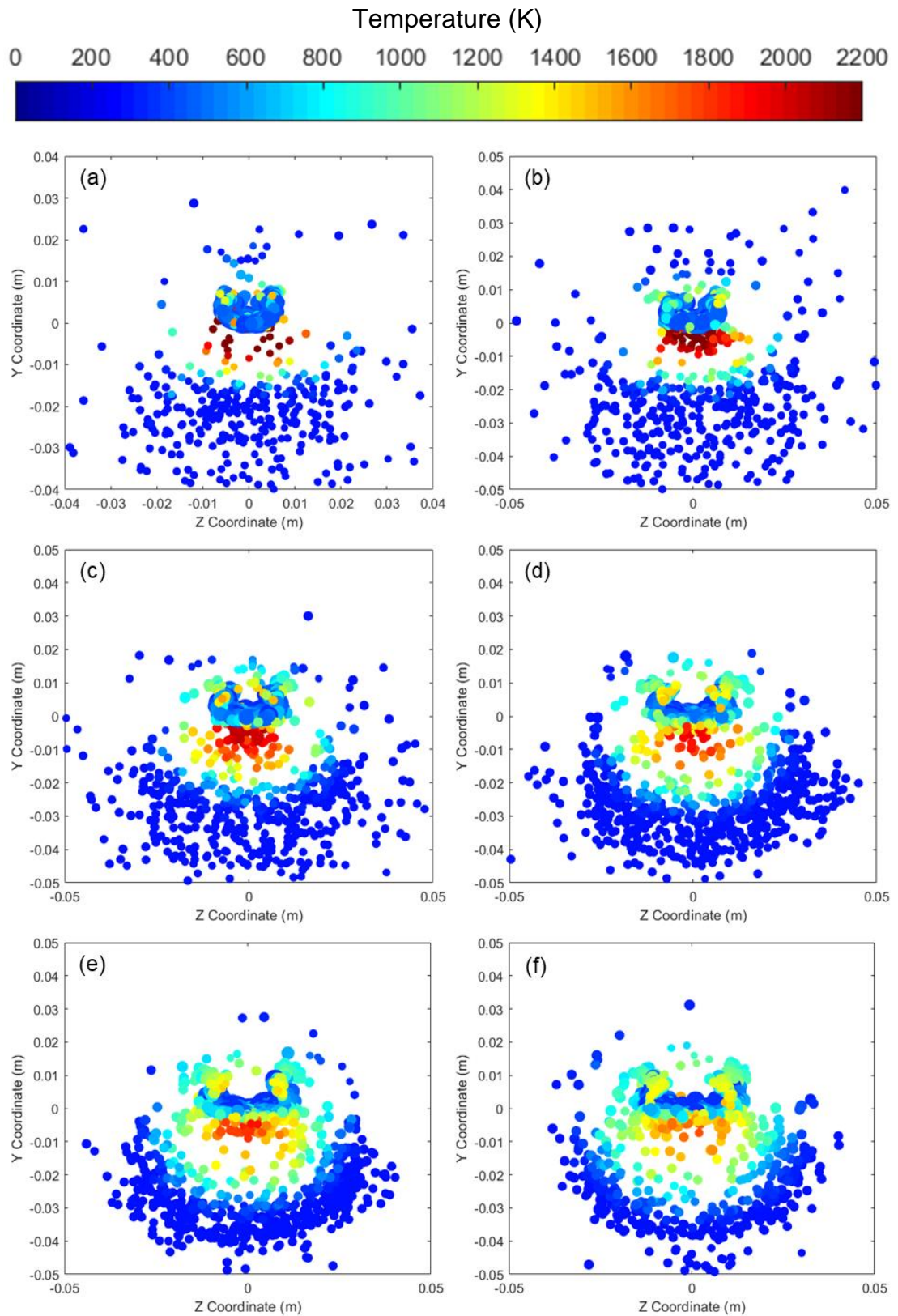


Figure 5-38: Effect of distance from the nozzle exit (standoff distance) on inflight particle temperatures with a shroud attachment (a) 85 mm, (b) 105 mm, (c) 125 mm, (d) 145 mm, (e) 165 mm and (e) 185 mm.

5.13 Summary

This chapter employs the use of detailed reaction mechanisms along with the eddy dissipation concept combustion model and investigates the effect of the combustion model on the adiabatic flame temperature within the combustion chamber. The eddy dissipation model with a single step reaction over predicts the gas temperature by as much as 300 K within the combustion chamber as compared to the adiabatic flame temperature. The eddy dissipation concept with a robust reaction mechanism avoids the over prediction in the flame temperature as seen with the eddy dissipation model employed within prior suspension high velocity oxy fuel thermal spray studies. Additionally, this chapter has developed an attachment to develop a hybrid nozzle for suspension high velocity oxy fuel thermal spray. The hybrid nozzle will improve the deposition of a coating from oxygen sensitive materials and the deposition of composite coatings formed from an oxygen sensitive material. An initial investigation is conducted to determine the importance of injection parameters for a radial injection of suspension within a high velocity oxy fuel flame. The windward trajectory and breakup location predicted from the numerical model are compared to experimental measurements obtained through high speed imaging. The windward trajectories match well to high speed imaging downstream from the breakup point. The breakup point however shows a large discrepancy of 17.4 % difference at low flow rates of 50 ml/min. There is improved agreement with the experimental data at higher flow rates with a discrepancy of just 4 % at 300 ml/min. Better agreement can be obtained through the use of interface resolving methods such as the volume of fluid model this approach however is orders of magnitude more computationally expensive.

From the investigations into the suspension injection flowrate, injection angle and the diameter of the injector are conducted. It is demonstrated that the injection conditions

significantly influence the inflight particle conditions. The injection conditions must ensure sufficient momentum to penetrate into the gas to maximise heat and momentum transfer from the flame to the suspension droplets. However, an excessively high flow rate must be avoided to avoid adversely cooling or decelerating the jet. For the conditions investigated it was seen that the optimum flow rate occurred between of 150 – 200 ml/min. Increasing the flow rate further to 300 ml/min resulted in an additional gas velocity and gas temperature decrease of 1100 m/s and 1400 K respectively. Increasing the suspension flow rate from 150 ml/min to 300 ml/min witnessed a decrease in the maximum velocity and temperature of 450 m/s and 550 K respectively.

Injectors can additionally maximize the injection velocity by reducing the diameter of the injector orifice which allows for the use of lower suspension flow rates by increasing the suspension penetration and hence increase in-flight particle velocities and temperatures. Reducing the injector diameter from 0.6 mm to 0.3 mm witnessed an increase in the maximum velocity and average temperature by as much as 300 m/s and 180 K. Smaller injectors are however more prone to clogging and therefore the smallest injector that does not promote clogging should be employed to inject the suspension. It is seen that the angle of injection influences the particle velocities and temperatures. A positive injection angle results in higher inflight particle velocities due to the higher initial velocity component in the crossflow direction. A negative injection angle allows for an increase in the inflight particle temperatures as the suspension is injected with an initial velocity opposing the crossflow. The suspension must be decelerated and then accelerated in the direction of the crossflow. This allows for increase in the time the particles are exposed to the high temperature jet improving the heat transfer to the particles. All three injection types are useful as high melting

point materials will benefit from a negative injection and low melting point materials will benefit from a positive injection.

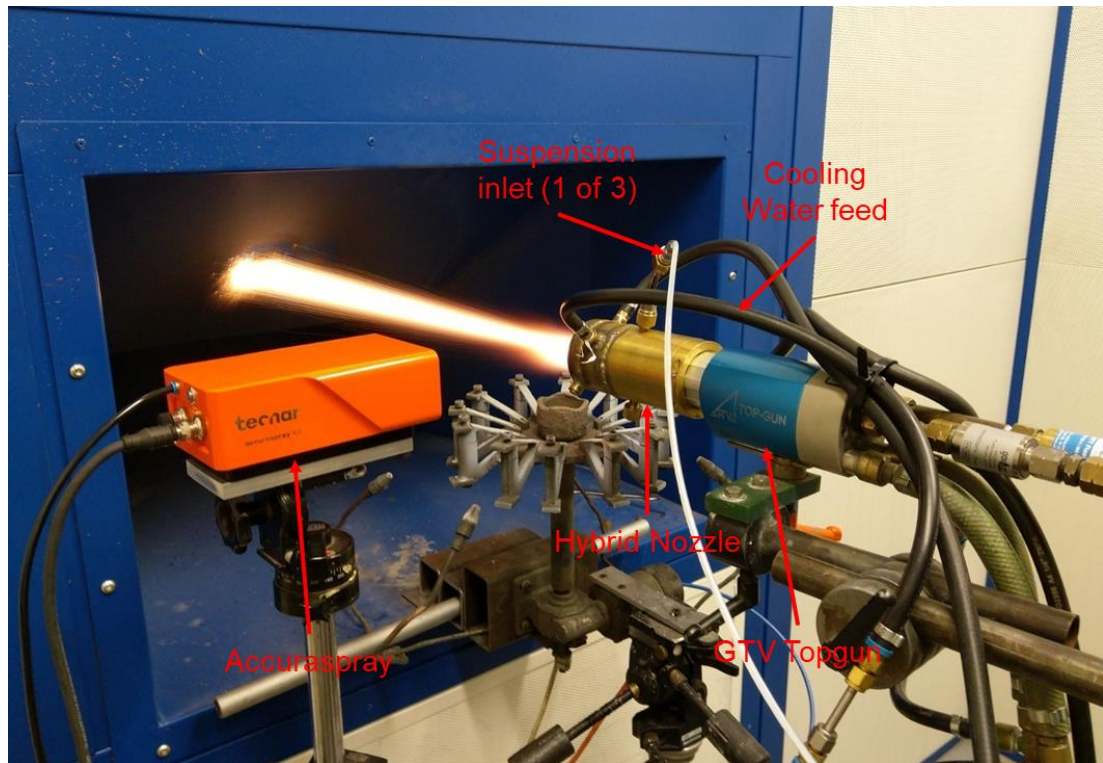


Figure 5-39: Hybrid nozzle attached to the GTV Topgun SHVOF thermal spray system.

Finally, an attachment to develop a hybrid suspension high velocity oxy fuel thermal spray process has been designed and manufactured. The hybrid nozzle designed and manufactured is shown in figure 5-39. The hybrid suspension high velocity oxy fuel thermal spray process is a new process developed and documented within this thesis. The hybrid nozzle is a design that combines an axial injection into the combustion chamber with a shroud attachment that allows for a radial injection into the shroud with a shrouding gas to prevent air entrainment into the shroud. The effect of the diameter of the shroud at the exit on the air entrainment, gas velocity and gas temperature are investigated. The 28 mm diameter for the shroud exit is employed as it allows for small air entrainment which can be prevented with the addition of the

shrouding gas. Additionally, it allows for a lower velocity at the injection location than the 24 mm shroud exit diameter considered. This will allow suspension to penetrate the jet more readily. The effect of the shrouding gas flow rate is considered and it is seen that a flow rate of 2 g/s is sufficient to prevent any air entrainment within the shroud. The effect of the standoff distance with the shroud attachment is investigated to determine the optimum spray distance for the shroud and it is suggested that at the operating conditions employed within this chapter that a standoff distance of 125 mm – 145 mm be employed to maximise inflight particle velocities and temperatures.

Chapter 6: Investigation into the Effect of the Nusselt Number Correlation

6.1 Introduction

Within SHVOF thermal spray heat is transferred between the high temperature gas flow and the suspension. Within the DPM model the particle temperature is determined using a simple heat balance given by equation 6.1. Where the particle temperature is given by T_p , the gas temperature is given by T_g , where the time is given by t , the surface area of the particle is given by A_p , the mass of the particle is given by m , the specific heat capacity of the particle is given by c_p and h_{fg} refers to the latent heat.

$$(m \cdot c_p)_p \frac{dT_p}{dt} = hA_p(T_g - T_p) - \frac{dm}{dt} h_{fg} \quad (Eq\ 6.1)$$

To determine the heat transfer coefficient, h , a Nusselt number correlation is employed which determines the ratio of convective to conductive heat transfer. There are a wide variety of Nusselt number correlations available within the literature focusing on heat transfer to spherical and non-spherical particles [172], [173], [174] & [175]. Currently within SHVOF thermal spray to determine the heat transfer coefficient the Ranz-Marshall correlation is the only model that has been employed to determine the Nusselt number as outlined within the literature review. The Ranz-Marshall correlation is given by equation 6.2, it is an incompressible correlation which was established at low Mach numbers and low Reynolds numbers for application to spray dryers. The popularity of this model came about from the observation that the correlation extrapolates well five times above the range of Reynolds numbers at which the experiments were conducted [128]. The Ranz-Marshall correlation is the only correlation employed by Ansys Fluent. Alternative correlations can be employed

through the use of user defined functions (UDF's) written in C++. A prior numerical investigation into SHVOF thermal spray by Jadidi et al [20] has shown that the Ranz-Marshall correlation under-predicts the particle temperatures by as much as 500 K in comparison to Accuraspray G3 measurements. Researchers have looked at fine tuning the constants within the Ranz-Marshall correlation for HVOF thermal spray application to better predict particle temperatures [176].

$$Nu = \frac{hd_p}{k_\infty} = 2.0 + 0.6Re_d^{1/2}Pr^{1/3} \quad (Eq\ 6.2)$$

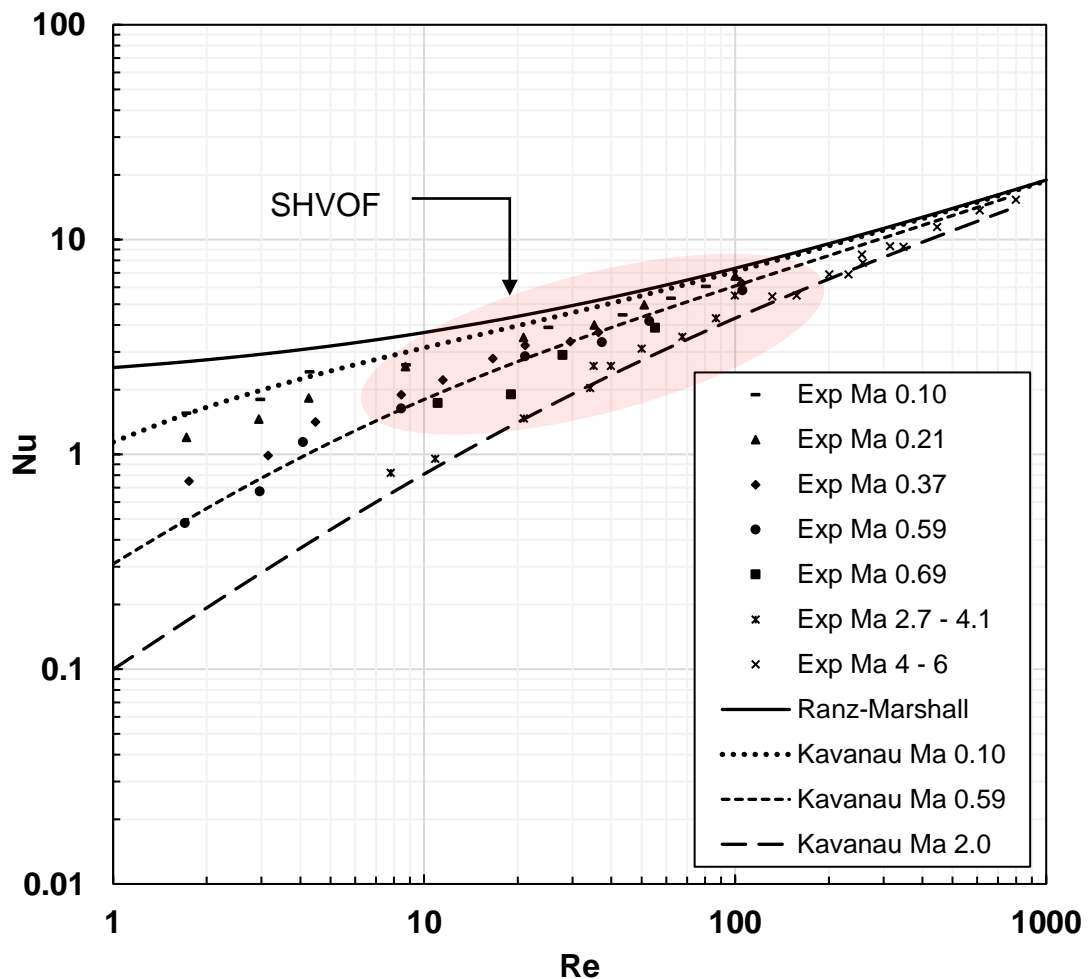


Figure 6-1: Convective heat transfer coefficient for a sphere in a rarefied gas at varying Mach numbers adapted from [130].

Carlson et al. [177] and Drake et al. [131] measured the heat transfer coefficient for particles within a rarefied supersonic and subsonic gas flow respectively. The Nusselt number varied from Mach numbers (0.1 - 6) is plotted in figure 6-1. Their findings show a dependency of the Nusselt number on the Mach number. Therefore, the Nusselt number correlation must account for the effect of the Mach number to accurately predict the heat transfer coefficient which numerical models employed for SHVOF thermal spray have failed to do. An alternative compressible Nusselt number correlation to the Ranz-Marshall correlation has been applied to cold spray and high velocity oxy fuel (HVOF) thermal spray but has not yet been employed within SHVOF thermal spray. The compressible correlation [178] which is given by equation 6.3 accounts for Mach number as well as the Reynolds number and Prandtl number effects on the Nusselt number correlation. The compressible correlation is only valid for Mach numbers greater than 0.24 and where the gas temperature exceeds the particle temperature.

$$Nu = 2.0 + 0.4Re_p^{0.5} Pr^{1/3} \exp(0.1 + 0.872 Ma) \quad (Eq\ 6.3)$$

When particle length scales are of the order of the length scales between particles the effects of rarefaction are significant. The Knudsen number (Kn) which is given in equation 6.4 can be used to evaluate the effects of rarefaction. The Knudsen number is defined as the ratio of the molecular free path length, λ , to the representative physical length scale which in particle laden flows is given by the particle diameter, d_p . Alternatively, the Knudsen number is proportional to the ratio of the flow Mach number, Ma , to the particle Reynolds number, Re_p , where, γ , refers to the heat capacity ratio. The Knudsen number for the particles can be as large as 1.0 for SHVOF thermal spray which is later shown within this chapter.

$$Kn = \frac{\Lambda}{d_p} \approx \sqrt{\frac{\pi\gamma}{2}} \left(\frac{Ma}{Re_p} \right) \quad (Eq 6.4)$$

As the Knudsen number increases the effects of rarefaction become significant and non-continuum effects must be considered. For particle laden flows, as the Knudsen number of the particles increases into the slip flow regime, the first observable non continuum effect occurs on the surface of the particles. A temperature jump and velocity slip are apparent on the surface of particles [27]. As the Knudsen number increases further into the free molecular flow regime there is no interaction between gas molecules approaching the surface of the particles and those leaving the surface. Hence, the gas molecules arriving at a surface will have the full freestream velocity. Figure 6-2 shows the change in the particle boundary layer in the different flow regimes.

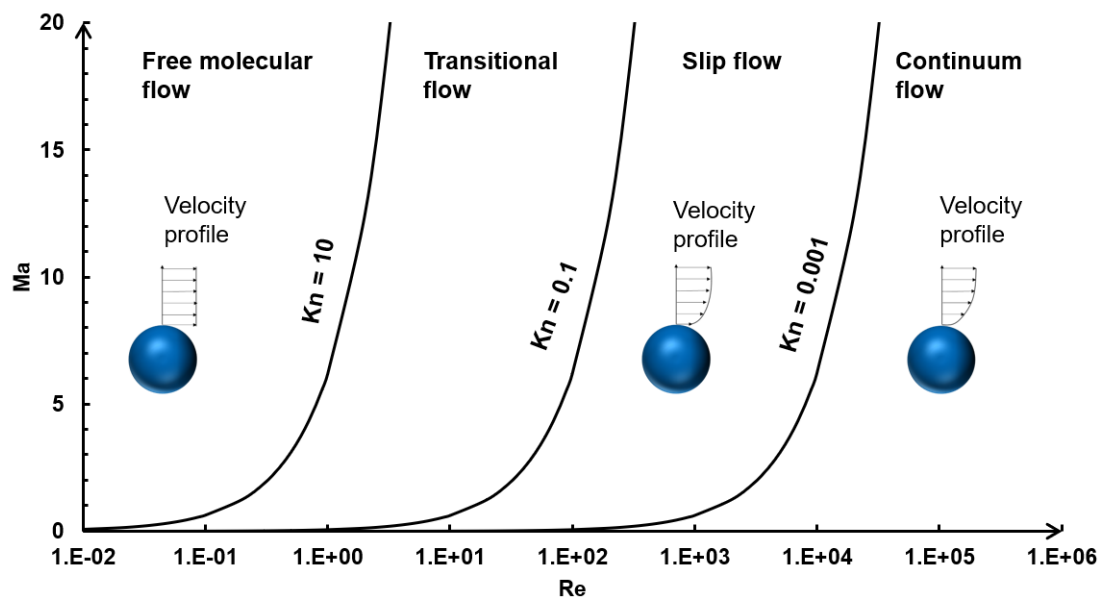


Figure 6-2: Effect of Knudsen number on different flow regimes, adapted from [27].

Kavanau et al. [130] developed a correlation (equation 6.5) for the Nusselt number that accurately determines the heat transfer coefficient for compressible flows within the slip regime. Their correlation asymptotically approaches the value predicted by

Sauer et al [179] for free molecular flow. Figure 6-1 also compares the Nusselt number correlation to the experimentally obtained measurements from Drake et al. and Carlson et al. with varying flow Mach number from 0.10 - 6.0. The correlation by proposed by Kavanau et al. is shown to fit well to particles within a rarefied supersonic flow as well as subsonic flows. The correlation was plotted against experimental measurements for the Nusselt number for particles in a rarefied gas in subsonic and supersonic conditions.

$$Nu = \frac{Nu_0}{1.0 + 3.42Nu_0 \frac{Ma}{Re_p Pr}} \quad (Eq 6.5)$$

This chapter employs three Nusselt number correlations; the Ranz-Marshall correlation, the compressible correlation and the Kavanau correlation. The aim is to evaluate the effectiveness of three different Nusselt number correlations in order to better predict inflight particle temperatures. The numerical model is validated using time of flight technique and two colour pyrometry measurements of the inflight particle velocities and temperatures respectively. For the experimental investigation, the Accuraspray 4.0 system from Technar (Saint-Bruno-de-Montarville, Canada) is employed to obtain inflight velocity and temperature measurements of the particles. Particle velocities and temperatures are obtained at four locations within the free-jet. Through the use of more physically representative correlations to determine the heat transfer correlation a better understanding of how the particle temperature vary inflight can be established.

6.2 Modelling Methodology

The premixed hydrogen and oxygen are injected into the combustion chamber using an annular inlet located 4 mm from the centre of the combustion chamber and with a width of 1 mm. A steady state gas flow field is established before injecting any suspension. To model the gas phase the continuity, momentum conservation, ideal gas law, energy conservation, species fraction and the realizable k- ϵ turbulence model with an enhanced wall function are solved for using the SIMPLE algorithm; the governing equations for which are described in chapter 3.

The suspension which consists of 20% Cr₂O₃ and 80% H₂O by weight is injected using a two-way coupled multicomponent DPM model. A cone injection is employed consisting of 20 particle streams, a cone angle of 1 degree has been calculated based upon [152]. A Two-way turbulence coupling, secondary breakup and the pressure dependent boiling models have been employed. The unsteady discrete phase is solved for once with every 10 gas phase iterations with a DPM time step of 1×10^{-5} s. The DPM time step has been chosen such that DPM particles move forward no more than one cell on average. The inverse distance node-based averaging is employed to distribute the DPM source term amongst neighbouring cells [153]. The Compressible and Kavanau correlations for the Nusselt number are implemented using UDF's which are provided in Appendix II.

The nozzle geometry, fluid domain geometry, fluid mesh and the numerical schemes for the gas phase are identical to those applied within Chapter 5. The boundary conditions for the gas phase and the discrete phase are outlined in table 6-1. The temperature boundary condition on the walls is based on prior numerical models that have used a constant temperature value of 500 K [20].

Table 6-1: Boundary conditions employed within the model.

Surface	Values	Temperature (K)
Total Gas Flow Rate	0.0059 Kg/s	300
H₂ Flow Rate	440 l/min	-
O₂ Flow Rate	220 l/min	-
Outlet Condition	1 atm	Zero Gradient
Equivalence Ratio	1	-
Suspension Flow Rate	50 ml/min	300
Wall Boundary Condition	0 m/s	500

6.3 Experimental Methodology

6.3.1 Inflight Measurements of Ensembled Averaged Particle Velocity and Temperature

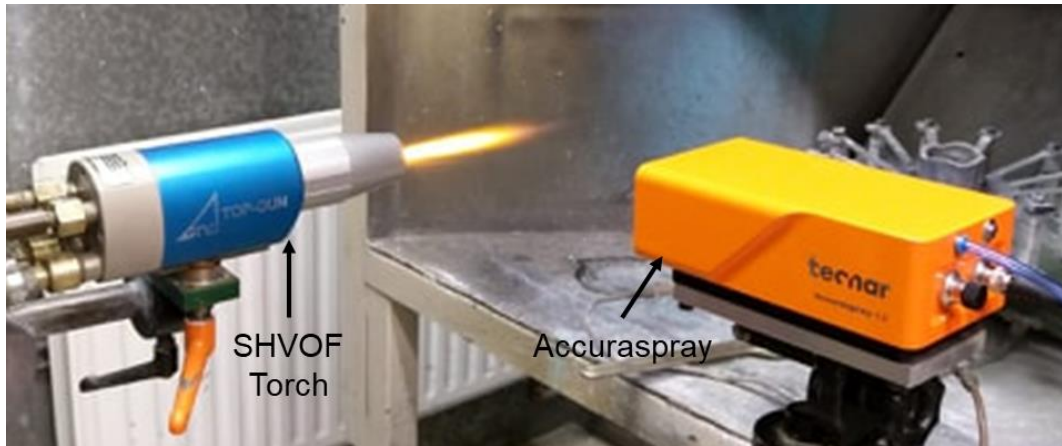


Figure 6-3: Accuraspray system in operation with SHVOF thermal spray.

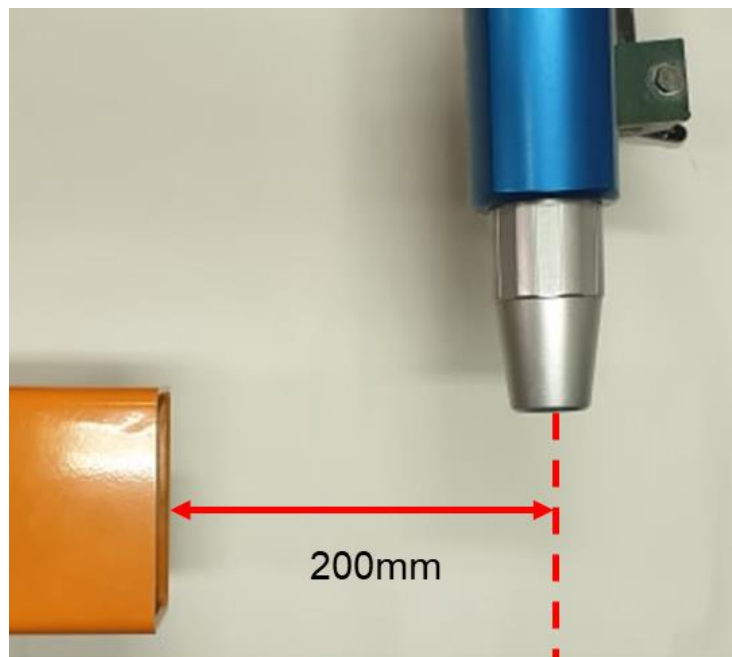


Figure 6-4: Accuraspray measurement device positioning to the SHVOF thermal spray gun.

The inflight particle velocities and temperatures were measured using the Accuraspray G4 device (Technar, Saint-Bruno-de-Montarville, Canada). The Accuraspray system

measures the ensembled average values of the inflight particle velocities and temperatures. The Accuraspray 4.0 system takes the average measurement from a volume of approximately 3.2mm x 10 mm x 25mm. Figure 6-3 shows the Accuraspray system in operation with the SHVOF thermal spray gun. The measurements were taken using a two colour pyrometer that evaluates the radiation intensity from the particle at two wavelengths. Planks law describes the radiation emitted from a body which is given by equation 6.6. Where, I , refers to the radiation intensity at a wavelength, λ , for a body at temperature, T , with an emissivity, ϵ , a diameter, d , where C_1 and C_2 are calibration constants. The radiation intensity is measured at two wavelengths (λ_1 and λ_2) at the same location and the temperature can be determined from equation 6.7 [108], [180], [181].

$$I(\lambda, T) = \epsilon d^2 \frac{C_1}{\lambda^5} \frac{1}{\exp\left(\frac{C_2}{\lambda T}\right) - 1} d\lambda \quad (Eq 6.6)$$

$$T = \frac{C_2(\lambda_1 - \lambda_2)}{\lambda_1 \lambda_2} \left[\ln\left(\frac{I_{\lambda_1}}{I_{\lambda_2}}\right) + 5 \ln\left(\frac{\lambda_1}{\lambda_2}\right) \right]^{-1} \quad (Eq 6.7)$$

The particle velocities were determined using a “time of flight” approach [182], where the radiation emitted from the particles is detected at two locations parallel to the direction of travel of the particles. The distance between the two measurement locations is known and hence from the time delay between the two corresponding signals the velocity can be determined. The Accuraspray sensor was placed at four different measurement locations (75, 100, 125 and 150 mm) downstream from the SHVOF gun exit. The sensor was placed at a distance of 200 mm radially from the jet axis [183] as shown in figure 6-4. A 75-kW flame was established, and a suspension comprised of 80% H₂O and 20% Cr₂O₃ by weight is injected at a flow rate of 50 ml/min into the center of the combustion chamber. The measurements for the inflight particle velocity and temperature were obtained at the four measurement locations.

6.3.2 Dynamic Light Scattering

Dynamic light scattering is a technique used to measure the particle size distribution due to the Brownian motion of the particles [184]. Smaller particles move at a higher velocity than larger particles. Light is shone onto the suspension and the particles within the suspension diffract the light. The light is scattered by the particles within the suspension in all directions. The scattered light is measured at an angle and the diffusion coefficient is calculated from the scattered light intensity. From the diffusion coefficient the particle size can be determined by the Stokes-Einstein equation [185]. The particle size distribution within the Cr₂O₃ and H₂O suspension was measured using dynamic light scattering with the Zetasizer instrument (Malvern Panalytical, Malvern, United Kingdom).

6.3.3 Scanning Electron Microscope

Scanning electron microscope (SEM) is an imaging technique that produces an image by focusing a beam of electrons onto a sample. The electrons interact with the atoms in the sample and produce a signal that contains information about the surface topography of the sample. Different types of signals are produced including secondary electrons, backscattered electrons and characteristic x-rays. The electron beam is produced thermionically from the tungsten cathode. Electrons are accelerated by applying a voltage which usually ranges from 0.2 kV to 40 kV, with the value depending on the sample being scanned. The SEM image taken within this chapter was taken from the XL30 SEM device (Philips, The Netherlands) using the secondary electron mode. An acceleration voltage, spot and working distance of 15 kV, 5 and 10.1 mm were used respectively.

6.4 Effect of the Nusselt Number Correlation on Gas Temperature and Evaporation Rates

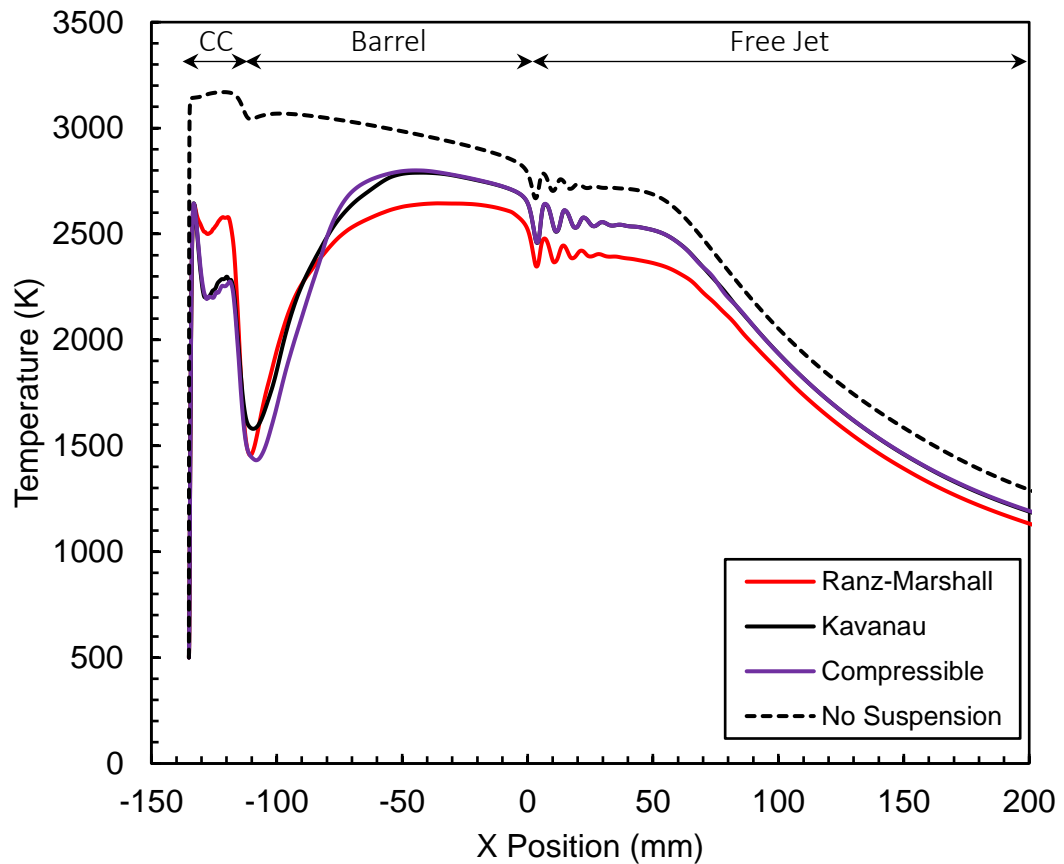


Figure 6-5: Centreline Gas temperature for the three Nusselt correlations.

The two-way coupling between the discrete phase and the continuous phase accounts for the effect of the discrete phase on the continuous phase as well as the effect of the continuous phase on the discrete phase. Therefore, the effect of the Nusselt number correlation on the gas phase and particularly the gas temperature and the suspension evaporation rate must be considered. Figure 6-5 show the centerline gas temperature predicted by the Ranz–Marshall, Kavanau and the compressible correlations. From figure 6-5, it can be seen that both the Kavanau and the compressible correlation predict a very similar temperature while the Ranz–Marshall correlation predicts a

significantly higher gas temperature within the combustion chamber and a lower gas temperature within the barrel and the free jet. The heat transferred to the suspension is proportional to the heat transfer coefficient. Kavanau et al. [130] and Drake et al. [131] evaluated the heat transfer coefficient for particles within high Mach flows. From these studies it can be demonstrated that as the Mach number increases the heat transfer coefficient decreases. Incompressible correlations for the Nusselt number are unable to capture this behaviour. An overestimate of the heat transfer coefficient will result in a lower and delayed evaporation rate which produce the higher gas temperatures within the combustion chamber and lower gas temperatures in the barrel and the free jet which is illustrated with the Ranz-Marshall correlation.

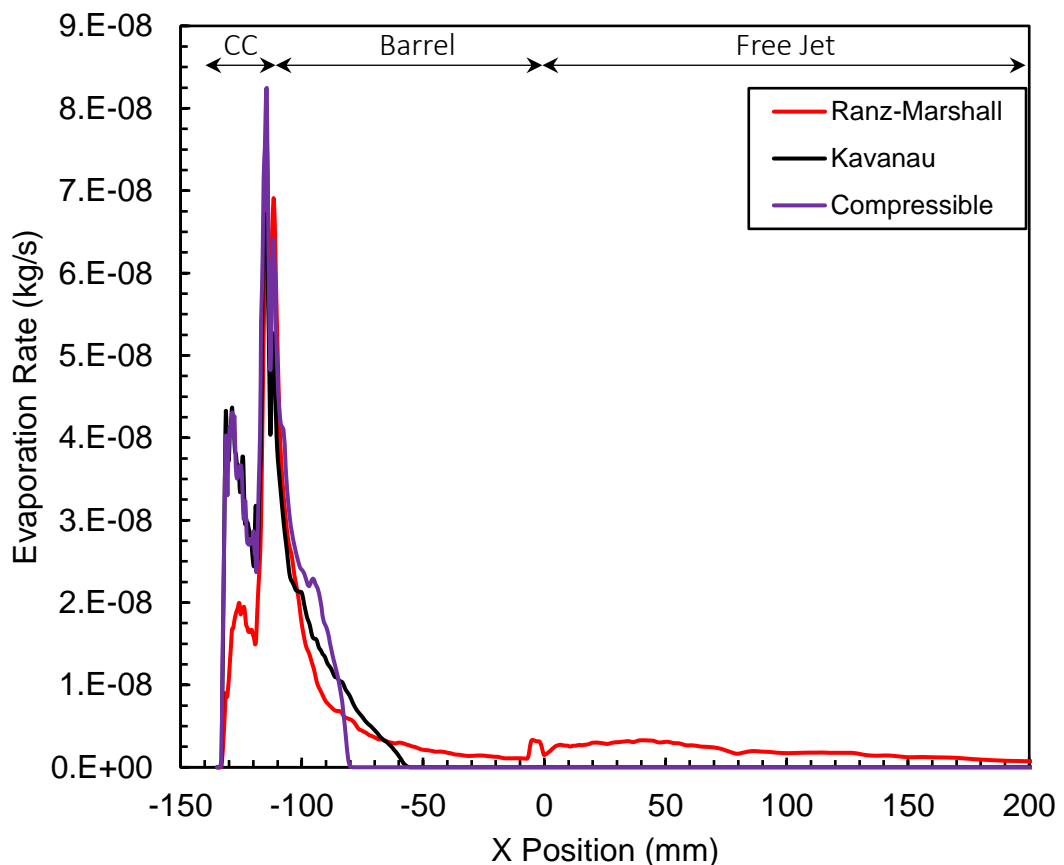


Figure 6-6: Centreline evaporation rates for the three Nusselt correlations.

Accurately modelling the evaporation of the liquid component of the suspension is vital in accurately predicting inflight particle temperatures. Evaporation results in phase change from the suspension to the flow field which influences the flow field. Additionally, only once the liquid component of the suspension has vaporized can the suspension droplet temperature exceed the evaporation temperature of the liquid. Hence, the evaporation rate can significantly impact the inflight particle temperatures which is one of the main parameters of interest to determine the effect of the operating conditions on the coating structure and properties.

Figure 6-6 shows the centerline evaporation rate predicted by the Ranz–Marshall, Kavanau and Compressible correlations. From figure 6-6, it can be seen that a very similar evaporation rate profile is predicted by the Kavanau and the compressible correlation. Both the correlations predict a maximum centreline evaporation rate within the combustion chamber of approximately 4.2×10^{-8} kg/s, whilst the Ranz–Marshall correlation predicts a lower maximum evaporation rate of 2.0×10^{-8} kg/s. In addition to this, it can be seen from figure 6-6 that the compressible correlation predicts evaporation to commence earliest at a distance of 80 mm (inside the nozzle) from the nozzle exit. The Kavanau correlation predicts evaporation to commence at 60 mm (inside the nozzle) from the nozzle exit. Whilst the Ranz–Marshall correlation predicts the evaporation to continue all the way to 200 mm (outside the nozzle) from the nozzle exit. A typical standoff distance for SHVOF thermal spray is 85 mm from the nozzle exit and hence this correlation predicts that moisture will still be present within the particles as they deposit onto a substrate. Particles within this state will not adhere well to the substrate upon impacting the substrate. The reduction in the gas temperature within the free jet region seen in figure 6-5 for the Ranz-Marshall correlation is in large part a result of the heat requirement to vaporize the liquid.

6.5 Effect of the Nusselt Number Correlation on the Average Inflight Particle Velocities and Temperatures

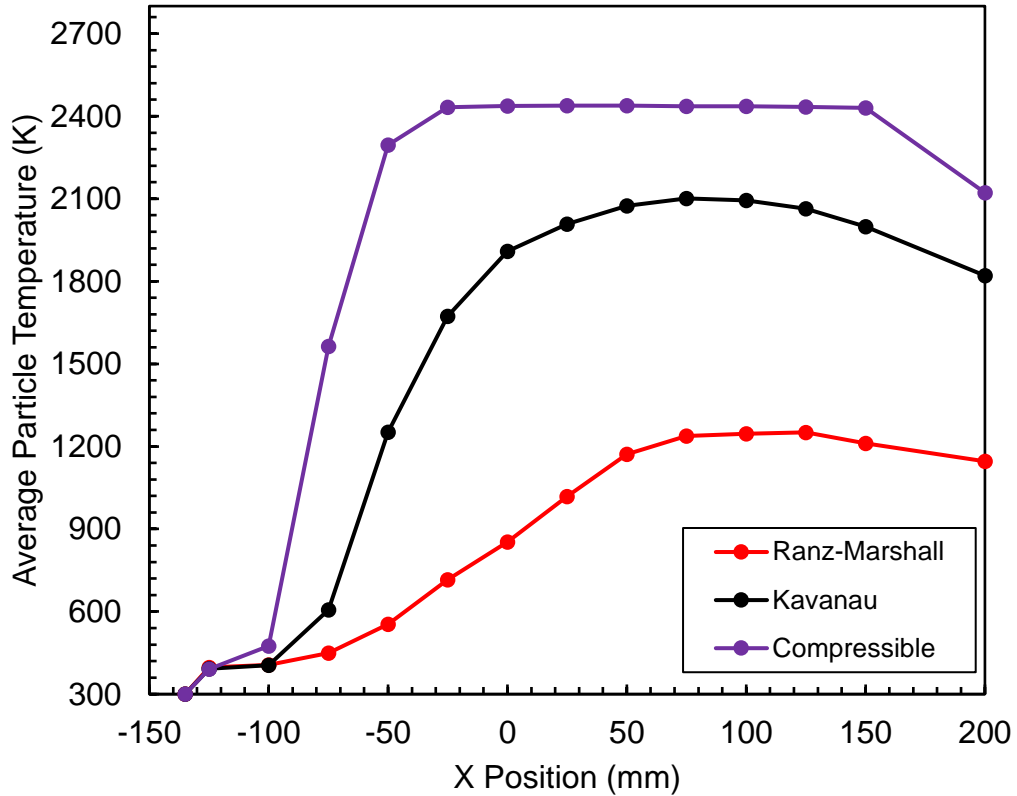


Figure 6-7: Average inflight particle temperatures for the three Nusselt correlations.

Alternative heat transfer coefficients have been employed to address the under prediction in the particle temperature seen within the literature by Jadidi et al. [20]. The effect of Nusselt number correlation on the inflight particle dynamics must be considered. Figure 6-7 shows the average inflight particle temperatures predicted by the three different Nusselt correlations. It can be seen from figure 6-7 that the compressible correlation predicts the highest average particle temperatures and lowest average particle temperatures is predicted by the Ranz–Marshall correlation. The higher temperatures predicted by the compressible correlation is in large part due to the evaporation rate. The compressible correlation predicts evaporation to commence earliest allowing for greater duration of heating which results in the highest particle

temperature. The Ranz–Marshall correlation predicts evaporation to commence later than the other two correlations which leaves a shorter duration for particle heating. Hence, the Ranz–Marshall correlation predicts the lowest average inflight particle temperatures.

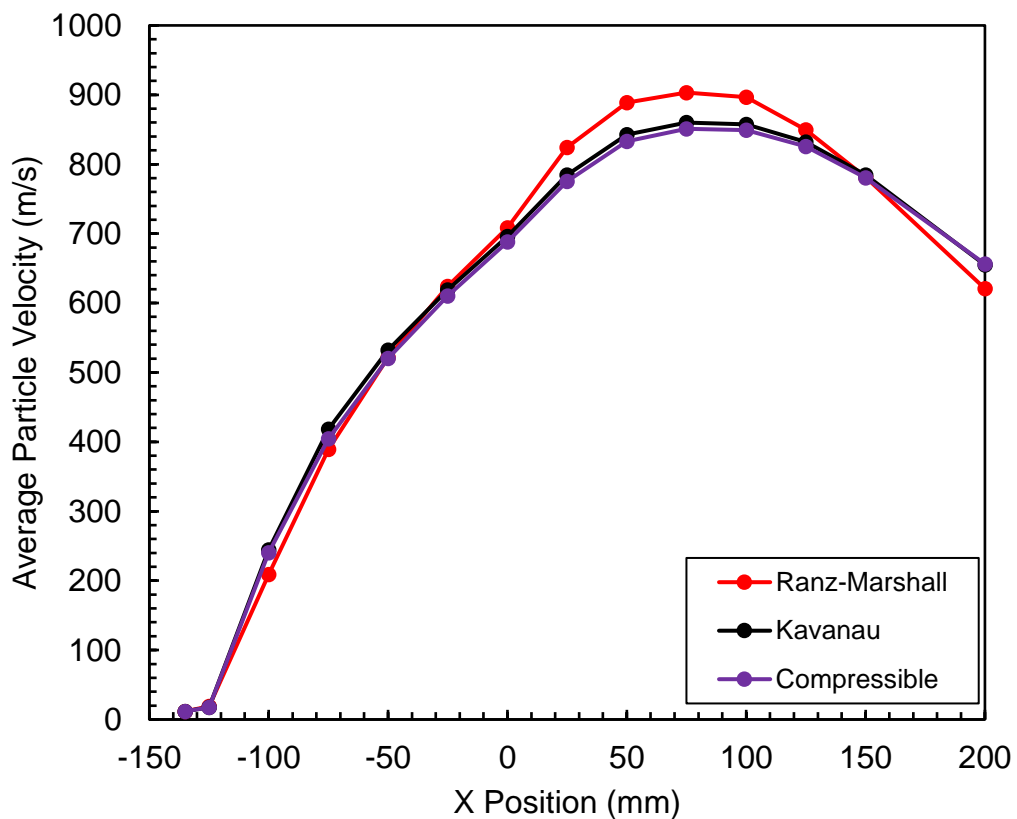


Figure 6-8: Average inflight particle velocities for the three Nusselt correlations.

Figure 6-8 shows the average inflight particle velocities predicted by the three different Nusselt correlations. It can be seen from figure 6-8 that the Kavanau and compressible correlation predict a very similar inflight particle velocity. The particle velocities predicted by the Ranz-Marshall correlation deviates from the other two correlations downstream from the nozzle exit. The gas temperatures predicted by the Ranz-Marshall correlation differs slightly from the other two correlations considered. The difference in the gas temperature prediction will affect the gas velocity and the difference in the particle velocity prediction with the Ranz-Marshall correlation.

6.6 Effect of the Nusselt Number Correlations on the Distribution of Inflight Particle Conditions Prior to Impact

The average inflight particle conditions give a broad overview on the inflight particle states. However, for a more complete picture the distribution can shed more light into how the Nusselt number effects the particle velocities, temperatures, diameters, and the liquid left within the suspension prior to deposition. Each of the distributions are taken at a standoff distance (SOD) of 85 mm as this is the distance typically sprayed for SHVOF using the operating conditions specified [13], [186].

Figures 6-9 (a), (b) and (c) show the particle temperature distribution predicted from the Ranz–Marshall (a), Kavanau (b) and the compressible (c) correlations at 85 mm from the nozzle exit. Comparing the particle temperature distribution for the Ranz–Marshall (a), Kavanau (b) and the compressible (c) correlations it can be seen that there are drastically different particle temperature distributions predicted by the three correlations. The Ranz–Marshall correlation predicts the widest range of particle temperatures; the model predicts particle temperatures ranging from 1000 K up to 2500 K. The Kavanau correlation predicts a particle temperature distribution ranging from 1800 K – 2500 K. The compressible correlation predicts a very narrow particle temperature distribution predicting all particles have a temperature of around 2400 – 2500 K. The melting temperature of Cr_2O_3 is 2708 K [187] all three models will predict non molten particles. However, the Kavanau and Compressible correlation predict that the particle temperature is much closer to the melting point of Cr_2O_3 than the Ranz–Marshall correlation.

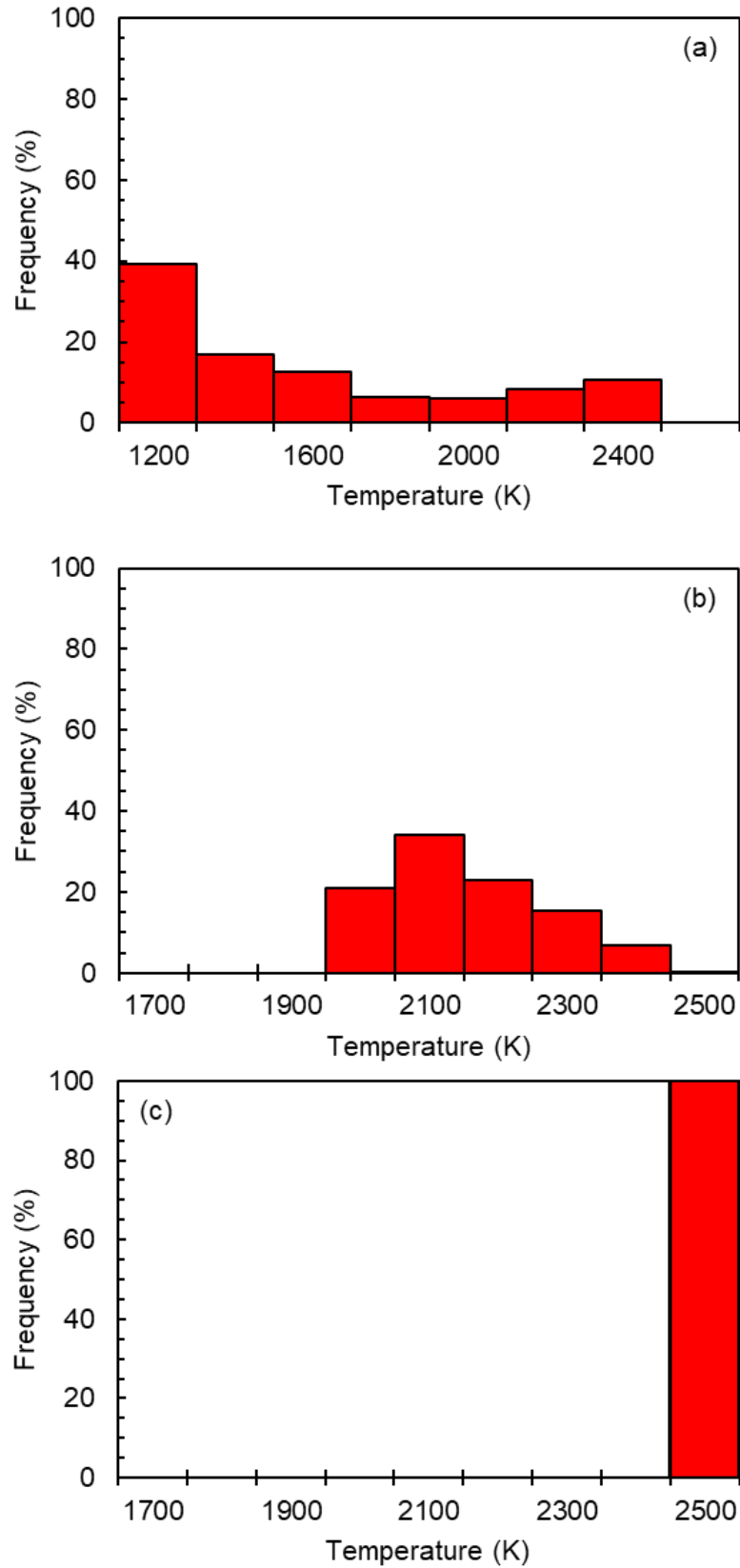


Figure 6-9: Particle temperature distribution Ranz – Marshall (a), Kavanau (b) and compressible (c) correlations at a standoff distance (SOD) of 85 mm.

Within SHVOF thermal spray it is crucial to ensure the liquid component of the suspension is completely vaporized and the particles are sufficiently heated so that they can well adhere to the substrate. Figures 6-10 (a), (b) and (c) show the particle liquid mass fraction distribution predicted from the Ranz–Marshall (a), Kavanau (b) and the compressible (c) correlations at 85 mm from the nozzle exit. Comparing the distribution of the liquid mass fraction it can be seen that the distribution predicted from the Ranz–Marshall correlation differs significantly from the other two correlations. The Ranz Marshall correlation predicts that over 50 % of the particles will have some moisture retained within the droplet upon impacting the substrate. The significantly lower particle temperature seen by the Ranz-Marshall correlation in figure 6-9 is a result of the high degree of particles that have not fully vaporised their liquid component. Over 50% of suspension droplets contain some degree of volatile material. The high moisture content particles are unlikely to deposit onto the substrate to form a well adhered coating. Moisture can negatively affect the contact between impacting particles and the substrate which can contribute to poor adhesion of the particle [188]. Hence, this model suggests a much lower deposition efficiency. Both the Kavanau and the compressible correlations predict that the particles impacting the substrate will not contain any moisture within them.

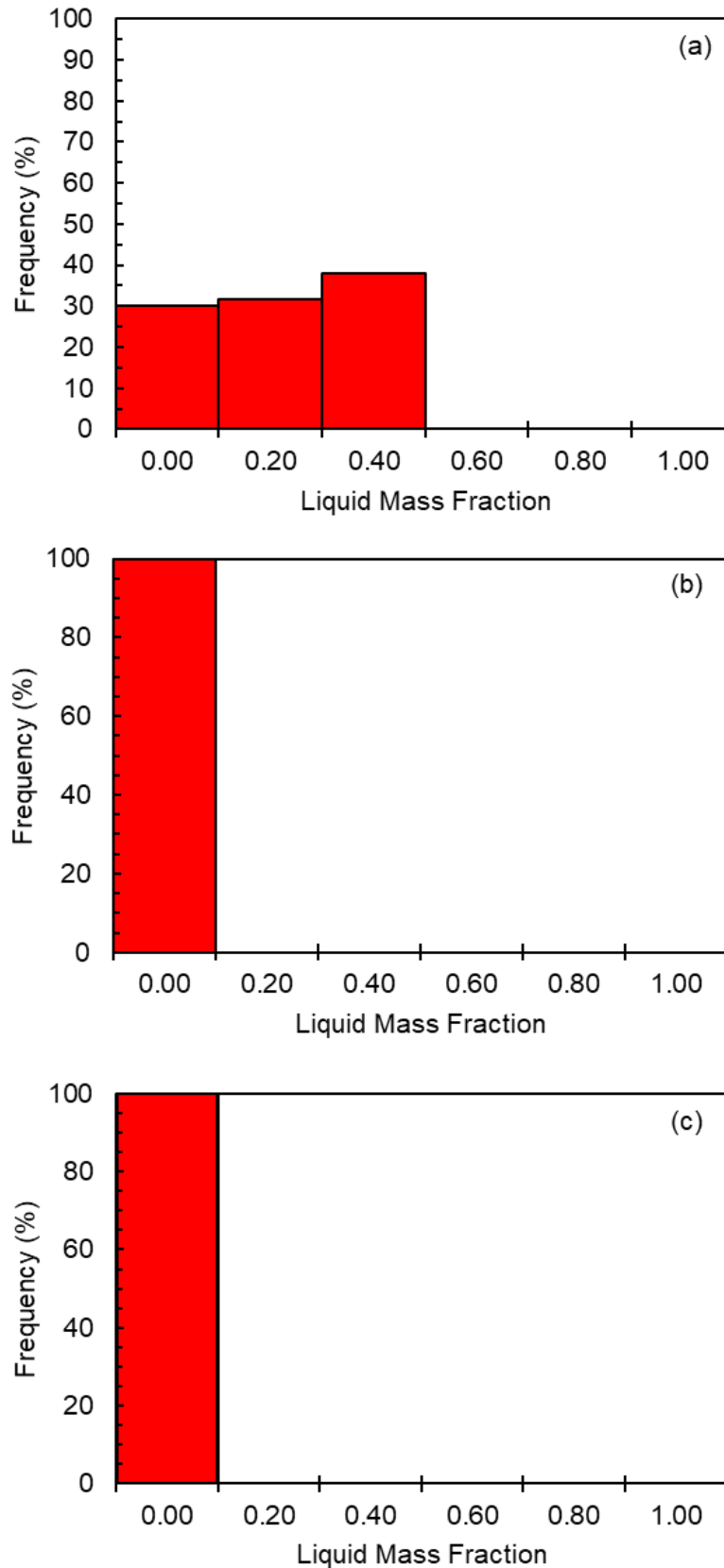


Figure 6-10: Particle liquid mass fraction distribution Ranz – Marshall (a), Kavanau (b) and compressible (c) correlations at a SOD of 85 mm.

SHVOF thermal spray produces dense coatings with a low porosity due to the high particle velocities seen within the process in comparison to other thermal spray processes such as suspension plasma spray. Figures 6-11 (a), (b) and (c) show the inflight particle velocity distribution predicted from the Ranz–Marshall (a), Kavanau (b) and the compressible (c) correlations at 85 mm from the nozzle exit. It can be seen that both the Kavanau and the compressible correlation provide a very similar velocity distribution with the particle velocity spanning 800 – 900 m/s whilst the Ranz-Marshall correlation deviates significantly from the other two correlations with a distribution spanning 900 – 1000 m/s.

Figures 6-12 (a), (b) and (c) show the particle diameter distribution predicted from the Ranz–Marshall (a), Kavanau (b) and the compressible (c) correlations at 85 mm from the nozzle exit. It can be seen that both the Kavanau and the compressible correlations provide a very similar particle diameter distribution with the particle diameters ranging from 7.5 μm – 12.5 μm . Both correlations provide a maximum frequency of 80 % – 85 % at 10 μm whilst the Ranz-Marshall correlation deviates significantly from the other two models. The Ranz-Marshall correlation predicts a wider distribution of particle diameters that span 7.5 μm – 17.5 μm . The Ranz-Marshall correlation predicts larger particles as the suspension droplets have a large quantity of liquid within the droplets.

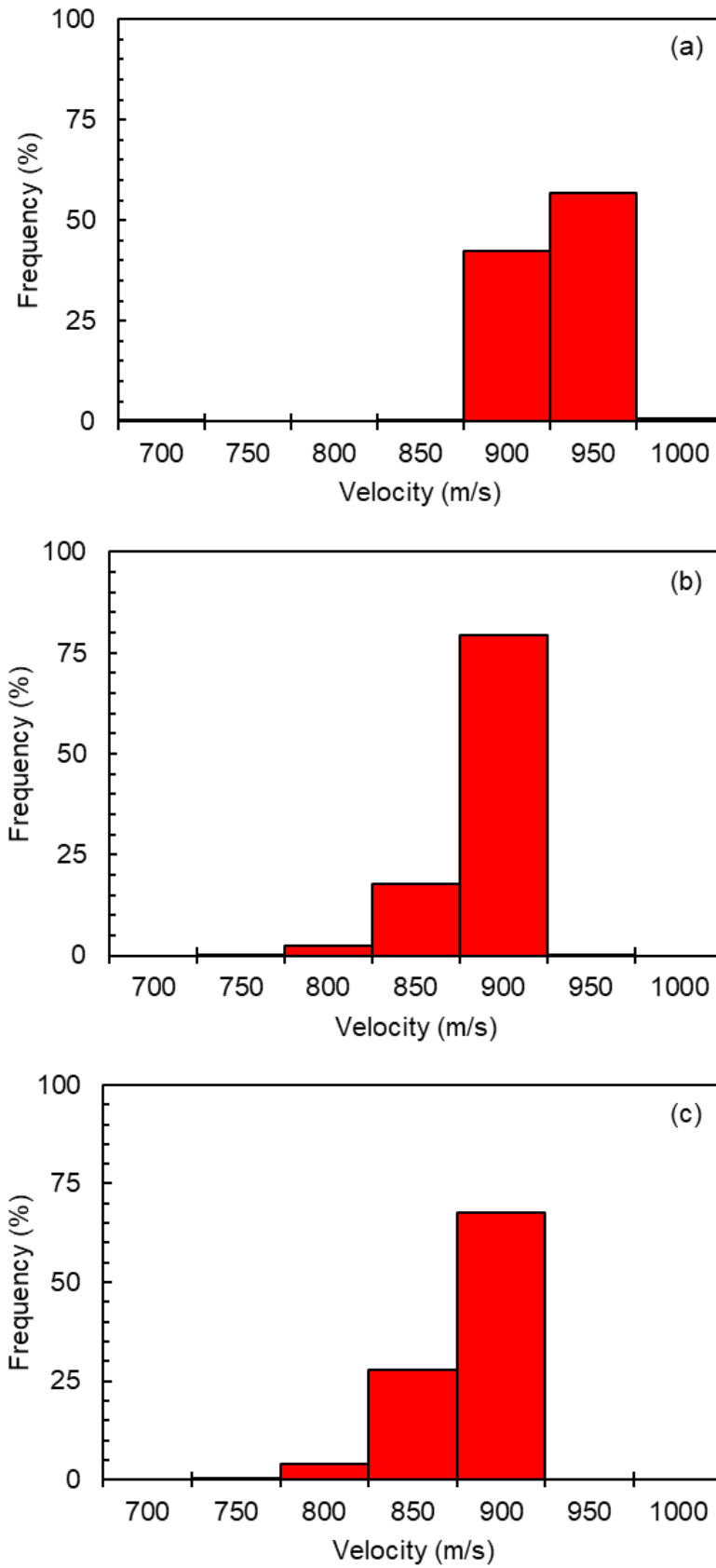


Figure 6-11: Particle velocity distribution Ranz – Marshall (a), Kavanau (b) and compressible (c) correlations at a SOD of 85 mm.

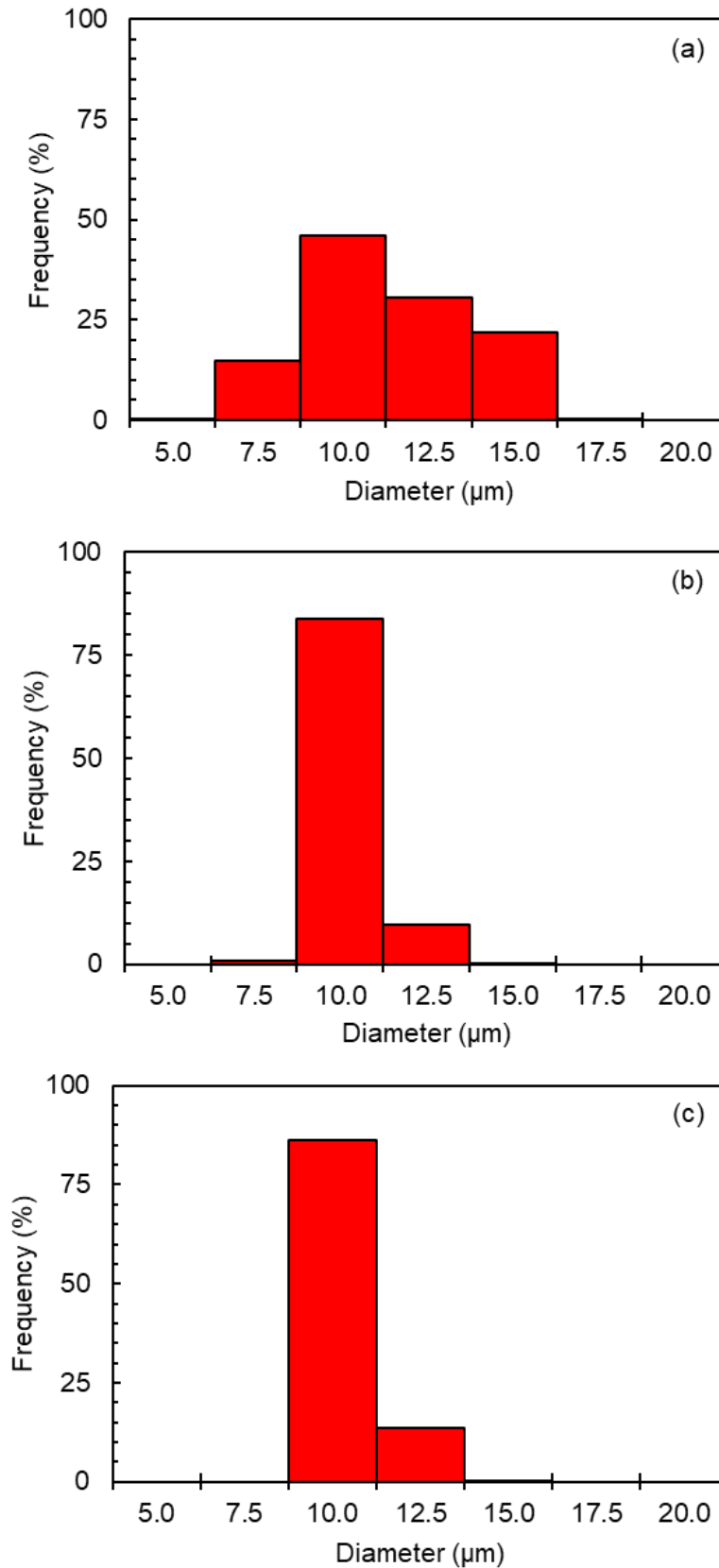


Figure 6-12: Particle diameter distribution Ranz – Marshall (a), Kavanau (b) and compressible (c) correlations at a SOD of 85 mm.

6.7 Experimental Measurements of Inflight particle velocities and temperatures.

Figure 6-13 shows the initial particle size distribution for Cr_2O_3 within the suspension used for the Accuraspray measurements. The particle diameters within the suspension is obtained using dynamic light scattering [184] with the Zetasizer instrument (Malvern Panalytical, Malvern, United Kingdom). Two peaks are seen within the distribution as one peak correlates to the non-agglomerated particle distribution, nominal particle size from the supplier is 500 nm which corresponds to the initial peak. The second peak corresponds to particles that have agglomerated within the suspension. Figure 6-14 shows an SEM image of the particles within the suspension. The suspension was dropped onto a substrate and the moisture was left to dry off. The particles were then imaged using the XL30 SEM device. The SEM images obtained of the suspension further demonstrate this as both the nominal particle and much larger agglomerates can be identified.

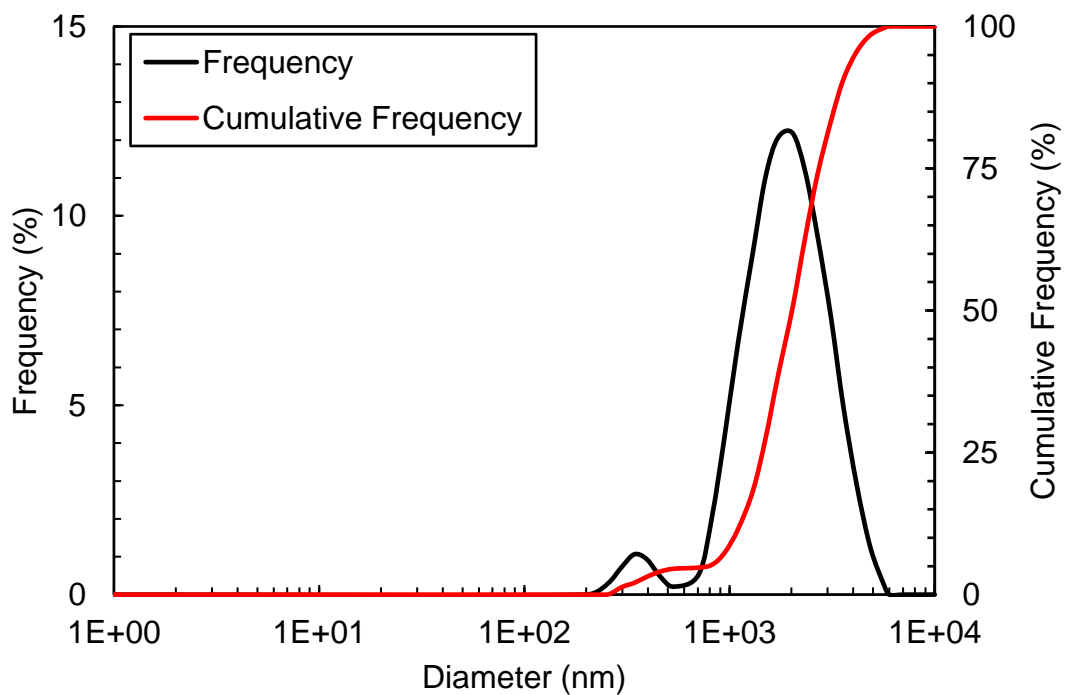


Figure 6-13: Particle size distribution of Cr_2O_3 particles in the suspension.

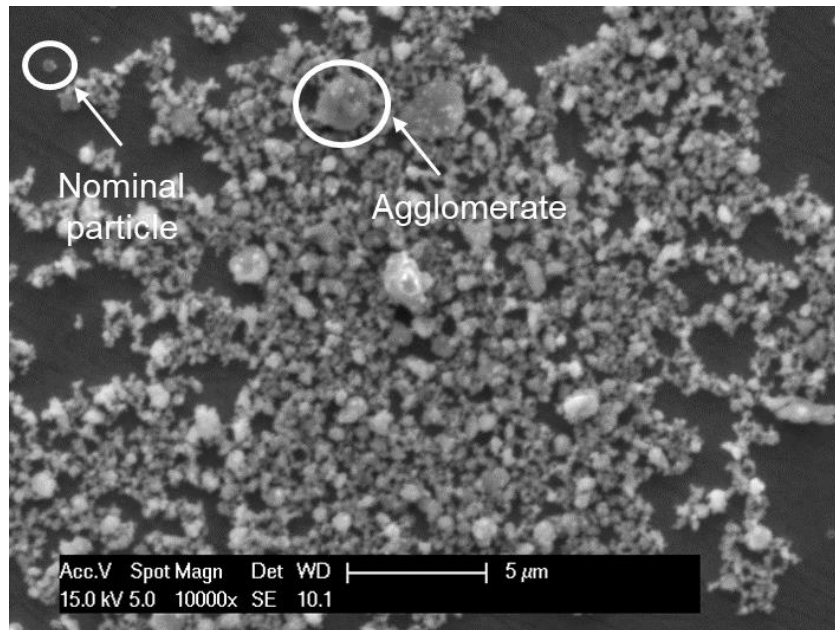


Figure 6-14: SEM image of Cr_2O_3 particles within the suspension.

Experimental measurements of the inflight particle velocity and temperature were taken using the time of flight approach and two colour pyrometry method respectively. Ensemble averages of the inflight particle velocity and temperature measurements were taken at distance 75 mm, 100 mm 125 mm and 150 mm downstream from the nozzle exit. Figures 6-15 and 6-16 show the ensemble average particle velocity and temperature at various standoff distances respectively. It can be seen from figure 6-15 that there is a rapid reduction in the inflight particle velocity from 970 m/s at a standoff distance of 75 mm to 540 m/s at a standoff distance of 150 mm. The particle velocity decreases by 430 m/s with the increase in the standoff distance of 75 mm. It can also be seen from figure 6-15 that there is a rapid decrease in the particle temperature from 2250 K at a standoff distance of 75 mm to 2010 K at a standoff distance of 150 mm. Again, a significant drop of 240 K is seen with the increase in the standoff distance of 75 mm. the time varying data obtained using the Accuraspray device is available within Appendix III.

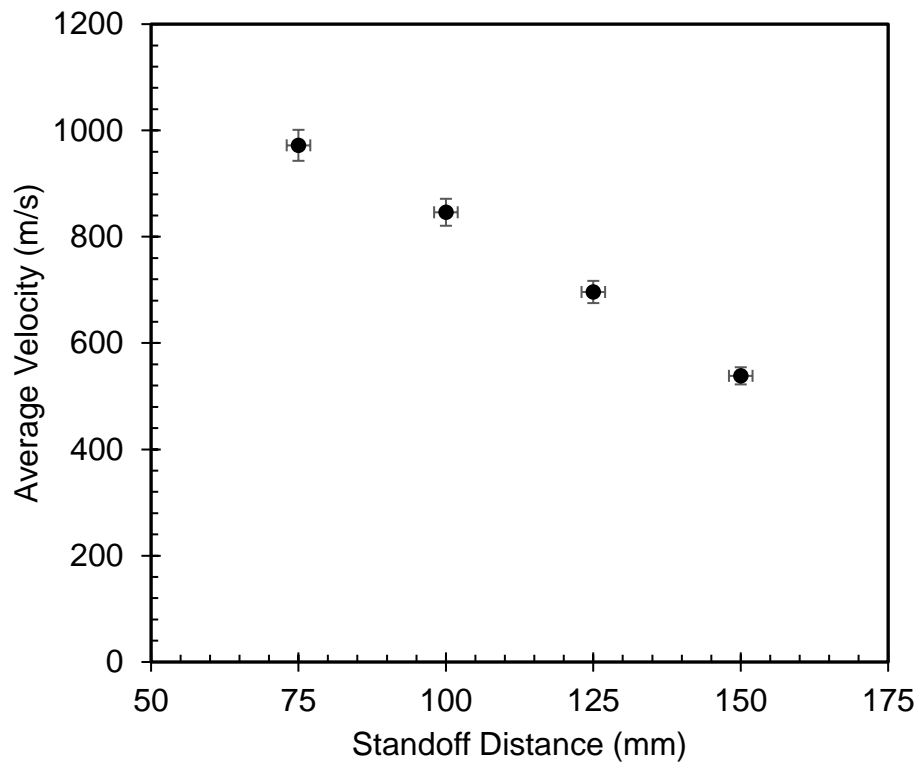


Figure 6-15: Particle velocity measurements at various standoff distances.

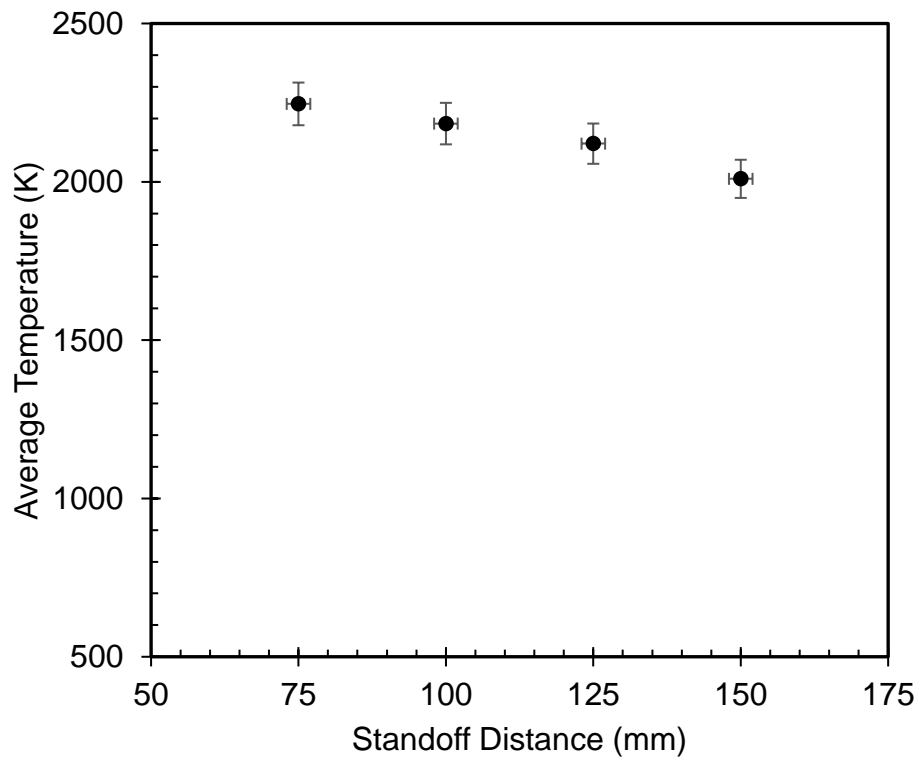


Figure 6-16: Particle temperature measurements at various standoff distances.

It must be noted that there are limitations with the measurement technique employed with the Accuraspray 4.0 diagnostic system. For example, the measurements correspond to an ensembled average value. The particle velocity and temperature measurements do not provide information on the distribution of particle velocities and temperatures nor the standard deviation from the mean. As the particle velocity and temperature measurements are based upon the detected radiation emitted by particles. The measurements are slightly weighted towards larger sized particles. Larger particles have a greater surface area and hence larger particles emit more radiation. Mauer et al. [18] compared the particle velocity and temperature measurements taken from Accuraspray G3 and DPV-2000 for HVOF thermal spray. They evaluated the accuracy of the two-colour pyrometry and time of flight measurements taken by Accuraspray G3 by comparing it to an alternative measurement technique. DPV-2000 uses a single point measurement technique where particle velocity and temperatures can be measured for individual particles. This technique works well for typical particle sizes within HVOF thermal spray but is unable to measure submicron and nanoscale particles within SHVOF thermal spray. They found that both sets of measurements obtained corresponded well to one another, which suggests that the particle diameter does not have a significant impact on the sensor's accuracy. Additionally, the minimum temperature of particles that the Accuraspray system can detect is approximately 1000 °C due to the limited amount of thermal radiation emitted by a cold particle. This will not affect the accuracy of the measurements taken as the particle temperatures well exceed this value as shown in Figure 6-9.

6.8 Validation - Comparison of Nusselt Number Correlations to Accuraspray Measurements

The particle temperature predictions from the three Nusselt number correlation considered have compared to the two colour pyrometry measurements within figure 6-17. All average numerical values were taken using the same measurement volume as the Accuraspray device to allow for a direct comparison. It can be seen from figure 6-17 that the compressible correlation provides a significant improvement in the particle temperature prediction over the Ranz–Marshall correlation. The Ranz-Marshall correlation deviates from the experimental values by an average of 42.9 % whilst the compressible correlation deviates from the experimental values by an average of 12.3%. The compressible correlation accounts for the Mach number effects on the Nusselt number which the Ranz-Marshall correlation does not. The compressible correlation however over predicts the particle temperature by as much as 400 K. There are two conditions within the compressible correlation for it to be valid. The compressible correlation is only valid for Mach numbers greater than 0.24 and where the gas temperature exceeds the particle temperature. At a standoff distance of 150 mm the particle temperature exceeds the gas temperature. This is likely to be the cause of the increase in error between the compressible correlation and the experimental measurements at large standoff distances.

Further improvements to the prediction of inflight average particle temperatures over the compressible correlation are seen by the Kavanau correlation. The Kavanau correlation accounts for the Mach number effects and the Knudsen number effects onto the Nusselt number. The Kavanau correlation deviates from the experimental values by an average of 4.8%. The Kavanau correlation was developed for applications to particles within a rarefied flow. When the flow lies outside the continuum regime a

velocity slip and temperature jump is present onto the surface of the particles, heat transfer and drag coefficients need to account for this. The first order velocity slip was initially derived by Maxwell and is given by equation 6.8 [189]. Similarly, the first order temperature jump was initially derived by Smoluchowki and is given by equation 6.9. The velocity of the gas at the surface and the wall velocity is given by U_s and U_w respectively, the temperature of the gas at the surface and the wall temperature is given by T_s and T_w respectively, Kn , refers to the Knudsen number, n , refers to the wall normal component, γ , refers to the ratio of specific heats and Pr , refers to the Prandtl number. The terms σ_v and σ_T refer to the tangential momentum accommodation coefficient and the thermal accommodation coefficient respectively. The coefficients range from 0 to 1 and take a value of 1 for most engineering materials [190]. The Ranz-Marshall correlation was developed by fitting experimental measurements to a correlation at conditions where the velocity slip and temperature jump are negligible and therefore it will not provide an accurate prediction where a velocity slip and a temperature jump is present.

$$U_s - U_w = \left(\frac{2 - \sigma_v}{\sigma_v} \right) Kn \frac{\partial U_s}{\partial n} \quad (Eq 6.8)$$

$$T_s - T_w = \left(\frac{2 - \sigma_T}{\sigma_T} \right) \left(\frac{2\gamma}{\gamma + 1} \right) \frac{Kn}{Pr} \frac{\partial T}{\partial n} \quad (Eq 6.9)$$

Figure 6-18 evaluates the Knudsen number of the particles within supersonic region of the flow. It can be seen that the particle Knudsen number sits within the range of 0.1 – 1 in the supersonic region of the flow. As the particle Knudsen number well exceeds 0.001 hence the particles are not continuum regime. The particles sit within the transitional flow regime where effects of rarefaction are significant. The Nusselt number correlation must account for the effects of rarefaction on the heat transfer between the gas flow and the suspension. The Kavanau correlation accounts for these effects and hence provides the best overall prediction of inflight particle temperatures.

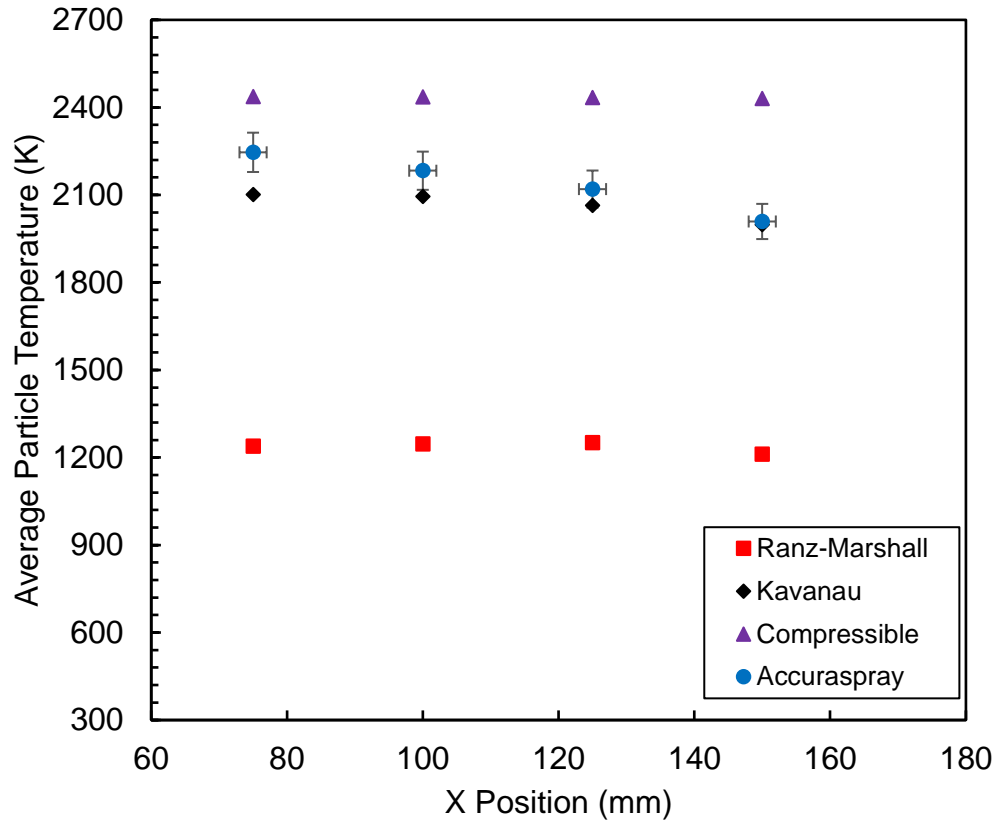


Figure 6-17: Comparison of inflight particle temperatures for the three Nusselt correlations with the Accuraspray measurements.

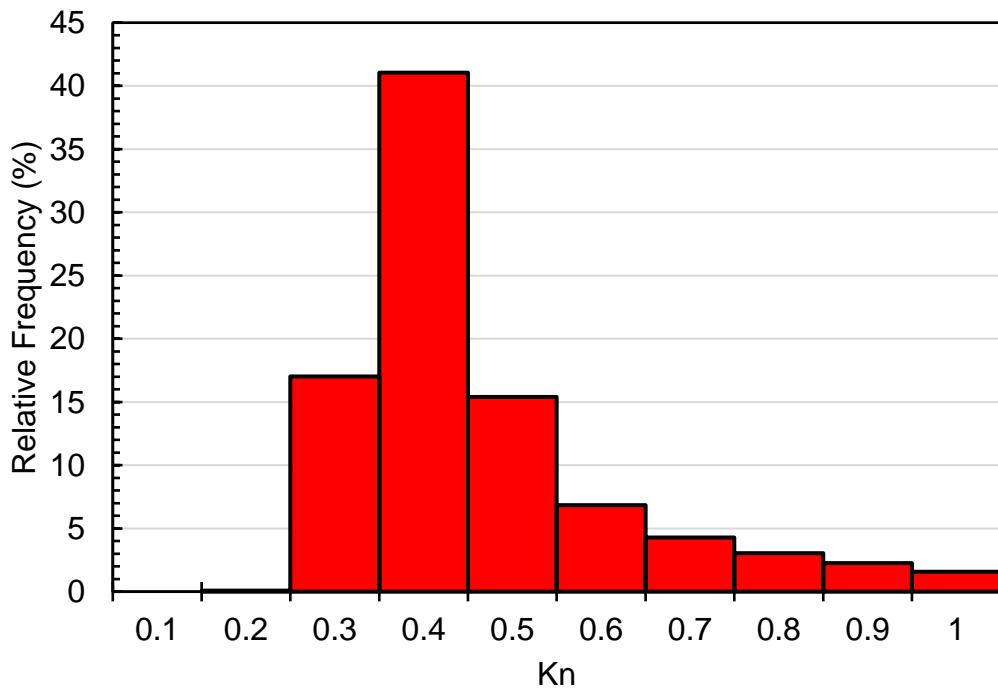


Figure 6-18: Particle Knudsen number in the supersonic region of the flow.

Jadidi et al [20] compared their SHVOF model using the Ranz-Marshall correlation to that of Accuraspray G3 which underpredicted the particle temperatures by 500 K. A larger difference of around 800 – 900 K is seen in this investigation using the Ranz-Marshall correlation against the experimental measurements. Akbarnozari et al. [108] modified the Accuraspray G3 system which is based upon measuring the intensity of radiation at two locations and at two wavelengths to a single location double wavelength approach (Accuraspray G4). The new measurements technique demonstrated a better correlation with changes with microstructure at varying flow rates for SPS thermal spray and SHVOF thermal spray. Therefore, the difference between the underprediction seen by Jadidi et al. and this investigation is likely due to modifications made with the Accuraspray diagnostic system.

Figure 6-19 compares the predicted average inflight particle velocities for the three Nusselt correlations against that of the experimentally obtained values from the time-of-flight approach. It can be seen from figure 6-19 that all three models compare well with the experimental velocity measurements at low standoff distances. The difference between the Accuraspray measurement and the velocity predicted from the Kavanau correlation is small (1.2 %). However, at large standoff distances the error between the experimental measurement and the numerical prediction for the velocity increases. The difference between the experimental and numerical values is as large as 40 % at a standoff distance of 150 mm. Jadidi et al. [20] compared the particle velocity to Accuraspray G3 measurements also using the correlation of Crowe et al. [127]. The correlation of Crowe was developed to account for Knudsen number effects onto the drag coefficient for spherical particles. Jadidi et al models saw large deviations of up to 20% in the particle velocity compared with the Accuraspray G3 measurements.

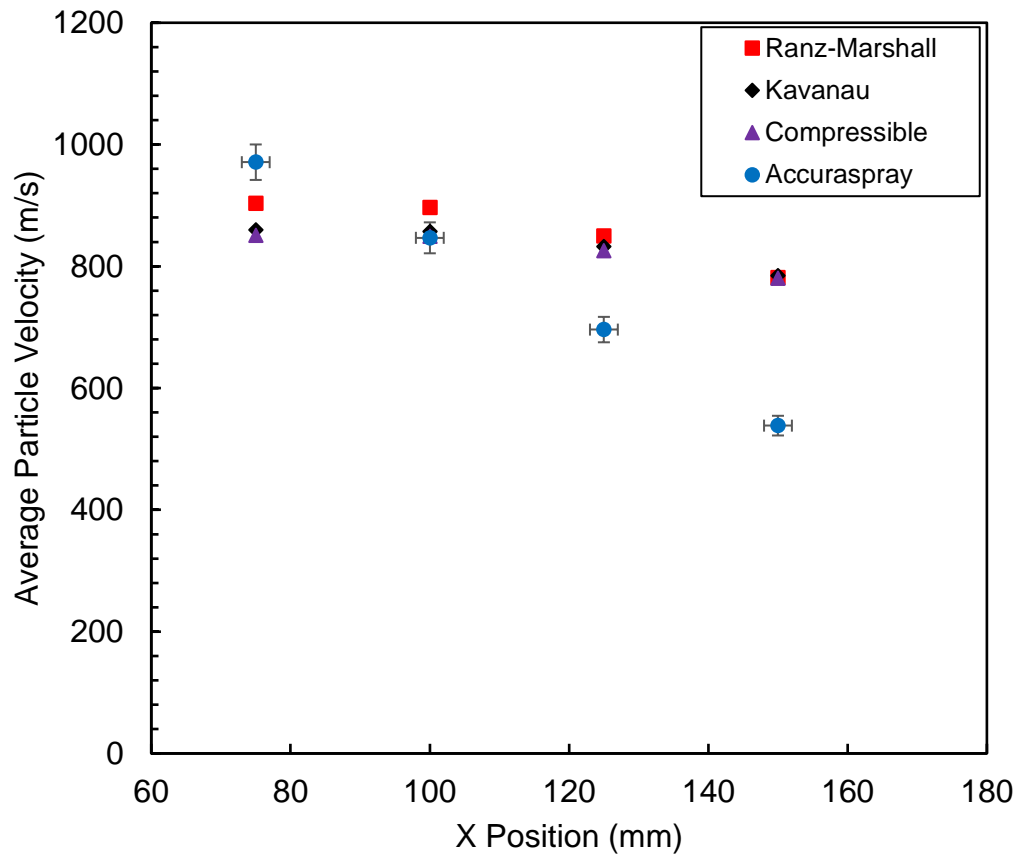


Figure 6-19: Comparison of inflight particle velocity for the three Nusselt correlations against the Accuraspray measurements.

There is little sensitivity of the average particle velocity to the Nusselt number is seen at this location. There are several factors that may contribute to the large difference between the numerical values and experimental data seen in figure 6-19. The particle velocity is most heavily impacted by the drag correlation, the drag correlation employed within this investigation accounts for the Knudsen number effects on the drag coefficient and should therefore provide a similar accuracy to the experimental data seen with the Nusselt number correlation within this investigation. Alternatively, the difference between the experimental data and numerical data is more likely to be a result of the mixing within the jet. The RANS models are known to under predict the mixing in jets [191], mixing within the jet results in movement of particles away from

the center of the jet. As particles move out from the center of the jet, they experience lower gas velocities which results in lower particle velocities. To capture this more accurately a higher-fidelity approach such as large eddy simulation (LES) could be investigated since this has shown improved accuracy for the prediction of single-phase jets, however, this approach is considerably more computationally expensive.

There are additional challenges faced for employing scale resolving methods in supersonic flows. Within the application of scale resolving methods the choice of numerical scheme must consider the dissipative and dispersive errors over the range of resolvable wave numbers that are introduced from the numerical scheme [192]. When shocks exist within the flow there are additional considerations that follow. The shocks must be accurately resolved without introducing spurious oscillations, also referred to as Gibbs phenomenon [193]. The choice of the numerical scheme must produce physical behavior both within and without the shocks [194], [195]. The Fluent solver employs a second order central difference scheme for LES applications. Central difference numerical schemes are suitable for the considerations of scale resolving methods as these schemes have a low dissipation however they give rise to the spurious oscillations around the shock waves [196]. Central difference schemes introduce high frequency oscillations that do not diminish as the grid is refined [197]. The Essentially Non-Oscillatory (ENO) scheme was introduced to ensure a high order scheme can capture the smooth regions of the flow with a sufficient accuracy. The ENO scheme uses an adaptive stenciling procedure that results in a non-oscillatory interpolation across discontinuities [198]. The Weighted Essentially Non-Oscillatory (WENO) scheme was implemented as an improvement over the ENO scheme. The WENO scheme uses a weighted average of the candidate stencils. It is most commonly used to capture shock waves and discontinuities due to their high order accuracy and

capability in capturing discontinuities within the flow [199]. WENO schemes have been found to introduce numerical dissipation and dampen some turbulence scales within the flow. More recently the Targeted Essentially Non-Oscillatory (TENO) scheme has been developed and investigated for application to shock containing turbulent flows. The TENO scheme has shown to be less dissipative than the WENO scheme more commonly employed for shock containing turbulent flows. Currently Ansys Fluent has been the solver of choice to model SHVOF thermal spray due to the stability of the solver and the native support for compressible flows, combustion modelling and DPM models. To employ WENO and TENO schemes in a high-fidelity simulation of SHVOF thermal spray the numerical model will have to be employed in an alternative open source CFD solver. Open source solvers offer a wider range of numerical schemes and offers greater ease to implement alternative numerical schemes that are not natively available within the open source solver.

This investigation has shown that the choice of the Nusselt number to determine the heat transfer coefficient has a significant impact on the prediction of the particle temperatures within SHVOF thermal spray. The Ranz-Marshall correlation is the only correlation that has been employed to determine the heat transfer coefficient within Ansys Fluent. It provides a poor prediction in the prediction of particle temperatures with an average error of 42.9% against experimental measurements. Significant improvements can be obtained by accounting for the Mach number effects on the Nusselt number correlation. Further improvements still can be obtained by accounting for the Mach number and Knudsen number effects onto the Nusselt number correlation. This study has shown the Kavanau correlation provides prediction of the particle temperatures with an average error as low as 4.7 %, the correlation should be implemented in future SHVOF thermal spray numerical studies.

6.9 Summary

In summary, three different Nusselt number correlations have been investigated to better predict the particle temperatures within SHVOF thermal spray. Ensembled averaged particle temperatures predicted from an incompressible, a compressible and a rarefied Nusselt number correlation are compared to experimental measurements obtained using a two colour pyrometry approach. This study has demonstrated that the flow within SHVOF thermal spray lies outside of the continuum flow regime. It has shown that significant improvements can be made in predictions of the inflight particle temperatures when accounting for the Mach number and the Knudsen number effects on the Nusselt number correlation. The Ranz–Marshall correlation was derived from measurements of droplets at Reynolds numbers up to 200 and very low Mach numbers. It was developed for application to spray dryers where the gas operates at very low Mach numbers and was never intended as a one fit model applicable to all flow regimes. As the Mach number increases the heat transfer coefficient reduces. This is one of the limitations of this model, the Ranz-Marshall correlation does not account for the effect of the Mach number. In addition to this, the Ran-Marshall correlation does not account for the effects of rarefaction and hence typically overestimates the Nusselt number outside of the continuum flow regime.

It is demonstrated that accounting for the Mach number effects onto the Nusselt number correlation provides a significant improvement in the prediction of inflight particle temperatures. There is a reduction in the discrepancy between numerical predictions and experimental measurements from 42.9 % to 12.3 % by accounting for Mach number effects onto the Nusselt number correlation. Further improvements in the particle temperatures can be seen by also accounting for the Knudsen number effects on the model to determine the heat transfer coefficient. The discrepancy

between numerical predictions and experimental measurements reduces further from 12.3 % to 4.7 % by additionally accounting for the Knudsen number effects onto the Nusselt number correlation. The Ranz-Marshall correlation is the sole model used with the literature to model SHVOF thermal spray. There are significant improvements in the particle temperature prediction with the compressible or in particular the Kavanau correlation.

The particle velocity is compared to experimental measurements obtained from a time of flight approach using Accuraspray G4. All three models to determine the heat transfer coefficient compare well with the Accuraspray velocity measurements at low standoff distances. The difference between the Accuraspray measurement and the velocity predicted from the Kavanau correlation is small (1.2 %) at a standoff distance of 75 mm. However, at large standoff distances the error between the Accuraspray measurement and the numerical prediction for the velocity increases. The difference between the experimental and numerical values is as large as 40 % at a standoff distance of 150 mm. It is suggested that the underprediction is a result of the underprediction in the mixing using the Reynolds averaged Navier-Stokes models. Scale resolving simulations such as large eddy simulations have shown to improve the prediction in the mixing over the Reynolds averaged Navier-Stokes models. Suitable numerical schemes will be required to accurately resolve the flow within and without shocks. To accurately implement scale resolving simulations model will have to be employed within an open source CFD solver to implement suitable numerical schemes.

Chapter 7: A High-Fidelity and Multi-Scale Investigation into the Primary Breakup

7.1 Introduction

Breakup of liquid jets has been extensively studied both experimentally and computationally due to the wide range of applications that utilise atomization of liquid jets. The breakup of liquid jets plays a fundamental role within diesel engines, suspension thermal spray, gas turbines and rocket engines to name a few [200], [201] & [202]. Breakup investigations within the combustion chamber for SHVOF thermal spray through experimental methods are very limited owing to the direct observational inaccessibility of the combustion chamber. Additionally, there are several challenges when trying to measure dense regions of flow. The liquid jet rapidly disintegrates into droplets of a few micrometres; experimental techniques must have sufficient temporal and spatial resolution to capture the breakup process [203]. The liquid is surrounded by gases undergoing combustion; visualizing into the centre of the chamber where the suspension is injected is impeded by radiation emitted from combustion. Owing to the size of the combustion chamber (22 mm length) instrumentation must be placed outside of the chamber. Hence, computational investigations provide an invaluable tool to investigate primary breakup.

Current approaches in modelling the injection of suspension within the combustion chamber fail to account for the primary breakup of the suspension. Prior modelling investigations have used the DPM framework to model the suspension injection [78], [76] & [20]. The DPM framework can only model droplet structures and cannot capture ligament and jet core structures that are needed to model primary breakup.

Traditionally, to model the injection of suspension into the combustion chamber with the DPM framework, the blob method is employed. Within the blob method, the suspension is typically injected as a set of discrete droplets with a diameter equivalent to the injector diameter. The droplet injection velocity is calculated from the mass flow rate. The droplets can then undergo secondary breakup, evaporation, heating and acceleration. The DPM model provides a robust treatment for droplet tracking away from the dense regions of the flow; however, in the dense regions of the flow such as near the liquid column; this approach is flawed. Within the dense regions ligaments and the liquid column are the dominant structures present.

Traditional means of modelling primary breakup in CFD using methods such as interface reconstruction methods such as the volume of fluid (VOF) or level set (LS) methods are unfeasible to resolve the full scale of droplet structures within SHVOF thermal spray. The VOF model, requires a mesh fine enough to resolve the smallest droplet structures. Droplets formed from the primary breakup of jets occupy a wide range of scales and are of orders of magnitude smaller than the injector diameter [102]. Running a full VOF simulation of the combustion chamber would require a mesh resolution down to the 3 μm . The droplets tend to occupy roughly a third of the combustion chamber volume and to resolve to this extent would require a mesh of the order of 20 billion cells which is currently infeasible. This could be alleviated to some extent through the use of adaptive mesh refinement, however, given the number of droplets involved this is unlikely to be efficient. Hence, it would be too computationally expensive to resolve the breakup phenomenon from large scale structures down to the smallest scale droplets. Within this chapter, the primary breakup is modelled using the VOF model and the droplets formed from primary breakup are then transferred to a DPM framework. The small-scale structures that require the most

computational resources within the VOF framework can then be modelled at a much lower computational cost using the DPM framework.

One of the challenges within SHVOF thermal spray is to prevent suspension from blocking the nozzles as it is injected into the combustion chamber. Blockages occur when particles impact the nozzle walls with a velocity higher than the critical impact velocity for bonding to occur [204]. The critical impact velocity varies depending on other parameters such as the particle temperature, particle diameter and the particle mass. As particles bond to the wall they disrupt the flow, large build up on particles onto the nozzle walls results in a severe disruption to the flow within the nozzle. There are at least two ways to reduce blockages from occurring within the nozzle. If the particle velocity can be reduced to below the critical velocity, particles that impact the wall will not bond with the wall. Alternatively, the nozzle geometry and the injector design can aim to reduce the likelihood of collisions of particles with the walls of the nozzle. Flow profiles within the nozzle can be adjusted so that particles remain far from the nozzle walls. Reducing the velocity of particles will have undesirable impacts on the coating porosity as goal to optimise the nozzle geometry looks to maximise the inflight particle velocities to ensure dense coatings with a low porosity. Therefore, it is more desirable to look to reduce the likelihood of particle collisions with the nozzle walls.

$$We = \frac{\rho_l |U_g - U_l|^2 d}{\sigma} \quad (Eq 7.1)$$

The injector design within this study is varied from the standard SHVOF configurations by including a co-flow around the liquid injection, a design of a co-flow injector is given in figure 7-1. The addition of a co-flow should force droplets to remain within the centre of the combustion chamber and hence reduce particle

collisions with the wall of the combustion chamber. This thesis chapter investigates the effect of the Weber number (Equation 7.1) by varying the co-flow velocity, on the primary breakup within SHVOF thermal spray. The terms in equation 7.1 refer to liquid density, ρ_l , gas velocity, U_g , liquid velocity, U_l , diameter of injector, d , and the surface tension, σ . There are several other non-dimensional parameters that play a role in the breakup of a co-axial jet, these include the gas Reynolds number, Re_g , the liquid Reynolds number, Re_l , the momentum flux ratio, M , and the momentum ratio, MR (Xiao et al., 2014). The role of the Weber number is investigated within this thesis since the Weber number characterizes the tendency for the jet to breakup due to the competition between inertia forces and surface tension forces (Pai et al., 2009). Three Weber numbers are investigated by varying the co-annular gas velocity around the liquid injection. Three co-flow gas velocities of 0 m/s, 200 m/s and 300 m/s are investigated which correspond to the three Weber numbers of 100, 180 and 415. The addition of a co-flow provides a significant design change for thermal spray. The Sauter mean diameter (SMD) is compared to experimental measurements for a coaxial jet at the same Weber numbers to provide a benchmark for the computational results. The SMD is defined as the diameter of a sphere that has the same volume/surface area ratio as a droplet of interest.

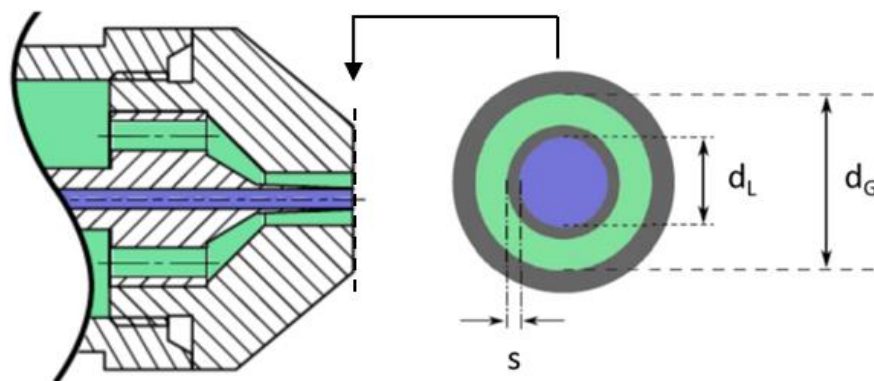


Figure 7-1: Co-flow Injector design [205]

7.2 Modelling Methodology

A SHVOF thermal spray nozzle is comprised of a combustion chamber and a barrel as shown in figure 7-2. Typically, when modelling SHVOF thermal spray the entire nozzle and the free jet is modelled. However, the combustion chamber alone has been modelled for this investigation, as the primary breakup and the combustion is confined to the combustion chamber. This approach allows for a significant reduction in the mesh count as opposed to modelling the entire SHVOF thermal spray system. Modelling the full geometry including the combustion chamber barrel and the free jet is unfeasible even for a coupled VOF and DPM approach. A careful consideration of the geometry has allowed for a high-fidelity approach to be employed within the combustion chamber with current HPC capabilities. This approach can obtain detailed characterisation of droplet formed from primary breakup to inform lower fidelity investigations. The initial droplet diameter, velocity and position can be extracted from and fed into a lower fidelity investigation. This will allow for more representative initial condition for the DPM injection for a pure DPM investigation. This should improve particle trajectory, heat transfer, momentum transfer and evaporation rate calculations within a pure DPM investigation.

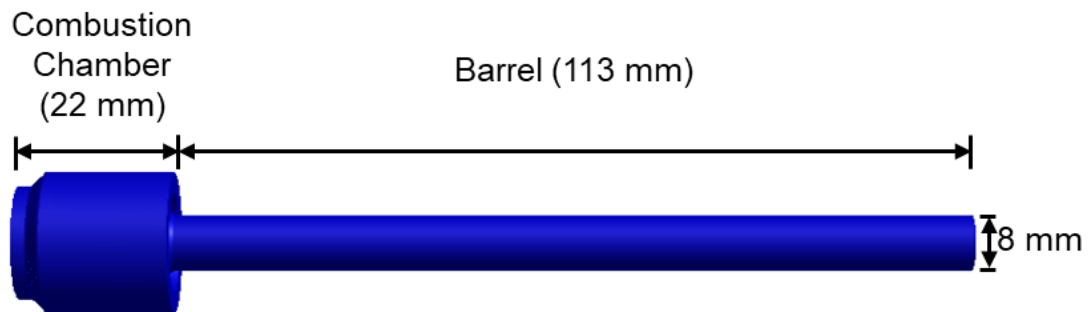


Figure 7-2: Geometry of SHVOF thermal spray nozzle.

The initial mesh was created following LES near-wall resolution recommendations of an average $\Delta x^+ < 100$, $\Delta y^+ < 1$ and $\Delta z^+ < 30$. A structured mesh was generated using a multiblock method within Ansys ICEM. The mesh is shown in figure 7-3 is comprised of 4.5 million cells before mesh refinement. To reduce the computational cost an adaptive mesh refinement is employed here to increase the mesh density around the interface between the two phases. Five levels of dynamic mesh refinement have been employed with the gradient of the volume fraction.

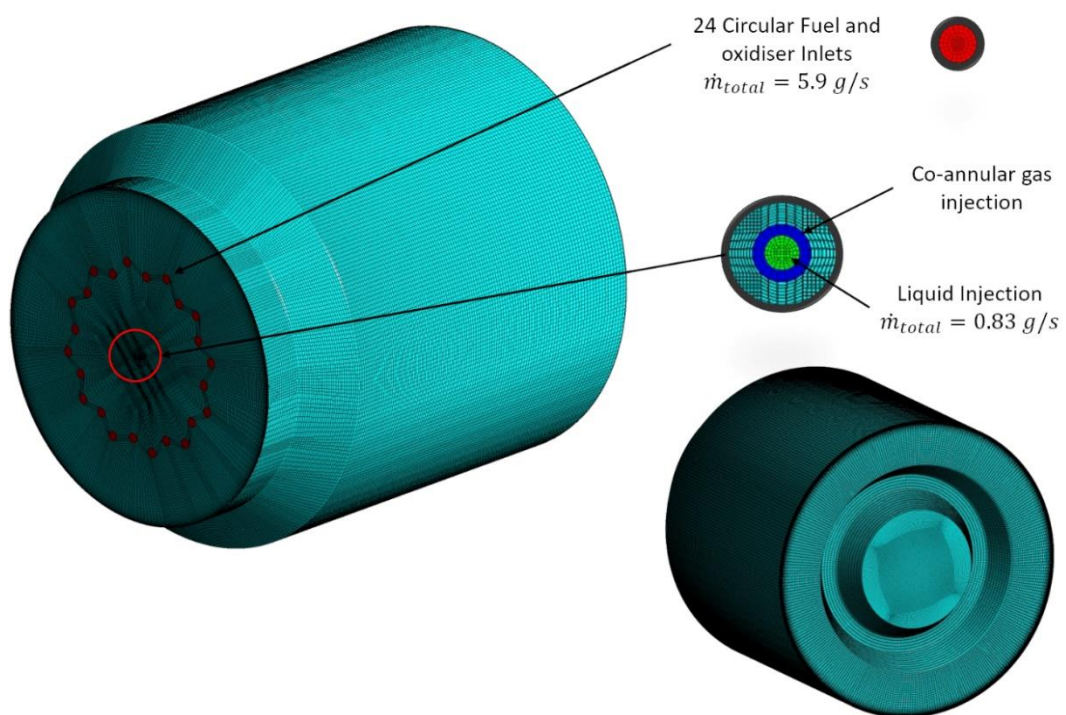
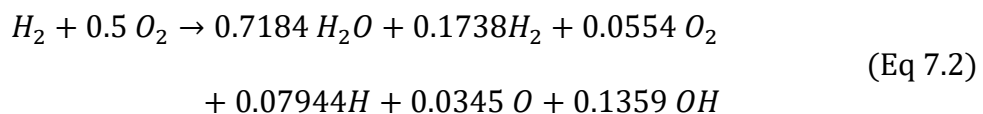


Figure 7-3: Fully structured mesh for the SHVOF thermal spray combustion chamber.

The governing equations for the fluid mass conservation, energy conservation and the momentum conservation have been solved for. Within this study the eddy dissipation model (EDM) model has been employed due to the significant reduction in computational cost over the eddy dissipation concept (EDC) model. With the current modelling approach employed within this chapter the computational cost needs to be

carefully considered to ensure the model is suitable for design and optimization studies. There is a significant cost increase in solving 20 reaction rates per time step as opposed to 1 reaction rate per time step will make this numerical approach too computationally expensive for design and optimisation studies. This is especially so since the multi-phase algorithms used here do not lend themselves well to parallel efficiency such as those commonly used in single-phase CFD. There are alternative combustion models that have been developed such as the premixed and partially premixed combustion models. These combustion models however are only valid for deflagration flames and are not suitable for SHVOF thermal spray. The single step global reaction has been employed which is given in equation 7.2. The Large Eddy Simulation (LES) scale resolving method has been employed within this investigation. The LES scale resolving approach has been employed within this study as it is able to resolve greater range of multiphase structures over unsteady Reynolds Averaged Navier-Stokes (URANS) models. Scale resolving methods have shown superior performance of these approaches over URANS for modelling jet breakup [206], [207]. Convergence was obtained when the residuals fell to below 1e-04 for the continuity momentum and equations and 1e-06 for the energy and species equations.



Within this study water is injected into the centre of the combustion chamber using a VOF framework. The injection of water into the combustion chamber is considered to provide useful and highly detailed information on the physical processes for the current application. The impact of solid particles, particle size distribution, shape of particles and the mass loading of particles on liquid suspension surface tension properties is not well understood so it was not modelled here. Further extensive experimental

measurements are needed for detailed characterisation before extending the breakup model to a suspension jet. The liquid jet is injected into the combustion chamber using VOF framework. As droplets form from primary breakup they are converted to the DPM framework. VOF resolved droplet are converted to DPM modelled droplets based upon their size and sphericity. The default and recommended values for the radius standard deviation and the radius surface orthogonality of 0.5 and 0.5 were used respectively. The volume equivalent sphere diameter is a user specified range. The lower value was set to zero to ensure that the smallest scales were converted to DPM. Care was taken to ensure the upper limit was larger than the largest expected droplet diameter. A co-flow gas stream is injected annularly around the liquid injection as shown in figure 7-3, no perturbations were introduced into the co-flow inlet. The premixed hydrogen and oxygen were injected through the 24 circular holes indicated in red in figure 7-3. A pressure outlet boundary condition is specified on the outlet of the combustion chamber. The average pressure at the outlet is obtained from a steady state gas flow model which has been employed within chapter 6. Table 7-1 shows the operating conditions employed within this investigation. The operating conditions correspond to standard conditions that are employed within SHVOF thermal spray and correspond to a flame power of 75 kW for hydrogen flame and a suspension flow rate of 50 ml/min [208].

Table 7-1: Table of boundary conditions employed

Surface	Boundary Condition	Temperature (K)
Fuel Inlet	0.0059 kg/s	300
Water Inlet	0.000833 kg/s	300
Walls	No slip	500
Outlet	60,000 Pa	Zero Gradient

7.3 Mesh Requirements for the Coupled VOF and DPM Framework

Both VOF resolved droplets and DPM modelled droplets have different meshing requirements. For droplets resolved with the VOF method a sufficient number of cells must span the droplet to ensure the curvature of the droplet is accurately captured [209]. Typically, for atomization simulations using a pure VOF method, poorly resolved droplets where the droplet diameter is more than four times the cell spacing ($d_p < 4\Delta x$) are deleted from the simulation [210] & [211]. The poorly resolved droplets are deleted as they have a negative impact on the solver stability. With DPM modelled droplets the cell size must be larger than the droplets modelled. Within the DPM model droplets are treated as point entities. Source terms are applied within the Navier – Stokes equations to account for the momentum and energy transfer between the discrete phase and the continuous phase. The source term is only applied to the cell that contains the DPM entity. With droplets larger than the cell resolution the droplet will affect the flow within neighbouring cells. An additional source term is required for the neighbouring cells that will be affected by droplets larger than the cell size [210].

There are several approaches that have been developed within the literature to ensure the DPM model produces physical behaviour on fine meshes [154]. The cube averaging method (CAM) developed by Link et al. [212] marks the cells in cubic region a factor larger than the droplet diameter. The droplets are treated as porous cubes within the cubic region where the source terms are calculated and distributed over the cubic region. The source terms are then converted back from the cubic region and mapped to the original grid. The two-grid method (TGM) developed by Farzaneh et al. [213] and Deb et al. [214] implemented a coarse grid for the discrete phase and a fine grid for the continuous phase. The source terms are mapped from the coarse grid

to the fine grid and the source terms are weighted by the volume of the fine grid to the coarse grid. The diffusion based method (DBM) developed by Capecelatro et al. [215] distributes source terms from the discrete phase to the continuous phase with the use of a weighted function also referred to as a statistical kernel function. Source terms are distributed over the neighbouring cells using the statistical kernel function. Zhang et al. [154] compared computational cost, impact on the flow field and the robustness for the CAM, TGM and the DBM methods within OpenFOAM. It was seen that the methods produced a very similar solution and however the DBM method was significantly more computationally expensive than the CAM and the TGM methods.

Within this study an aggressive adaptive mesh refinement algorithm is employed to account for the different mesh resolutions required for VOF resolved droplets and DPM modelled droplets. With an adaptive mesh refinement technique, the cells within the mesh are split based on a solution variable within the flow. The gradient of the volume fraction has been employed for the solution variable. In regions where there is a large change in the volume fraction the cells will be split. This occurs only along the interface and hence only the cells containing an interface will be refined. The number of refinements outlines how many times the base mesh will be split. Two levels of refinement will result in cells with $1/64^{\text{th}}$ of the volume of the base mesh. The refinement is carried out periodically so as the interface moves the new cells containing the interface are refined. The refined cells that no longer contain the interface are coarsened back to the base mesh. As droplets are converted from a VOF framework to a DPM framework the mesh is immediately reverted back to the base mesh. Figure 7-4 shows the mesh surrounding the VOF interface, it can be seen from figure 7-4 that the mesh is suitably refined near the interface to accurately capture the interface. The refined mesh is coarsened back to the base mesh once the droplet has

been converted from VOF to DPM. The base mesh is of the order of $100\ \mu\text{m}$ which is larger than the largest DPM droplets and the refined mesh is off the order of $3\ \mu\text{m}$ which is smaller than the smallest VOF droplets. This allows for a finer mesh to be employed for VOF resolved droplets and a coarser mesh to be employed with DPM modelled droplets. The minimum cell spacing is well below $1/12^{\text{th}}$ of the injector diameter which has been shown to be sufficient to capture the spray dynamics using this multiscale approach [106] & [105]. The adaptive mesh refinement also allows for a significant reduction in the computational cost of the numerical model. As a much coarser base mesh can be employed and a fine mesh is only employed within the cells where the interface is found at any given instance.

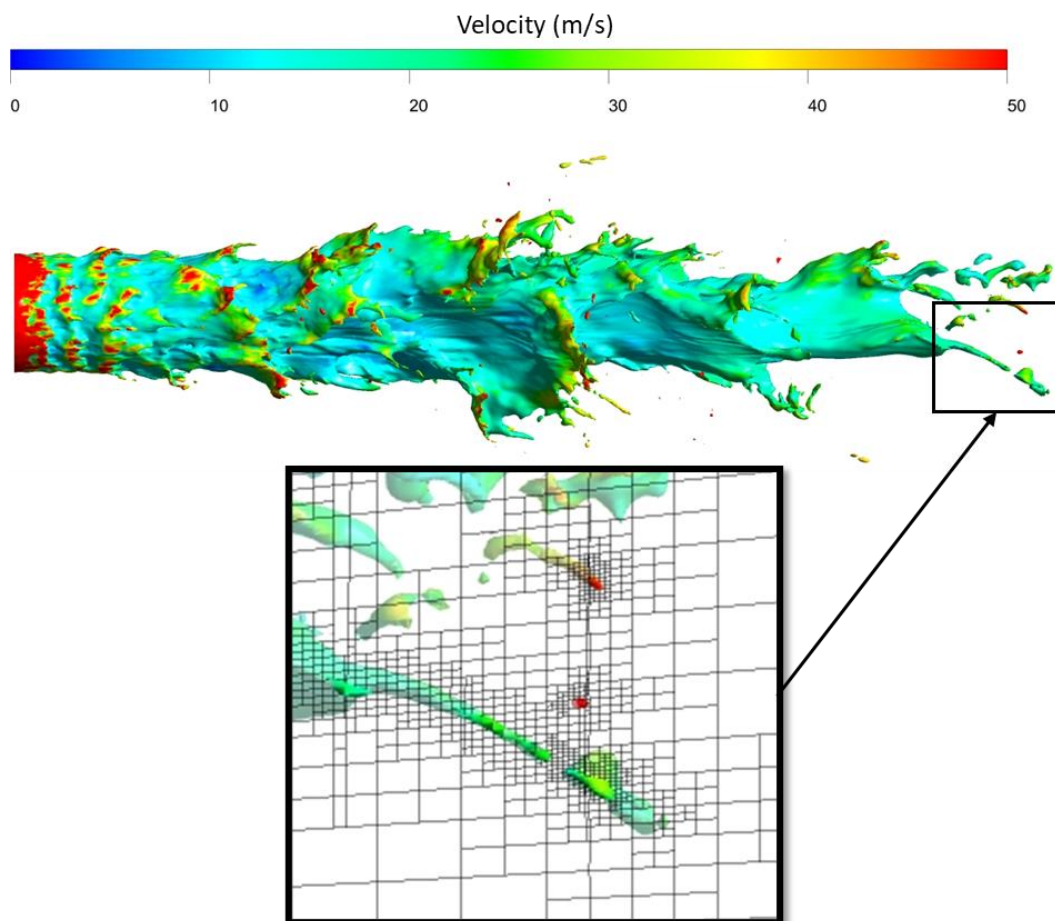


Figure 7-4: Mesh around the VOF iso-surface coloured by the flow velocity magnitude for a co-flow velocity of 300 m/s.

7.4 Effect of Co-Flow on the Gas Velocity and Gas Temperature Within the Combustion Chamber

Traditionally to model the inlets within the combustion chamber, they are simplified to an annular inlet to allow for a reduction in the cell count [60]. Within this study the exact inlet geometry comprising of two sets of twelve circular holes spaced at two different radial distances from the centre of the combustion chamber have been meshed and modelled. Figures 7-5 show the instantaneous velocity magnitude contours at varying liquid jet injection Weber numbers of 100, 180 and 415 in figures A, B and C respectively. Figures 7-6 show the instantaneous static temperature contours for the Weber numbers of 100, 180 and 415 in figures A, B and C respectively. Recirculation zones form near the walls of the combustion chamber that aid in the mixing of the hot products of combustion with the cold inlet gases. Effective mixing is essential for a premixed combustion reaction to progress effectively. Premixed combustion needs a continuous supply of high temperature gases to progress the reaction. Which is delivered through effective mixing of the hot gaseous products with the cold reactants.

A number of assumptions within the DPM model make it unsuitable for use near the injector. The DPM model assumes the liquid structures are spherical; near the injector ligaments and the jet core are the expected dominant structures that are. Additionally, the DPM model assumes the liquid droplets are sufficiently disperse within the flow and that the mass loading is less than 10 -12% [126]. Locally near the injector the liquid is dominant phase within the cells. The DPM model is therefore unsuitable for modelling structures near the injector, instead the VOF model is more suited for use for the injection. The VOF model has not previously been used to model SHVOF, the VOF model within Ansys fluent also does not offer a robust evaporation model. Additionally, the pure VOF model is too computationally expensive to model SHVOF

thermal spray. The small structures require a significant computational cost to track throughout the domain. The DPM model is very well suited to tracking droplets formed from primary breakup. Away from the liquid core these two assumptions are valid. The droplets are well dispersed within the flow and the secondary phase structures seen take the form of droplets away from the liquid core.

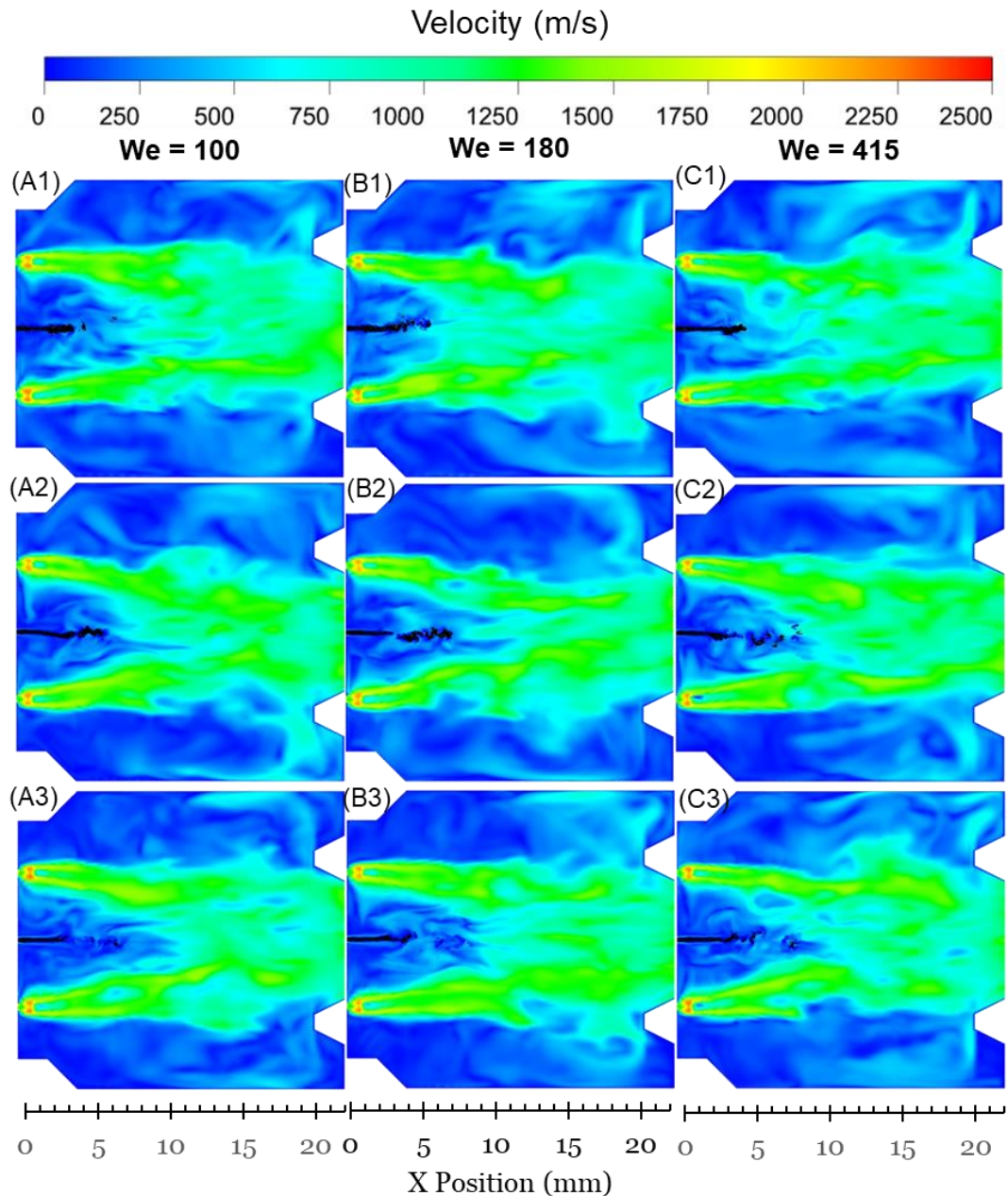


Figure 7-5: Instantaneous velocity contours given in throughflows (TF) with (black) VOF iso-surfaces (We = 100) (A1) 36 TF, (A2) 43 TF, (A3) 50 TF, (We =180) (B1) 36 TF, (B2) 43 TF, (B3) 50 TF, (We = 415) (C1) 36 TF, (C2) 43 TF and (C3) 50 TF.

It can be seen from figure 7-6 that locally near the liquid injection region there is a very low temperature of ~ 300 K. With a standalone DPM model, currently employed within the literature for this application [216], a temperature of approximately 2500 K is predicted within this region and as shown in chapter 6. The DPM model only accounts for the effect of the secondary phase on the temperature field through a source term for droplet heat transfer. The VOF model on the other hand directly accounts for the effect of the secondary phase through the energy equation. The standalone DPM gives an over-prediction of gas temperature within the liquid injection region which may result in evaporation initiating earlier due to the over prediction in the gas temperature at the suspension inlet. Similarly, the gas velocity will be over predicted near the liquid jet injection with the DPM model. The DPM model accounts for the momentum transfer between the discrete phase and the continuous phase with a source term in the momentum conservation equation. The gas velocity is of the order of 200 m/s with the DPM model. With the VOF model the gas velocity by the injection is around 15 m/s. Within the liquid column region, it is expected that the velocity is approximately the liquid injection velocity. When the standalone DPM model is employed the velocity immediately near the injector is more than 10 times the injection velocity. Hence employing the VOF in these regions is able to better predict the velocity and temperature near the liquid injection.

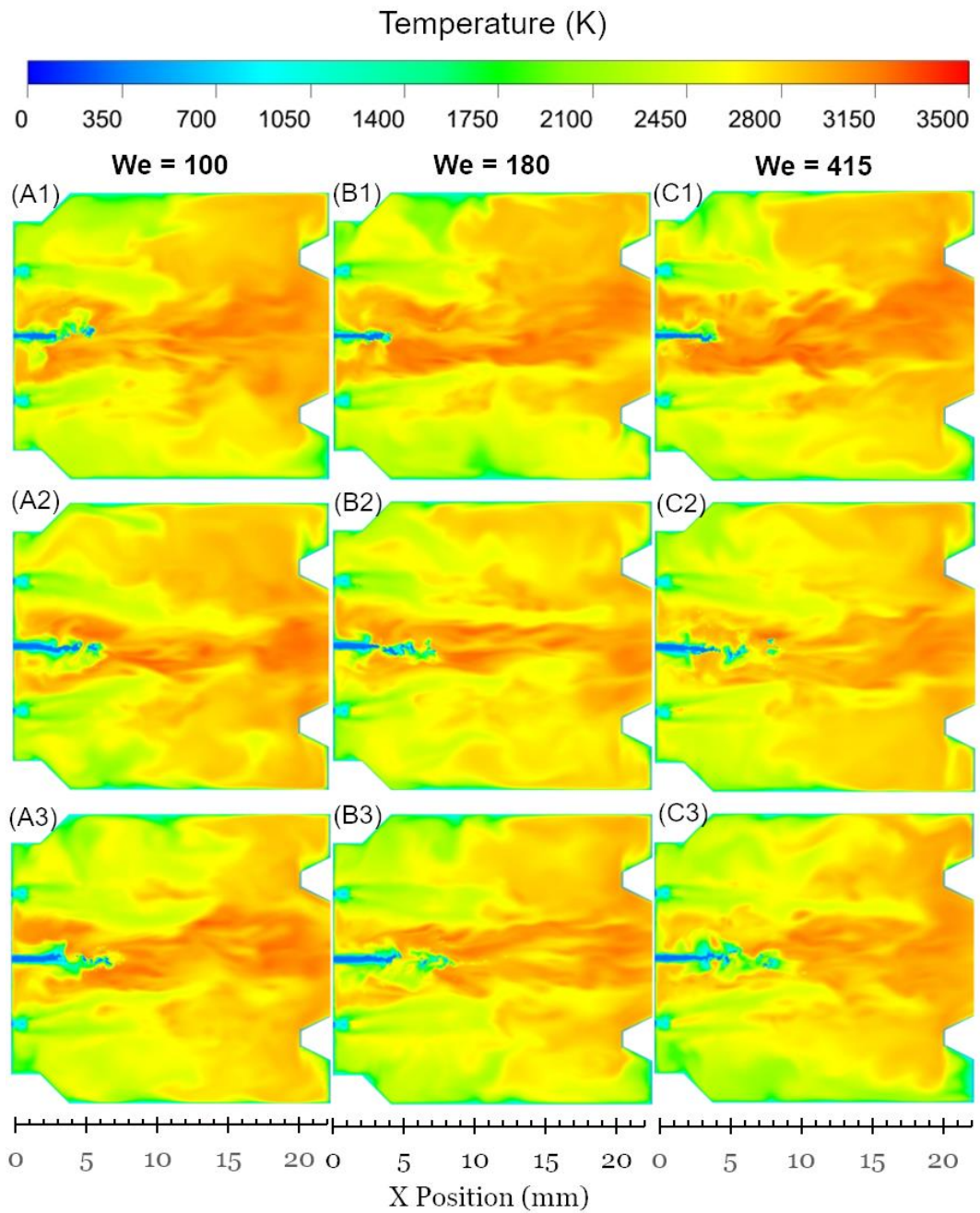


Figure 7-6: Instantaneous temperature contours given in throughflows (TF), ($We = 100$) (A1) 36 TF, (A2) 43 TF, (A3) 50 TF, ($We = 180$) (B1) 36 TF, (B2) 43 TF, (B3) 50 TF, ($We = 415$) (C1) 36 TF, (C2) 43 TF and (C3) 50 TF.

7.5 Effect of the Co-Flow on the Primary Breakup

Prior studies within the SHVOF thermal spray modelling literature have ignored the primary breakup of the jet [217], [20], [59]. Experimental investigations within the combustion chamber are currently outside that capability of current experimental methodologies. Therefore, the understanding of the primary breakup of the liquid jet within the combustion chamber is very limited. The understanding of the jet breakup mechanism within the combustion chamber is very limited due to the lack of both experimental and computational investigations that have studied the breakup. The primary breakup process characterises the size of droplets that are released within the flow. The droplet size plays an important role onto the evaporation of liquid within the suspension, mass transfer to the droplets, momentum transfer to the droplets and the trajectories of droplets within the nozzle. All of these processes will impact the overall quality of the coating and its properties. Improved understanding of the primary breakup process can allow for an optimisation of the size of the droplets that are injected into the flow.

Figure 7-7 shows the breakup of the liquid jet within the combustion chamber. It can be seen that there are two breakup modes for the liquid jet. The first breakup mode for the droplets occurs from the formation of small ligaments on the surface of the jet shown on the bottom left of figure 7-7. The mechanism behind the primary breakup of liquid jets in co-axial gas flow has been well documented within the primary breakup literature. Surface perturbations are formed on the interface between the liquid and gas by primary shear instability. Surface perturbations are stretched into ligaments due to the relative velocity difference between the two fluids. As the ligaments are accelerated, support from the bulk liquid is diminished and the ligaments elongate. The surface of the ligaments are continually subject to strong accelerating forces from the

gas jet leading to Rayleigh-Taylor instabilities. As the Rayleigh-Taylor waves amplify the ligaments, they break off the main jet forming a droplet. The second breakup mode is through the ejection of large ligament structures shown on the bottom right of figure 7-7. The large ligament structures disintegrate into droplets orders of magnitude smaller than the large, ejected structures. Depending upon the Weber number of the droplets formed the small droplets formed will break up into further smaller droplets. Within this study once the droplets are formed, they are immediately converted to the DPM framework to allow for the most cost-effective and practical approach to modelling the range of liquid structures.

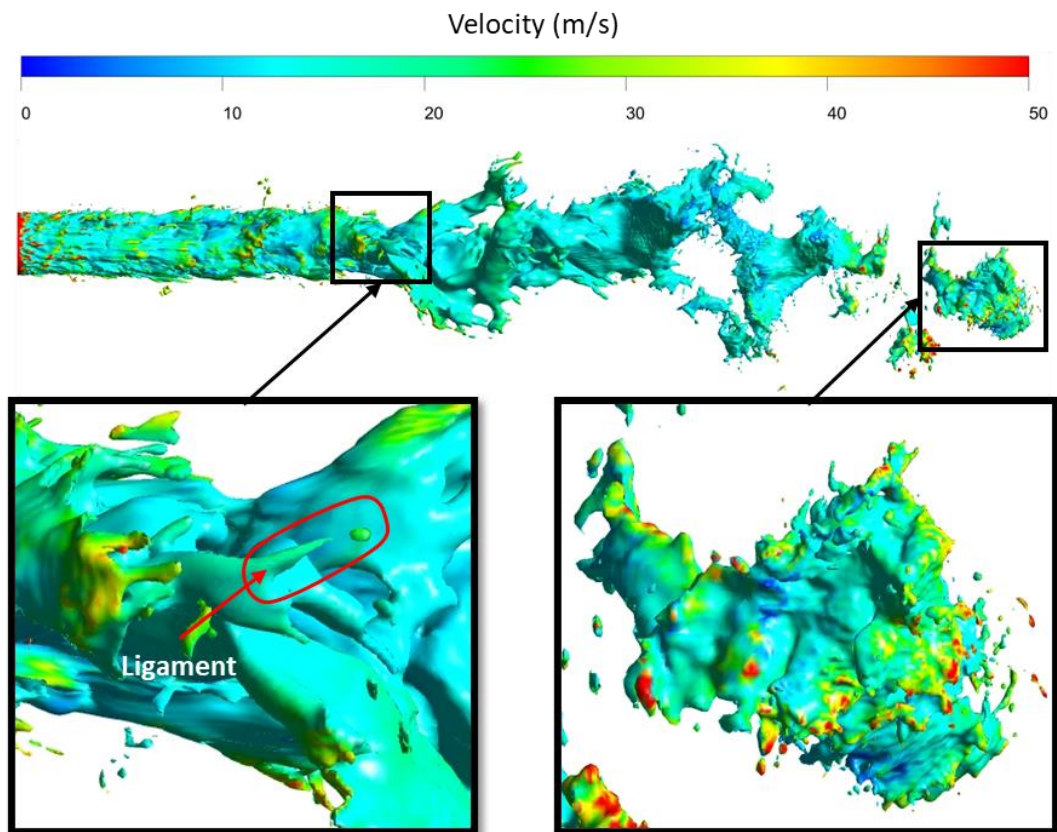


Figure 7-7: Breakup Modes Within the Combustion Chamber

Figure 7-8 shows the instantaneous iso-surfaces of the liquid jet injection into the combustion chamber ($We= 100$) at (a) 0.00065 s and (b) 0.0007 s, ($We= 180$) at (c) 0.00065 s and (d) 0.0007 s, ($We= 415$) at (e) 0.00065 s and (f) 0.0007 s. The addition

of a co-axial gas flow to the liquid injection delays the formation of large ligaments from the surface of the liquid jet. This can be seen in figure 7-8 by comparing the isosurface plots for a Weber number of 100 and a Weber number of 180 close to the injector inlet. As can be seen the liquid jet core is destroyed in a shorter distance for the lower Weber number. This is the opposite trend to that normally observed for liquid jets; however, it should be noted that the gas within the combustion chamber is hot and highly turbulent. It is thought that its interaction with the liquid jet excites the initial interface perturbation followed by large scale interface distortion. The recirculation zones set up within the combustion chamber also mean that the surrounding gas flows in an opposite direction to the liquid jet. The addition of the gas co-flow rectifies this direction and is of sufficiently lower turbulence intensity and temperature. Hence, there is a delayed break-down of the jet core. Comparisons of the jet length at different Weber numbers can be used to benchmark the numerical accuracy. These have not been included as experimental measurements are typically taken at conditions very different to those found within an SHVOF thermal spray combustion chamber. It is not possible to provide a meaningful comparison of the intact core jet length from the numerical predictions with measurements from the literature due to the interaction of the jet and the hot and highly turbulent combustion chamber gases. It should be noted that synthetic turbulence was not introduced into co-flow inlet. Owing to the highly turbulent nature of the of the combustion chamber this is unlikely to have any significant effect as the turbulence will be dominated by the turbulence within the combustion chamber rather than inlet conditions. However, further investigation should be undertaken to study its effect on the jet breakup as it may influence the jet breakup. This was not studied due to the lack of experimental measurements within the combustion chamber allowing for any meaningful comparison.

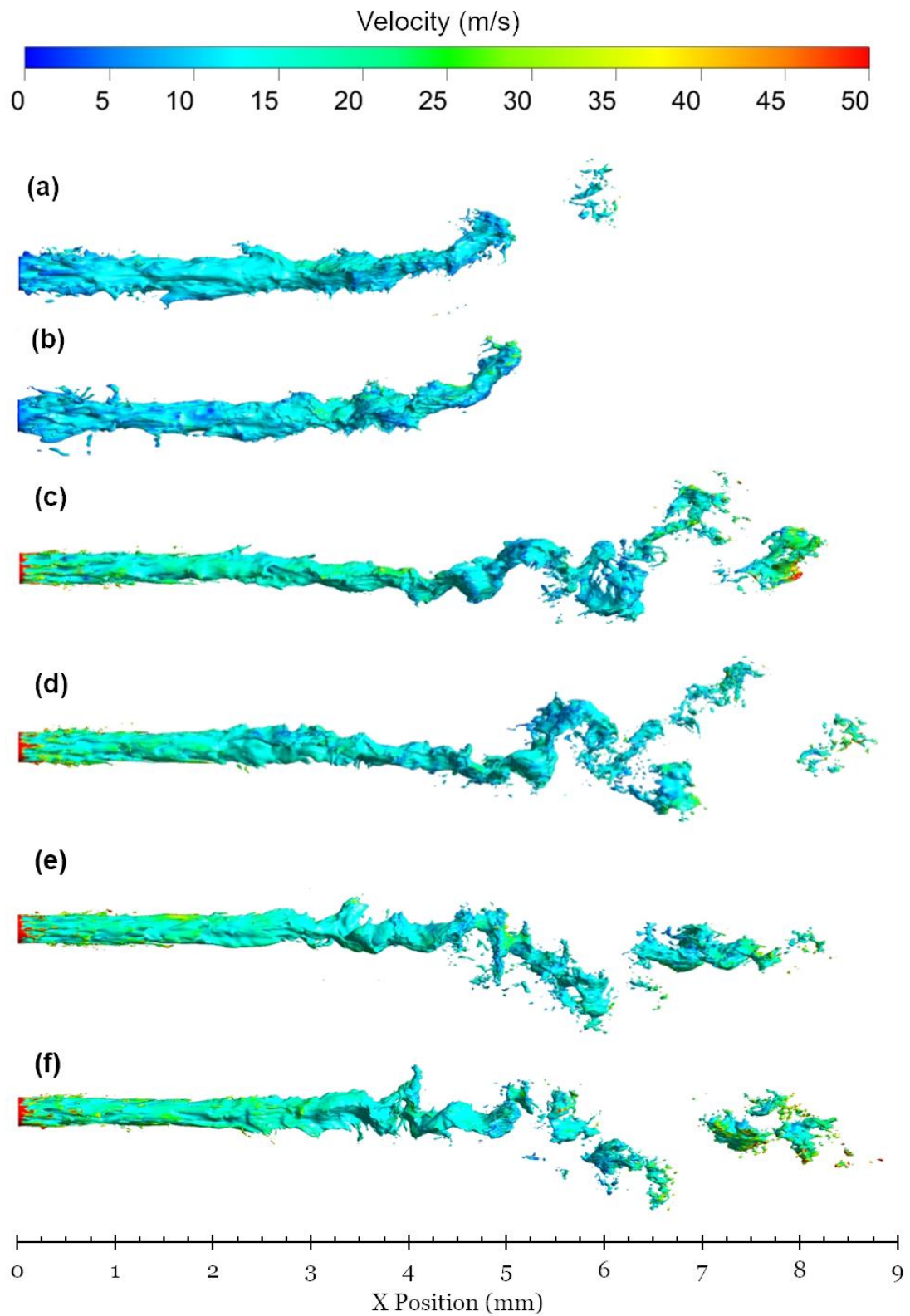


Figure 7-8: Instantaneous iso-surfaces of the liquid jet injection into the combustion chamber given in throughflows ($We= 100$) at (a) 46 TF and (b) 50 TF, ($We= 180$) at (c) 46 TF and (d) 50 TF, ($We= 415$) at (e) 46 TF and (f) 50 TF.

Figure 7-9 (a), (b) and (c) show droplet diameter distributions for droplets that form from the primary breakup of the liquid jet at the Weber numbers of 100, 185 and 415 respectively. It can be seen that the droplet diameter distributions at the three Weber numbers follow a log normal distribution. It is reported by Kazuya et al. [218] that log-normal distributions are typically seen within primary breakup distributions. There is a peak frequency at a diameter and as the droplet diameter decreases from the peak value the frequency of the droplets decreases. A cut-off diameter is seen at a diameter smaller than the peak value as surface tension forces prevent the formation of smaller droplets. Table 7-2 shows the mean and standard deviation of the log-normal distributions from the histograms in figure 7-9. It can be seen from table 7-2 that at the Weber numbers considered that there is little variation in the mean and standard deviation of the droplet diameters.

Currently for a pure DPM investigation, droplets with a diameter equivalent to the injector diameter are injected into the combustion chamber the droplets are subject to secondary breakup and evaporation; this is referred to as the “blob method” [20]. The injection velocity is calculated from the mass flow rate of the of the liquid and the diameter of the injector. The droplet diameter distributions provided from figure 7-10 and table 7-3 provide a valuable input for DPM only investigations. A more representative droplet distribution can now be injected into the combustion chamber using the framework developed within this chapter. Droplet distributions that accounts for the effect of the primary breakup on the droplet diameter and droplet velocities can be employed within pure DPM investigations. More representative injections into the combustion chamber will allow for improved predictions of suspension heating, momentum transfer, trajectories and evaporation. Which will better improve inflight particle velocity and temperature predictions. This modified approach for the droplet

diameter injected into the domain is often referred to as “the enhanced blob method” or the “improved blob method” [219].

Table 7-2: Mean and standard deviation of log normal distribution for droplet diameter.

We	Mean $\ln(\mu m)$	Standard Deviation
100	2.8982	0.32
180	2.9331	0.30
415	2.9683	0.30

The droplet Weber number provides a useful tool to evaluate the mode of droplet secondary breakup. The mode for the droplet secondary breakup is controlled by the droplet Weber number as outlined within section 2.5. Figure 7-10 shows the effect of gas co-flow velocity on the Weber number of droplets produced from primary breakup. The droplet diameter distribution in figure 7-9 and the local gas velocity are used to determine the droplet Weber number. It can be seen from figure 7-10 (a), (b) and (c) that as the co-flow velocity increases the spread of droplet Weber numbers increases. In addition to this the distribution of Weber numbers shifts slightly towards the right where droplets occupy a higher Weber number at a higher co-flow velocity. The mode of secondary breakup will be different as the co-flow velocities increases. With no co-flow the droplets have a very low Weber number, it ranges from 10 to 30. From the droplet breakup literature it would suggest that the mode of secondary breakup will be dominated by vibrational breakup and bag breakup [47] & [48]. While for a 200 m/s

co-flow velocity the Weber number ranges from 15 – 55. This would suggest that secondary breakup will be dominated by bag and stamen breakup. Finally, at a co-flow velocity of 300 m/s the Weber number ranges from 25 – 95. Therefore, this would suggest that mode of secondary breakup will be dominated by bag and stamen breakup and stripping breakup. The conditions used to evaluate the effect of the Weber number on the mode of secondary breakup are very different to those found within an SHVOF thermal spray combustion chamber. This may affect which breakup mode occurs at a given Weber number. Additionally, the droplet breakup modes are evaluated for pure liquid droplets rather than a suspension droplet. Further study into the secondary breakup of suspension droplets is needed to identify if and how the nanoparticles effect the mode of secondary breakup.

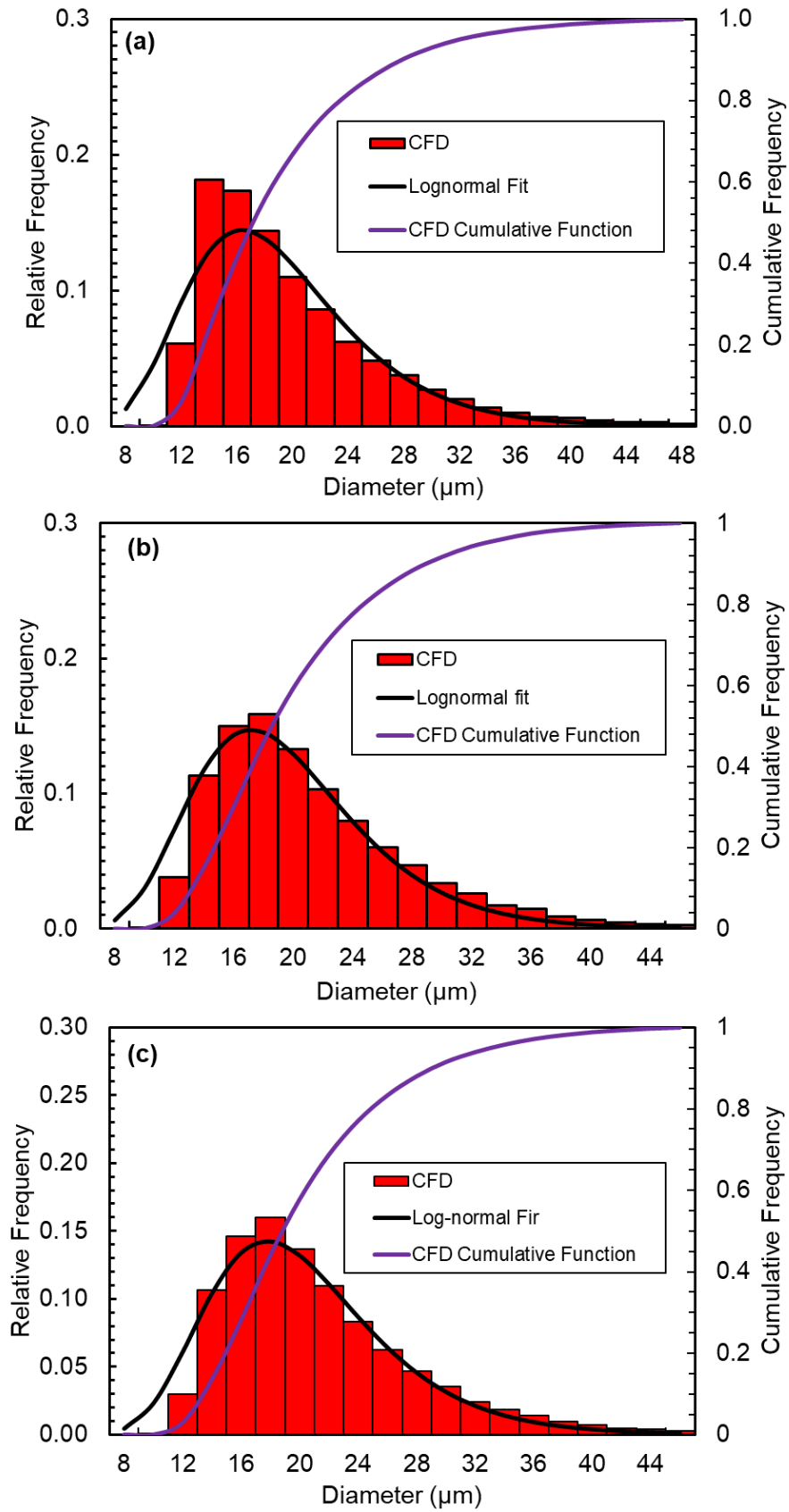


Figure 7-9: Droplet diameter distributions from primary breakup at Weber numbers

(a) 100, (b) 180 and (c) 415.

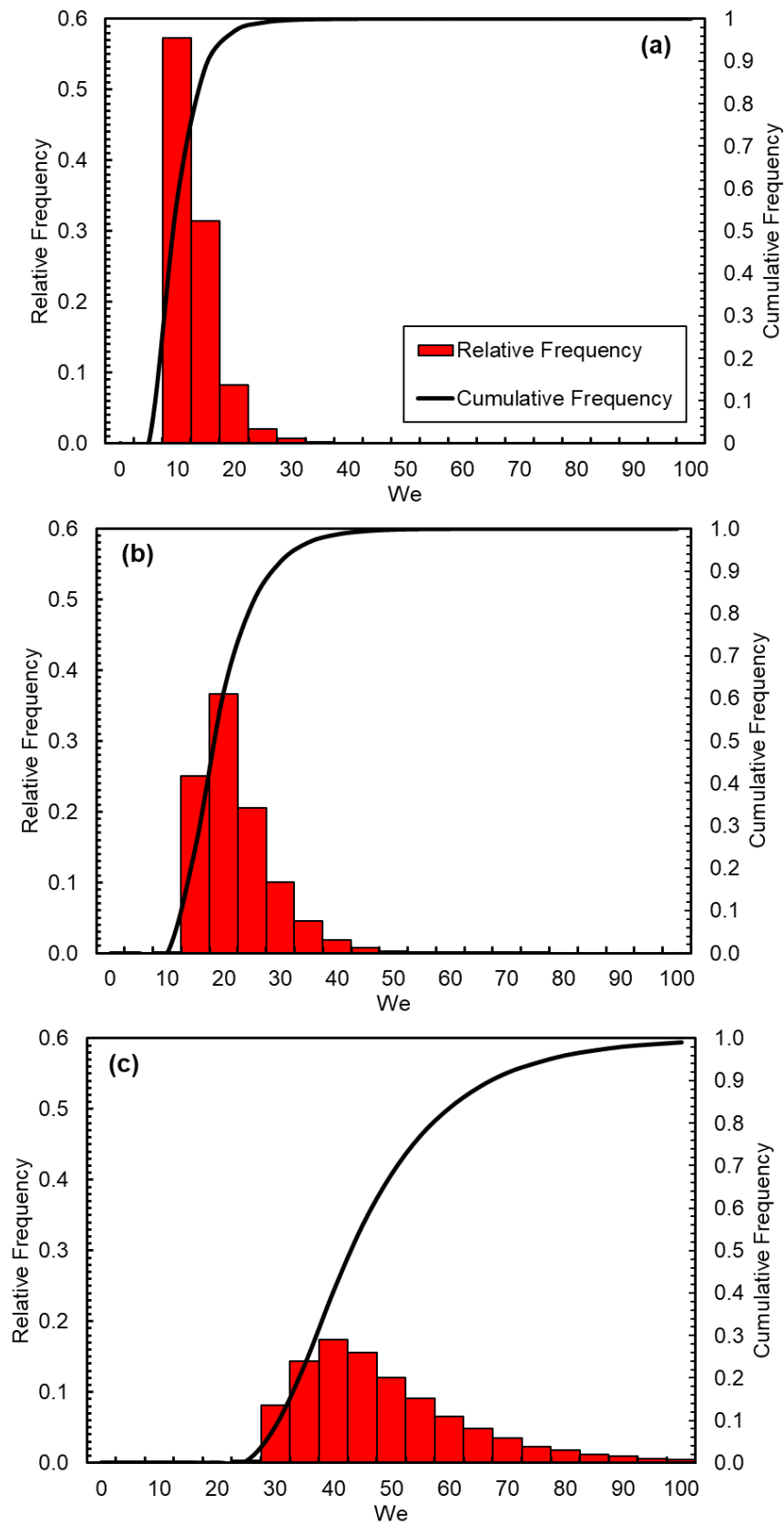


Figure 7-10: Effect of co-flow velocity (a) 0 m/s, (b) 100 m/s and (c) 200 m/s on the Weber number of droplets subsequent to primary breakup.

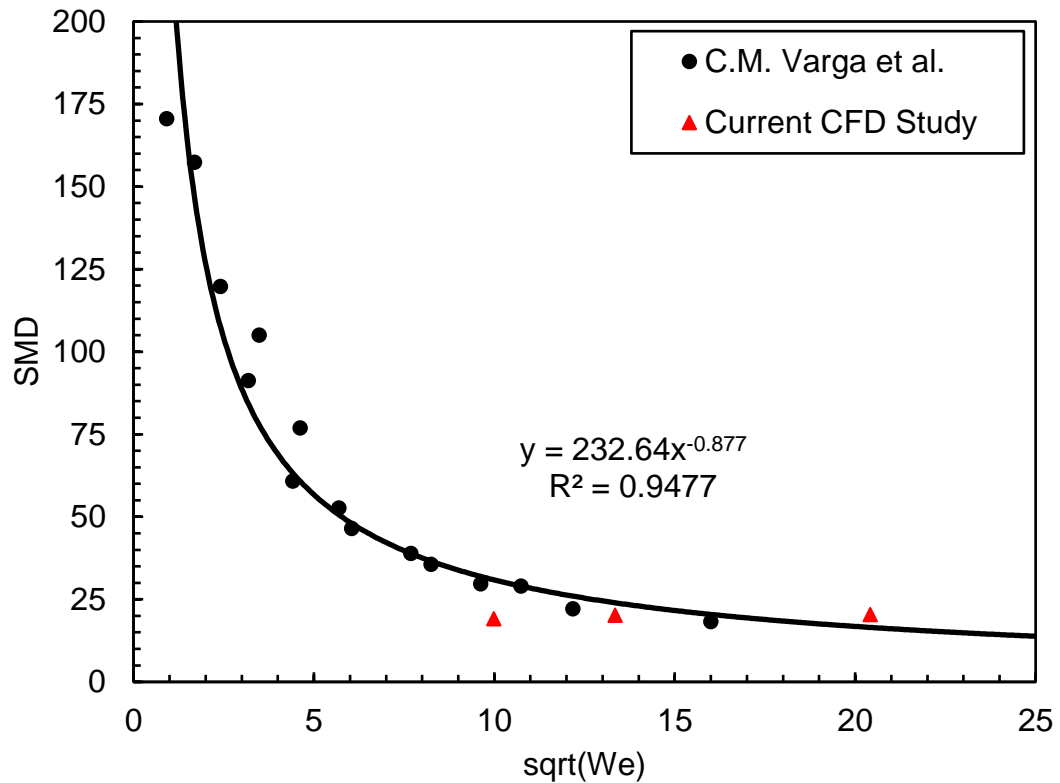


Figure 7-11: Comparison of Sauter mean diameter (SMD) of droplets from primary breakup to existing experimental breakup literature.

Experimental observations and measurements within the combustion chamber are very limited due to lack of optical access within the combustion chamber. Therefore, experimental measurements taken at similar Weber numbers, liquid injector diameter and co-flow velocity can allow for an understanding if the numerical values are in a range similar to that expected. Figure 7-11 compares the Sauter mean diameter (SMD) for the droplets from primary breakup compared with the experimental measurements of Varga et al. [45]. It can be seen from figure 7-11 that the droplet diameters predicted within this study match up very well to those measured by Varga et al. through phase-doppler anemometry (PDA) at Weber numbers of 180 and 415; however, there is a small underprediction in the droplet SMD at the Weber number of 100. The measurements taken by Varga et al. considered co-axial injection of liquid and gas

flow where both phases travel in the same direction. For the case of where the liquid jet Weber corresponds to 100 there is no co-flow with the liquid injection. The gas flow is in the direction opposing the liquid injection. Additionally, the experimental measurements are taken at much lower temperatures. The experiment is conducted by injecting a co-axial jet into stagnant air. This may have an effect on the mean diameter which leads to the small under-prediction witnessed. However, the experimental data provides a useful tool for comparison.

7.6 Effect of Co-Flow on Clogging within the Combustion Chamber

Clogging is a serious issue for suspensions with a high particle loading within SHVOF thermal spray. Clogging results in a waste of feedstock material, time to restore and maintain the SHVOF thermal spray nozzles. Small suspension droplets are particularly susceptible to causing clogging as they have a low mass inertia. Their low mass inertia makes them susceptible to adverse flow behaviour within the combustion chamber. Optimizing the suspension injection will allow for a significant reduction in the number of particles that impact with the walls of the combustion chamber. This study has employed a co-flow around the liquid injection to force the flow field around the liquid column in the direction of nozzle exit, which can be seen in figure 7-1. Figure 7-12 (a), (b) and (c) shows the time averaged velocity vector field for the Weber numbers of 100, 180 and 415 respectively. The solution has been time averaged over 0.0007s (approximately 50 throughflows). Figure 7-13 plots the time averaged axial centre line velocities at the Weber numbers of 100, 180 and 415. Small droplets are unable to overcome the backflow region near the liquid column shown in figure 7-13 owing to insufficient momentum. Such droplets can deposit themselves onto the walls

of the combustion chamber due to backflow illustrated within the velocity vector field in figure 7-12. With the addition of a co-flow it can be seen that the region of backflow becomes smaller. Droplets will be less likely to deposit upon the wall of the combustion chamber and thus reducing the risk of nozzle clogging.

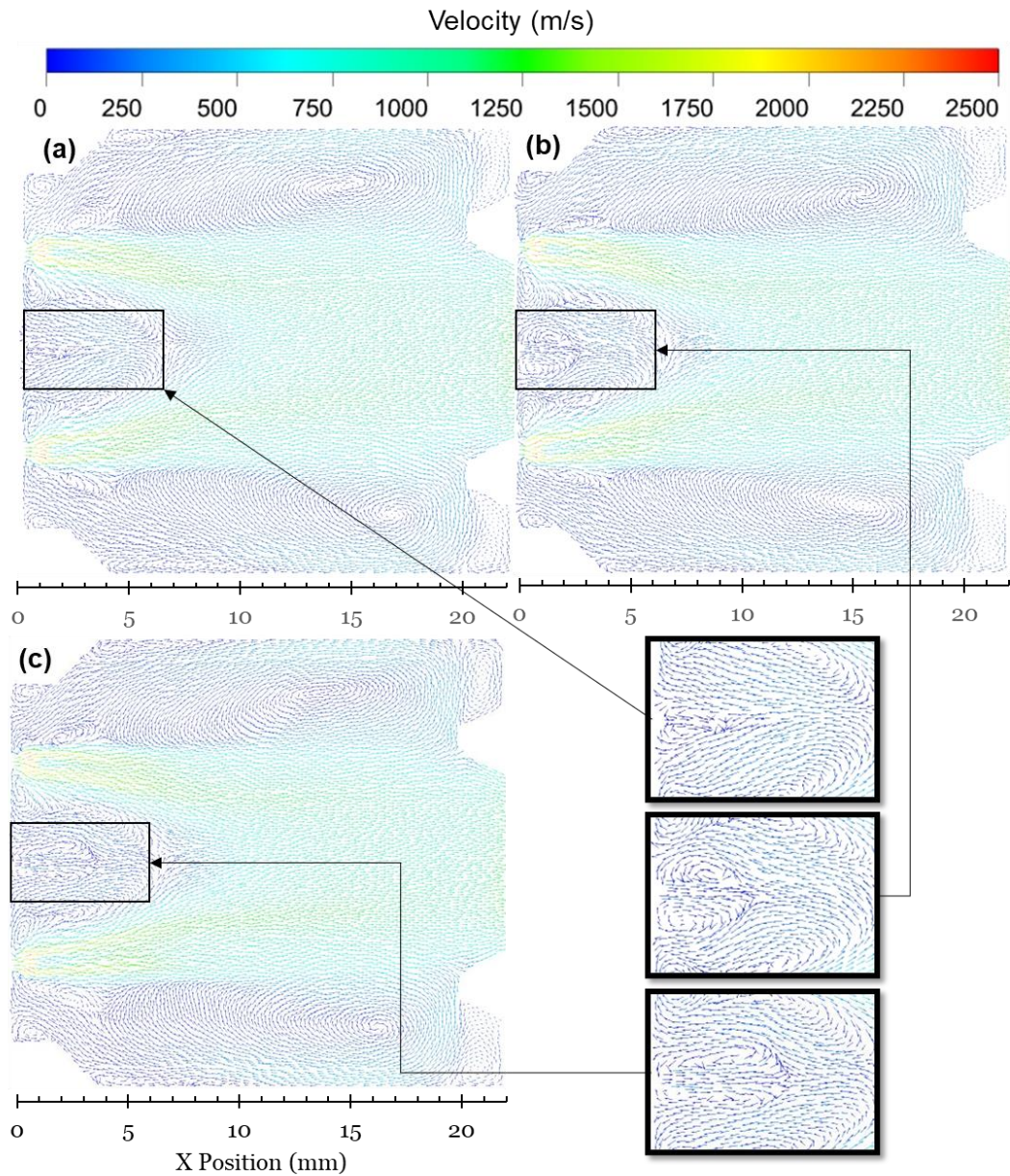


Figure 7-12: Time averaged velocity at Weber numbers (a) 100, (b) 180 and (c) 415.

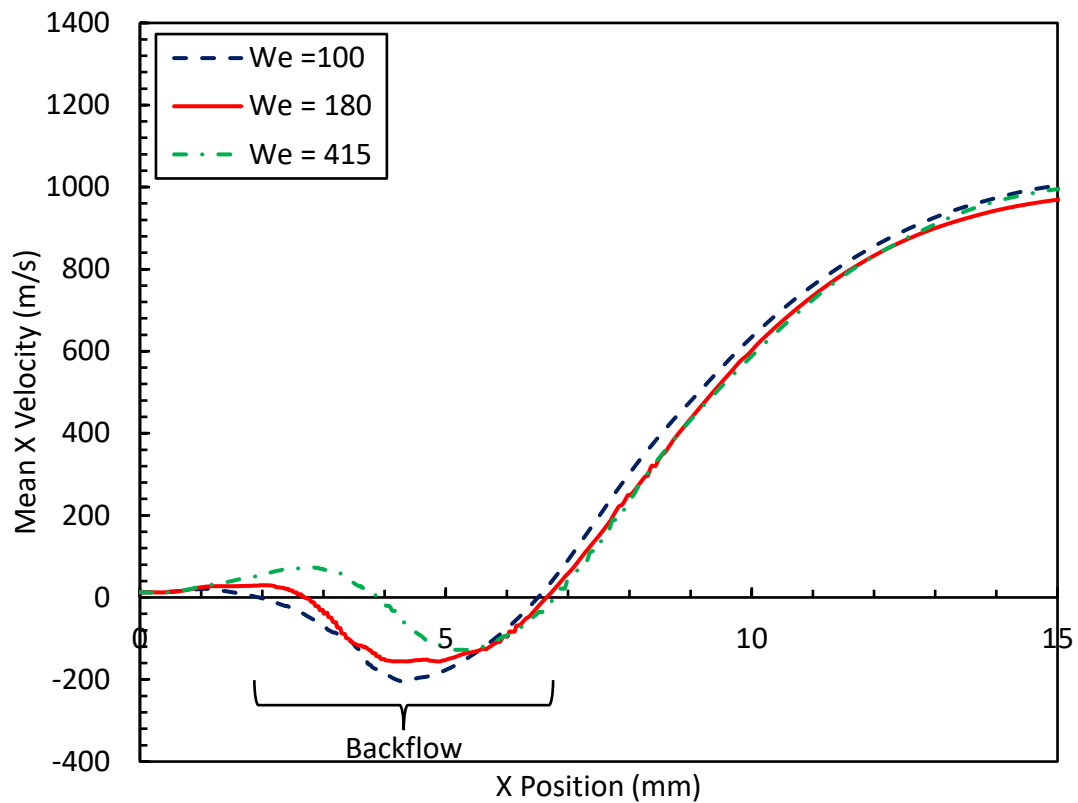


Figure 7-13: Time averaged axial centre line velocity profiles at the Weber numbers considered.

Droplets with a higher velocity will be able to more readily overcome the backflow region in the combustion chamber due to their greater momentum. Figure 7-14 shows the relationship between the droplet diameter and the droplet velocity from droplets formed from the primary breakup of the liquid column at Weber numbers of 100, 180 and 415. It can be seen that as the Weber number increases the droplet velocity increases. With a higher co-flow velocity greater momentum is transferred to the liquid from the gas allowing for the droplets to obtain a higher velocity. It can also be seen in figure 7-14 that as the droplet diameter increases the velocity of the droplets decreases. The decay takes an exponential form for all the Weber numbers considered. The distributions shown in figure 7-14 can be represented by equation 7.3, where a , b

and c are coefficients that are fitted to the data for the three Weber numbers. The values of “ a ”, “ b ”, “ c ” and the coefficient of determination “ R^2 ” is given in table 7-3.

Equation 7.3 is obtained from a curve fit of the numerical data to a correlation using the MATLAB statistical toolbox. The value of “ a ” varies with the Weber number, as the Weber number increases the value of “ a ” increases. The three curves at the different Weber numbers take a similar exponential form. As can be seen, the decay constant ‘ b ’ is similar for all three cases taking a value of around 2.0. This would indicate that it is independent of the Weber number. The vertical shift in curves appears a function of Weber number and is controlled by parameter ‘ We^c ’. The constant “ c ” is similar for all three Weber numbers and takes a value between 0.51 – 0.46. The addition of a co-flow gas injection provides a smaller backflow region and a higher velocity for droplets. High droplet velocities only aid in clogging when droplets are close to the walls as particle impacts with the wall are more likely to result in the particle successfully bonding with the wall. High droplet velocities do not promote clogging if the particles remain within the centre of the combustion chamber.

$$u_p = a * d_p^{-b} + We^c \quad (Eq\ 7.3)$$

Table 7-3: Coefficients for the statistical fit between the droplet velocity and droplet diameter formed from primary breakup and coefficient of determination values.

We	a	b	c	R^2
100	4264	2.10	0.51	0.9898
180	4598	2.10	0.51	0.9717
415	4932	1.975	0.46	0.9973

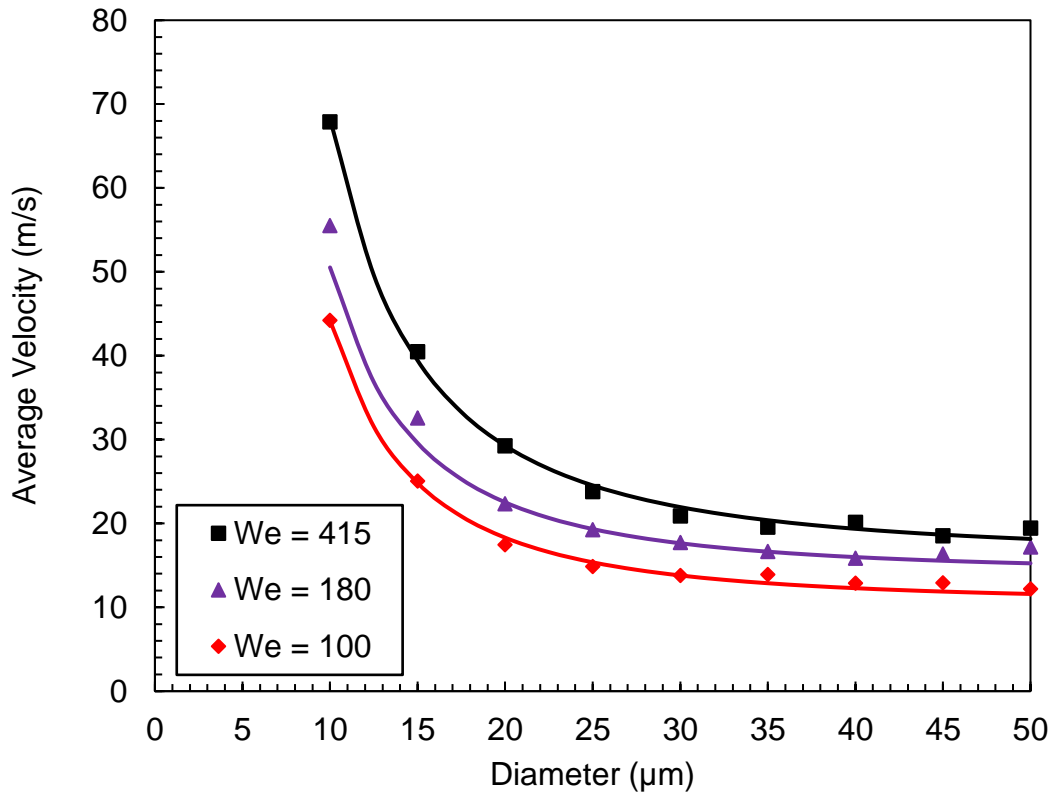


Figure 7-14: Droplet diameter vs. average droplet velocity of the droplets formed from primary breakup.

Figure 7-15 shows the liquid column and the droplets within the combustion chamber at Weber numbers of 100, 180 and 415. It can be seen from figure 7-15 that the higher droplet velocity results in a reduction in the number of droplets that remain around the liquid column. Significantly fewer droplets can be found near the nozzle wall indicated by the arrow in figure 7-15 (a). Particles that impact this wall with sufficient momentum will bond to this wall and create a blockage near the suspension injector. The reduction of particles that get carried and trapped within this region will aide in the preventing of clogging at this location. It can also be seen that with a high co-flow velocity more droplets remain within the centre of the combustion chamber. As particles remain within the centre of the combustion chamber, they are less likely to impact the nozzle walls and bond to the nozzle walls.

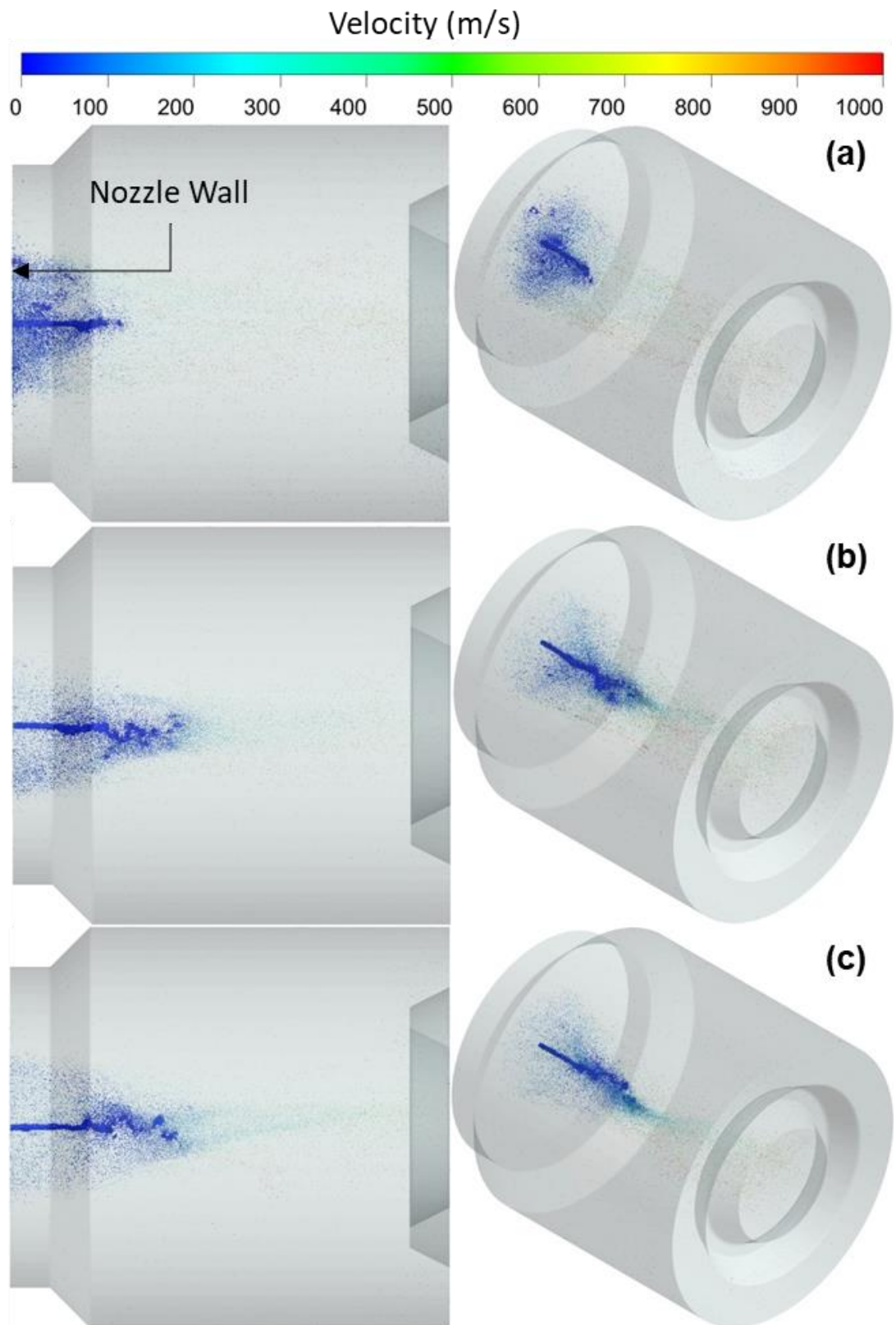


Figure 7-15: Liquid column and droplets within the combustion chamber coloured by the velocity magnitude for (a) $We = 100$, (b) $We = 180$ and (c) $We = 400$.

7.7 Summary

For the first time the primary breakup of the liquid jet injection has been investigated for SHVOF thermal spray. A number of factors have allowed for a high-fidelity investigation into the primary breakup for this application. Firstly, the geometry modelled has been carefully selected to minimise the computational cost. The combustion chamber alone is modelled within this investigation as the primary breakup is confined to the combustion chamber alone. This has allowed for a drastic reduction in the computational domain modelled and hence the computational cost. Secondly, a multiscale modelling approach has been employed as the large-scale structures are resolved using the volume of fluid framework and the small scale structures are modelled using a discrete particle model framework. This approach allows for a significant reduction in the computational cost as the small scale droplet structures that require the most computational cost to resolve within the volume of fluid framework are modelled at a fraction of the cost within a discrete particle model framework. This hybrid approach provides many advantages over the traditional standalone multiphase models. The hybrid VOF and DPM approach allows for significant reduction in the computational cost over a standalone VOF model. This approach offers a considerably higher fidelity than the DPM model currently employed within SHVOF thermal spray. A discussion on the meshing strategy employed for this hybrid multiscale approach has been provided. This study has identified two modes of droplet formation. The first is from ligament formation and detachment from the surface of the jet. The second mode is from ejection of large liquid lumps that disintegrate into smaller droplets.

A co-flow of gas around the liquid injection has been introduced within this study to correct the backflow seen near the liquid injection within the combustion chamber.

Three co-flow velocities are considered of 0 m/s, 200 m/s and 400 m/s corresponding to Weber numbers of 100, 180 and 415. The co-flow forces droplets away from recirculation zones that exist around the liquid core. It has been suggested that the introduction of a co-flow around the injector will aid in reducing clogging within the combustion chamber. As shown, the co-flow results in a smaller region of backflow, which smaller droplets are able to overcome more readily. Additionally, this study has shown that the addition of the co-flow will result in an increase in the droplet velocity subsequent to primary breakup. The SMD from primary breakup is compared to experimental measurements at the same Weber numbers. The numerical model is shown to be in good agreement with the experimental measurements.

The droplet diameters from primary breakup are obtained within this study. The droplet diameter distributions from the primary breakup follow a log normal distribution. This modelling approach has allowed for a characterisation of droplets produced from primary breakup for the first time within SHVOF thermal spray. This high-fidelity approach provides a useful tool to inject more physically representative droplet diameter and velocities for pure DPM models. Finally, a correlation between the diameter of the droplets produced from primary breakup and the droplet velocity is obtained. The correlation presented allows for a useful tool to provide more physically representative droplet velocities for pure DPM investigations. The correlation is provided by equation 7.3.

Chapter 8: Conclusion

8.1 Key Findings

Chapter 4 has modelled four commercially available suspension high velocity oxy fuel thermal spray nozzles to understand the effect of the combustion chamber length, barrel length and total length on the gas and suspension dynamics. The understanding developed within this study will aid the design of the next generation of SHVOF thermal spray nozzles, the key findings from this investigation are summarised as follows:

- It has been shown that the residence time of particles within the flow is influenced by the total length of the nozzle. Longer nozzles allow for greater residence time of particles within the flow which enhances heat and momentum transfer from the gas phase to the suspension.
- It can also be seen the nozzle length influences the gas velocity magnitude and the gas temperature. Shorter nozzles allow for a higher gas velocity and temperature which also enhances momentum and heat transfer to the suspension accordingly.
- It is essential for suspension feedstocks to allow sufficient time for accelerating, heating and vaporization of the liquid component of the suspension to ensure particle impact with the substrate at maximum velocities and temperatures.
- The next generation of nozzles should optimise the length of the nozzle to provide the optimum trade-off between the higher velocities delivered from

reducing the nozzle length and the longer duration of time the particles spend within the flow obtained from increasing the nozzle length.

Chapter 5 has developed a new thermal spray technology for spraying composite coatings. Initially a numerical model for radial injection of suspension outside of the nozzle is implemented. The numerical model is compared and validated with experimental observations obtained using high speed imaging. The numerical model is used to develop a hybrid nozzle for composite coating applications, the key findings are outlined as follows:

- The eddy dissipation model (EDM) previously employed for the combustion within the SHVOF thermal spray literature over predicts the combustion chamber temperature when compared to the adiabatic flame temperature within the combustion chamber by as much as 12.5 %. The over prediction of the combustion chamber temperature has been addressed by employing a detailed reaction mechanism using the eddy dissipation concept (EDC) model. This approach is more computationally expensive however it provides a significantly higher accuracy compared with the eddy dissipation model previously employed within the modelling literature. This approach provides an improvement in the adiabatic flame temperature of 12.5 % when compared to the eddy dissipation model.
- A radial injection of suspension into the free jet is investigated to inform the design of a hybrid nozzle. The effect of the suspension mass flow rate, angle of injection and the diameter of the injector are investigated to optimise the radial injection into the shroud.

- It is demonstrated that the suspension flow rate significantly influences the gas and particle dynamics. As the suspension flow rate increases the penetration of the droplets into the jet, heat loss from the jet and momentum loss from the jet increases. Therefore, the optimum flow rate must ensure maximum penetration with minimum heat and momentum removal of the jet.
- The numerical model is compared to experimental measurements of the jet trajectory and the breakup point at six different suspension feed rates using high speed imaging. The results show satisfactory agreement with the experimental measurements.
- The effect of varying the injection angle into the jet has been investigated. Three injection angles are considered, a perpendicular injection, a negative angled injection of 15 degrees and a positive angled injection of 15 degrees. It is shown that a positive angled injection increases the particle velocities and reduces the particle temperatures. A positive injection provides the suspension with a velocity component in the same direction as the gas flow. Using a negative angled injection increases the particle temperatures and reduces the particle velocities. As the injection is angled in the direction opposing the flow, the particles must be decelerated and then accelerated in the direction of the flow. This allows for an increase in the duration of time particles spend in the jet.
- The effect of the suspension injector diameter is also considered, it is shown that reducing the suspension injector diameter increases penetration of the liquid jet into the crossflow. Greater penetration of suspension allows for greater momentum and heat transfer to the suspension droplets which results in an increase in the particle velocities and temperatures respectively. Reducing

the injector diameter however makes injectors more prone to clogging. Therefore, the minimum injector diameter that does not allow clogging to occur should be employed to inject the suspension. Removable injectors within the shroud have been employed to allow for the optimum injector diameter for the material being sprayed.

- A hybrid nozzle has been designed within this thesis, which utilises an axial injection within the combustion chamber with a shrouding attachment, a shrouding gas and a radial injection within the shrouding attachment.
- The angle of the shrouding attachment has been designed to minimise air entrainment from the atmosphere into the jet and maximise the penetration of suspension into the jet to improve the deposition of oxygen sensitive materials. The expansion angle of the shroud is optimised to minimise air entrainment into the shroud which compromises the inert environment within the shroud. It is found that at angles larger than 7 degrees air entrains into the shroud. The addition of a shrouding gas can allow for larger shrouding angles to be employed by delaying the mixing of atmospheric oxygen into the jet.

Prior numerical models employed within suspension high velocity oxy fuel thermal spray underpredict the particle temperature by as much as 500 K. Chapter 6 has addressed the underprediction of the particle temperature by investigating the effect of the Nusselt number correlation used to determine the heat transfer coefficient. The key findings of this investigation is outlined as follows:

- Three Nusselt number correlations which account for different flow effects were considered. Particle temperature predictions were compared for an incompressible correlation previously employed for this application, a

compressible correlation which accounts for Mach number effects and a Rarefied correlation that accounts for Knudsen number effects. It has been demonstrated that accounting for Mach number and Knudsen number effects in the Nusselt number correlation greatly increase particle temperatures by as large as 1200 K. This avoids the underprediction seen with the incompressible Nusselt number correlations employed for this application.

- Particle temperatures are compared to experimentally measured values using a two colour pyrometry method. It is demonstrated that the incompressible correlation significantly underpredicts the fluid heat transfer coefficient at the particle surface. The incompressible correlation under predicts the particle temperature by an average of 42.9%. It is shown that accounting for Mach and Knudsen number effects on the Nusselt number improves temperature predictions. The compressible correlation improves the particle temperature predictions by an average value of 30.6%. Further still accounting for the Knudsen number effects on the Nusselt number produces the best overall prediction for the particle temperature. The rarefied correlation improves the particle temperature prediction by an average value of 38.1%.
- Comparisons of particle velocity measurements obtained from a time-of-flight approach to the numerical model have demonstrated a significant over prediction at large standoff distances. The difference between the Accuraspray measurement and the velocity predicted from the Kavanau correlation is small (1.2 %) at a standoff distance of 75 mm. However, at large standoff distances the error between the Accuraspray measurement and the numerical prediction for the velocity increases. The difference between the experimental and numerical values is as large as 40 % at a standoff distance of 150 mm. It is

suggested that this over prediction is caused by the under prediction in the mixing rate from the RANS models. Scale resolving simulations such as hybrid RANS-LES or LES have shown better agreement in the prediction of the mixing rate of turbulent jets [191].

Finally, Chapter 7 has employed a multiscale high-fidelity simulation of the combustion chamber to produce the first study investigating the primary breakup within SHVOF thermal spray. The key findings are summarised as follows:

- The geometry modelled within this investigation has been reduced to the combustion chamber to allow for a high-fidelity model of the combustion chamber. modelling the combustion chamber alone allows for a drastic reduction in the computational cost of this approach.
- The numerical approach consists of a coupled volume of fluid and discrete particle model with a scale resolving simulation. The volume of fluid framework is employed to resolve the large-scale structures such as the liquid core, ligament and droplet formation. The discrete particle model is employed to model and track the small-scale droplet structures. This approach offers a lower computational cost over the standalone volume of fluid method and a significantly higher fidelity over the discrete particle model previously employed for this application.
- Two methods for droplet formation are outlined and these are the formation of droplets from ligament detachment off the main jet and the disintegration of large liquid lumps ejected off the liquid jet.
- This framework is employed to investigate the effect of a co-flow of inert gas around the liquid injection. The co-flow is introduced to prevent droplets from

entering recirculation zones in an attempt to reduce clogging within the combustion chamber. The co-flow reduces the backflow region which can significantly alter the particle trajectories within the combustion chamber. It is shown that the addition of a gas co-flow results in a significant reduction in particles trapped within recirculation zones. This is highly likely to reduce clogging within the nozzle which currently presents a significant problem.

- The droplet diameters from primary breakup have been characterised. The droplet diameter distributions from the primary breakup follow a log normal distribution. The SMD from primary breakup is compared to experimental measurements at the same Weber numbers. The comparisons to experimental measurements provide confidence in the numerical modelling approach employed within this investigation.

8.2 Contribution to Knowledge

This thesis has employed the first numerical investigation into a radial injection of suspension for suspension high velocity oxy fuel thermal spray. The numerical model is compared with experimental measurements obtained using high speed imaging. This thesis has demonstrated a sensitivity to the suspension flow rate, angle of injection and the injector diameter. Radial injections of suspensions will allow for improved deposition of oxygen sensitive materials such as graphene which is showing promising results for wear resistant applications.

A hybrid nozzle has been designed within this thesis for improved deposition of composite coatings. The hybrid nozzle combines an axial injection within the combustion chamber, physical shroud attachment, a shrouding gas and a radial injection within the shroud attachment. The hybrid nozzle has been developed to deposit composite coatings. The composite coatings deposited from the hybrid nozzle will likely improve composite coatings formed from a constituent material that is sensitive to oxygen at high temperatures. The hybrid nozzle is a fundamentally new design developed as a part of this thesis. The hybrid nozzle allows for two materials of drastically different properties and oxygen sensitivities to be sprayed simultaneously.

This thesis has substantially improved the predictions of the numerical models employed to determine the heat transfer coefficient within suspension high velocity oxy fuel thermal spray. Three different models to determine the heat transfer coefficient for the suspension have been employed. The temperature predictions from an incompressible correlation, compressible correlation and a rarefied correlation are compared to experimental measurements obtained using a two colour pyrometry

method. The latter two correlations are applied for the first time for suspension high velocity oxy fuel thermal spray within this thesis. It is shown that significant improvements in particle temperature predictions can be obtained by accounting for Mach number and Knudsen number effects on the heat transfer coefficient. This thesis has shown that Mach number and Knudsen number effects play a significant role in the heat transfer to the suspension.

This first ever high-fidelity multiscale investigation into a SHVOF thermal spray combustion chamber has been undertaken. The modelling approach employed can be utilised for a range of multiphase combustion applications. The simulation utilised a coupled volume of fluid and discrete particle model for the liquid injection into the combustion chamber. This modelling approach is able to capture the primary breakup of the liquid jet which prior numerical modelling studies have neglected. The geometry is carefully chosen to focus computational resources within areas of interest. Within this investigation only the combustion chamber is modelled, the outlet condition is obtained from a lower fidelity and a lower computational cost approach.

A framework is developed to utilise high fidelity investigations into the suspension high velocity oxy fuel thermal spray combustion chamber to characterise the injection which can be used to inform lower fidelity models. From the high-fidelity simulation droplet diameter distributions and droplet velocity distributions can be obtained for the droplets that are formed from primary breakup. The characterization of droplet velocities and droplet diameters can be used to provide more physical injections into a pure DPM investigation. Owing to the significant challenges surrounding validating numerical models within the combustion chamber the pure DPM investigation can provide confidence for the numerical modelling approach. As the particle velocities

and temperatures can be compared to experimental measurements obtained within the free jet using a two-colour pyrometry and time of flight method, respectively.

This thesis introduces a co-flow around the liquid injection and offers an argument as to why this injection method offers a reduction of clogging and waste of suspension from the numerical predictions. This injector type offers a significant design change to injectors employed within suspension high velocity oxy fuel thermal spray. This thesis has developed a correlation between the droplet diameter and the droplet velocity produced from the primary breakup of the liquid jet. The correlation is given by equation 7.3 and offers a more representative initial condition for a pure discrete particle model investigation.

8.3 Outline for Future Work

There is still much to learn about suspension high velocity oxy fuel thermal spray and the numerical methods employed can still be further improved. From the current understanding developed within this thesis on the nozzle geometry further investigations should optimise the nozzle length to maximise the gas velocity and temperature whilst also allowing sufficient time for the liquid component to vaporise. This should allow for higher particle velocities and temperature upon impacting the substrate.

The combustion reaction employed within this study provides a significant improvement in gas temperature predictions however, it is considerably more computationally expensive than the global one step reaction previously employed. An investigation into the effect of the size of the reaction mechanism on the accuracy of the flame temperature with the eddy dissipation concept model may allow for reduction in the computational cost [220], [221], [222]. A sensitivity study comparing the accuracy against the computational cost will significantly aid numerical studies. This will allow for the optimum reaction mechanism size to be employed with the multiscale high-fidelity approach.

The temperature predictions have been significantly improved through the use of more physically representative Nusselt number correlations. Currently numerical modelling approaches employed only account for the heat transfer between the continuous phase and the discrete phase through convection. Further investigation into the effect of heat transfer through radiation should be evaluated [223]. It should be considered if the heat transfer to particles through radiation is significant. Additionally, the evaporation rate for suspension droplets differ to that of pure liquids. A numerical model that accounts

for the effect of particles on the evaporation of the liquid within the discrete particle model framework should be developed, implementation and validation. This however requires an extensive experimental investigation into the breakup and evaporation of suspension droplets.

Numerical models do not include Brownian motion of nanoparticles within the liquid, the effect of particle size distributions, particle shape distributions and do not model for particle agglomeration which gives rise to a number of different particle structures upon impacting the substrate. Development, implementation and validation of a model that can account for these effects will significantly improve our understanding of suspension high velocity oxy fuel thermal spray and will be very relevant to similar areas of engineering such as spray dryers and other suspension thermal spray processes.

Finally, this thesis presents a multiscale high-fidelity approach to modelling the combustion chamber within suspension high velocity oxy fuel thermal spray. There is significant understanding and development that is required with this numerical approach. Within this thesis a water jet is injected into the combustion chamber as the breakup of a pure liquid jet is more well understood. To improve the robustness of this approach to model a suspension jet, a model that accounts for the effect of particle loading on the surface tension of the suspension droplets must be implemented and validated. Additionally, fine cells introduce large instabilities due to the source terms generated within the discrete particle model. Studies are required to improve the robustness of the discrete particle model for fine meshes. Implementing algorithms that better distribute source terms will significantly improve numerical stability and accuracy of this numerical modelling approach.

Chapter 9: Bibliography

- [1] D. Tejero-Martin, M. Rezvani Rad, A. McDonald, T. Hussain, Beyond Traditional Coatings: A Review on Thermal-Sprayed Functional and Smart Coatings, *J. Therm. Spray Technol.* 28 (2019) 598–644.
- [2] S. Gu, S. Kamnis, Numerical modelling of in-flight particle dynamics of non-spherical powder, *Surf. Coatings Technol.* 203 (2009) 3485–3490. doi:10.1016/j.surfcoat.2009.05.024.
- [3] Z. Liu, X. Ren, Z. Yan, H. Zhu, T. Zhang, W. Zhu, X. Li, Effect of Inlet Air Heating on Gas Turbine Efficiency under Partial Load, *Energies.* 12 (2019) 12–17.
- [4] J.V. (Joachim V. Heberlein, P. Fauchais, M.I. Boulos, Thermal spray fundamentals : from powder to part, Springer Books, 2014.
- [5] J.C. Miranda, A. Ramalho, Abrasion resistance of thermal sprayed composite coatings with a nickel alloy matrix and a WC hard phase. Effect of deposition technique and re-melting, *Tribol. Lett.* 11 (2001) 37–48.
- [6] Thermal Spray Powder Market | Growth, Trends, and Forecast, (n.d.). <https://www.mordorintelligence.com/industry-reports/thermal-spray-powder-market> (accessed May 28, 2020).
- [7] H. Singh, A. Ang, S. Matthews, H. De Villiers-Lovelock, B.S. Singh, Thermal Spray for Extreme Environments, *J. Therm. Spray Technol.* 28 (2019) 1339–1345.
- [8] J. Matějček, P. Chráska, J. Linke, Thermal spray coatings for fusion applications - Review, *J. Therm. Spray Technol.* 16 (2007) 64–83.

- [9] A. Vardelle, C. Moreau, J. Akedo, H. Ashrafizadeh, C.C. Berndt, J.O. Berghaus, M. Boulos, J. Brogan, A.C. Bourtsalas, A. Dolatabadi, M. Dorfman, T.J. Eden, P. Fauchais, G. Fisher, F. Gaertner, M. Gindrat, R. Henne, M. Hyland, E. Irissou, E.H. Jordan, K.A. Khor, A. Killinger, Y.-C. Lau, C.-J. Li, L. Li, J. Longtin, N. Markocsan, P.J. Masset, J. Matejcek, G. Mauer, A. McDonald, J. Mostaghimi, S. Sampath, G. Schiller, K. Shinoda, M.F. Smith, A.A. Syed, N.J. Themelis, F.-L. Toma, J.P. Trelles, R. Vassen, P. Vuoristo, The 2016 Thermal Spray Roadmap, *J. Therm. Spray Technol.* 25 (2016) 1–65.
- [10] C.U. Hardwicke, Y.C. Lau, Advances in thermal spray coatings for gas turbines and energy generation: A review, *J. Therm. Spray Technol.* 22 (2013) 564–576.
- [11] K. Szymański, A. Hernas, G. Moskal, H. Myalska, Thermally sprayed coatings resistant to erosion and corrosion for power plant boilers - A review, *Surf. Coatings Technol.* 268 (2015) 153–164.
- [12] F. Baino, E. Verné, Glass-based coatings on biomedical implants: a state-of-the-art review, *Biomed. Glas.* 3 (2017) 1–17.
- [13] S. Bano, I. Ahmed, D.M. Grant, A. Nommeots-Nomm, T. Hussain, Effect of processing on microstructure, mechanical properties and dissolution behaviour in SBF of Bioglass (45S5) coatings deposited by Suspension High Velocity Oxy Fuel (SHVOF) thermal spray, *Surf. Coatings Technol.* 372 (2019) 229–238.
- [14] Y.Z. Yang, J.M. Tian, J.T. Tian, Z.Q. Chen, X.J. Deng, D.H. Zhang, Preparation of graded porous titanium coatings on titanium implant materials by plasma spraying, *J. Biomed. Mater. Res.* 52 (2000) 333–337.
- [15] A. Killinger, P. Müller, R. Gadow, What Do We Know, What are the Current Limitations of Suspension HVOF Spraying?, *J. Therm. Spray Technol.* 24

(2015) 1130–1142.

- [16] F. Venturi, T. Hussain, Radial Injection in Suspension High Velocity Oxy-Fuel (S-HVOF) Thermal Spray of Graphene Nanoplatelets for Tribology, *J. Therm. Spray Technol.* 29 (2020) 255–269.
- [17] A. Dolatabadi, J. Mostaghimi, V. Pershin, Effect of a cylindrical shroud on particle conditions in high velocity oxy-fuel spray process, *Sci. Technol. Adv. Mater.* 3 (2002) 245–255.
- [18] G. Mauer, R. Vaßen, D. Stöver, Comparison and applications of DPV-2000 and accuraspray-g3 diagnostic systems, *J. Therm. Spray Technol.* 16 (2007) 414–424.
- [19] A. Moridi, S.M. Hassani-Gangaraj, M. Guagliano, M. Dao, Cold spray coating: review of material systems and future perspectives, *Surf. Eng.* 30 (2014) 369–395.
- [20] M. Jadidi, S. Moghtadernejad, A. Dolatabadi, Numerical Modeling of Suspension HVOF Spray, *J. Therm. Spray Technol.* 25 (2016) 451–464.
- [21] W.P. Jones, A.J. Marquis, K. Vogiatzaki, Large-eddy simulation of spray combustion in a gas turbine combustor, *Combust. Flame.* 161 (2014) 222–239.
- [22] C. Caruyer, S. Vincent, E. Meillot, J.-P. Caltagirone, Modeling the first instant of the interaction between a liquid and a plasma jet with a compressible approach, *Surf. Coatings Technol.* 205 (2010) 974–979.
- [23] P.J. Morris, Y. Du, K. Kara, Jet noise simulations for realistic jet nozzle geometries, *Procedia Eng.* 6 (2010) 28–37.
- [24] M. Bai, Z. Pala, T. Hussain, Microstructure and phase stability of suspension

- high velocity oxy-fuel sprayed yttria stabilised zirconia coatings from aqueous and ethanol based suspensions, *J. Eur. Ceram. Soc.* 38 (2017) 1–0.
- [25] R. Gadow, A. Killinger, J. Rauch, Introduction to High-Velocity Suspension Flame Spraying (HVSFS), *J. Therm. Spray Technol.* 17 (2008) 655–661.
- [26] M. Bai, R. Khammas, L. Guan, J. Murray, T. Hussain, Suspension high velocity oxy-fuel spraying of a rutile TiO₂ feedstock: Microstructure, phase evolution and photocatalytic behaviour, *Ceram. Int.* 43 (2017) 15288–15295.
- [27] P.H. Oosthuizen, W.E. Carscallen, *Compressible fluid flow*, 1st ed., McGraw-Hill, 1997.
- [28] M. Jadidi, S. Moghtadernejad, A. Dolatabadi, A Comprehensive Review on Fluid Dynamics and Transport of Suspension/Liquid Droplets and Particles in High-Velocity Oxygen-Fuel (HVOF) Thermal Spray, *Coatings*. 5 (2015) 576–645.
- [29] T.. Adamson, J.. Nicholls, On the Structure of Jets from Highly Underexpanded Nozzles Into Still Air, *J. Aerosp. Sci.* 26 (1959) 16–24.
- [30] R. Baidya, A. Pesyridis, M. Cooper, Ramjet Nozzle Analysis for Transport Aircraft Configuration for Sustained Hypersonic Flight, *Appl. Sci.* 8 (2018) 574.
- [31] J.A. Miller, G.A. Fisk, Combustion Chemistry, *Chem. Eng. News.* 65 (1987) 1–503.
- [32] J. Li, Z. Zhao, A. Kazakov, F.L. Dryer, An updated comprehensive kinetic model of hydrogen combustion, *Int. J. Chem. Kinet.* 36 (2004) 566–575.
- [33] M. Ó Conaire, H.J. Curran, J.M. Simmie, W.J. Pitz, C.K. Westbrook, A

- comprehensive modeling study of hydrogen oxidation, *Int. J. Chem. Kinet.* 36 (2004) 603–622.
- [34] S. Kamnis, S. Gu, 3-D modelling of kerosene-fuelled HVOF thermal spray gun, *Chem. Eng. Sci.* 61 (2006) 5427–5439.
- [35] S. Gordon, B.J. McBride, NASA Reference Computer Program for Calculation Complex Chemical Equilibrium Compositions and Applications, 1994.
- [36] M. Pai, I. Bermejo-Moreno, O. Desjardins, H. Pitsch, Role of Weber number in the primary breakup of liquid jets in crossflow, 2009.
- [37] H. Tabbara, S. Gu, A study of liquid droplet disintegration for the development of nanostructured coatings, *AIChE J.* 58 (2012) 3533–3544.
- [38] W. von Ohnesorge, Formation of drops by nozzles and the breakup of liquid jets, *J. Appl. Math. Mech.* 16 (1936) 355–358.
- [39] H.P. Bjarne, The physics behind water mist systems, in: *IWMA Conf.*, 2004: pp. 1–15.
- [40] C. Shao, K. Luo, M. Chai, J. Fan, Sheet, ligament and droplet formation in swirling primary atomization, *AIP Adv.* 8 (2018) 45211.
- [41] A.H. (Arthur H. Lefebvre, *Atomization and sprays*, Hemisphere Pub. Corp, 1989.
- [42] R. Andrew, H. Meng, *Numerical Modelling of Tunnel Fires and Water Mist Suppression*, University of Nottingham, 2006.
- [43] P.A. Vesilind, The Rosin-Rammler particle size distribution, *Resour. Recover. Conserv.* 5 (1980) 275–277.

- [44] D.B. Siano, The log-normal distribution function, *J. Chem. Educ.* 49 (1972) 755.
- [45] C.M. Varga, J.C. Lasheras, E.J. Hopfinger, Initial breakup of a small-diameter liquid jet by a high-speed gas stream, *J. Fluid Mech.* 497 (2003) 405–434.
- [46] D.R. Guildenbecher, C. López-Rivera, P.E. Sojka, Secondary atomization, *Exp. Fluids.* 46 (2009) 371–402.
- [47] L.-P. Hsiang, G.M. Faeth, Near-limit drop deformation and secondary breakup, *Int. J. Multiph. Flow.* 18 (1992) 635–652.
- [48] M. Pilch, C.A. Erdman, Use of breakup time data and velocity history data to predict the maximum size of stable fragments for acceleration-induced breakup of a liquid drop, *Int. J. Multiph. Flow.* 13 (1987) 741–757.
- [49] Z. Liu, S.S. Hwang, R.D. Reitz, Breakup mechanisms and drag coefficients of high-speed vaporizing liquid drops, *At. Sprays.* 6 (1996) 353–376.
- [50] Z. Liu, R.D. Reitz, An analysis of the distortion and breakup mechanisms of high speed liquid drops, *Int. J. Multiph. Flow.* 23 (1997) 631–650.
- [51] T.G. Theofanous, G.J. Li, T.N. Dinh, Aerobreakup in Rarefied Supersonic Gas Flows, *J. Fluids Eng.* 126 (2004) 516.
- [52] J.. Nicholls, A.. Ranger, Aerodynamic shattering of liquid drops., *AIAA J.* 7 (1969) 285–290.
- [53] P. Roy Choudhury, Slurry fuels, *Prog. Energy Combust. Sci.* 18 (1992) 409–427.
- [54] Y. Gan, L. Qiao, Combustion characteristics of fuel droplets with addition of

- nano and micron-sized aluminum particles, *Combust. Flame*. 158 (2011) 354–368.
- [55] Y. Gan, Y.S. Lim, L. Qiao, Combustion of nanofluid fuels with the addition of boron and iron particles at dilute and dense concentrations, *Combust. Flame*. 159 (2012) 1732–1740.
- [56] R. Gadow, A. Killinger, M. Kuhn, D. Lopéz, Verfahren und Vorrichtung zum thermischen Spritzen von Suspensionen, German patent, DE102005038453A1, 2005.
- [57] A. Killinger, M. Kuhn, R. Gadow, High-Velocity Suspension Flame Spraying (HVSFS), a new approach for spraying nanoparticles with hypersonic speed, *Surf. Coatings Technol.* 201 (2006) 1922–1929.
- [58] A. Killinger, R. Gadow, G. Mauer, A. Guignard, R. Vaßen, D. Stöver, Review of New Developments in Suspension and Solution Precursor Thermal Spray Processes, *J. Therm. Spray Technol.* 20 (2011) 677–695.
- [59] E. Gozali, M. Mahrukh, S. Gu, S. Kamnis, Numerical analysis of multicomponent suspension droplets in high-velocity flame spray process, *J. Therm. Spray Technol.* 23 (2014) 940–949.
- [60] M. Jadidi, A.Z. Yeganeh, A. Dolatabadi, Numerical Study of Suspension HVOF Spray and Particle Behavior Near Flat and Cylindrical Substrates, *J. Therm. Spray Technol.* 27 (2018) 59–72.
- [61] S. Kamnis, S. Gu, Numerical modelling of propane combustion in a high velocity oxygen–fuel thermal spray gun, *Chem. Eng. Process. Process Intensif.* 45 (2006) 246–253.

- [62] Ansys Inc, ANSYS Fluent v19 R1 Theory Guide, 2019.
- [63] S. Takahashi, T. Nonomura, K. Fukuda, A numerical scheme based on an immersed boundary method for compressible turbulent flows with shocks: Application to two-dimensional flows around cylinders, *J. Appl. Math.* 2014 (2014).
- [64] B.P. Leonard, Order of accuracy of QUICK and related convection-diffusion schemes, *Appl. Math. Model.* 19 (1995) 640–653.
- [65] H. Kobayashi, T. Nakashima, T. Tamura, K. Maruta, T. Niioka, Turbulence measurements and observations of turbulent premixed flames at elevated pressures up to 3.0 MPa, *Combust. Flame.* 108 (1997) 104–110.
- [66] Chung K. Law, L. k. Chung, *Combustion Physics*, Cambridge University Press, 2006.
- [67] S. Gu, D.G. McCartney, C.N. Eastwick, K. Simmons, Numerical Modeling of In-Flight Characteristics of Inconel 625 Particles During High-Velocity Oxy-Fuel Thermal Spraying, *J. Therm. Spray Technol.* 13 (2004) 200–213.
- [68] M. Mahrukh, A. Kumar, S. Gu, Effects of angular injection, and effervescent atomization on high-velocity suspension flame spray process, *Surf. Coatings Technol.* 302 (2016) 368–382.
- [69] M. Mahrukh, A. Kumar, S. Gu, S. Kamnis, E. Gozali, Modeling the Effects of Concentration of Solid Nanoparticles in Liquid Feedstock Injection on High-Velocity Suspension Flame Spray Process, *Ind. Eng. Chem. Res.* 55 (2016) 2556–2573.
- [70] J. Ordóñez-Miranda, J.J. Alvarado-Gil, R. Medina-Ezquivel, Generalized

- Bruggeman formula for the effective thermal conductivity of particulate composites with an interface layer, in: *Int. J. Thermophys.*, Springer, 2010: pp. 975–986.
- [71] L. Liu, M. Fu, J. Wu, The distribution of SMD downstream the discharge orifices of effervescent atomizers, *GONGCHENG RE WULI XUEBAO*. 22 (2001) 653–656.
- [72] L. Qian, J. Lin, Modeling on effervescent atomization: A review, *Sci. China Physics, Mech. Astron.* 54 (2011) 2109–2129.
- [73] L. Qian, J. Lin, H. Xiong, T. Leung Chan, Theoretical investigation of the influence of liquid physical properties on effervescent atomization performance, *J. Fluids Eng. Trans. ASME*. 133 (2011).
- [74] A. Farrokhpanah, T. Coyle, J. Mostaghimi, Numerical Study of Suspension Plasma Spraying, *J. Therm. Spray Technol.* 26 (2016) 12–36.
- [75] F. Jabbari, M. Jadidi, R. Wuthrich, A. Dolatabadi, A Numerical Study of Suspension Injection in Plasma-Spraying Process, *J. Therm. Spray Technol.* 23 (2014) 3–13.
- [76] E. Dongmo, R. Gadow, A. Killinger, M. Wenzelburger, Modeling of combustion as well as heat, mass, and momentum transfer during thermal spraying by HVOF and HVSFs, *J. Therm. Spray Technol.* 18 (2009) 896–908.
- [77] E. Dongmo, A. Killinger, M. Wenzelburger, R. Gadow, Numerical approach and optimization of the combustion and gas dynamics in High Velocity Suspension Flame Spraying (HVSFS), *Surf. Coatings Technol.* 203 (2009) 2139–2145.

- [78] M. Taleby, S. Hossainpour, Numerical Investigation of High Velocity Suspension Flame Spraying, *J. Therm. Spray Technol.* 21 (2012) 1163–1172.
- [79] S.A. Morsi, A.J. Alexander, An investigation of particle trajectories in two-phase flow systems, *J. Fluid Mech.* 55 (1972) 193–208.
- [80] E. Gozali, S. Kamnis, S. Gu, Numerical investigation of combustion and liquid feedstock in high velocity suspension flame spraying process, *Surf. Coatings Technol.* 228 (2013) 176–186.
- [81] E. Gozali, M. Mahrukh, S. Gu, S. Kamnis, Numerical investigation on effects of nanoparticles on liquid feedstock behavior in High Velocity Oxygen Fuel (HVOF) suspension spraying, *Surf. Coatings Technol.* 280 (2015) 370–377.
- [82] N. Curry, K. VanEvery, T. Snyder, N. Markocsan, Thermal Conductivity Analysis and Lifetime Testing of Suspension Plasma-Sprayed Thermal Barrier Coatings, *Coatings.* 4 (2014) 630–650.
- [83] A. Vardelle, C. Moreau, N.J. Themelis, C. Chazelas, A Perspective on Plasma Spray Technology, *Plasma Chem. Plasma Process.* 35 (2014) 491–509.
- [84] P. Fauchais, V. Rat, J.F. Coudert, R. Etchart-Salas, G. Montavon, Operating parameters for suspension and solution plasma-spray coatings, *Surf. Coatings Technol.* 202 (2008) 4309–4317.
- [85] G. Bolelli, D. Bellucci, V. Cannillo, R. Gadow, A. Killinger, L. Lusvarghi, P. Müller, A. Sola, Comparison between Suspension Plasma Sprayed and High Velocity Suspension Flame Sprayed bioactive coatings, *Surf. Coatings Technol.* 280 (2015) 232–249.
- [86] D.G. Thomas, Transport characteristics of suspension: VIII. A note on the

- viscosity of Newtonian suspensions of uniform spherical particles, *J. Colloid Sci.* 20 (1965) 267–277.
- [87] K. Toda, H. Furuse, Extension of Einstein's viscosity equation to that for concentrated dispersions of solutes and particles, *J. Biosci. Bioeng.* 102 (2006) 524–528.
- [88] I.M. Krieger, T.J. Dougherty, A Mechanism for Non-Newtonian Flow in Suspensions of Rigid Spheres, *Trans. Soc. Rheol.* 3 (1959) 137–152.
- [89] T. Dabak, O. Yucel, Shear viscosity behavior of highly concentrated suspensions at low and high shear-rates, *Rheol. Acta.* 25 (1986) 527–533.
- [90] B.A. Horri, P. Ranganathan, C. Selomulya, H. Wang, A new empirical viscosity model for ceramic suspensions, *Chem. Eng. Sci.* 66 (2011) 2798–2806.
- [91] E. Meillot, S. Vincent, C. Caruyer, D. Damiani, J.P. Caltagirone, Modelling the interactions between a thermal plasma flow and a continuous liquid jet in a suspension spraying process, *J. Phys. D. Appl. Phys.* 46 (2013) 1–11.
- [92] M. Vujanović, Z. Petranović, W. Edelbauer, J. Baleta, N. Duić, Numerical modelling of diesel spray using the Eulerian multiphase approach, *Energy Convers. Manag.* 104 (2015) 160–169.
- [93] W.F. Noh, P. Woodward, SLIC (Simple Line Interface Calculation), in: *Proc. Fifth Int. Conf. Numer. Methods Fluid Dyn.*, Springer, Berlin, Heidelberg, 1976: pp. 330–340.
- [94] A.W.Y. Tan, J.Y. Lek, W. Sun, A. Bhowmik, I. Marinescu, X. Song, W. Zhai, F. Li, Z. Dong, C.B. Boothroyd, E. Liu, Influence of particle velocity when propelled using N₂ or N₂-He mixed gas on the properties of cold-sprayed

Ti6Al4V coatings, *Coatings*. 8 (2018) 327.

- [95] S. Subramaniam, Lagrangian-Eulerian methods for multiphase flows, *Prog. Energy Combust. Sci.* 39 (2013) 215–245.
- [96] K. Singh, M. Sharabi, S. Ambrose, C. Eastwick, R. Jefferson-Loveday, Prediction of film thickness of an aero-engine bearing chamber using coupled vof and thin film model, in: *Proc. ASME Turbo Expo*, American Society of Mechanical Engineers (ASME), 2019.
- [97] A.K. Balasubramanian, V. Kumar, P. Nakod, J. Schütze, A. Rajan, Multiscale modelling of a doublet injector using hybrid VOF-DPM method, in: *American Institute of Aeronautics and Astronautics (AIAA)*, 2020.
- [98] J.L. Hee, K. Simmons, B. Kakimpa, D. Hann, Computationally Efficient Modelling of Oil Jet-Breakup and Film Formation for Bearing Chamber Applications, in: *ASME Turbo Expo 2018 Turbomach. Tech. Conf. Expo.*, ASME International, 2018: pp. 1–12.
- [99] S. He, G. Chen, C. Guo, Investigation of mixing and slag layer behaviours in the RH degasser with bottom gas injection by using the VOF–DPM coupled model, *Ironmak. Steelmak.* 46 (2019) 771–776.
- [100] A.A. Adeniyi, H.P. Morvan, K.A. Simmons, A coupled Euler-Lagrange CFD modelling of droplets-to-film, 121 (2017) 1897–1918.
- [101] H. Grosshans, R.-Z. Szász, L. Fuchs, Development of a Combined VOF-LPT Method to Simulate Two-phase Flows in Various Regimes, in: *7th Int. Symp. Turbul. Shear Flow Phenom.*, 2011: pp. 1–6.
- [102] G. Tomar, D. Fuster, S. Zaleski, S. Popinet, Multiscale simulations of primary

atomization, *Comput. Fluids*. 39 (2010) 1864–1874.

- [103] D. Kim, F. Ham, H. Le, M. Herrmann, X. Li, M.C. Soteriou, W. Kim, High-Fidelity Simulation of Atomization in a Gas Turbine Injector High Shear Nozzle, in: *Annu. Conf. Liq. At. Spray Syst.*, 2014: pp. 1–10.
- [104] D. Kim, O. Desjardins, M. Herrmann, P. Moin, The Primary Breakup of a Round Liquid Jet by a Coaxial Flow of Gas, in: *Chicago*, 2007.
- [105] J. Shinjo, A. Umemura, Fluid dynamic and autoignition characteristics of early fuel sprays using hybrid atomization LES, *Combust. Flame*. 203 (2019) 313–333.
- [106] A. Umemura, J. Shinjo, Detailed SGS atomization model and its implementation to two-phase flow LES, *Combust. Flame*. 195 (2018) 232–252.
- [107] A. Umemura, Turbulent atomization subgrid model for two-phase flow large eddy simulation (theoretical development), *Combust. Flame*. 165 (2016) 154–176.
- [108] A. Akbarozari, S. Amiri, O. Bamber, J. Grenon, M. Choquet, L. Pouliot, Improvement of Online Diagnostic System to Monitor In-flight Particles in Thermal Spray Processes, in: *Int. Therm. Spray Conf., JTST*, 2019: pp. 957–964.
- [109] M. Nelkin, In what sense is turbulence an unsolved problem?, *Science* (80-.). 255 (1992) 566–570.
- [110] N. Mazellier, J.C. Vassilicos, Turbulence without Richardson-Kolmogorov cascade, *Phys. Fluids*. 22 (2010) 1–25.
- [111] P.A. Durbin, B.A.P. Reif, *Statistical theory and modeling for turbulent flows*,

Wiley, 2011.

- [112] P.R. Spalart, Strategies for turbulence modelling and simulations, in: *Int. J. Heat Fluid Flow*, Elsevier Science Inc, 2000: pp. 252–263.
- [113] P. Sagaut, S. Deck, M. Terracol, *Multiscale and Multiresolution Approaches in Turbulence*, Imperial College Press, 2013.
- [114] N.D. Katopodes, *Free-Surface Flow*, Elsevier, 2019.
- [115] E. Roohi, A.P. Zehri, M. Passandideh-Fard, Numerical simulation of cavitation around a two-dimensional hydrofoil using VOF method and LES turbulence model, *Appl. Math. Model.* 37 (2013) 6469–6488.
- [116] A. Abbà, A.C. Cercignani, L. Valdetaro, Analysis of subgrid scale models, *Comput. Math. with Appl.* 46 (2003) 521–535.
- [117] F. Nicoud, F. Ducros, Subgrid-scale stress modelling based on the square of the velocity gradient tensor, *Flow, Turbul. Combust.* 62 (1999) 183–200.
- [118] L. Davidson, W. Selada, *An Introduction to Turbulence Models*, 2016.
- [119] P.K. Kundu, I.M. Cohen, D.R. Dowling, *Fluid mechanics*, Academic Press, 2012.
- [120] B.F. Magnussen, B.H. Hjertager, On mathematical modeling of turbulent combustion with special emphasis on soot formation and combustion, *Symp. Combust.* 16 (1977) 719–729.
- [121] B. Magnussen, On the structure of turbulence and a generalized eddy dissipation concept for chemical reaction in turbulent flow, in: *19th Aerosp. Sci. Meet.*, American Institute of Aeronautics and Astronautics, Reston, Virginia, 1981: pp.

1–8.

- [122] S. Iavarone, M. Cafiero, M. Ferrarotti, F. Contino, A. Parente, A multiscale combustion model formulation for NO_x predictions in hydrogen enriched jet flames, *Int. J. Hydrogen Energy*. 44 (2019) 23436–23457.
- [123] I.R. Gran, B.F. Magnussen, A numerical study of a bluff-body stabilized diffusion flame. Part 2. Influence of combustion modeling and finite-rate chemistry, *Combust. Sci. Technol.* 119 (1996) 191–217.
- [124] M.J. Evans, C. Petre, P.R. Medwell, A. Parente, Generalisation of the eddy-dissipation concept for jet flames with low turbulence and low Damköhler number, *Proc. Combust. Inst.* 37 (2019) 4497–4505.
- [125] A. De, E. Oldenhof, P. Sathiah, D. Roekaerts, A. De, E. Oldenhof, · D Roekaerts, P. Sathiah, Numerical Simulation of Delft-Jet-in-Hot-Coflow (DJHC) Flames Using the Eddy Dissipation Concept Model for Turbulence–Chemistry Interaction, *Flow, Turbul. Combust.* 87 (2011) 537–567.
- [126] Ansys Inc, ANSYS Fluent v19 R1 User’s Guide, 2019.
- [127] C.T. Crowe, Drag coefficient of particles in a rocket nozzle., *AIAA J.* 5 (1967) 1021–1022.
- [128] W. Ranz, W. Marshall, Evaporation from Drops, Parts I, *Chem Eng Prog.* 48 (1952) 141–146.
- [129] W. Ranz, W. Marshall, Evaporation from drops Part II, *Chemical.* 45 (1952) 173–180.
- [130] L.L. Kavanau, J.M. Drake, Heat transfer from spheres to a rarefied gas in subsonic flow., California, 1977.

- [131] J.R.M. Drake, G.. Backer, Heat Transfer From Sphere to a Rarefied Gas in Supersonic Flow, *Trans. American Soc. Mech. Eng.* 74 (1952) 1241–1249.
- [132] R.D. Reitz, Modeling Atomization Processes in High-Pressure Vaporizing Sprays, *At. Spray Technol.* 3 (1987) 309–337.
- [133] Y.-C. Liu, L.-S. Chao, Modified Effective Specific Heat Method of Solidification Problems, *Mater. Trans.* 47 (2006) 2737–2744.
- [134] P. Lamberg, R. Lehtiniemi, A.-M. Henell, Numerical and experimental investigation of melting and freezing processes in phase change material storage, *Int. J. Therm. Sci.* 43 (2004) 277–287.
- [135] H. Grosshans, R.-Z. Szász, L. Fuchs, Development of an efficient statistical volumes of fluid-Lagrangian particle tracking coupling method, *Int. J. Numer. Methods Fluids.* 74 (2014) 898–918.
- [136] C. Bilger, S. Cant, Atomization and breakup of liquid kerosene at elevated pressure, *At. Sprays.* 28 (2018) 1123–1144.
- [137] T. Pringuey, Large Eddy Simulation of Primary Liquid-Sheet Breakup, University of Cambridge, 2012.
- [138] B.R. Latimer, A. Pollard, Comparison of pressure-velocity coupling solution algorithms, *Numer. Heat Transf.* 8 (1985) 635–652.
- [139] E. Dongmo, M. Wenzelburger, R. Gadow, Analysis and optimization of the HVOF process by combined experimental and numerical approaches, *Surf. Coatings Technol.* 202 (2008) 4470–4478.
- [140] M. Mahrukh, A. Kumar, S. Gu, Experimental Study of the Effects of Using Different Precursor Concentrations, Solvent Types, and Injection Types on

Solution Precursor High-Velocity Oxygen Fuel (HVOF) Nanostructured Coating Formation, *Ind. Eng. Chem. Res.* 56 (2017) 4957–4969.

- [141] P.D.C. Mingheng Li, Multi-scale modeling and analysis of an industrial HVOF thermal spray process, *Chem. Eng. Sci.* 60 (2005) 3649–3669.
- [142] A.S.M. Ang, N. Sanpo, M.L. Sesso, S.Y. Kim, C.C. Berndt, Thermal spray maps: Material genomics of processing technologies, *J. Therm. Spray Technol.* 22 (2013) 1170–1183.
- [143] S. Elghobashi, On predicting particle-laden turbulent flows, *Appl. Sci. Res.* 52 (1994) 309–329.
- [144] R. Monchaux, M. Bourgoïn, A. Cartellier, Analyzing preferential concentration and clustering of inertial particles in turbulence, *Int. J. Multiph. Flow.* 40 (2012) 1–18.
- [145] T.C.W. Lau, G.J. Nathan, The effect of Stokes number on particle velocity and concentration distributions in a well-characterised, turbulent, co-flowing two-phase jet, *J. Fluid Mech.* 809 (2016) 72–110.
- [146] K. Korpiola, J.P. Hirvonen, L. Laas, F. Rossi, The influence of nozzle design on HVOF exit gas velocity and coating microstructure, *J. Therm. Spray Technol.* 6 (1997) 469–474.
- [147] M.W. Lee, J.J. Park, D.Y. Kim, S.S. Yoon, H.Y. Kim, D.H. Kim, S.C. James, S. Chandra, T. Coyle, J.H. Ryu, W.H. Yoon, D.S. Park, Optimization of supersonic nozzle flow for titanium dioxide thin-film coating by aerosol deposition, *J. Aerosol Sci.* 42 (2011) 771–780.
- [148] A. Dolatabadi, V. Pershin, J. Mostaghimi, New Attachment for Controlling Gas

Flow in the HVOF Process, *J. Therm. Spray Technol.* 14 (2005) 91–99.

- [149] S. Matthews, Shrouded plasma spray of Ni–20Cr coatings utilizing internal shroud film cooling, *Surf. Coatings Technol.* 249 (2014) 56–74.
- [150] J.W. Murray, G.A. Rance, F. Xu, T. Hussain, Alumina-graphene nanocomposite coatings fabricated by suspension high velocity oxy-fuel thermal spraying for ultra-low-wear, *J. Eur. Ceram. Soc.* 38 (2018) 1819–1828.
- [151] M. Jadidi, Numerical Modeling of Suspension and Particle Transport in Thermal Spray Processes, Concordia University, 2017.
- [152] W.E. Ranz, Some experiments on orifice sprays, *Can. J. Chem. Eng.* 36 (1958) 175–181.
- [153] S. V Apte, K. Mahesh, T. Lundgren, Accounting for finite-size effects in simulations of disperse particle-laden flows, *Int. J. Multiph. Flows.* 34 (2008) 260–271.
- [154] J. Zhang, T. Li, H. Ström, T. Løvås, Grid-independent Eulerian-Lagrangian approaches for simulations of solid fuel particle combustion, *Chem. Eng. J.* 387 (2020) 123964.
- [155] M. Farokhi, M. Birouk, Application of Eddy Dissipation Concept for Modeling Biomass Combustion, Part 1: Assessment of the Model Coefficients, *Energy and Fuels.* 30 (2016) 10789–10799.
- [156] S. Emami, H. Jafari, Y. Mahmoudi, Effects of Combustion Model and Chemical Kinetics in Numerical Modeling of Hydrogen-Fueled Dual-Stage HVOF System, *J. Therm. Spray Technol.* 1 (2019) 1–13.
- [157] Z. Ren, G.M. Goldin, V. Hiremath, S.B. Pope, Simulations of a turbulent non-

- premixed flame using combined dimension reduction and tabulation for combustion chemistry, *Fuel*. 105 (2013) 636–644.
- [158] M. Jadidi, S. Moghtadernejad, A. Dolatabadi, Penetration and breakup of liquid jet in transverse free air jet with application in suspension-solution thermal sprays, *Mater. Des.* 110 (2016) 425–435.
- [159] W. Menkirch, Density sensitive flow visualization, *Methods Exp. Phys.* 18 (1981) 345–403.
- [160] PNR | Manufacturers of Industrial Spray Nozzles, Spraying Systems and Associated Products., (n.d.). <https://www.pnr.co.uk/> (accessed June 10, 2020).
- [161] J. Sekar, A. Rao, S. Pillutla, A. Danis, S.Y. Hsieh, Liquid jet in cross flow modeling, in: *Proc. ASME Turbo Expo, American Society of Mechanical Engineers (ASME)*, 2014.
- [162] Z. Rek, J. Gregorc, M. Bouaifi, C. Daniel, Numerical simulation of gas jet in liquid crossflow with high mean jet to crossflow velocity ratio, *Chem. Eng. Sci.* 172 (2017) 667–676.
- [163] M. Herrmann, The influence of density ratio on the primary atomization of a turbulent liquid jet in crossflow, *Proc. Combust. Inst.* 33 (2011) 2079–2088.
- [164] M. Herrmann, Detailed numerical simulations of the primary atomization of a turbulent liquid jet in crossflow, *J. Eng. Gas Turbines Power.* 132 (2010) 1–10.
- [165] P. Li, Z. Wang, M. Sun, H. Wang, Numerical simulation of the gas-liquid interaction of a liquid jet in supersonic crossflow, *Acta Astronaut.* 134 (2017) 333–344.
- [166] S. Kawai, S. Lele, Mechanisms of Jet Mixing in a Supersonic Crossflow: A

- Study Using Large-Eddy Simulation, in: 44th AIAA/ASME/SAE/ASEE Jt. Propuls. Conf. & Exhib., American Institute of Aeronautics and Astronautics, Reston, Virginia, 2008: pp. 1–16.
- [167] L. Pawlowski, Suspension and solution thermal spray coatings, *Surf. Coatings Technol.* 203 (2009) 2807–2829.
- [168] R.H. Perry, D.W. Green, *Perry's chemical engineers' handbook*, McGraw-Hill, 2008.
- [169] T. Kinoshita, S.L. Chen, P. Siitonen, P. Kettunen, Densification of plasma-sprayed titanium and tantalum coatings, *J. Therm. Spray Technol.* 5 (1996) 439–444.
- [170] J.W. Murray, A.S.M. Ang, Z. Pala, E.C. Shaw, T. Hussain, Suspension High Velocity Oxy-Fuel (SHVOF)-Sprayed Alumina Coatings: Microstructure, Nanoindentation and Wear, *J. Therm. Spray Technol.* 25 (2016) 1700–1710.
- [171] M. Jankovic, J. Mostaghimi, A New Nozzle Design for dc Plasma Spray Guns, *Plasma Chem. Plasma Process.* 15 (1995) 607–628.
- [172] N. Kishore, S. Gu, Momentum and heat transfer phenomena of spheroid particles at moderate Reynolds and Prandtl numbers, *Int. J. Heat Mass Transf.* 54 (2011) 2595–2601.
- [173] Z. Duan, B. He, Y. Duan, Sphere Drag and Heat Transfer, *Sci. Rep.* 5 (2015) 1–7.
- [174] K.B. Anoop, T. Sundararajan, S.K. Das, Effect of particle size on the convective heat transfer in nanofluid in the developing region, *Int. J. Heat Mass Transf.* 52 (2009) 2189–2195.
- [175] A. Aissa, M. Abdelouahab, A. Noureddine, M. El Ganaoui, B. Pateyron, Ranz

and Marshall correlations limits on heat flow between a sphere and its surrounding gas at high temperature, *Therm. Sci.* 19 (2015) 1521–1528.

[176] R.M. Young, E. Pfender, Nusselt number correlations for heat transfer to small spheres in thermal plasma flows, *Plasma Chem. Plasma Process.* 7 (1987) 211–229.

[177] D.J. Carlson, R.F. Hoglund, Particle drag and heat transfer in rocket nozzles, *AIAA J.* 2 (1964) 1980–1984.

[178] A. Nastic, B. Jodoin, Evaluation of Heat Transfer Transport Coefficient for Cold Spray Through Computational Fluid Dynamics and Particle In-Flight Temperature Measurement Using a High-Speed IR Camera, *J. Therm. Spray Technol.* 27 (2018) 1491–1517.

[179] F.M. Sauer, Convective Heat Transfer from Spheres in a Free-Molecule Flow, *J. Aeronaut. Sci.* 18 (1951) 353–354.

[180] Z. Salhi, P. Gougeon, D. Klein, C. Coddet, Influence of plasma light scattered by in-flight particle on the measured temperature by high speed pyrometry, *Infrared Phys. Technol.* 46 (2005) 394–399.

[181] P. Gougeon, C. Moreau, In-flight particle surface temperature measurement: Influence of the plasma light scattered by the particles, *J. Therm. Spray Technol.* 2 (1993) 229–233.

[182] P. Gougeon, C. Moreau, V. Lacasse, M. Lamontagne, I. Powell, A. Bewsher, A new Sensor for on-line Diagnostics of Particles under Thermal Spraying Conditions., *Adv. Proc. Tech.* 6 (1994) 199–210.

[183] S. Zimmermann, E. Vogli, M. Kauffeldt, M. Abdulgader, B. Krebs, B. R  ther,

- K. Landes, J. Schein, W. Tillmann, Supervision and Measuring of Particle Parameters During the Wire-Arc Spraying Process with the Diagnostic Systems Accuraspray-g3 and LDA (Laser-Doppler-Anemometry), *J. Therm. Spray Technol.* 19 (2010) 745–755.
- [184] W. Brown, *Dynamic light scattering: the method and some applications*, Clarendon Press, 1993.
- [185] R. Pecora, Dynamic light scattering measurement of nanometer particles in liquids, *J. Nanoparticle Res.* 2 (2000) 123–131. <https://link.springer.com/article/10.1023/A:1010067107182> (accessed July 9, 2020).
- [186] T. Owoseni, M. Bai, T. Hussain, N.H. Faisal, T.L. Lee, J. Kelleher, Neutron diffraction residual stress measurements in suspension HVOF sprayed Al₂O₃ and YSZ coatings, in: *Int. Therm. Spray Conf.*, ASM International, 2019: pp. 490–495.
- [187] H. Yang, C. Lee, S.Y. Hwang, The effect of nano-sized Cr₂O₃ addition on the characteristics of NiCr-Cr₂O₃-Ag-BaF₂/CaF₂ coating, *Surf. Coatings Technol.* 201 (2006) 38–44.
- [188] V. Pershin, M. Lufitha, S. Chandra, J. Mostaghimi, Effect of substrate temperature on adhesion strength of plasma-sprayed nickel coatings, *J. Therm. Spray Technol.* 12 (2003) 370–376. doi:10.1361/105996303770348249.
- [189] S.A. Rooholghdos, E. Roohi, Extension of a second order velocity slip/temperature jump boundary condition to simulate high speed micro/nanoflows, *Comput. Math. with Appl.* 67 (2014) 2029–2040. doi:10.1016/j.camwa.2014.05.004.

- [190] Z. Liu, J. Zhou, H. Wu, New correlations for slip flow and heat transfer over a micro spherical particle in gaseous fluid, *Powder Technol.* 338 (2018) 129–139. doi:10.1016/j.powtec.2018.07.006.
- [191] S. M. Kresta, A. W. Etchells III, D. S. Dickey, V. Atiemo-Obeng, *Advances in Industrial Mixing: A Companion to the Handbook of Industrial Mixing*, Wiley Books, 2015.
- [192] M. Alhawwary, Z.J. Wang, Fourier analysis and evaluation of DG, FD and compact difference methods for conservation laws, *J. Comput. Phys.* 373 (2018) 835–862.
- [193] K.R. Meadows, D.A. Caughey, J. Casper, Computing unsteady shock waves for aeroacoustic applications, *AIAA J.* 32 (1994) 1360–1366.
- [194] S. Pirozzoli, *Numerical Methods for High-Speed Flows*, *Annu. Rev. Fluid Mech.* 43 (2011) 163–194.
- [195] M. Roostaei, A. Nouri, V. Fattahpour, D. Chan, Evaluation of numerical schemes for capturing shock waves in modeling proppant transport in fractures, *Pet. Sci.* 14 (2017) 731–745.
- [196] B. Fiorina, S.K. Lele, An artificial nonlinear diffusivity method for supersonic reacting flows with shocks, *J. Comput. Phys.* 222 (2007) 246–264.
- [197] G. Zhao, M. Sun, A. Memmolo, S. Pirozzoli, A general framework for the evaluation of shock-capturing schemes, *J. Comput. Phys.* 376 (2019) 924–936. doi:10.1016/j.jcp.2018.10.013.
- [198] D. Ghosh, *Compact-Reconstruction Weighted Essentially Non-Oscillatory Schemes for Hyperbolic Conservation Laws*, University of Maryland , 2013.

<http://drum.lib.umd.edu/handle/1903/14350> (accessed July 16, 2020).

- [199] A. Hamzehloo, D.J. Lusher, S. Laizet, N.D. Sandham, On the performance of WENO / TENO schemes to resolve turbulence in DNS / LES of high-speed compressible flows, *Int. J. Numer. Methods Fluids*. (2020) 1–22. doi:10.1002/fld.4879.
- [200] F. Xiao, M. Dianat, J.J. McGuirk, LES of turbulent liquid jet primary breakup in turbulent coaxial air flow, *Int. J. Multiph. Flow*. 60 (2014) 103–118.
- [201] X.-S. Tian, H. Zhao, H.-F. Liu, W.-F. Li, J.-L. Xu, Three-dimensional large eddy simulation of round liquid jet primary breakup in coaxial gas flow using the VOF method, *Fuel Process. Technol.* 131 (2015) 396–402.
- [202] M. Ghiji, L. Goldsworthy, P.A. Brandner, V. Garaniya, P. Hield, Analysis of diesel spray dynamics using a compressible Eulerian/VOF/LES model and microscopic shadowgraphy, *Fuel*. 188 (2017) 352–366.
- [203] F. Xiao, Z.G. Wang, M.B. Sun, J.H. Liang, N. Liu, Large eddy simulation of liquid jet primary breakup in supersonic air crossflow, *Int. J. Multiph. Flow*. 87 (2016) 229–240.
- [204] T. Schmidt, F. Gärtner, H. Assadi, H. Kreye, Development of a generalized parameter window for cold spray deposition, *Acta Mater.* 54 (2006) 729–742.
- [205] F. Zhang, T. Müller, T. Zirwes, S. Wachter, T. Jakobs, P. Habisreuther, N. Zarzalis, D. Trimis, T. Kolb, Numerical and Experimental Investigation of Primary Breakup of High-Viscous Fluid at Elevated Pressure, in: *Conf. Liq. At. Spray Syst.*, Paris, France, 2019: pp. 1–8.
- [206] J. Cousin, A. Berlemont, T. Ménard, S. Grout, Primary breakup simulation of a

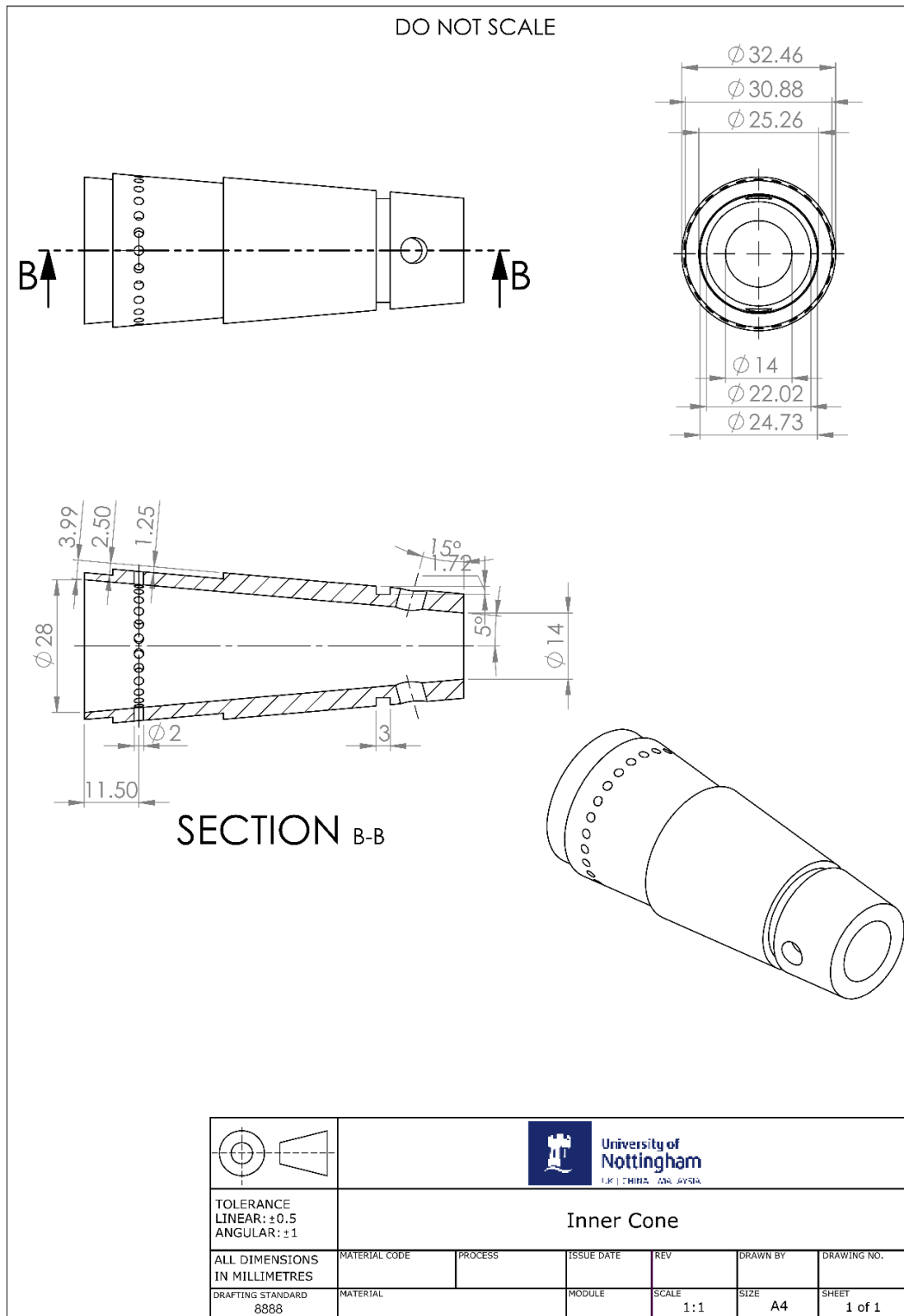
- liquid jet discharged by a low-pressure compound nozzle, *Comput. Fluids*. 63 (2012) 165–173.
- [207] W. Strasser, F. Battaglia, K. Walters, Application of a Hybrid RANS-LES CFD Methodology to Primary Atomization in a Coaxial Injector, in: *ASME International*, 2015.
- [208] T.A. Owoseni, J.W. Murray, Z. Pala, E.H. Lester, D.M. Grant, T. Hussain, Suspension high velocity oxy-fuel (SHVOF) spray of delta-theta alumina suspension: Phase transformation and tribology, *Surf. Coatings Technol.* (2018).
- [209] G. Strotos, I. Malgarinos, N. Nikolopoulos, M. Gavaises, Predicting droplet deformation and breakup for moderate Weber numbers, *Int. J. Multiph. Flow*. 85 (2016) 96–109.
- [210] Y. Ling, S. Zaleski, R. Scardovelli, Multiscale simulation of atomization with small droplets represented by a Lagrangian point-particle model, *Int. J. Multiph. Flow*. 76 (2015) 122–143. doi:10.1016/j.ijmultiphaseflow.2015.07.002.
- [211] J. Shinjo, A. Umemura, Simulation of liquid jet primary breakup: Dynamics of ligament and droplet formation, *Int. J. Multiph. Flow*. 36 (2010) 513–532. doi:10.1016/j.ijmultiphaseflow.2010.03.008.
- [212] J.M. Link, L.A. Cuypers, N.G. Deen, J.A.M. Kuipers, Flow regimes in a spout-fluid bed: A combined experimental and simulation study, *Chem. Eng. Sci.* 60 (2005) 3425–3442.
- [213] M. Farzaneh, S. Sasic, A.E. Almstedt, F. Johnsson, D. Pallarès, A novel multigrid technique for Lagrangian modeling of fuel mixing in fluidized beds,

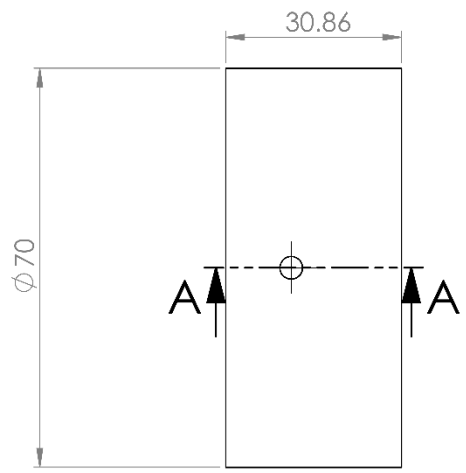
Chem. Eng. Sci. 66 (2011) 5628–5637.

- [214] S. Deb, D.K. Tafti, A novel two-grid formulation for fluid-particle systems using the discrete element method, *Powder Technol.* 246 (2013) 601–616.
- [215] J. Capecelatro, O. Desjardins, An Euler-Lagrange strategy for simulating particle-laden flows, *J. Comput. Phys.* 238 (2013) 1–31.
- [216] H. Gerhardtter, M. Knoll, R. Prieler, M. Landfahner, M. Mühlböck, P. Tomazic, C. Hochenauer, Determining the heating characteristics of non-spherical particles in combusting flows, *Appl. Therm. Eng.* 151 (2019) 124–133.
- [217] S. Chadha, R. Jefferson-Loveday, T. Hussain, Modelling Knudsen number effects in suspension high velocity oxy fuel thermal spray, *Int. J. Heat Mass Transf.* 152 (2020) 119454.
- [218] S. Kazuya, K. Seiichi, O. Yoshiaki, Numerical Analysis of Jet Breakup Behavior Using Particle Method, *J. Nucl. Sci. Technol.* 41 (2004) 715–722.
- [219] F. Perini, R.D. Reitz, Improved atomization, collision and sub-grid scale momentum coupling models for transient vaporizing engine sprays, *Int. J. Multiph. Flow.* 79 (2016) 107–123.
- [220] J. Ströhle, T. Myhrvold, Reduction of a detailed reaction mechanism for hydrogen combustion under gas turbine conditions, *Combust. Flame.* 144 (2006) 545–557.
- [221] T. Varga, T. Nagy, C. Olm, I.G. Zsély, R. Pálvölgyi, Valkó, G. Vincze, M. Cserhádi, H.J. Curran, T. Turányi, Optimization of a hydrogen combustion mechanism using both direct and indirect measurements, *Proc. Combust. Inst.* 35 (2015) 589–596.

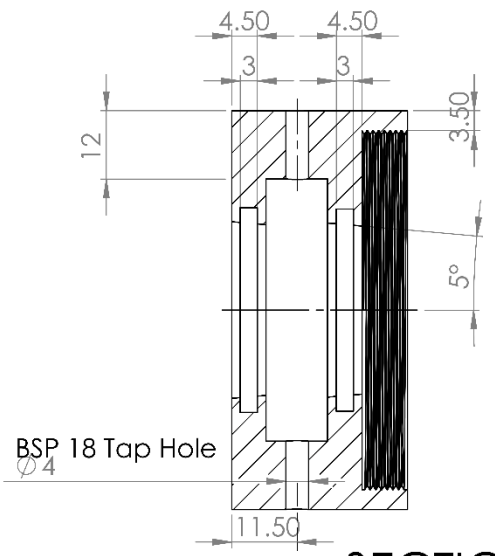
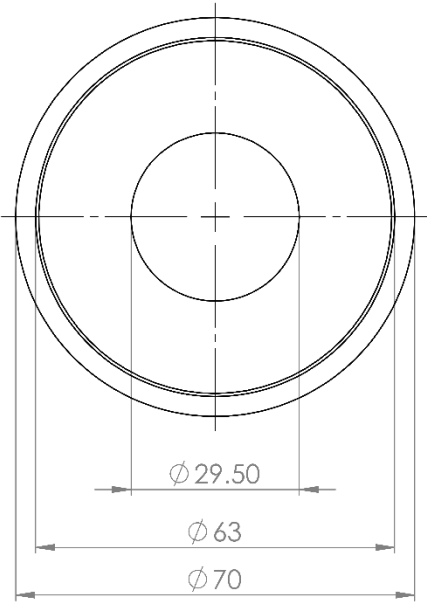
- [222] L.M. Das, Hydrogen-oxygen reaction mechanism and its implication to hydrogen engine combustion, *Int. J. Hydrogen Energy*. 21 (1996) 703–715.
- [223] M.G. Carvalho, T.L. Farias, Modelling of heat transfer in radiating and combusting systems, *Chem. Eng. Res. Des.* 76 (1998) 175–184.

Appendix I – Design of Shroud to Deposit Oxygen Sensitive Materials



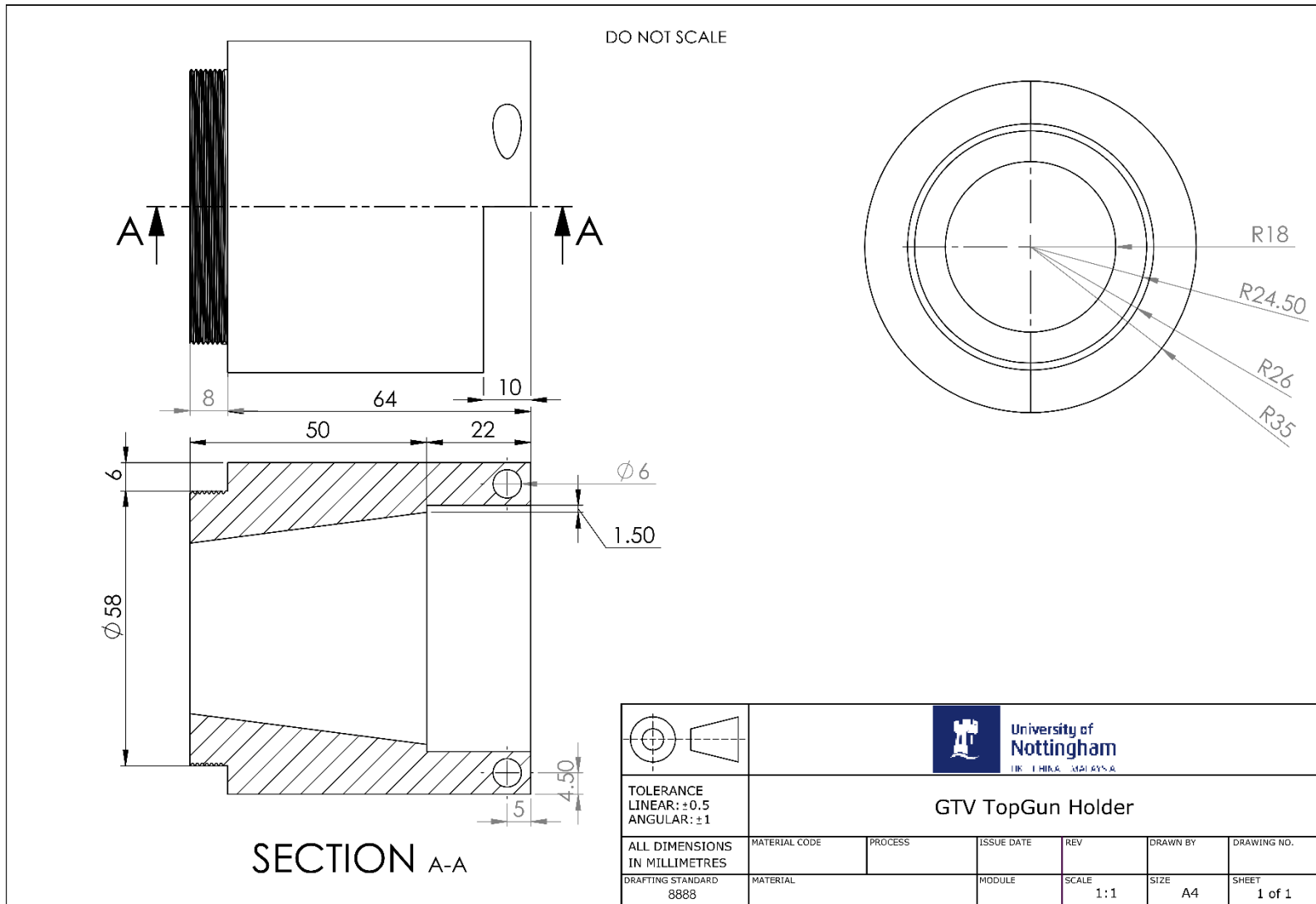


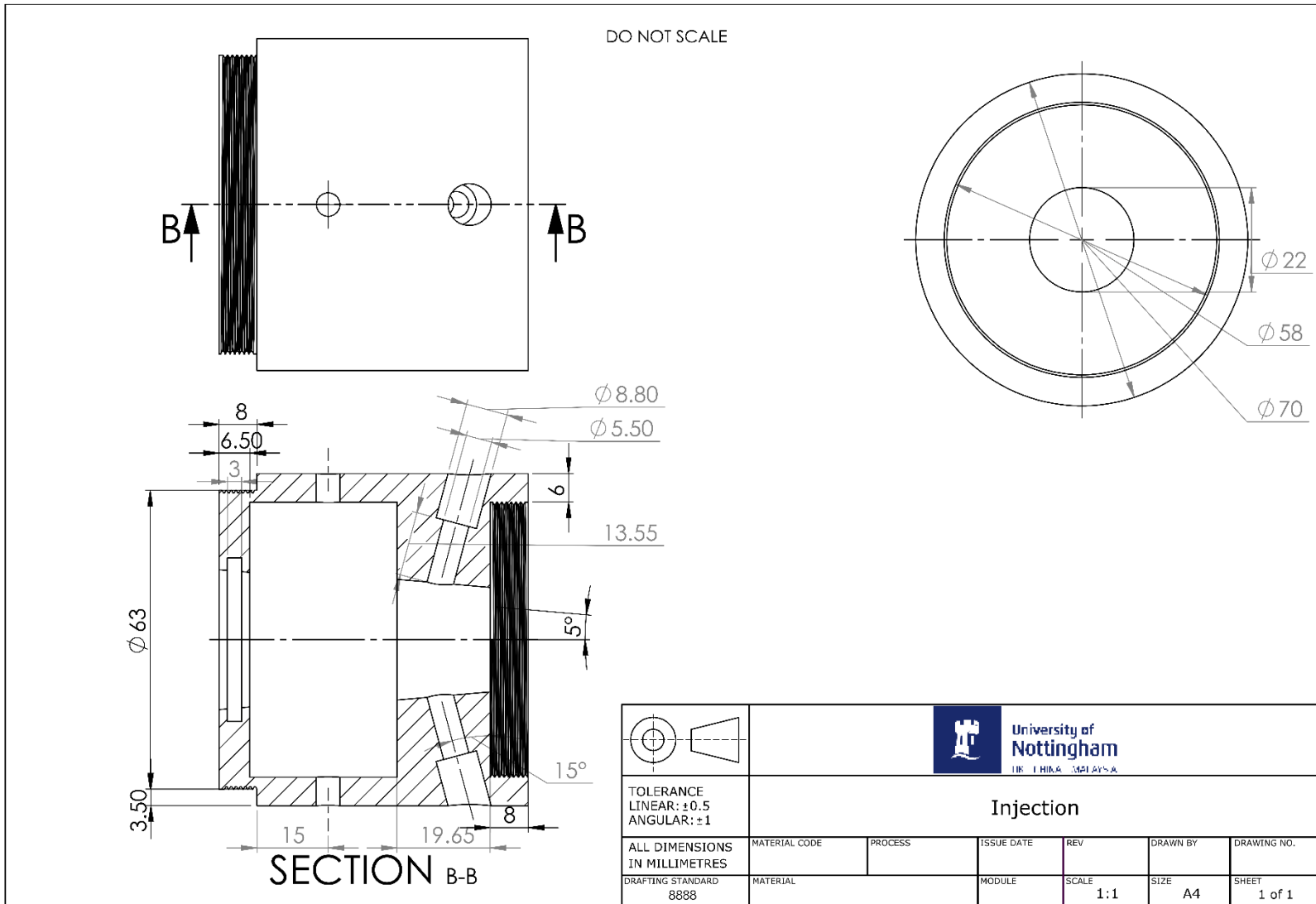
DO NOT SCALE

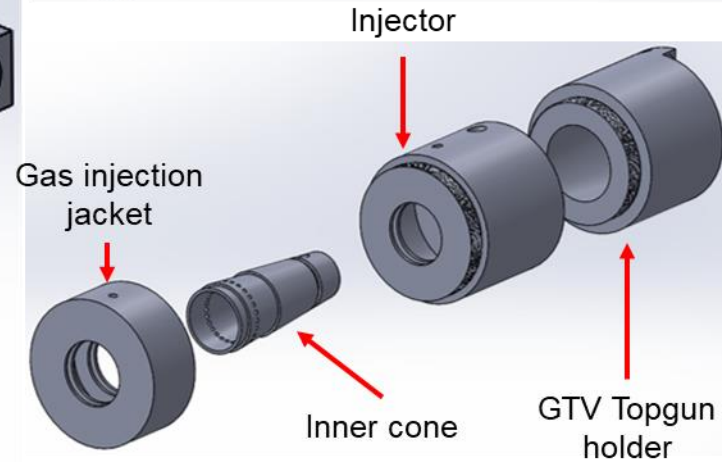
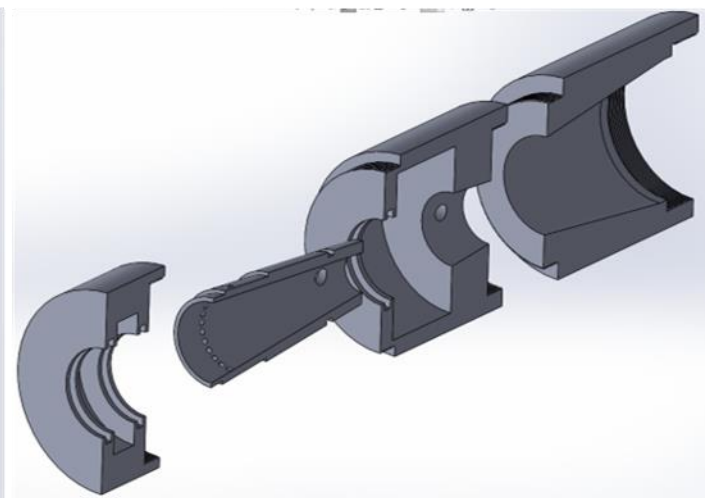
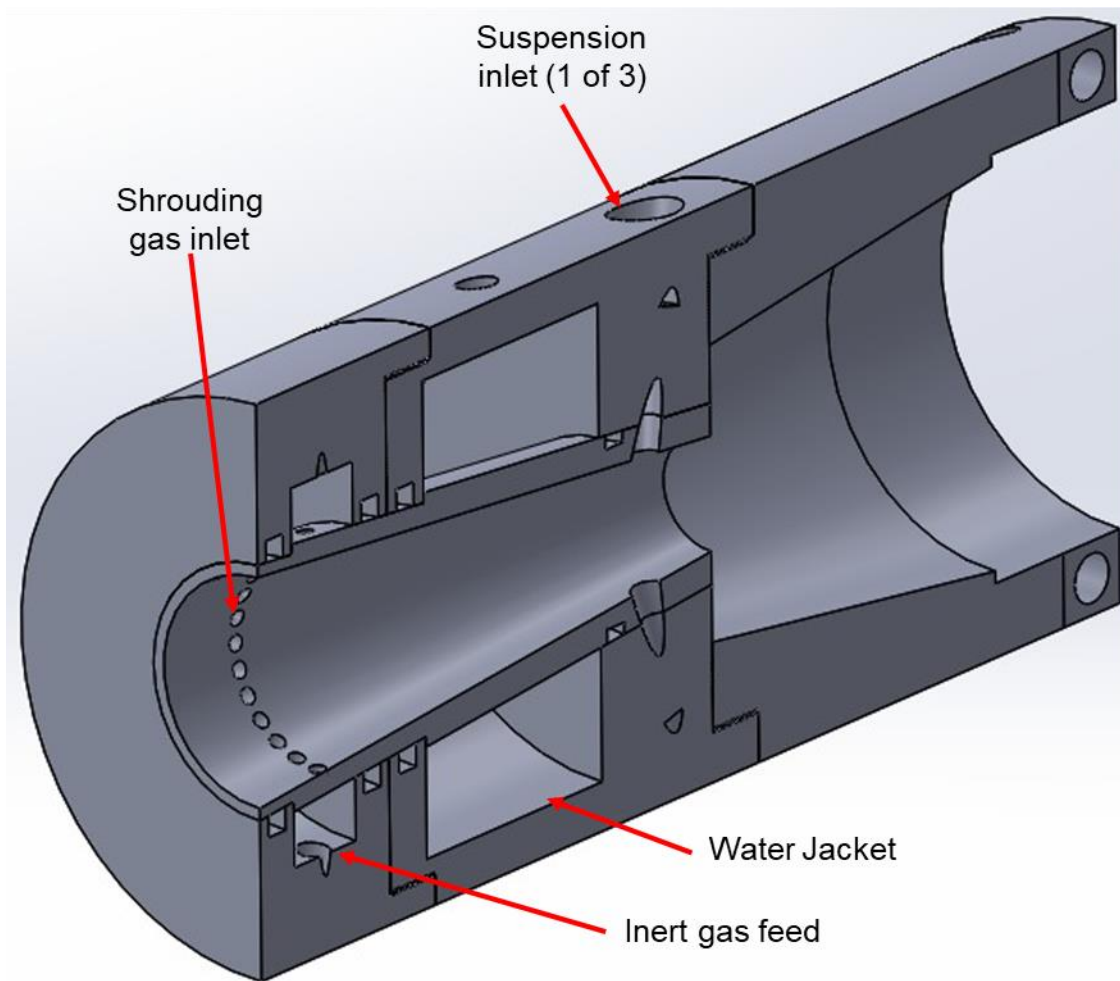


SECTION A-A

	<p>TOLERANCE LINEAR: ± 0.5 ANGULAR: ± 1</p> <p>ALL DIMENSIONS IN MILLIMETRES</p>												
<p>DRAFTING STANDARD 8888</p>		<p>MATERIAL CODE</p>		<p>PROCESS</p>		<p>ISSUE DATE</p>		<p>REV</p>		<p>DRAWN BY</p>		<p>DRAWING NO.</p>	
<p>MATERIAL</p>		<p>MODULE</p>		<p>SCALE 1:1</p>		<p>SIZE A4</p>		<p>SHEET 1 of 1</p>					







Appendix II – UDF and UDM Developed for Suspension High Velocity Oxy Fuel Thermal Spray

```
/*
*****
*/
/*      UDF      for      suspension      viscosity      model      */
/*
*****
*/

#include "udf.h"
#include "dpm_mem.h"

real U, R;

DEFINE_INIT(variable_setup,domain)
{
    /* if memory for the particle variable titles has not been
    *allocated yet, do it now */
    if (NULLP(user_particle_vars)) Init_User_Particle_Vars();
    /* now set the name and label */
    strcpy(user_particle_vars[0].name,"volume-fraction-particle");
    strcpy(user_particle_vars[0].label,"Volume Fraction Particle");
}

DEFINE_DPM_SCALAR_UPDATE(volume_fraction,cell,thread,initialize,tp)
{
    real Water;
    real Cr2O3 = 5520;
    real T = TP_T(tp);
    if (T <= 385)
    {
        Water = 815.88 + 1.5078*T - 0.003*T*T;
    }
}
```

```

    }
    if (T > 373)
    {
        Water = 961;
    }
    TP_USER_REAL(tp,0) = MIN((TP_COMPONENT_I(tp,1) * TP_MASS(tp)
/ Cr2O3) / (TP_MASS(tp) / TP_RHO(tp)), 1);
}

```

```

DEFINE_DPM_PROPERTY(viscosity,c,t,tp,T)

```

```

{
    /* get moisture fraction and store them */
    real C = MAX(1- TP_USER_REAL(tp,0),DPM_SMALL);
    real Water;
    if (T <= 385)
    {
        Water = 0.0153 - 0.0000811*T + 0.000000109*T*T;
    }
    if (T > 373)
    {
        Water = 0.000215;
    }
    real mu = Water * (1 + 2.5 * C + 14.1 * C * C);
    mu = MIN(mu, 1);
    return mu;
}

```

```

/*****
/*      UDM      for      suspension      drag      coefficient      */
*****/

#include "udf.h"
#include "dpm_mem.h"

real U, R;

DEFINE_DPM_DRAG(particle_drag_force,Re,tp)
{
    cell_t c = TP_CELL(tp);
    Thread *t = TP_CELL_THREAD(tp);
    real Cd0, drag_force, func_g, func_h, Ma, mw_mix=0;
    real mw[MAX_SPE_EQNS], yi[MAX_SPE_EQNS];
    int i=0;
    Material *mix, *sp;
    /* Set up molecular weight & mass fraction arrays */
    mix = THREAD_MATERIAL(t);
    if (Re < 0.01)
    {
        Cd0 = 24.0 / Re;
    }
    if (0.01 <= Re < 1.0)
    {
        Cd0 = 22.73 / Re + 0.0903 / pow(Re,2) + 3.69;
    }
    if (1.0 <= Re < 10.0)
    {
        Cd0 = 29.1667 / Re - 3.8889 / pow(Re,2) + 1.222;
    }
}

```

```

}
if (10.0 <= Re < 100.0)
{
    Cd0 = 46.5 / Re - 116.67 / pow(Re,2) +0.6167;
}
else if (Re >= 100.0)
{
    Cd0 = 98.33 / Re - 2778/ pow(Re,2) +0.3644;
}
mixture_species_loop(mix,sp,i)
{
    mw[i] = MATERIAL_PROP(sp,PROP_mwi);
    yi[i] = C_YI(c,t,i);
    mw_mix += yi[i] / mw[i]; /* value is inverse of MW */
}
real Td = TP_T(tp);
real Tc = C_T(c, t);
real Cp = C_CP(c,t);
U = sqrt(C_U(c,t) * C_U(c,t) + C_V(c,t) * C_V(c,t) + C_W(c,t) * C_W(c,t));
func_g = (1 + 12.278 * Re + 0.548 * pow(Re,2)) / (1 + 11.278 * Re);
R = UNIVERSAL_GAS_CONSTANT * mw_mix;
real gamma = Cp / (Cp - R);
Ma = U / sqrt(gamma * R * Tc);
func_h = (5.6 / (1 + Ma)) + 1.7 * pow(Td / Tc, 0.50);
real Cd = 2 + (Cd0 -2) * exp(-3.07 * sqrt(gamma) * func_g * Ma / Re) +
(func_h / (Ma * sqrt(gamma))) * exp(- Re / (2 * Ma));
drag_force = 18 * Cd * Re / 24;
return drag_force;
}

```

```

/*****/

/* UDM for the heat transfer coefficient accounting for the Knudsen number effects */

/*****/

#include "udf.h"
#include "dpm_mem.h"

real U, R;

DEFINE_DPM_HEAT_MASS(multivap,tp,Cp,hgas,hvap,cvap_surf,Z,dydt,dzdt)
{
    int ns;
    Material *sp;
    real dens_total = 0.0; /* total vapor density*/
    real P_total = 0.0; /* vapor pressure */
    int nc = TP_N_COMPONENTS(tp); /* number of particle components */
    Thread *t0 = TP_CELL_THREAD(tp); /* thread where the particle is in*/
    Material *gas_mix = THREAD_MATERIAL(DPM_THREAD(t0, tp)); /* gas
mixture
    material */
    Material *cond_mix = TP_MATERIAL(tp); /* particle mixture material*/
    cphase_state_t *c = &(tp->cphase[0]); /* cell information of particle location*/
    real molwt[MAX_SPE_EQNS]; /* molecular weight of gas species */
    real Tp = TP_T(tp); /* particle temperature */
    real mp = TP_MASS(tp); /* particle mass */
    real molwt_bulk = 0.; /* average molecular weight in bulk gas */
    real Dp = DPM_DIAM_FROM_VOL(mp / TP_RHO(tp)); /* particle diameter */
    real Ap = DPM_AREA(Dp); /* particle surface */
    real Pr = c->sHeat * c->mu / c->tCond; /* Prandtl number */
    real gamma = Cp / (Cp - R);
    real Ma = U / sqrt(gamma * R * c->temp);

```

```

    real Nu_0 = 2.0 + 0.6 * sqrt(tp->Re) * pow(Pr, 1./3.); /* incompressible Nusselt
number */

    real Nu = Nu_0 / (1 + 3.42 * Nu_0 * Ma / (tp->Re * Pr)); /* Kavanau Nusselt number
*/

    real h = Nu * c->tCond / Dp; /* Heat transfer coefficient*/
    real dh_dt = h * (c->temp - Tp) * Ap; /* heat source term*/
    dydt[0] += dh_dt / (mp * Cp);
    dzdt->energy -= dh_dt;

    mixture_species_loop(gas_mix,sp,ns)
    {
        molwt[ns] = MATERIAL_PROP(sp,PROP_mwi); /* molecular weight of gas
species */
        molwt_bulk += c->yi[ns] / molwt[ns]; /* average molecular weight */
    }
    /* prevent division by zero */
    molwt_bulk = MAX(molwt_bulk,DPM_SMALL);
    for (ns = 0; ns < nc; ns++)
    {
        int gas_index = TP_COMPONENT_INDEX_I(tp,ns); /* gas species index of
vaporization */
        if(gas_index >= 0)
        {
            /* condensed material */
            Material * cond_c = MIXTURE_COMPONENT(cond_mix, ns);
            /* vaporization temperature */
            real vap_temp = MATERIAL_PROP(cond_c,PROP_vap_temp);
            /* diffusion coefficient */
            real D = DPM_BINARY_DIFFUSIVITY(tp,cond_c,TP_T(tp));
            /* Schmidt number */
            real Sc = c->mu / (c->rho * D);

```

```

/* mass transfer coefficient */
real k = (2. + 0.6 * sqrt(tp->Re) * pow(Sc, 1./3.)) * D / Dp;
/* bulk gas concentration (ideal gas) */
real cvap_bulk = c->pressure / UNIVERSAL_GAS_CONSTANT / c->temp
* c->yi[gas_index] / molwt_bulk / solver_par.molWeight[gas_index];
/* vaporization rate */
real vap_rate = k * molwt[gas_index] * Ap
* (cvap_surf[ns] - cvap_bulk);
/* no vaporization below vaporization temperature, no condensation */
if (Tp < vap_temp || vap_rate < 0.0)
    vap_rate = 0.;

dydt[1+ns] -= vap_rate;
dzdt->species[gas_index] += vap_rate;
/* dT/dt = dh/dt / (m Cp)*/
dydt[0] -= hvap[gas_index] * vap_rate / (mp * Cp);
/* gas enthalpy source term */
dzdt->energy += hgas[gas_index] * vap_rate;

P_total += cvap_surf[ns];
dens_total += cvap_surf[ns] * molwt[gas_index];
}
}
/* multicomponent boiling */
P_total *= Z * UNIVERSAL_GAS_CONSTANT * Tp;
if (P_total > c->pressure && dydt[0] > 0.)
{
    real h_boil = dydt[0] * mp * Cp;
    /* keep particle temperature constant */

```

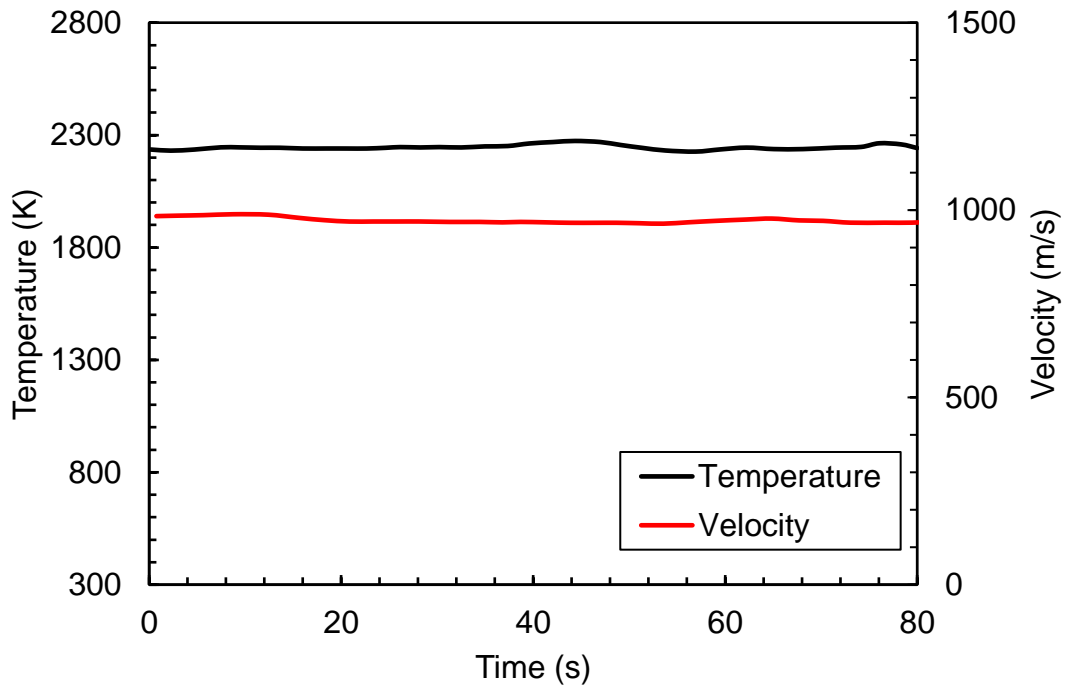
```

dydt[0] = 0.;
for (ns = 0; ns < nc; ns++)
{
  int gas_index = TP_COMPONENT_INDEX_I(tp,ns);
  if (gas_index >= 0)
  {
    real boil_rate = h_boil / hvap[gas_index] * cvap_surf[ns] *
      molwt[gas_index] / dens_total;
    /* particle component mass source term */
    dydt[1+ns] -= boil_rate;
    /* fluid species source */
    dzdt->species[gas_index] += boil_rate;
    /* fluid energy source */
    dzdt->energy += hgas[gas_index] * boil_rate;
  }
}
}
}

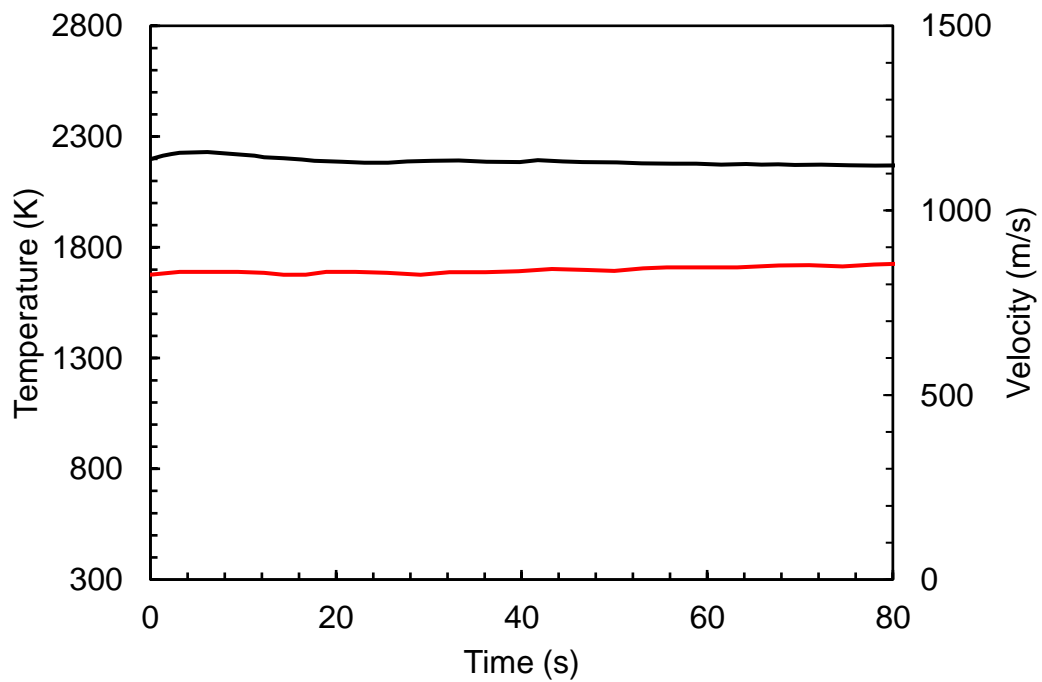
```

Appendix III – Time Varying Accuraspray

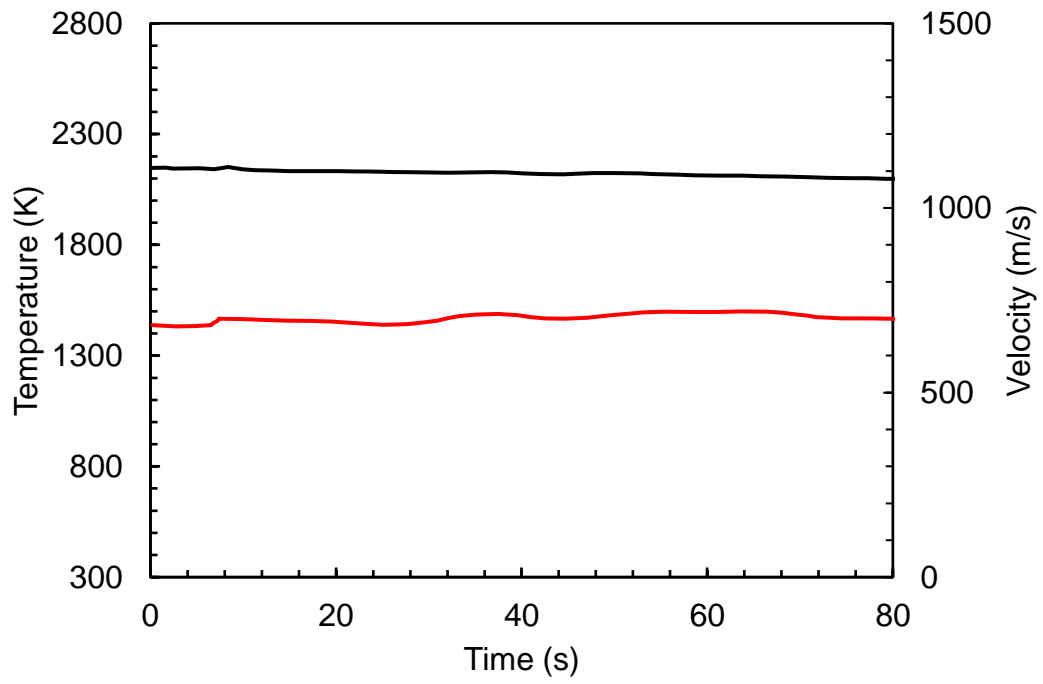
Measurements



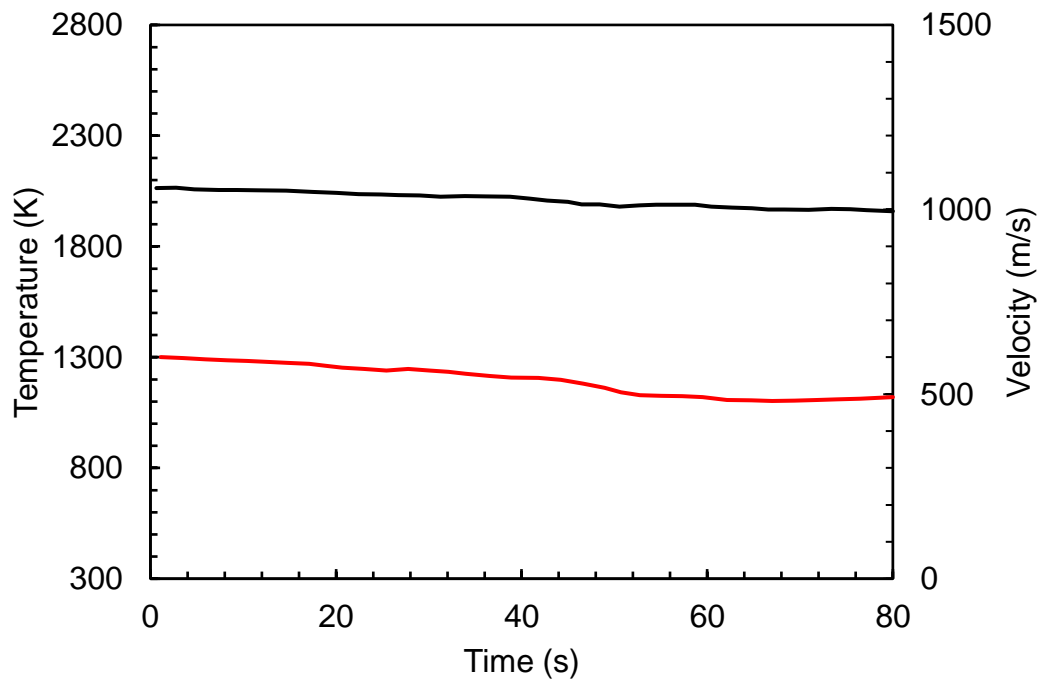
Ensemble average inflight velocity and temperature a stand-off distance of 75mm.



Ensemble average inflight velocity and temperature a stand-off distance of 100 mm.



Ensemble average inflight velocity and temperature a stand-off distance of 125 mm.



Ensemble average inflight velocity and temperature a stand-off distance of 150 mm.